# Genetic and Molecular Dissection of the Corkscrew Phosphatase in Synaptic Function and Neurological Disease

By

Shannon Nicole Leahy

Dissertation

Submitted to the Faculty of the

Graduate School of Vanderbilt University

In partial fulfillment of the requirements

for the degree of

DOCTOR OF PHILOSOPHY

in

Biological Sciences

August 9, 2024

Nashville, Tennessee

Approved:

Kendal Broadie, Ph.D

Katherine Friedman, Ph.D

Ege Kavalali, Ph.D

Douglas McMahon, Ph.D

Maulik Patel, Ph.D

# Acknowledgements

My work here at Vanderbilt would not have been possible without the support of various people within and outside the lab. First, I would like to acknowledge all those within the Vanderbilt Biological Sciences and Program in Developmental Biology for providing me with many wonderful training opportunities. Dr. Chris Wright especially worked tirelessly to foster a welcoming and stimulating academic environment. I would also like to thank those at the University of Notre Dame who first introduced me to the joys of research, Dr. Kevin Vaughan, Dr. Michelle Whaley, and Dr. Felicity Sterling. I will forever cherish those beginning years into research when every experiment, even if just weighing mice, felt like an exciting venture into the unknown.

I would especially like to thank my mentor Dr. Kendal Broadie for making me into the scientist I am today. I will forever be thankful for his guidance throughout this time. I would also like to thank all Broadie lab members including Emma Rushton, Dr. Jim Sears, Dr. Dominic Vita, Dr. Chunzhu Song, Dr. Danielle Golovin, Dr. Randy Golovin, Vanessa Miller, Nick Nelson, Nick Baumann, Arline Pierre-Louis, Darius Booth, Andrew Mellies, and Aashi Gurijali and all of whom I have had the pleasure and honor of working with. Without all of you lab would have been a lot less fun. I would especially like to thank Emma Rushton, Dr. Jim Sears, and Dr. Dominic Vita for advising me throughout this project.

Finally, I would like to thank all my friends and family outside the lab who helped keep me sane throughout the more stressful parts of this dissertation. I would especially like to thank my parents for continuing to pick up the phone when I was panicking over the trivial things. I appreciate them for always being there for me, nurturing my love for science, and encouraging me to pursue this PhD. I would not have made it here without your constant support.

**Funding:** MH084989; 5R01AR068128-08; T32 PDB Training Grant, Gisela Mosig Fund

Introduction Figures created using Biorender.

## Table of Contents

**Chapters**

## List of Figures

**Figure** **Page**

## List of Tables

## List of Abbreviations

| | |
|---|---|
| ANOVA | analysis of variance |
| AZ | active zone |
| BDSC | Bloomington *Drosophila* Stock Center |
| BRP | bruchpilot |
| BSA | bovine serum albumin |
| CAMKII | calmodulin-dependent protein kinase II |
| CNS | central Nervous System |
| csw | corkscrew |
| dfmr1 | *Drosophila* fragile X mental retardation 1 |
| DMSO | dimethylsulfoxide |
| Dlg | discs-large |
| EAAT | excitatory amino acid transporters |
| EJC | excitatory junction current |
| Elav | embryonic lethal abnormal vision |
| ERK | extracellular signal-regulated kinase |
| FMRP | Fragile X Mental Retardation Protein |
| Fmr1 | fragile X mental retardation 1 |
| FXS | Fragile X syndrome |
| GAPDH | glyceraldehyde 3-phosphate dehydrogenase |
| GoF | gain-of-function |
| GluR | glutamate Receptor |
| HFS | high frequency stimulation |
| hiPSC | human induced pluripotent stem cell- |
| HRP | horseradish peroxidase |
| JMML | Juvenile myelomonocytic leukemia |
| JNK | c-Jun N-terminal kinase |
| KH | K homology |
| KO | knockout |
| LLPS | Liquid–Liquid Phase Separation |
| LoF | loss-of-function |
| LTD | long-term depression |
| LTM | long-term memory |
| LTP | long-term potentiation |
| MAPK | mitogen-activated protein kinase |
| mEJC | miniature excitatory junction current |
| NES | nuclear export signal |
| NLS | nuclear localization signal |
| NMJ | neuromuscular junction |
| NS | Noonan syndrome |
| NSML | Noonan syndrome with multiple lentigines |
| PCC | Pearson correlation coefficient |
| pERK | phosphorylated extracellular signal-regulated kinase |
| PG | perineurial glia |
| PKA | protein kinase A |

| | |
|---|---|
| PKC | protein kinase C |
| PPR | paired-pulse ratio |
| PTP | protein tyrosine phosphatase |
| PTPN11 | protein tyrosine phosphatase non-receptor type 11 |
| RBP | RNA binding protein |
| RGG | arginine-glycine-glycine |
| RIP | RNA immunoprecipitation |
| RNAi | RNA interference |
| ROI | region of interest |
| RRP | readily releasable pool |
| SC | sodium cacodylate |
| SH2 | Src Homology 2 |
| SHP2 | SH2 domain containing protein tyrosine phosphatase-2 |
| SPG | subperineurial glia |
| SSR | subsynaptic reticulum |
| SV | synaptic vesicle |
| SYN | synapsin |
| TD | tudor domain |
| TBST | tris-buffer saline with 0.1% Tween-20 |
| TEM | transmission electron microscopy |
| TEVC | two electrode voltage-clamp |
| TRiP | Transgenic RNAi Project |
| UAS | upstream activating sequence |
| vglut | vesicular glutamate transporter |
| VNC | ventral nerve cord |
| WG | wrapping glia |

# Chapter I

## Introduction

Cognition is the fundamental mental process of acquiring and understanding knowledge. This core function is mediated by the central nervous system (CNS), which is composed of neural circuits. These circuits are neurons communicating via intercellular connections called synapses. Synapses are signaling junctions that translate electrical action potentials into the fusion of neurotransmitter-filled vesicles with the cell membrane. This results in neurotransmitter release and binding to postsynaptic receptors to propagate the signal forward. The amino acid glutamic acid (glutamate) is the primary excitatory neurotransmitter mediating cognition signaling. Genetic perturbations in this synaptic connectivity function lead to a wide range of neurological diseases,[1] including Fragile X syndrome (FXS)[2] and Noonan syndrome (NS).[3,4] Both of these disease states cause cognitive impairment via well-defined single gene mutations. The aim of my dissertation was to test for putative intersecting synaptic roles, including mechanisms that go awry in both single and combined disease models, and determine whether targeted genetic and pharmaceutical interventions could restore normal synaptic function. *Drosophila* models for both FXS and NS disease states are well-established, and the *Drosophila* neuromuscular junction (NMJ) has been used as a glutamate synapse model for nearly 50 years. I therefore employed this system for all of my dissertation studies.

## The *Drosophila* Neuromuscular Junction

### Overview

*Drosophila* has been indispensable for the discovery of conserved cellular and molecular mechanisms central to both normal physiology and a vast spectrum of heritable disease states. Five Nobel Prizes, which are awarded to those who “conferred the greatest benefit to humankind,” have recognized *Drosophila* research, ranging from the mechanisms of chromosomal inheritance (1933) to the control of daily circadian rhythms (2017). *Drosophila* discoveries are facilitated by a short life cycle, reduced genetic complexity, and wealth of sophisticated genetic tools.[5,6] One such tool is the UAS/Gal4 system for targeted gene expression which exploits the yeast Gal4 transcriptional activator downstream of a tissue-specific promoter, such as the neuron-specific *elav* (*embryonic lethal abnormal vision*) gene.[7,8] The Gal4 recognizes an Upstream Activating Sequence (UAS) in transgenic constructs for controlled expression or RNA interference (RNAi) knockdown, for example specifically in neurons.[9] By utilizing this system human genes can be expressed in *Drosophila* to study disease-causing mutations. Moreover, >75% of human disease genes have functional homologs in *Drosophila* making it an exceptional model for most disease states.[10] In particular, many neurological diseases have been modeled in *Drosophila*, ranging from neurodevelopmental to neurodegenerative conditions. Since these disease states are caused predominantly by synaptic dysfunction, the *Drosophila* NMJ has long been a core component of disease modeling. This well-established glutamate synapse model shares striking similarities to the glutamatergic synapses of the mammalian CNS,[11] although synapses are formed between a presynaptic motor neuron and postsynaptic muscle. The functions of action potentials voltage changes across the membrane,[12] depolarization-dependent synaptic vesicle (SV) fusion at the specialize active zone (AZ) membrane sites,[13] and glutamate neurotransmitter release into the synaptic cleft to bind postsynaptic glutamate receptors[11] are all highly conserved. The large presynaptic boutons and postsynaptic syncytial muscle allow easy visualization and manipulation for studying synaptic properties, including both synaptic structure and function.

### ***Drosophila* NMJ structure**

In the *Drosophila* larva, 36 motor neurons project from each hemisegment of the ventral nerve cord (VNC; analogous to mammalian spinal cord) to form peripheral motor nerves, and then defasciculate at specified branch points to synapse onto specific muscle targets. Each motor neuron and muscle are individually identified with a fully characterized developmental lineage and specific name. The invariant innervation between animals allows for comparisons across genotypes.[14] The motor neuron axon contacts the muscle in large varicosities called synaptic boutons. Three bouton classes are distinguished based on morphology, composition, and postsynaptic elaboration.[11]

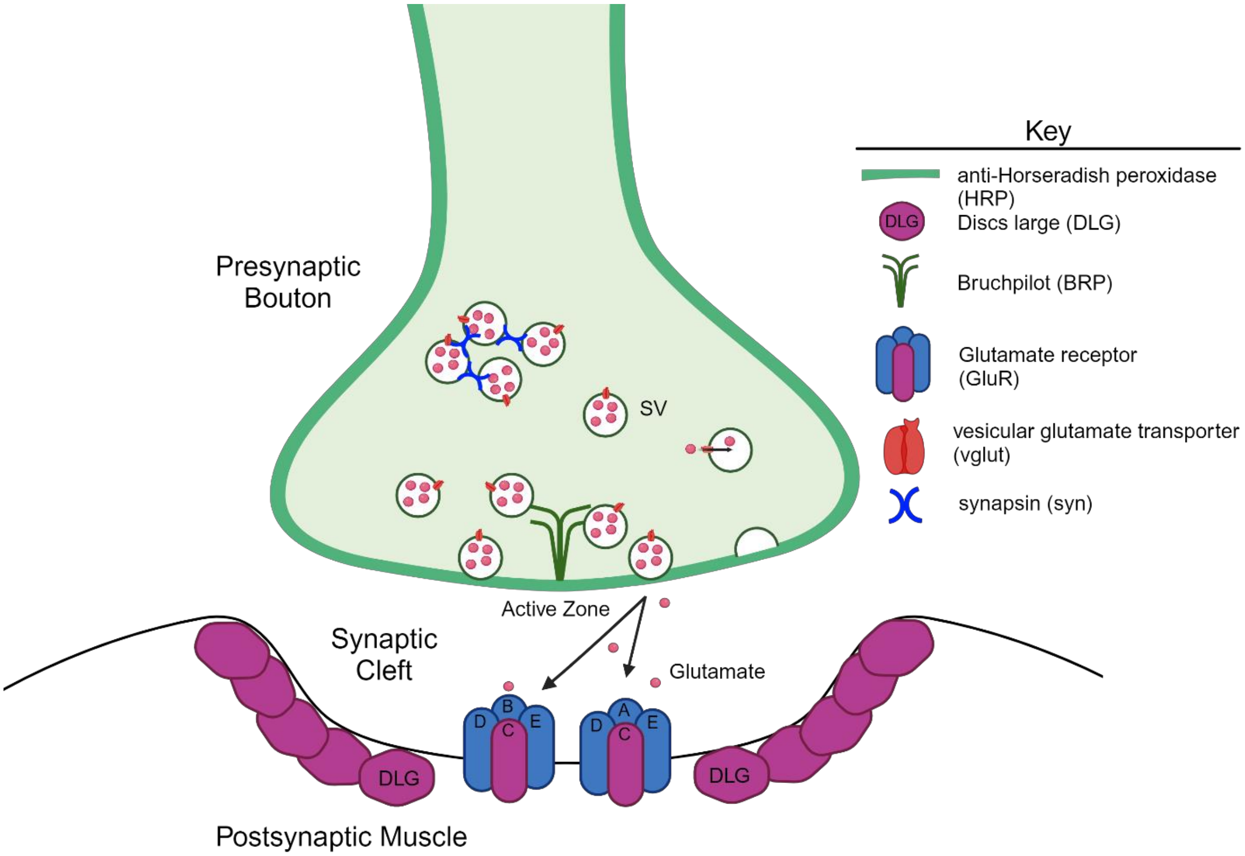

**Figure 1.1: *Drosophila* Neuromuscular Junction (NMJ) Glutamatergic Model Synapse**
A graphical representation of the *Drosophila* NMJ. The presynaptic bouton membrane can be marked via anti-horseradish peroxidase (HRP). In the presynaptic bouton the active zone (AZ) "T-bar" is assembled primarily from Bruchpilot (BRP) which localizes synaptic vesicles (SVs) filled with glutamate. In response to an action potential SVs fuse with the membrane and glutamate is released into the synaptic cleft. Glutamate activates the four subunit glutamate receptors (GluRs) that are stabilized by the scaffold Disc Large (Dlg) in the postsynaptic muscle. Via endocytosis SVs are reformed and refilled with glutamate by the vesicular glutamate transporter (vglut) which is present on all SVs. Synapsin (syn) sequesters a subset of SVs from fusing in response to action potentials until a threshold of activity is reached.

Neurons with type I boutons form a 1-to-1 relationship with each muscle and are subcategorized into type Ib (big; 3-6 um) and type Is (small; 2-4 um;[15]). Type Ib has an extensive postsynaptic subsynaptic reticulum (SSR) of muscle membrane folds, whereas type Is has minimal SSR. Neurons with modulatory type II (1-2 um) and type III (2-3 um) synaptic boutons contain dense core vesicles of slower-acting neuropeptides and biogenic amines, lack SSR, and are present on a small subset of muscles.[11,15] Type I boutons have a high active zone (AZ) density with a T-bar architecture, whereas type II/III

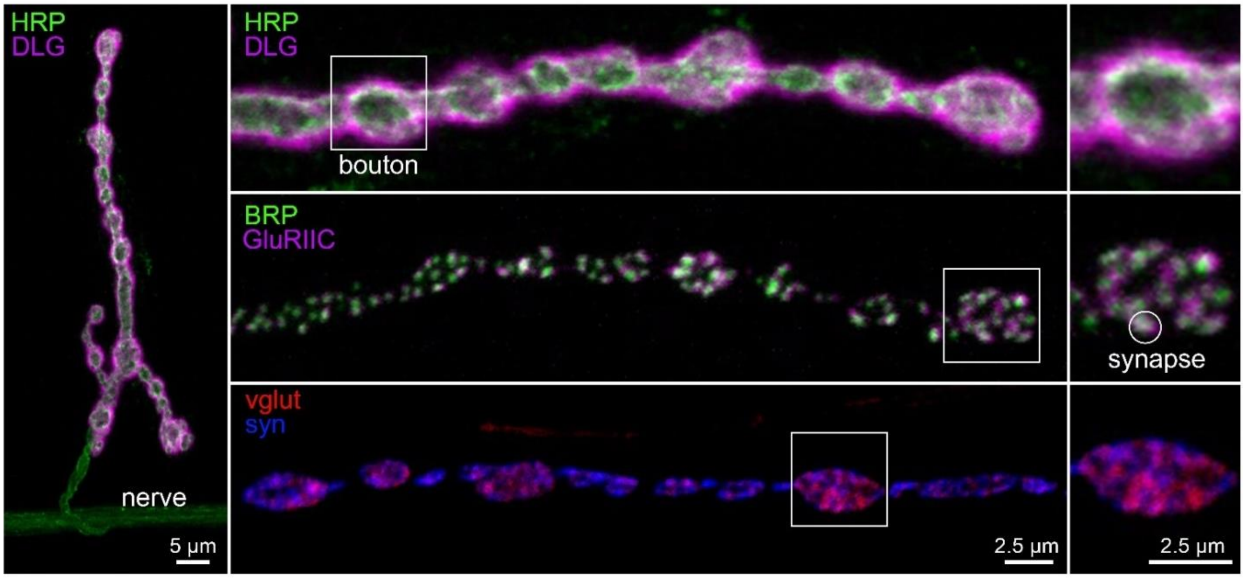

**Figure 1.2: Immunocytochemistry of synaptic architecture at the *Drosophila* NMJ**
Visualization of several structural components at the wandering third instar muscle 4 NMJ. Left: The entirety of the NMJ with presynaptic membrane marked with anti-horseradish peroxidase (HRP) and postsynaptic membrane marked with Disc Large (Dlg). Top Right: A magnified image of representative boutons of the NMJ marked with HRP and Dlg. Middle Right: Representative boutons with anti-bruchpilot (BRP) marking presynaptic active zones and anti-glutamate receptor subunit C (GluRIIC) marking corresponding postsynaptic glutamate receptors. Together these antibodies mark functional synapses. Bottom Right: Presynaptic synaptic vesicles (SVs) marked with anti-vesicular glutamate transporter (vglut) and SV associated phosphoprotein anti-synapsin (syn).

boutons have fewer AZs and lack T-bars.[16] AZs contain the Bruchpilot (Brp; human homologue ELKS/CAST) scaffold[15] and the apposing postsynaptic muscle domains contain the Discs Large (Dlg; human homologue PSD-95) scaffold.[11,17,18] Two ionotropic glutamate receptor (GluR; human homologue AMPA-type GluRs) classes[11,18] are distinguished based on the presence of either GluRIIA or GluRIIB subunits alongside three essential subunits (GluRIIC, D, and E).[19] The variable subunits confer differing neurotransmission current amplitudes and plasticity properties.[20] These synaptic components are schematized in Figure 1.1.

I have used the above synaptic bouton categories, ultrastructural features, and molecular markers to quantify NMJ synaptic structure, including synaptic area, branch number, and bouton number.[21] With immunofluorescence and confocal microscopy, I use anti-horseradish peroxidase (HRP) antibody, which recognizes a presynaptic membrane glycan, together with the anti-Dlg antibody, which marks the postsynaptic SSR.[11,21] In

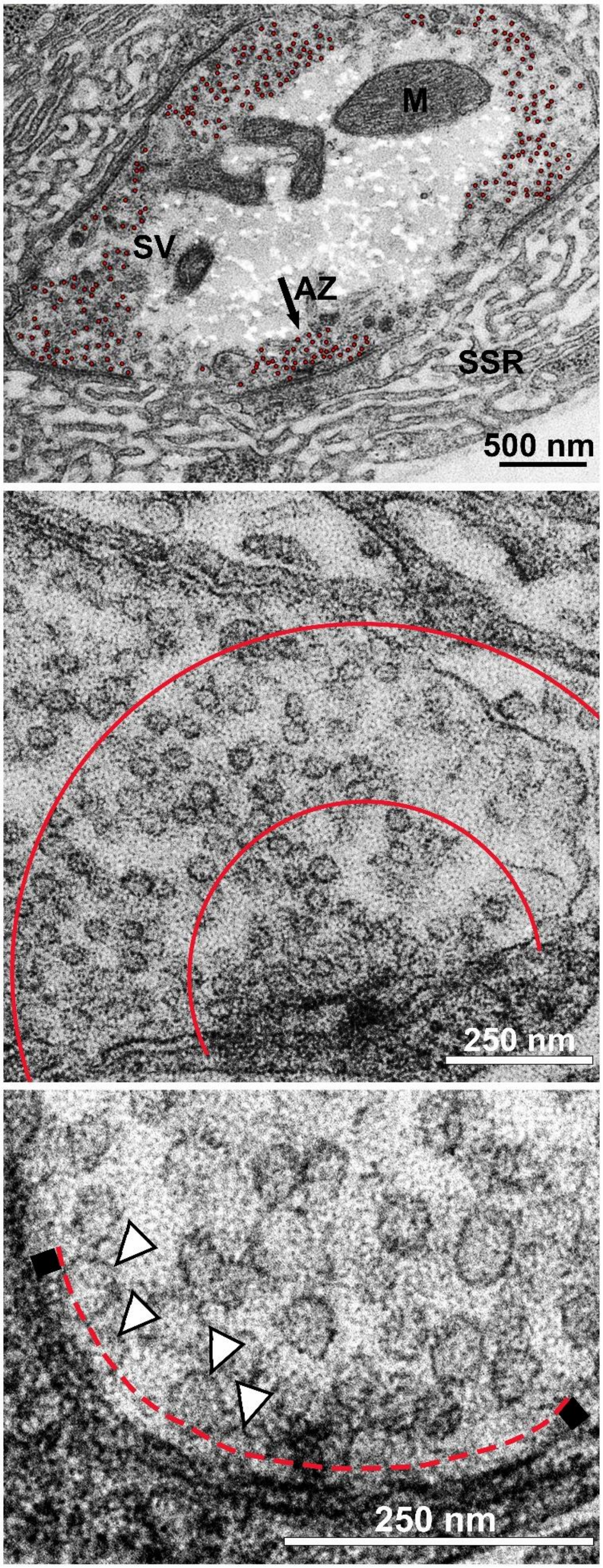

**Figure 1.3: Ultrastructural analysis of synaptic architecture at the NMJ** Transmission electron microscopy (TEM) allows for the visualization of synaptic vesicles (SVs) of type Ib boutons. Top: A representative image of a synapse with all SVs marked with a red dot. Abbreviations: synaptic vesicle (SV), active zone (AZ), subsynaptic reticulum (SSR), and mitochondria (M). Middle: A representative active zone displaying SVs within 0-200 nm and 200-400 nm of the middle of the presynaptic membrane density as marked by the T-bar. Bottom: Higher magnification of the presynaptic membrane density containing an active zone t-bar with docked SVs, or SVs within <20nm of the membrane, marked with an arrow.

addition to mature boutons, I have quantified immature satellite boutons newly budded from these boutons.[11,22] Synapses can measured with anti-Brp antibody for presynaptic AZs[21] and anti-GluR antibodies for postsynaptic specializations.[23] Synaptic vesicle pools can be quantified with anti-vesicular glutamate transporter (vglut) antibody,[24] or associated markers such as anti-synapsin (syn).[24] Representative immunofluorescence images are shown in Figure 1.2. Synapses can be assayed at the ultrastructural level using transmission electron microscopy (TEM) for visualization of SV pools, presynaptic AZs, and postsynaptic SSR.[25,26] To further characterize SV distribution, numbers and densities can be analyzed.[25] The electron-dense T-bar is surrounded by a more extensive electron-dense presynaptic membrane specialized for vesicle fusion.[17,22,27] SV pool identity can be inferred based on the relative distance away from fusion competent membrane.[25] To measure SV docking, all vesicles within ½ vesicle diameter of this presynaptic density can be counted.[28–31] Representative TEM images with quantification methods are shown in Figure 1.3.

## Drosophila NMJ Glia

The NMJ is a tripartite synapse consisting of the presynaptic neuron, postsynaptic muscle, and perisynaptic glia.[11] Glia cells were traditionally thought to be support cells or "glue" within the central and peripheral nervous system. However, this cell type has been increasingly appreciated to be involved in various fundamental processes including maintaining ion homeostasis, regulating neurotransmitter levels at the synapse, and remodeling via engulfment and phagocytosis.[32] These processes are done by different glial subtypes. In the *Drosophila* peripheral nerve there has been reported to be three subtypes: subperineurial glia (SPG), perineurial glia (PG) and wrapping glia.[32] In the nerve the PG is the outermost glial layer, followed by SPG which establishes a diffusion barrier via septate junctions.[33] Together, the PG and SPG form the blood-brain barrier.[33] The innermost glial layer is the wrapping glia, a specialized peripheral glial cell type which enwraps all motor axons similar to non-myelinating Schwann cells in the mammalian peripheral nervous system.[32–34] Only SPG and PG have been reported to be present at the NMJ with neither subtype fully encapsulating any boutons.[32] The various glia subtypes at the VNC and NMJ can be visualized in Figure 1.4. At the NMJ SPG have been reported to be involved in modulating neurotransmission via wingless and Delta/Notch signaling in what appears to be independent pathways.[35,36] PG have no current reported roles at NMJ. Throughout this dissertation we utilize the UAS/Gal4 system to restrict or knockdown expression of NS and NSML genes specifically to glia. Before this dissertation work, these genes were not thought to have glial roles outside of the initial generation of glial cells or in an injury specific model.[37] The reversed polarity (repo) Gal4 allows for specific expression in all glia.[33] This specific Gal4 driver allows for a holistic look at glial NMJ function, regardless of glial subtype, although subtype specific Gal4 lines have been generated.

## Drosophila NMJ Function

The most direct way to test synaptic function at the NMJ is two-electrode voltage-clamp (TEVC) electrophysiology, a technique where membrane potential is controlled to study GluR ionic currents during neurotransmission.[38,39] In this recording configuration, two microelectrodes are inserted into the muscle to clamp at a set voltage. One microelectrode senses the membrane voltage, while the other injects current to maintain the clamped voltage.[38,39] The motor nerve is cut near the VNC to allow for directed control of signaling. Action potential-independent events, known as spontaneous events or miniature excitatory junctional currents (mEJCs), can be recorded in the absence of stimulation.[21,38] The frequency of these events is indicative of presynaptic SV fusion probability,[40] while the amplitude is indicative of postsynaptic response to individual SV fusion events.[40] Utilizing a suction (stimulating) electrode, the motor nerve can be stimulated to elicit an, action potential-dependent, excitatory junctional current (EJC).[21,38] The TEVC recording configuration with example mEJC and EJC traces is displayed in Figure 1.5. The stimulation paradigm can be changed to analyze basal neurotransmission as well as responses to high frequency stimulation (HFS) conditions leading to synaptic facilitation and/or depression.[41–43] Varying the frequency strength allows for investigation of functionally separate SV pools as well as different forms of synaptic plasticity.

Presynaptic activity drives modifications in release mechanisms leading to various forms of short and long-term synaptic plasticity.[44,45] Different forms of synaptic plasticity are favored depending on the type of synapse.[46,47] At the *Drosophila* NMJ high external [$Ca^{2+}$] combined with strong stimulation results in short-term neurotransmission depression. This is driven by exhaustion or impairment of SVs available for fusion. One key role for short-term depression is mediating sensory adaption or allowing diminished responses to novel stimulation.[48] In contrast, with reduced external [$Ca^{2+}$] at the NMJ, many forms of release strengthening are revealed, including short-term facilitation (<1 second), and maintained augmentation (>5 seconds) during stimulation trains, and post-tetantic potentiation following the train. [43,47,49] These various forms of short-term facilitation help

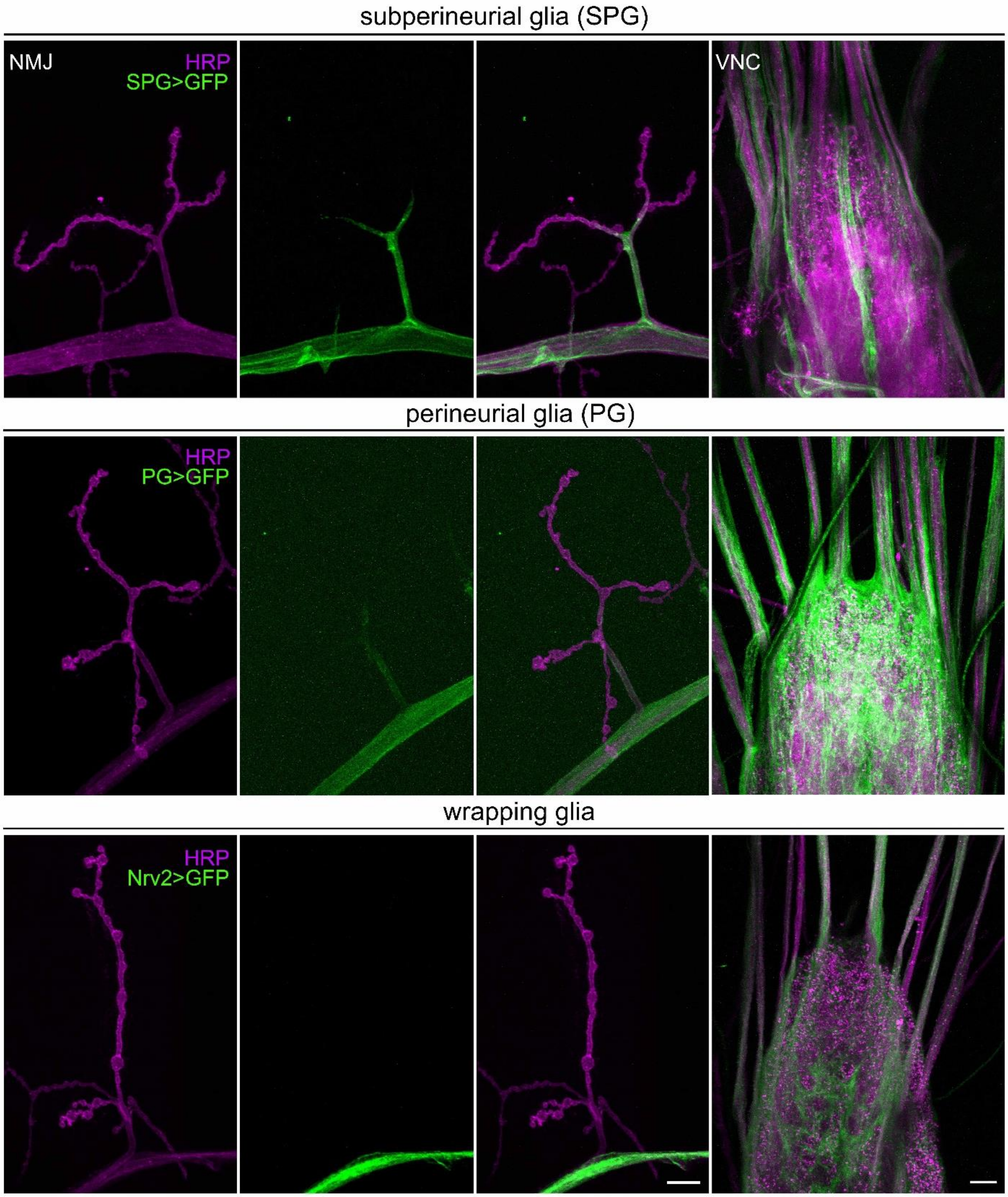

**Figure 1.4: Immunocytochemistry of glial subtypes at the *Drosophila* NMJ**
There are three glial subtypes present at the NMJ, the subperineurial glia (SPG), perineurial glia (PG), and wrapping glia. Left: The muscle 4 NMJ marked with HRP (magenta) and various glia subtype Gal4 driving GFP for visualization. SPG and PG infiltrate the NMJ, while the wrapping glia is only within the nerve. Right: The VNC marked with HRP (magenta) and various glia subtype Gal4 driving GFP for visualization. All glial subtypes are present within the VNC and motor neurons. Scale bars are 10 um.

strengthen synaptic connections and often act together with short-term depression to enhance or impair information transfer.[42,50] If either of these forms of plasticity persist, leading to sustained changes in synaptic strength, then long-term potentiation (LTP) or long-term depression (LTD) occur.[51] LTP and LTD have been demonstrated to be the basis of learning and memory.[52,53] Deficiencies in these forms of synaptic plasticity are thought to be the basis of various neurological diseases.[51] These changes in synaptic function are driven by perturbations in SV dynamics.

Synaptic vesicles can be functionally defined into different pools, including the readily releasable pool (RRP), the recycling pool, and the reserve pool.[54,55] The RRP represents SVs that are immediately releasable upon stimulation, making the RRP size the deciding factor in the functional response magnitude.[54,56] The RRP is the smallest of the pools, at the *Drosophila* NMJ it is ~0.4% of total SVs, and it is quickly depleted.[54] These SVs are morphologically docked at the AZ and molecularly primed for exocytosis.[11] Docked SVs can be visualized via TEM measurements, but not all docked vesicles are primed, so not all docked SVs are contributing to the RRP. Additionally, there is some evidence the RRP may include nearby SVs that do not appear docked.[56] A functional method of measurement is HFS that results in the immediate fusion of the RRP followed by replenishment from the recycling pool.[57] This method assumes replenishment is constant and utilizes known quantities of synaptic function to calculate RRP size.[50] Since all current RRP measurements can under or overestimate the true pool multiple forms of measurement are often necessary.

The RRP is replenished from the SV recycling pool, which makes up 14-19% of all SVs at the *Drosophila* NMJ.[54,58] The recycling pool can maintain release with moderate stimulation, as this pool “recycles” SVs via endocytosis. Endocytosis is the process of recovering SV membrane from the plasma membrane after exocytosis. There are multiple forms of vesicle endocytosis, including clathrin-mediated, fast compensatory, activity-dependent bulk, ultrafast, and kiss-and-run.[59] Except for kiss-and-run neurotransmission, all of these forms of endocytosis involve full fusion of the SV with the plasma membrane followed by variable membrane retrieval. Which form of endocytosis predominates is dependent on the stimulation/activity conditions, the endocytic membrane kinetics, and possibly additional factors.[59] Under most physiological conditions the recycling pool can

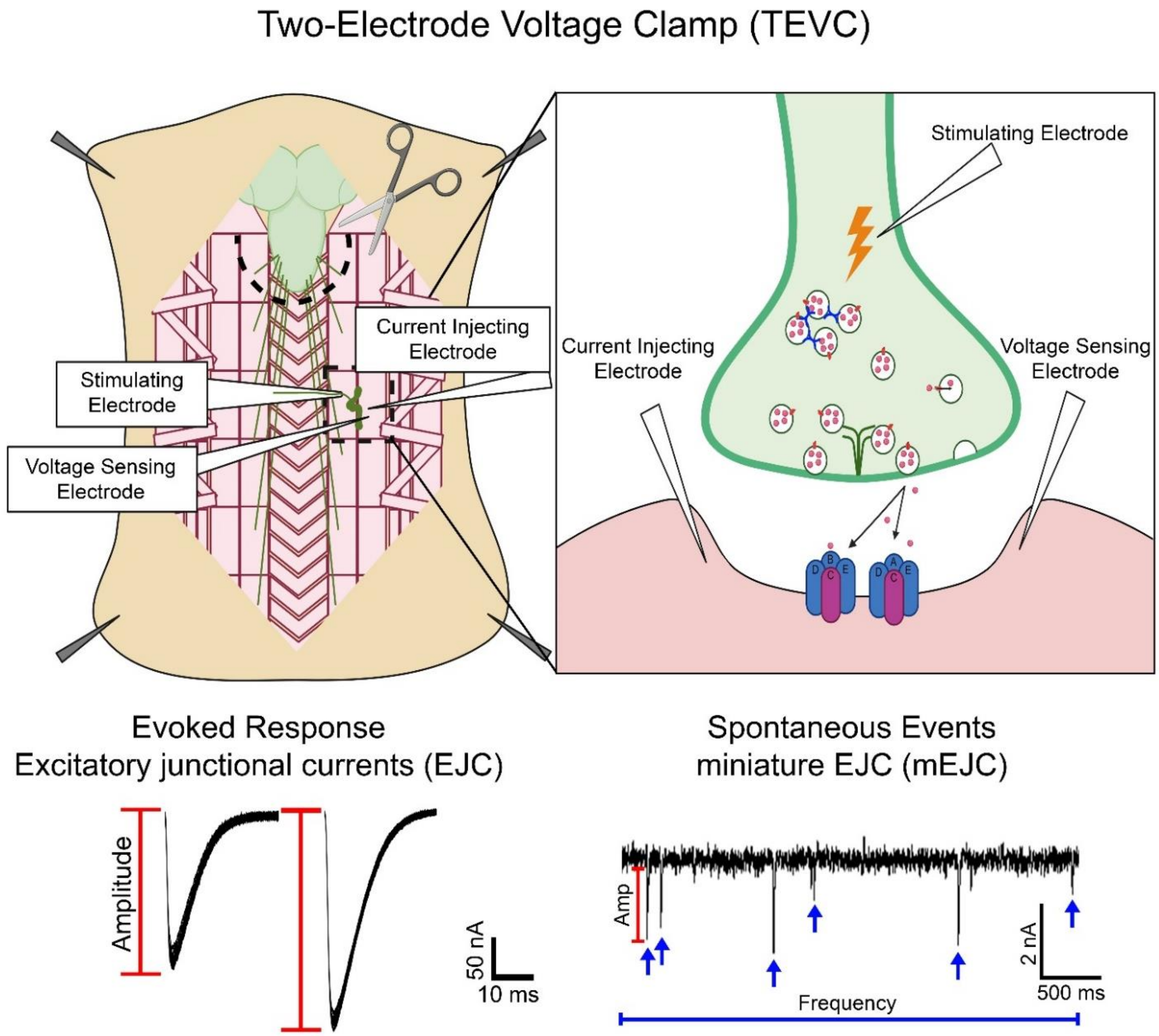

**Figure 1.5: TEVC electrophysiology allows for analysis of synaptic function**
Two-electrode voltage clamp (TEVC) electrophysiology at the *Drosophila* NMJ allows for analysis of action potential dependent and independent glutamatergic synaptic signaling. Top Left: An illustration of a dissected open wandering third instar larvae in the TEVC configuration. In this set up the VNC is removed leaving nerves available to be picked up via the stimulating (suction) electrode for a segment of interest. The current injecting and voltage sensing electrodes are embedded in muscle 6 in a segment of interest. Top Right: An illustration of a single synapse within muscle 6 highlighting the stimulating electrode is stimulating the presynaptic neuron while the other electrodes measure changes within the postsynaptic muscle. Bottom Left: Two representative basal action potential evoked responses, each is a summation of 10 traces. Changes in amplitude indicate changes in overall neurotransmission. Bottom Right: Representative action potential independent events from a single trace. Changes in amplitude indicate a change in receptor response or quanta released from single SVs. Changes in frequency indicate changes in SV fusion probability.

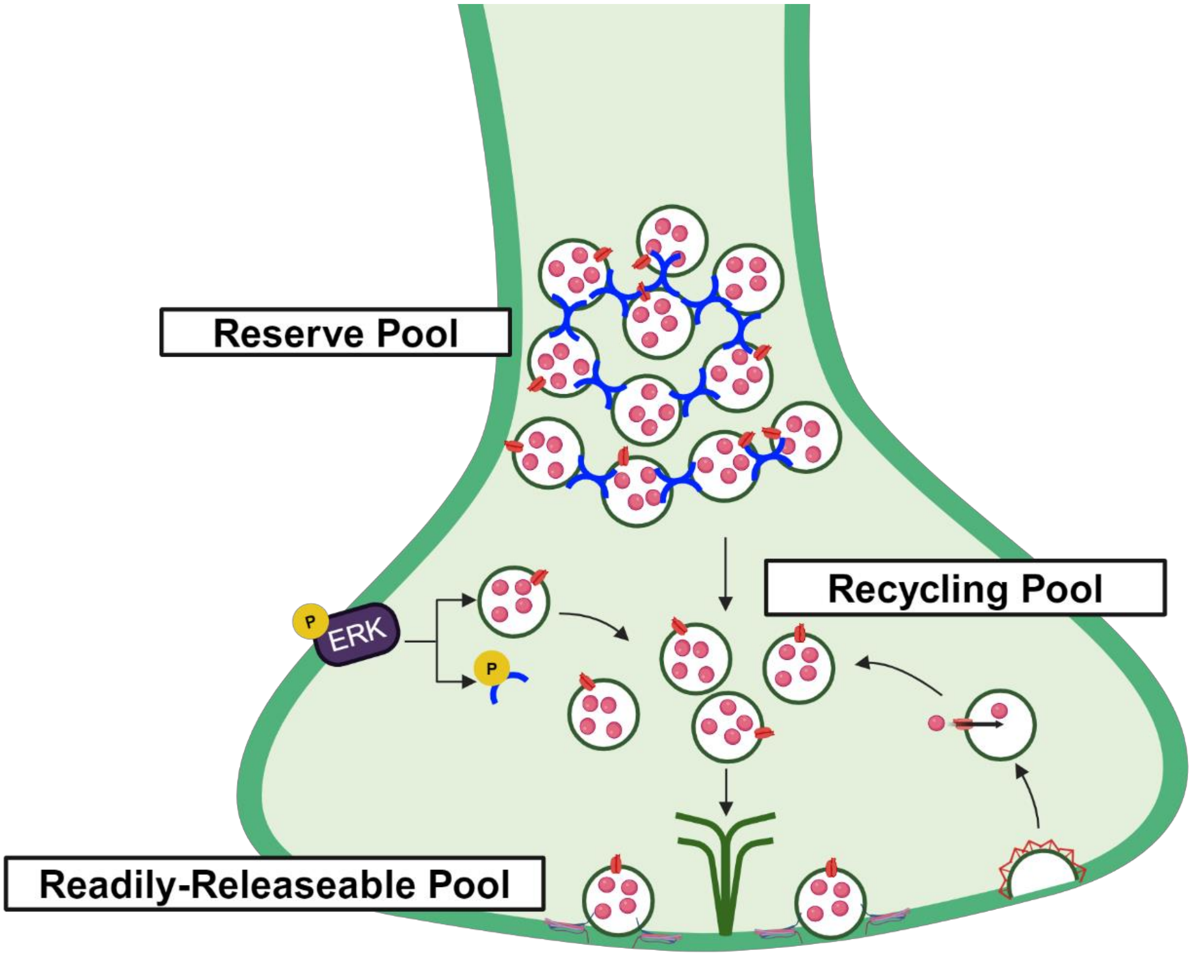

**Figure 1.6: Synaptic Vesicles (SVs) are functionally divided into three vesicle pools**
A graphical schematic of the three SV pools. The reserve pool contains the bulk of SVs and is held in “reserve” until other SV pools are depleted. Current evidence indicates that synapsin (syn) binds reserve SVs to each other making them unrecruitable via an action potential. With enough stimulation different signaling pathways, including the MAPK/ERK pathway, will phosphorylate syn and allow these SVs to mix with other pools. The recycling pool refills SVs with glutamate and can be recruited to the readily releasable pool (RRP). The RRP is the smallest pool and consist of docked and primed SVs in the active zone.

maintain neurotransmission. The reserve pool is recruited in intense HFS conditions that deplete the recycling pool. The reserve pool contains the bulk of SVs, about 80% of all SVs at the *Drosophila* NMJ, however recruitment of this pool remains poorly characterized.[54,55] The reserve pool is not clearly distinguishable from the recycling pool using imaging techniques, although reserve pool SVs are thought to be most distal to the AZ.[25,60,61] Synapsin (Syn) acting as a SV tether is perceived to maintain the reserve pool.[61–63] The *syn* triple knockout (KO) mouse model to eliminate the protein, loses distal

SVs with no change in docked SVs, indicating specific disruption of the reserve pool.[63,64] Additionally, these mice have normal basal glutamatergic neurotransmission, indicating a normal RRP, but are unable to maintain HFS function, indicating a disrupted reserve pool.[63,64] The current model suggests Syn crosslinks reserve pool SVs at rest, with HFS conditions resulting in Syn being phosphorylated and disassociates from SVs allowing plasma membrane recruitment.[62] The reserve pool can be analyzed functionally with sustained HFS,[65–67] or visualized via immunofluorescence by examining the overlap of anti-Syn and an SV marker.[24,68] A simple SV pool schematic is shown in Figure 1.6.

## Neuronal Diseases with Disrupted MAPK/ERK Signaling

### MAPK/ERK Signaling

Regulation of synaptic plasticity through modulation of SV pool dynamics is dependent on various signaling pathways throughout an organism's lifespan. Key kinase signaling pathways that modulate neurotransmission strength to control synaptic plasticity include protein kinase A (PKA), calmodulin-dependent protein kinase II (CAMKII), protein kinase C (PKC), and microtubule-associated protein kinase/extracellular regulated kinase (MAPK/ERK).[69] This last pathway involves initial activation of Ras/Rac GTPases and a subsequent three-tiered kinase signaling cascade for transduction of extracellular information into intracellular responses.[70,71] Four MAPK families are characterized, including ERK 1/2, ERK5, p38 MAPK, and the c-Jun N-terminal kinase (JNK).[70,71] The best characterized MAPK pathway (ERK1/2, henceforth referred to as the MAPK/ERK pathway) has been extensively investigated in the nervous system, where ERK activation is very tightly regulated.[52,69,72] The endpoint is ERK phosphorylation (pERK), with the best described consequence of transcription factor regulation within the nucleus.[71] In synaptic boutons, pERK has another local role in phosphorylating Synapsin leading to its dissociation from reserve pool SVs.[73–75] Numerous neurological disease states display elevated ERK activity,[52,76] and many studies link such elevated ERK signaling to cognitive deficits, particularly impairment of long-term memory (LTM) consolidation.[53,69,77,78] LTM requires spaced learning sessions during which ERK is activated and then decays in a temporal cycle. In this dissertation, I study perturbations in the MAPK/ERK pathway in the following *Drosophila* disease state models.

## Noonan Syndrome

Noonan syndrome (NS) is an autosomal dominant disorder first described by Jacqueline A. Noonan in 1968.[79] NS effects 1:1000-2500 individuals, making it the most common RASopathy, a group of genetic conditions characterized by mutations in the MAPK/ERK signaling pathway.[80,81] Patients present heterogeneously in symptoms of short stature (70%), craniofacial abnormalities, cardiac defects (most common: pulmonary valve stenosis), skeletal deformities, and behavioral cognitive defects. Currently there is no consensus on clinical diagnostic criteria, however these above symptoms are indicative of NS.[80,81] Other associated symptoms include developmental delay, deafness, as well as cutaneous, metabolic, lymphatic, and bleeding defects. Patients are diagnosed via genetic testing for pathogenic variants of the MAPK/ERK signaling pathway invariably show gain-of-function (GoF) mutations that lead to increased MAPK/ERK signaling.[77,82] Approximately 50% of NS cases are caused by GoF mutations in *protein tyrosine phosphatase* (PTP) *non-receptor type 11* (*PTPN11*), which encodes the protein src homology region 2 domain-containing phosphatase-2 (SHP2).[81,83,84] NS patients with *PTPN11* mutations display decreased cognitive abilities compared both to the general population and NS patients with different genetic causes.[3,4] This indicates that PTPN11 specifically has a neuronal role that is malfunctioning with GoF mutations.

PTPN11 is a protein phosphatase, an enzyme that removes a phosphate group from a protein, often acting to modify the affected protein's function.[85] Phosphatases frequently act in opposition to kinases to reset intracellular signaling. Commonly phosphatases target multiple substrates and due to this have the reputation of being "promiscuous" and "undruggable".[86] Despite this reputation, major drug design work has focused on inhibiting PTPN11 function by taking advantage of its autoinhibition mechanism.[87] Its phosphatase activation is regulated by autoinhibition, with phosphatase and N-SH2 domains interacting during inactivation, and an open conformation adopted only with signaling activation.[84] NS mutations cluster at interacting portions of N-SH2 and PTP domains to favor the open conformation with the exposed catalytic domain, leading to elevated MAPK/ERK signaling.[88] PTPN11 positively regulates MAPK/ERK signaling

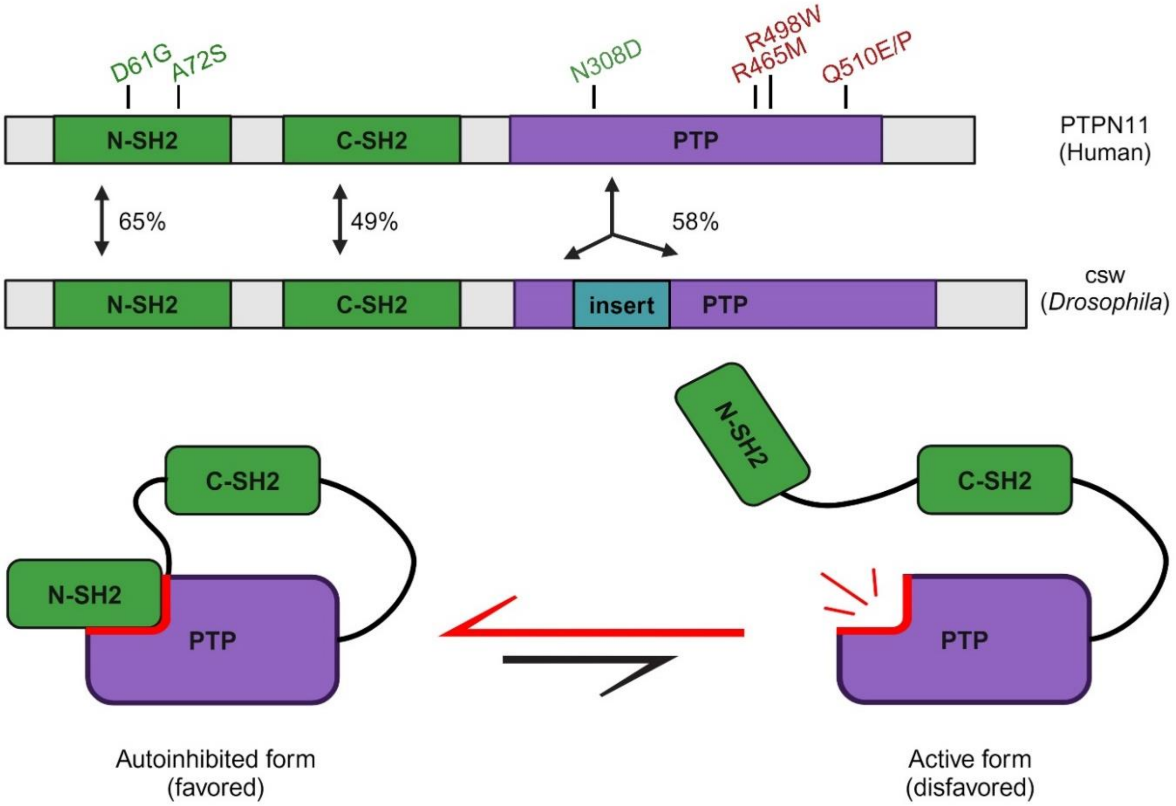

**Figure 1.7: PTPN11 and Csw protein functional domains and disease mutations**
Both PTPN11 and Csw consist of three functional domains—the protein tyrosine phosphatase (PTP) domain alongside the two tandem Src homology-2 (SH2) domains. Together these domains interact to mediate the interaction of the PTP domain with its substrates to control various cellular processes. Top: A comparison of PTPN11 and csw protein domains with key mutations marked. Disease mutations marked in green are activating phosphatase mutations leading to NS and/or JMML. Mutations marked in red are inactivating phosphatase mutations leading to NSML or PTP dead mutation. Percentages indicate percent similarity of domains as determined in Perkins et al, 1992. Bottom: A basic schematic of the shared Csw and PTPN11 activation mechanism. In its inactive, autoinhibited form the PTP active site is blocked by the N-SH2 domain. When activated via phosphorylation, the N-SH2 and PTP domains stop interacting and the protein performs its phosphatase activity. Under normal conditions the inactivated form is greatly favored. NS and NSML mutations lead to the active form being sustained for longer periods of time.

via its PTP domain phosphorylating negative regulators, thus leading to less overall negative regulation of the pathway.[81,83,84,89] In the absence of PTPN11, MAPK/ERK signaling is unable to function normally, causing embryonic lethality in mammals.[78,82] Disease models with equivalent patient mutations have been studied in mice, zebrafish, and *Drosophila*.[90–92] In all cases, MAPK/ERK signaling is elevated, with associated hearts defects. Additionally, 30-50% of NS patients show cognitive deficits,[4,81,93] with a *PTPN11* genotype-phenotype link causing learning and memory deficits.[3,52,90] The mouse NS disease model display LTP and memory deficits that are rescued by MAPK/ERK inhibition.[90] In the *Drosophila* NS disease model, MAPK/ERK-dependent long-term memory (LTM) is likewise disrupted.[52,91] The *Drosophila* homolog of PTPN11 is *corkscrew* (*csw*), which maintains close homology and function to PTPN11.[83,84] A comparison of these homologous proteins alongside common disease-causing mutations is shown in Figure 1.7. Although previous investigations clearly indicate MAPK/ERK-dependent deficits in the nervous system,[52,90] the synaptic impairments have not been studied and are a primary focus of this dissertation.

## Noonan Syndrome with multiple lentigines

Noonan Syndrome with multiple lentigines (NSML; a.k.a. LEOPARD syndrome) is an autosomal dominant disorder that presents very similarly to NS.[80,88,94] Like NS, patients present with short stature, craniofacial abnormalities, cardiac defects (most common: hypertrophic cardiomyopathy, then pulmonary valve stenosis), skeletal deformities, hearing deficits, and neurocognitive defects. NSML uniquely has lentigines, dispersed flat, brownish macules, that appear progressively with age, and which present mostly on the face, neck, and upper part of the trunk.[80,95] Upon finding key symptoms, NSML patients diagnosed via genetic testing show *PTPN11* loss-of-function (LoF) mutations in >95% of cases.[80,96,97] These mutations always affect the PTP domain to reduce phosphatase activity. Notably NS and NSML share most disease symptoms, but are molecularly opposites: GoF vs. LoF mutations, respectively. However, many studies have shown that in both disease states the SHP2 autoinhibition mechanism is disrupted to cause elevated MAPK/ERK signaling.[88,94] Less NSML patient work has been done, but about the same frequency of patients (30-50%) have been reported with cognitive deficits[3]. In the *Drosophila* NSML disease model, MAPK/ERK-dependent long-term memory (LTM) is disrupted, just like in the NS model.[52,91] Based on available evidence, we hypothesized that synaptic dysfunction in NS and NSML *Drosophila* disease models would act via the same mechanism. We additionally hypothesized that Fragile X Syndrome, a disease with upregulated MAPK/ERK signaling and disrupted LTM was also acting via a shared mechanism.

## Fragile X syndrome

Fragile X syndrome (FXS) is an X-linked dominant disorder first described by J. Purdon Martin and Julia Bell in 1943.[98] FXS effects approximately 1 in 5000 males and 1 in 7000 females, making it the most common heritable form of intellectual disability, and the second most common genetic cause of intellectual disability after Down Syndrome.[99] Due to FXS being X-linked, patients present differently depending on gender, with males generally having more severe symptoms. Patient behavioral symptoms include moderate to severe intellectual disability, learning and memory deficits, speech and language delay, autistic characteristics, anxiety, and hyperactivity.[99,100] Individuals are usually diagnosed within the first 36 months due to developmental delays.[101] Physical features of FXS are not usually evident at birth, but start to become apparent during early childhood. These non-neurological symptoms include craniofacial abnormalities (83%),[102] cardiac defects (most common: mitral valve prolapse-55%), skeletal deformities, growth abnormalities, recurrent otitis media (53%--complications include conductive hearing loss), sleep problems (27%), strabismus (16%), seizures (10%), and gastrointestinal problems (10%).[103] The clear phenotypic overlap between FXS and NS/NSML extends beyond the cognitive impairments to parallel hearing and cardiac deficits.

FXS is a monogenetic disorder caused by the inactivation of the *fragile X mental retardation 1* (*FMR1*) gene that encodes the Fragile X Mental Retardation Protein (FMRP).[99,102,104] This inactivation is most commonly caused by epigenetic silencing owing to trinucleotide (CGG) repeat expansion of >200 in the *FMR1* 5' untranslated region. This repeat expansion causes hypermethylation of the *FMR1* promoter region, resulting in epigenetic silencing of FMRP expression.[104] Individuals who carry the FXS premutation have 55-200 repeats, which has separate disease consequences.[105] Normally expansions occur between generations when passed on by a female with the premutation.[99,103] The premutation is seen in 1 in 850 males and 1 in 257–300 females making it much more common than the FXS prevalence.[102] FMRP is an mRNA-binding protein (RBP) primarily described as a translational repressor with a large but indeterminate range of transcript targets.[99,104,106] Identifying FMRP RNA targets via crosslinked immunoprecipitated RNA has identified 842 high confidence targets, one of

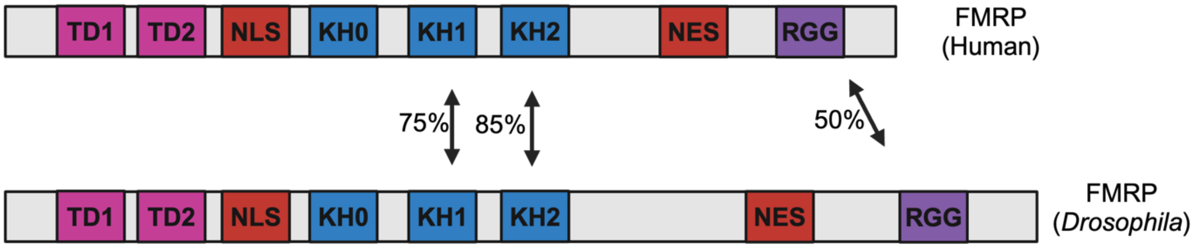

**Figure 1.8: Human and *Drosophila* FMRP protein functional domains**
The FMRP protein consists of 8 functional domains. From N to C terminus there are the two Tudor domains (TD1, TD2), the nuclear localization sequence (NLS), the predicted K homology domain (KH0), KH1 and KH2 domains, the nuclear export sequence (NES), and the arginine-glycine-glycine (RGG) domain. Percentages indicate percent similarity of domains as determined in Wan *et al*, 2000.

which is *PTPN11*.[107] FMRP has no confirmed target RNA-binding consensus sequence, but rather appears to bind transcripts throughout the open reading frame, perhaps acting as a dragging brake on translation.[107] FMRP has numerous other reported functions, such as an organizer of mRNA transport (shuttle protein) and direct channel-binding to regulate neuronal excitability.[99,104,108,109]

Based on *PTPN11* transcript being identified as an RNA target of FMRP,[107] this thesis work focuses on FMRP's role as an RBP. FMRP contains at least three canonical RNA-binding motifs, two K homology (KH) domains KH1 and KH2, and an arginine-glycine-glycine (RGG) box.[104] There is a third putative KH domain, KH0, that has been identified using X-ray crystallography,[110] however its RNA-binding capabilities have yet not been experimentally proven. Additionally, FMRP contains two Tudor domains, TD1 and TD2, that interact with RNA, chromatin and other proteins, as well as a nuclear localization and export sequence, NLS and NES.[104] Point mutations in KH1, Gly266Glu (G266E), and KH2, Ile304Asn (I304N), disrupt the ability of FMRP to bind to specific target mRNAs and phenocopy complete loss of FMRP seen in most cases of FXS.[111,112] Based on FMRP structure and these key mutations, clearly the RNA-binding capabilities are the core mechanism of this disease state. FMRP is highly conserved between humans and *Drosophila* with the two KH domains being 75% and 85% identical and the RGG domain being 50% identical making *Drosophila* an ideal FXS disease model.[113] A comparison of human and *Drosophila* FMRP with domains marked is shown in Figure 1.8. Although widely expressed, FMRP is particularly enriched in neurons, with expression peaking in critical periods of brain synaptic plasticity.[99,108,109] FMRP appears comparably expressed in all neuronal classes but has been studied predominantly in glutamatergic neurons. When FMRP is lost there is an increase in levels of target protein synthesis leading to impairments in synaptic development, refinement, neurotransmission, and plasticity.[99,108] FMRP loss impairs activity-dependent mechanisms, including synapse structural maturation and functional plasticity. Without FMRP, synaptic architecture and synaptic function is elevated leading to an apparent increase in circuit connectivity.[113–115] These activity-dependent synaptic changes are hypothesized to be the causative factor for FXS cognitive and behavioral impairments.

Numerous FXS disease models have been created by FMR1 knockout,[114] which replicate the repeat expansion epigenetic silencing phenotypes typical of human patients.[113,114,116] This includes mice, rats, zebrafish, organoids and *Drosophila* models. Interestingly, there are no known spontaneous animal models of fragile X disorders. The most well characterized of these FXS model organisms is the mouse model.[114,116] With a complete FMR1 knockout, these mice exhibit many symptoms seen in FXS patients including subtle craniofacial abnormalities, learning and memory deficits, neurostructural overelaboration, and enhanced ERK pathway activation.[114,116,117] Additionally, FXS mouse models have observed synaptic dysfunction including decreased short-term depression due to enhanced presynaptic glutamate release via up-regulation of the RRP.[118] Similar to the mouse model, the *Drosophila FMR1* (*dfmr1*) gene conserves all the RNA-binding domains and *dfmr1* deletion null mutants (e.g. $dfmr1^{50M}$) are fully rescued by transgenic expression of human *FMR1*, demonstrating functional conservation.[115,119] As in FXS patients, this *Drosophila* FXS disease model exhibit behavioral impairments including learning and memory deficits, hyperactivity, and autism-like social interactions.[113,115,120] At the *Drosophila* NMJ, *dfmr1* null mutants exhibit synaptic overgrowth, increased evoked neurotransmission, and increased spontaneous synaptic vesicle fusion frequency and amplitude, as well as altered coordinated movement.[115] There have been advances in mitigating FXS related phenotypes in both mouse and Drosophila disease models,[99,119,121] however clinical trials of candidate drugs have so far been largely unsuccessful.[122,123] To this end, further understanding the mechanisms behind neuronal phenotypes is essential to guide future treatment options.

Here, we do this by demonstrating how FMRP regulates a PTPN11 dependent neurotransmission pathway.

# Chapter II

# FMRP activity and control of Csw/SHP2 translation regulate MAPK-dependent synaptic transmission

Shannon N. Leahy[1], Chunzhu Song[1], Dominic J. Vita[1], Kendal Broadie[1,2,3,4*]

[1]Department of Biological Sciences, [2]Department of Cell and Developmental Biology, [3]Department of Pharmacology, [4]Vanderbilt Brain Institute, Vanderbilt University and Medical Center, Nashville, Tennessee, United States of America

This paper is published under the same title in the journal Public Library of Science (PLOS) Biology, 2023.

**Competing interests:** The authors have declared that no competing interests exist.

**Funding:** This work was supported by National Institutes of Mental Health Grant MH084989 to K. B. The funders had no role in study design, data collection and analysis, decision to publish, or preparation of the manuscript.

**Author Contributions:** Shannon N. Leahy**,** Conceptualization, Data curation, Formal analysis, Investigation, Methodology, Project administration, Validation, Visualization, Writing – original draft, Writing – review & editing, Chunzhu Song, Data curation, Formal analysis, Methodology, Writing – review & editing, Dominic J. Vita, Writing – review & editing, and Kendal Broadie, Conceptualization, Funding acquisition, Supervision, Writing – review & editing

Academic Editor: Bing Ye, University of Michigan, UNITED STATES

Received: April 1, 2022

Accepted: December 16, 2022

Published: January 26, 2023

Data Availability Statement: All relevant data are within the paper and its Supporting Information files.

# Abstract

Noonan syndrome (NS) and NS with multiple lentigines (NSML) cognitive dysfunction are linked to SH2 domain-containing protein tyrosine phosphatase-2 (SHP2) gain-of-function (GoF) and loss-of-function (LoF), respectively. In *Drosophila* disease models, we find both SHP2 mutations from human patients and *corkscrew* (*csw*) homolog LoF/GoF elevate glutamatergic transmission. Cell-targeted RNAi and neurotransmitter release analyses reveal a presynaptic requirement. Consistently, all mutants exhibit reduced synaptic depression during high-frequency stimulation. Both LoF and GoF mutants also show impaired synaptic plasticity, including reduced facilitation, augmentation, and post-tetanic potentiation. NS/NSML diseases are characterized by elevated MAPK/ERK signaling, and drugs suppressing this signaling restore normal neurotransmission in mutants. Fragile X syndrome (FXS) is likewise characterized by elevated MAPK/ERK signaling. Fragile X Mental Retardation Protein (FMRP) binds *csw* mRNA and neuronal Csw protein is elevated in *Drosophila fragile X mental retardation 1* (*dfmr1*) nulls. Moreover, phosphorylated ERK (pERK) is increased in *dfmr1* and *csw* null presynaptic boutons. We find presynaptic pERK activation in response to stimulation is reduced in *dfmr1* and *csw* nulls. *Trans*-heterozygous *csw*/+; *dfmr1*/+ recapitulate elevated presynaptic pERK activation and function, showing FMRP and Csw/SHP2 act within the same signaling pathway. Thus, a FMRP and SHP2 MAPK/ERK regulative mechanism controls basal and activity-dependent neurotransmission strength.

## Introduction

Noonan syndrome (NS) is an autosomal dominant genetic disorder caused by mutations in the mitogen-activated protein kinase (MAPK) pathway.[79,96] Missense mutations within the *protein tyrosine phosphatase non-receptor type 11* (*PTPN11*) gene account for >50% of all disease cases.[80] In both patients and disease models, the MAPK pathway is hyperactivated by NS gain-of-function (GoF) mutations that disrupt the auto-inhibition mechanism between the catalytic protein tyrosine phosphatase domain and N-Src homology-2 (SH2) domain of the *PTPN11* encoded SH2 domain-containing protein tyrosine phosphatase-2 (SHP2; [84,124]). In the NS with multiple lentigines (NSML) disease state, *PTPN11* loss-of-function (LoF) mutations decrease protein tyrosine phosphatase domain catalytic activity, but the mutants nevertheless maintain a more persistently active enzyme state with temporally inappropriate SHP2 function, causing elevated MAPK pathway hyperactivation similar to the GoF disease condition.[125] Consequently, NS and NSML patients share a great many symptoms associated with elevated MAPK signaling, including cognitive dysfunction (approximately 30% of cases) as well as long-term memory (LTM) impairments.[77,93] The *Drosophila* NS (GoF) and NSML (LoF) disease models from mutation of the *corkscrew* (*csw*) homolog likewise both increase MAPK activation, with GoF and LoF also phenocopying each other.[82,94] *Drosophila* LTM training generates repetitive waves of *csw*-dependent neural MAPK activation, with the LTM spacing effect misregulated by *csw* manipulations.[52] *PTPN11* GoF and LoF mutations from human patients transgenically introduced into the *Drosophila* model provide a powerful new means to compare with *csw* GoF and LoF mutants in the dissection of conserved neuronal requirements.[91]

Fragile X syndrome (FXS) is similarly well characterized by hyperactivated MAPK signaling within neurons,[76] and the causal Fragile X Mental Retardation Protein (FMRP) RNA-binding translational regulator is proposed to directly bind *PTPN11/SHP2* mRNA.[107,126] FMRP also binds many other neuronal transcripts[108] and could interact with SHP2 in multiple ways to coregulate the MAPK pathway. Moreover, like the NS and NSML disease states, FXS is likewise a cognitive disorder and the leading heritable cause of intellectual disability.[108] Like NS and NSML, the *Drosophila* FXS disease model also manifests strongly impaired LTM consolidation.[115,120] Mechanistically, MAPK signaling is well known to modulate glutamatergic synaptic neurotransmission strength via the control of presynaptic vesicle trafficking dynamics and glutamate neurotransmitter release probability.[127] Consistently, FMRP is also well characterized to regulate glutamatergic synaptic neurotransmission, including presynaptic release properties and activity-dependent functional plasticity.[118] Importantly, treatment with the MAPK inhibitor Lovastatin corrects hippocampal hyperexcitability in the mouse FXS disease model and ameliorates behavioral symptoms in human FXS patients.[128,129] In the *Drosophila* FXS disease model, *dfmr1* null mutants show elevated presynaptic glutamate release underlying increased neurotransmission strength,[115] as well as activity-dependent hyperexcitability and cyclic increases in glutamate release during sustained high-frequency stimulation trains.[41] Based on this broad foundation, we hypothesized that FMRP regulates PTPN11 (SHP2)/Csw translation to modulate presynaptic MAPK signaling, which, in turn, controls presynaptic glutamate release probability to determine both basal neurotransmission strength and activity-dependent synaptic plasticity.

To investigate this hypothesis, we utilized the *Drosophila* neuromuscular junction (NMJ) glutamatergic model synapse with the combined use of NS, NSML, and FXS disease models. We first tested both LoF and GoF conditions in both (1) *csw* mutants and (2) transgenic human *PTPN11* lines. In two-electrode voltage-clamp (TEVC) electrophysiological recordings, all of these mutant conditions elevate synaptic transmission. We next employed cell-targeted RNAi and spontaneous miniature excitatory junction current (mEJC) recordings to find Csw/SHP2 specifically inhibits presynaptic glutamate release probability. We next tested activity-dependent synaptic transmission using high-frequency stimulation (HFS) depression assays to show that the mutants display heightened transmission resiliency, consistent with elevated presynaptic function. We discovered that both LoF and GoF mutations impair presynaptic plasticity, with decreased short-term facilitation, maintained augmentation and post-tetanic potentiation (PTP), supporting altered presynaptic function. Consistent with elevated MAPK signaling in NS, NSML, and FXS disease models, feeding with MAPK-inhibiting drugs (Trametinib and Vorinostat) corrects synaptic transmission strength in mutants. As predicted, we found that FMRP binds *csw* mRNA and that FMRP loss increases Csw protein levels. Both *dfmr1* and *csw* nulls display elevated phosphorylated ERK (pERK) in presynaptic boutons. Importantly, *trans*-heterozygous double mutants (*csw*/+; *dfmr1*/+) exhibit presynaptic MAPK signaling and neurotransmitter release phenotypes, indicating FMRP and Csw/SHP2 operate to control MAPK/ERK signaling and synaptic function. These discoveries link previously unconnected disease states NS, NSML, and FXS via a presynaptic MAPK/ERK regulative mechanism controlling glutamatergic transmission.

## Results

### Corkscrew/PTPN11 loss and gain of function mutations both increase synaptic transmission

NS and NSML patients often exhibit cognitive deficits,[80] which we hypothesized may arise from altered synaptic transmission. To systematically test this hypothesis, we assay both *Drosophila* NS/NSML disease models of *csw* LoF and GoF,[82,94,130] as well as *PTPN11* mutations from human patients, including both LoF and GoF point mutants.[91] First, we use *csw*$^{5}$, a protein null LoF mutant,[130] together with UAS-*csw*$^{WT}$ for wild-type Csw overexpression[89] and UAS-*csw*$^{A72S}$ as a constitutive GoF mutation.[52,82] Second, we use human patient mutations *PTPN11*$^{N308D}$, *PTPN11*$^{Q510E}$, and *PTPN11*$^{Q510P}$ to capture the range of NS/NSML disease heterogeneity.[80,91] The transgenes were driven with ubiquitous *UH1*-Gal4 or neuronal *elav*-Gal4. The NMJ glutamatergic synapse is used to assay disease model neurotransmission in all variants.[13,131] Employing TEVC recording, we compare mutants to genetic background control (*w*$^{1118}$) and transgenic lines to driver controls (*UH1*-Gal4/*w*$^{1118}$ and *elav*-Gal4/*w*$^{1118}$). We test excitatory junction current (EJC) responses driven by motor nerve suction electrode stimulation (0.5 ms suprathreshold stimuli, 0.2 Hz) onto the voltage-clamped (−60 mV) ventral longitudinal muscle 6 in abdominal segments 3/4.[40] Each data point is the average of 10 sequentially evoked EJC responses recorded in 1 mM [Ca$^{2+}$] from the same NMJ terminal. Representative recordings and quantified results for all of these comparisons are shown in Fig 2.1.

In genetic background controls (*w*$^{1118}$), nerve stimulation causes consistent, high-fidelity neurotransmission (Fig 2.1A, left). In comparison, *csw*$^{5}$ LoF mutants display highly elevated synaptic function with an obvious increase in amplitude (Fig 2.1A, second from left). Quantified measurements show *csw*$^{5}$ EJC amplitudes (248.80 ± 12.51 nA, *n* = 14)

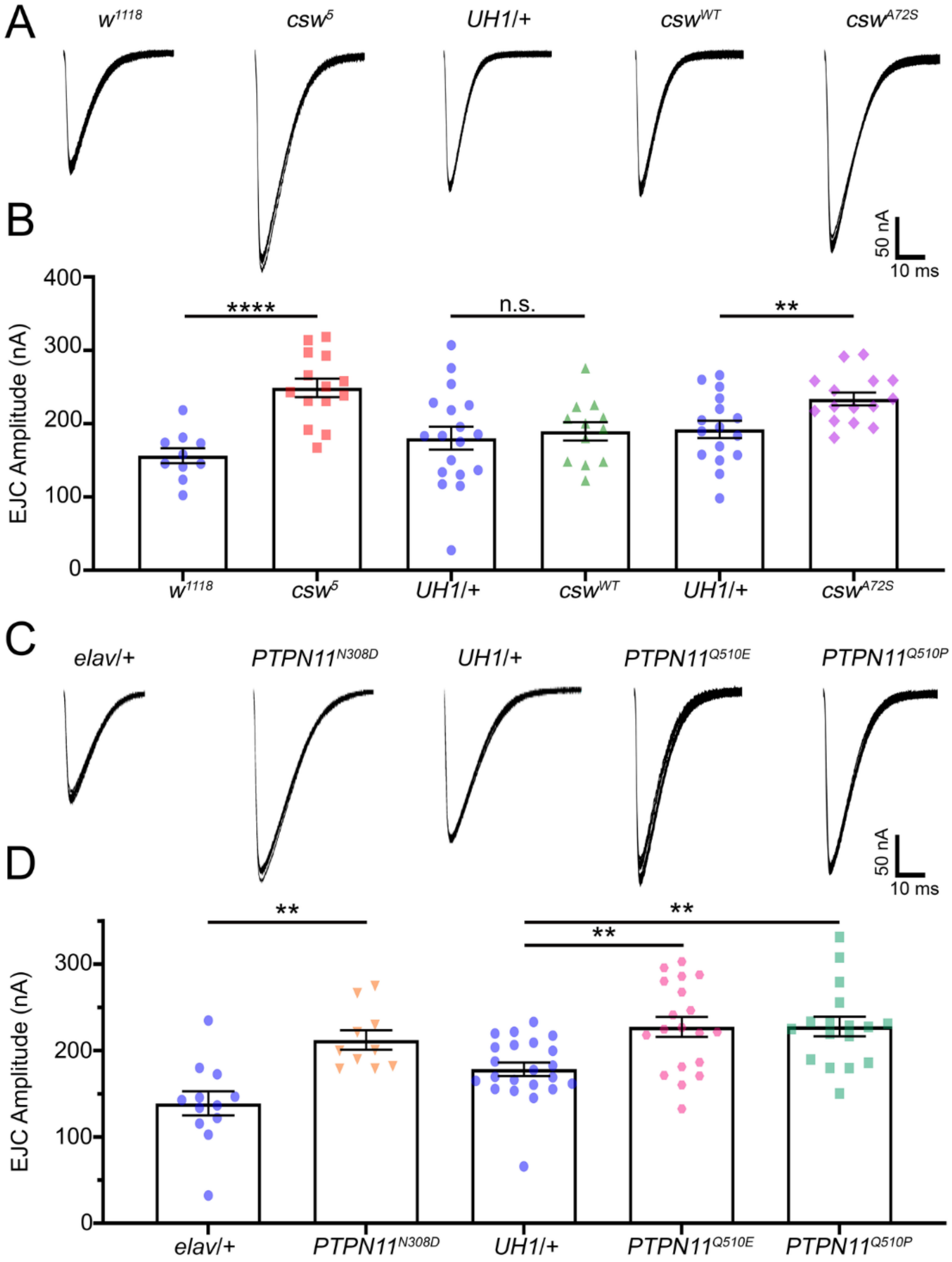

**Fig 2.1: Both loss- and gain-of-function *csw*/*PTPN11* mutants elevate NMJ transmission.**
TEVC recordings of nerve-stimulated evoked neurotransmission in both LoF and GoF mutations of *Drosophila csw* and human *PTPN11* mutations from NS/NSML patients. (**A**) Representative EJC traces for the *csw* mutant comparisons showing 10 superimposed evoked synaptic responses (1.0 mM Ca$^{2+}$) from *w*$^{1118}$ genetic background control, *csw*$^{5}$ null mutant, transgenic driver control (*UH1*-Gal4/*w*$^{1118}$), wild-type *csw* (*UH1*-Gal4>*csw*$^{WT}$), and *csw*$^{A72S}$ GoF mutant (*UH1*-Gal4>*csw*$^{A72S}$). (**B**) Quantification of the mean EJC amplitudes in all 5 genotypes using two-sided *t* tests. (**C**) Representative evoked EJC traces for the human patient *PTPN11* mutations showing 10 superimposed responses in paired control (*elav*-Gal4/*w*$^{1118}$) and GoF mutant (*elav*-Gal4>*PTPN11*$^{N308D}$; left), and control (*UH1*-Gal4/*w*$^{1118}$) and LoF mutants (*UH1-Gal4>PTPN11*$^{Q510E}$ and PTPN11$^{Q510P}$; right). (**D**) Quantification of the mean EJC amplitudes in all 5 genotypes using two-sided *t* test, Kruskal–Wallis and Dunn's multiple comparisons. The scatter plots show all of the individual data points as well as mean ± SEM. *N* = number of NMJs. Significance shown as: $p > 0.05$ (not significant, n.s.), $p < 0.001$ (**) and $p < 0.0001$ (****).

strongly elevated compared to controls (156.30 ± 10.28 nA, $n = 10$), which is a significant increase ($p < 0.0001$, two-sided *t* test; Fig 2.1B). Since NSML (LoF) and NS (GoF) disease states manifest closely parallel phenotypes, we next examined transgenically driven wild-type *csw* ($csw^{WT}$) and the GoF mutant ($csw^{A72S}$). In transgenic ubiquitous driver controls (*UH1*-Gal4/$w^{1118}$), nerve stimulation drives transmission comparable to the genetic background alone (Fig 2.1A, middle). Likewise, $csw^{WT}$ overexpression results in no detectable alteration in synaptic strength, with amplitudes comparable to controls (Fig 2.1A, second from right). In sharp contrast, the GoF mutant $csw^{A72S}$ exhibits a consistent elevation in transmission amplitude (Fig 2.1A, right). Quantification shows the *UH1*-Gal4/$w^{1118}$ control amplitude (180.10 ± 15.74 nA, $n = 18$) is comparable to *UH1*-Gal4>$csw^{WT}$ (189.50 ± 12.52 nA, $n = 12$), with no significant difference in transmission ($p = 0.671$, two-sided *t* test; Fig 2.1B, middle). The $csw^{A72S}$ GoF mutation causes significantly elevated neurotransmission. Quantified measurements show $csw^{A72S}$ EJC amplitudes (233.70 ± 8.71 nA, $n = 15$) are strongly increased compared to *UH1*-Gal4/$w^{1118}$ driver controls (192.10 ± 11.86 nA, $n = 16$), a significant elevation ($p = 0.009$, two-sided *t* test; Fig 2.1B). This increased neurotransmission is independent of changes in NMJ architecture (Fig 2.2A), including muscle size (Fig 2.2B), NMJ area (Fig 2.2C), branching (Fig 2.2D), and bouton number (Fig 2.2E), which show no significant changes. The elevated neurotransmission is also independent of changes in synapse number (Fig 2.3A), including active zone density (Fig 2.3B), postsynaptic glutamate receptors (Fig 2.3C), and synaptic apposition (Fig 2.3D), which are similarly unaltered. Expressing $csw^{WT}$ in the $csw^{5}$ null restores neurotransmission to the control levels (Fig 2.4A and 2.4B), indicating phenotype specificity. We therefore conclude that *csw* LoF and GoF increase glutamatergic synaptic transmission, comparable to the phenocopy of NS/NSML disease state symptoms in human patients.

To further test effects, we next assayed *PTPN11* patient mutations. Compared to transgenic controls, all the *PTPN11* mutations cause clearly strengthened synaptic function (Fig 2.1C). The NS $PTPN11^{N308D}$, NSML $PTPN11^{Q510E}$, and NSML $PTPN11^{Q510P}$ mutations all display consistent EJC elevations compared to the controls, similar to LoF/GoF *csw* animals (compare Fig 2.1A and 2.1C). For the GoF condition, the human $PTPN11^{N308D}$ mutation is driven only in neurons (*elav*-Gal4) since

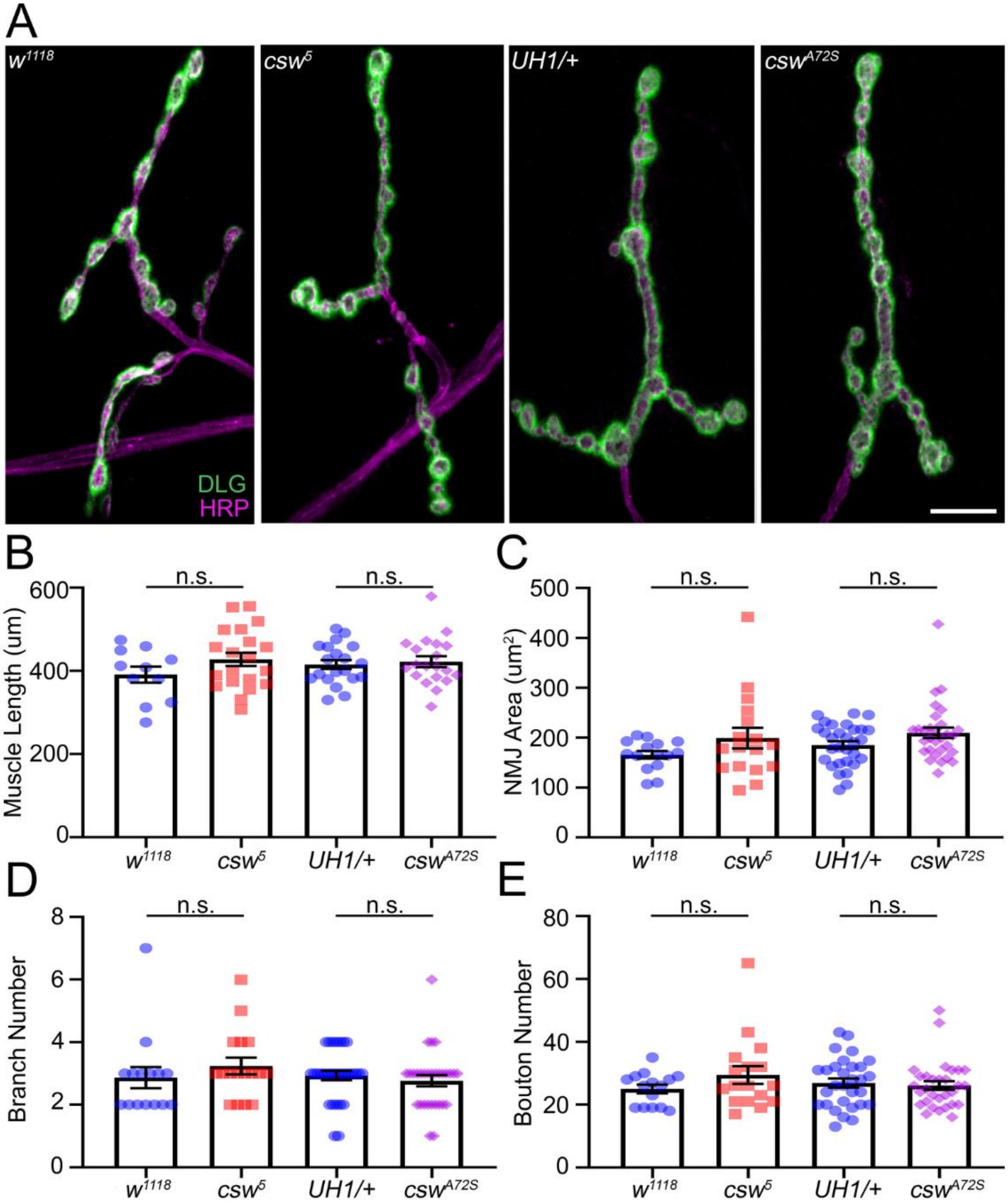

**Fig 2.2: NMJ architecture is unchanged in *csw* null and GoF mutants.**
(A) Representative NMJ images of the $w^{1118}$ genetic background control, $csw^{5}$ null mutant, *UH1*-Gal4/$w^{1118}$ transgenic driver control, and $csw^{A72S}$ GoF mutant (*UH1*-Gal4>$csw^{A72S}$) colabeled for presynaptic membrane marker anti-HRP (magenta) and postsynaptic scaffold DLG (green). Scale bar: 10 μm. (B) Quantification of muscle length for all 4 genotypes using two-sided *t* tests. (C) Quantification of NMJ area for all 4 genotypes using Mann–Whitney tests. (D) Quantification of NMJ branch number for all 4 genotypes using Mann–Whitney tests. (E) Quantification of NMJ synaptic bouton number for all 4 genotypes using Mann–Whitney tests. Scatter plots show all the individual data points as well as mean ± SEM. *N* = number of NMJs. Significance: $p > 0.05$ (not significant, n.s.).

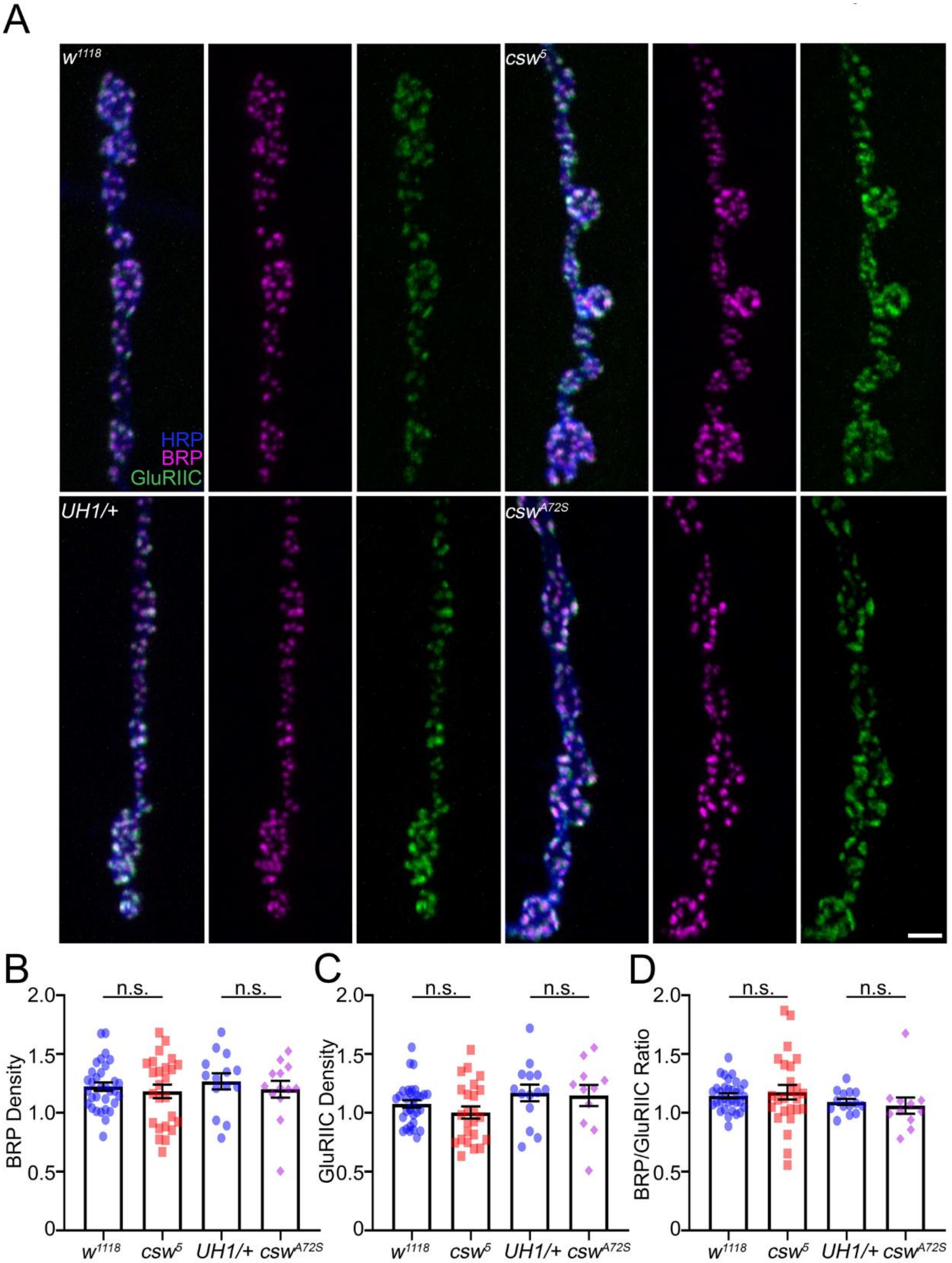

**Fig 2.3: Synapse number is unchanged in *csw* null and GoF mutants.**
(A) Representative NMJ images of the $w^{1118}$ genetic background control, $csw^5$ null mutant, *UH1*-Gal4/$w^{1118}$ transgenic driver control, and $csw^{A72S}$ GoF mutant (*UH1*-Gal4>$csw^{A72S}$) colabeled for presynaptic membrane marker anti-HRP (blue), active zone marker Brp (magenta), and postsynaptic GluRIIC (green). Scale bar: 2.5 µm. (B) Quantification of Brp puncta density for all 4 genotypes using two-sided *t* test/Mann–Whitney tests. (C) Quantification of GluRIIC puncta density for all 4 genotypes using two-sided *t* tests. (D) Quantification of the Brp:GluRIIC puncta ratio for all 4 genotypes using two-sided *t* test/Mann–Whitney tests. Scatter plots show all the individual data points as well as mean ± SEM. *N* = number of NMJs. Significance: $p > 0.05$ (not significant, n.s.).

ubiquitous expression results in lethality complications. Quantification compared to neuronal driver control (*elav*-Gal4/w$^{1118}$) EJC amplitude (138.70 ± 13.95 nA, *n* = 12) shows NS (GoF) *PTPN11*$^{N308D}$ EJC amplitude (212.20 ± 11.13 nA, *n* = 10) is significantly elevated (*p* = 0.001, two-sided *t* test, Fig 2.1D, left). The patient-derived *PTPN11* LoF mutations similarly display increased transmission amplitudes, including *PTPN11*$^{Q510E}$ (227.40 ± 11.64 nA, *n* = 19) and *PTPN11*$^{Q510P}$ (227.90 ± 11.28 nA, *n* = 17) compared to the matched ubiquitous driver controls (*UH1*-Gal4/*w*$^{1118}$; 178.40 ± 7.73 nA, *n* = 22). These changes are significant both together (*p* = 0.0006, Kruskal–Wallis; Fig 2.1D, right) and when compared individually for both *PTPN11*$^{Q510E}$ (*p* = 0.004, Dunn's multiple comparison; Fig 2.1D) and *PTPN11*$^{Q510P}$ (*p* = 0.003, Dunn's multiple comparisons; Fig 2.1D). The patient *PTPN11* mutants are not different from each other (*p* >0.999, Dunn's multiple comparisons; Fig 2.1D). Additionally, *PTPN11*$^{WT}$ overexpression results in no detectable alteration in synaptic strength, with amplitudes comparable to controls (Fig 2.4C and 2.4D). Taken together, these findings indicate that both *Drosophila csw* and human homolog *PTPN11* significantly limit neurotransmission strength. EJCs are elevated with both LoF and GoF, but not by simple overexpression. The next pressing question was to determine whether synaptic strengthening is due to increased presynaptic glutamate release, postsynaptic glutamate receptor responsiveness, or both together.

### Corkscrew/PTPN11 controls presynaptic transmission by altering glutamate release probability

Our next objective was to determine where Corkscrew acts to mediate synaptic changes in neurotransmission strength. To test requirements, we knocked down *csw* expression through RNA interference (RNAi) driven in the different cells contributing to the NMJ, including the presynaptic motor neuron and postsynaptic muscle.[32] We used targeted transgenic RNAi against *csw* (BDSC 33619;[132]) to test each cell-specific function. This line is from the Harvard Transgenic RNAi Project (TRiP), which provides a background control stock (BDSC 36303) containing all components except the UAS-RNAi.[133] To test RNAi efficacy and replication of *csw*$^{5}$ null phenotypes, we first used the ubiquitous *daughterless* UH1-Gal4 driver. To separate cellular requirements, we used neuronal *elav*-Gal4 and muscle *24B*-Gal4-specific drivers, each compared to their

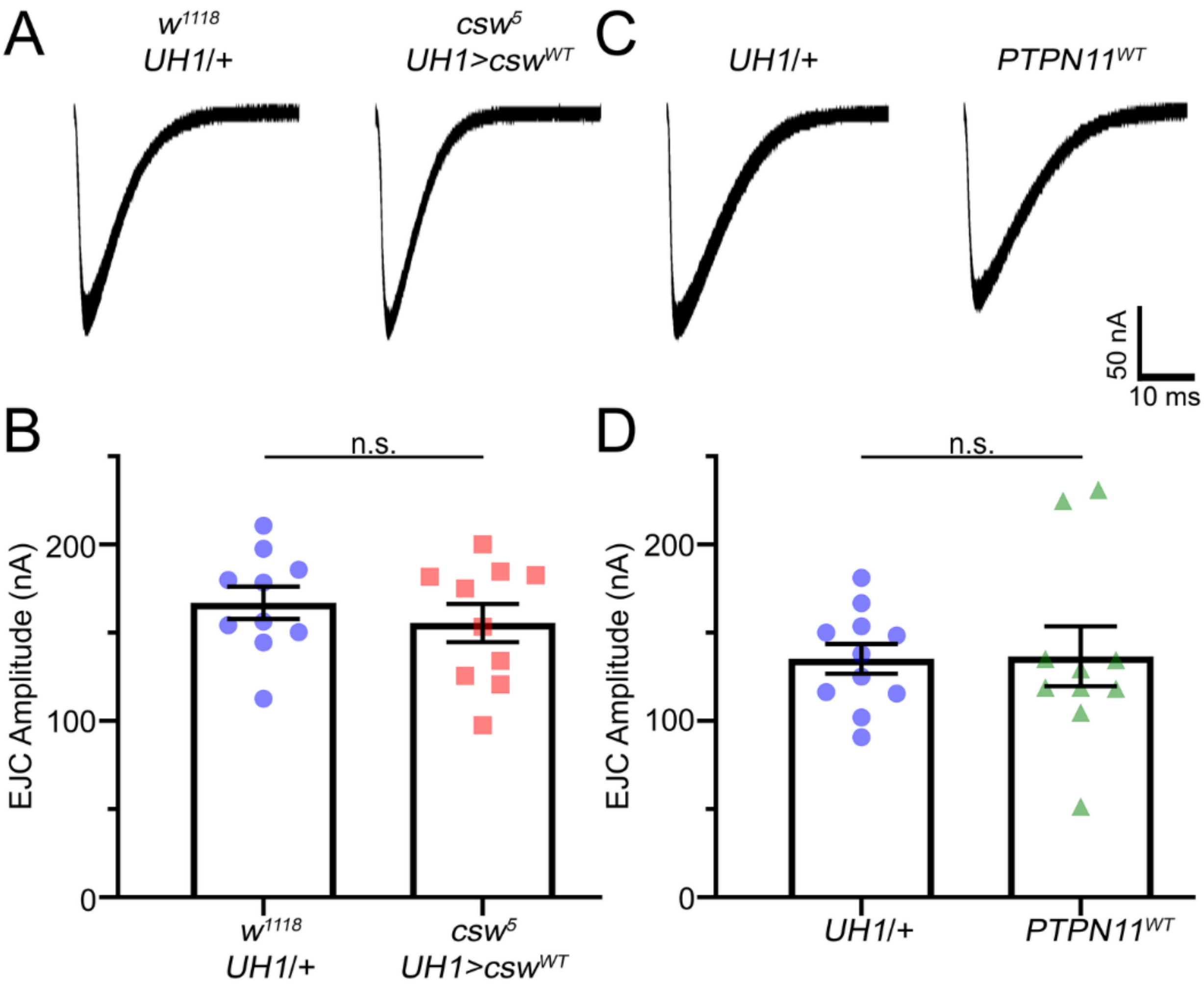

**Fig 2.4: Wild-type *Csw/PTPN11* expression restores neurotransmission in mutants.** (A) Representative EJC traces for the $csw^{5}$ null mutant rescued via expression of $csw^{WT}$ ($csw^{5}$ *UH1*-Gal4>$csw^{WT}$) and transgenic driver control (*UH1*-Gal4/$w^{1118}$) showing 10 superimposed responses (1.0 mM $Ca^{2}$). (B) Quantification of the mean EJC amplitudes using a two-sided *t* test. (C) Representative EJC traces for the wild-type *PTPN11* (*UH1*-Gal4>$PTPN11^{WT}$) and transgenic driver control (*UH1*-Gal4/$w^{1118}$) showing 10 superimposed evoked synaptic responses (1.0 mM $Ca^{2}$). (D) Quantification of the mean EJC amplitudes using a two-sided *t* test. Scatter plots show all the individual data points as well as mean ± SEM. *N* = number of NMJs. Significance: $p > 0.05$ (not significant, n.s.).

respective driver alone transgenic controls. With each RNAi knockdown, we once again utilized TEVC recordings of evoked EJC neurotransmission to measure synaptic strength. To further test *csw* functional roles, we analyzed spontaneous release events by assessing changes in both frequency and amplitude with miniature EJC (mEJC) recordings.[40] Changes in the mEJC frequency are correlated with alterations in presynaptic fusion probability, whereas changes in mEJC amplitudes indicate differential postsynaptic glutamate receptor function or altered vesicle size.[46,134] We made continuous mEJC recordings collected over 2 minutes using a gap-free configuration filtered at 10 kHz.[40] Each data point corresponds to the mean mEJC frequency and amplitude of all the recorded release events. Representative recordings and quantified results are shown in Fig 2.5.

The ubiquitous transgenic driver control (*UH1*-Gal4/TRiP BDSC 36303 control) exhibits neurotransmission indistinguishable from the $w^{1118}$ genetic background control (Fig 2.5A, left). Ubiquitous *csw* knockdown (UH1>*csw* RNAi) causes elevated neurotransmission closely consistent with the $csw^5$ null mutant (Fig 2.5A, second from left), demonstrating RNAi efficacy as well as null phenocopy (compare to Fig 2.1A, left). The quantified EJC measurements show UH1>*csw* RNAi (233.20 ± 17.45 nA, $n$ = 10) to be strongly elevated compared to controls (152.30 ± 15.65 nA, $n$ = 10), which is a significant increase ($p$ = 0.003, two-sided $t$ test; Fig 2.5B). The neuronal driver control (*elav*-Gal4/TRiP BDSC 36303 control) compared to neuronal-specific knockdown (*elav>csw* RNAi) also shows strong replication of the $csw^5$ null elevated transmission, indicating a primary *csw* requirement in the presynaptic neuron (Fig 2.5A, middle pair). Quantified measurements show *elav>csw* RNAi EJC amplitude (239.70 ± 19.45 nA, $n$ = 10) also strongly increased compared with the *elav*-Gal4/TRiP driver controls (159.90 ± 9.68 nA, $n$ = 12), which is significant ($p$ = 0.001, two-sided $t$ test; Fig 2.5B, middle). In contrast, targeted muscle RNAi knockdown (*24B>csw* RNAi) does not cause any change in evoked neurotransmission compared to the muscle driver control alone (*24B*-Gal4/TRiP BDSC 36303; Fig 2.5A, right pair), signifying that postsynaptic Csw does not detectably change synaptic function. When quantified, *24B*-Gal4/TRiP (156.50 ± 11.41 nA, $n$ = 10) is comparable to *24B>csw* RNAi (170.30 ± 11.24 nA, $n$ = 11), with no significant change in amplitude ($p$ = 0.401, two-sided $t$ test; Fig 2.5B, right). These

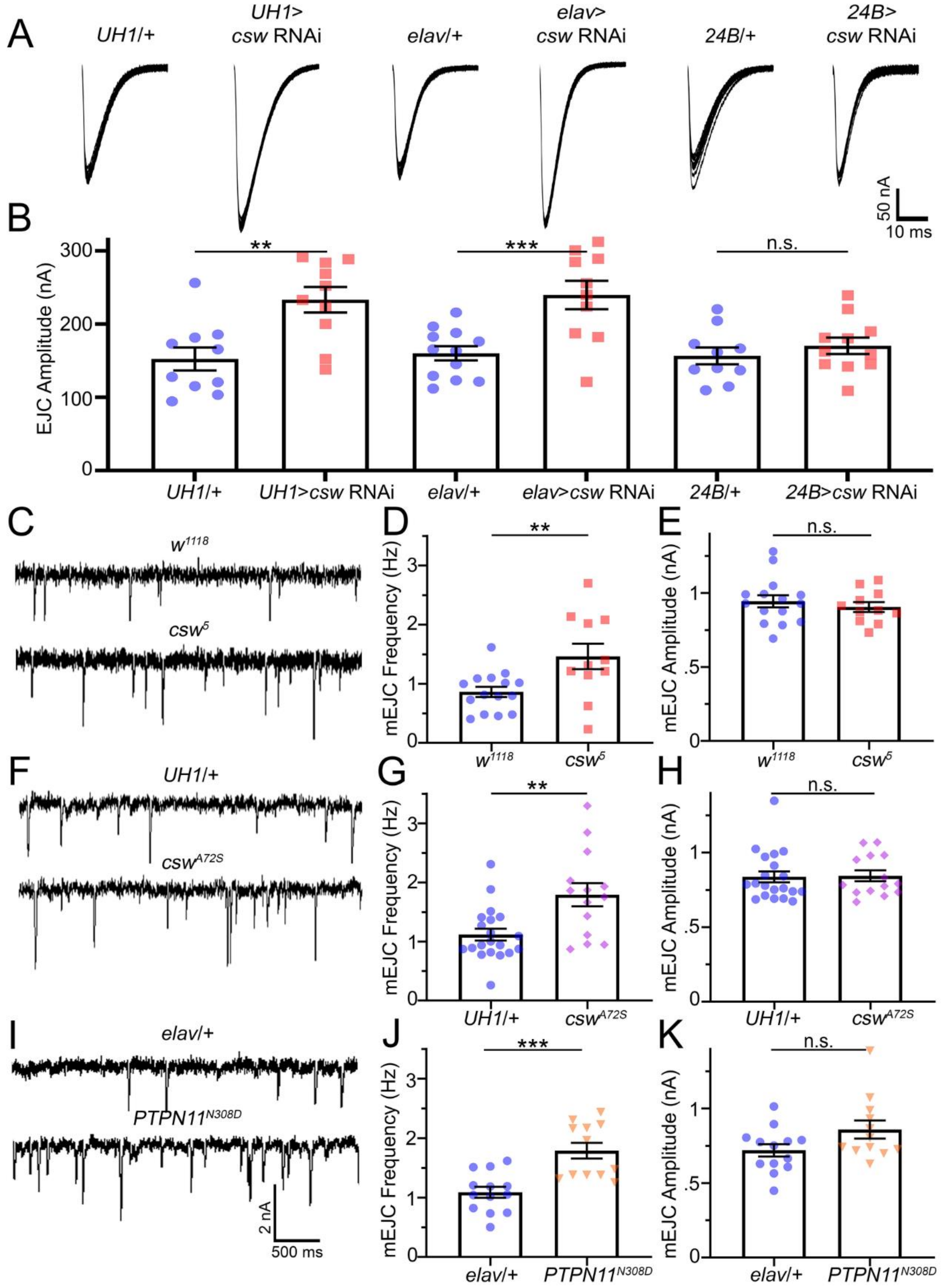

**Fig 2.5: Targeted neuronal *csw* knockdown increases presynaptic neurotransmission.**
Nerve stimulation–evoked recordings based on *csw* RNAi expressed ubiquitously (*UH1*-Gal4) or targeted to neurons (*elav*-Gal4), or muscles (*24B*-Gal4). (A) Representative EJC traces showing 10 superimposed responses (1.0 mM $Ca^{+2}$) from control (*UH1*-Gal4/TRiP) vs. *csw* RNAi; control (*elav*-Gal4/TRiP) vs. *csw* RNAi; and control (*24B*-Gal4/TRiP) vs. *csw* RNAi. (B) Quantification of EJC amplitudes using two-sided *t* tests. (C) Representative mEJC traces (1.0 mM $Ca^{2+}$) in genetic background control (*$w^{1118}$*, top) and *$csw^5$* null (bottom). (D) Quantification of the mEJC frequencies using a two-sided *t* test. (E) Quantification of the mEJC amplitudes using a two-sided *t* test. (F) Sample mEJC recordings from the driver control (*UH1*-Gal4/*$w^{1118}$*; top) compared to *$csw^{A72S}$* GoF (*UH1*-Gal4>*$csw^{A72S}$*; bottom). (G) Quantification of the mEJC frequencies using a two-sided *t* test. (H) Quantification of mEJC amplitudes using Mann–Whitney test. (I) Sample mEJC recordings in control (*elav*-Gal4/*$w^{1118}$*; top) compared to *$PTPN11^{N308D}$* GoF (*elav*-Gal4>*$PTPN11^{N308D}$*; bottom). (J) Quantification of the mEJC frequency using a Mann–Whitney test. (K) Quantification of mEJC amplitude using a Mann–Whitney test. Scatter plots show all the data points and mean ± SEM. *N* = number of NMJs. Significance: $p > 0.05$ (not significant, n.s.), $p < 0.05$ (*), $p < 0.001$ (**), and $p < 0.0001$ (***).

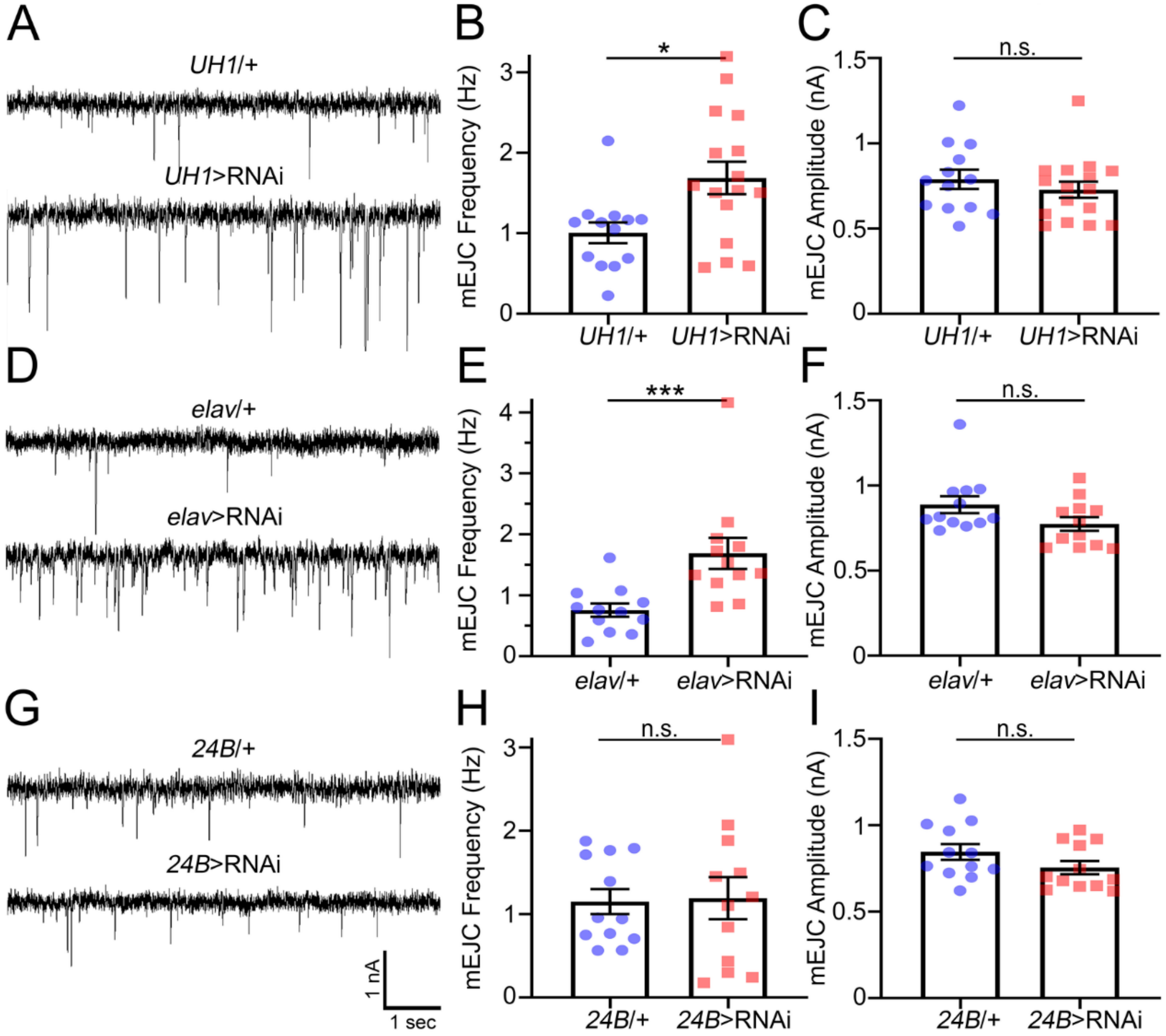

**Fig 2.6: Neuronal *csw* RNAi knockdown increases spontaneous fusion frequency.**
(A) Representative mEJC traces (1.0 mM Ca$^{+2}$) in driver control (*UH1*-Gal4/TRiP control, top) and *UH1*-Gal4>*csw* RNAi (bottom). (B) Quantification of the mEJC frequency using a two-sided *t* test. (C) Quantification of mEJC amplitude using a Mann–Whitney test. (D) Representative mEJC traces (1.0 mM Ca$^{+2}$) in driver control (*elav*-Gal4/TRiP control, top) and neuronal *elav*-Gal4>*csw* RNAi (bottom). (E) Quantification of the mEJC frequency using a Mann–Whitney test. (F) Quantification of the mEJC amplitude using a Mann–Whitney test. (G) Representative mEJC traces (1.0 mM Ca$^{+2}$) in driver control (*24B*-Gal4/TRiP, top) and muscle *24B*-Gal4>*csw* RNAi (bottom). (H) Quantification of the mEJC frequency using a two-sided *t* test. (I) Quantification of the mEJC amplitude using two-sided *t* test. Scatter plots show all the individual data points as well as mean ± SEM. *N* = number of NMJs. Significance: $p > 0.05$ (not significant, n.s.), $p < 0.05$ (*), and $p > 0.001$ (***).

findings indicate a primary *csw* requirement in presynaptic neurons regulating glutamate neurotransmitter release.

To further test pre- versus postsynaptic requirements, we next analyzed spontaneous mEJC release events. Compared to genetic background controls ($w^{1118}$), $csw^5$ null mutants exhibit an obvious increase in mEJC frequency, without any detectable alteration in amplitudes (Fig 2.5C). When quantified, mEJC frequency in $csw^5$ nulls (1.46 ± 0.22 Hz, *n* = 11) is increased compared to controls (0.86 ± 0.086 Hz, *n* = 15), a significant elevation (*p* = 0.009, two-sided *t* test; Fig 2.5D). There is no significant change in mEJC amplitudes (*p* = 0.489, two-sided *t* test; Fig 2.5E). Like the null mutant, GoF $csw^{A72S}$ animals show increased mEJC frequency compared to controls, with no increase in amplitude (Fig 2.5F). When quantified, UH1>$csw^{A72S}$ (1.79 ± 0.19 Hz, *n* = 14) have increased mEJC frequency compared to controls (1.12 ± 0.10 Hz, *n* = 20), which is a significant elevation (*p* = 0.002, two-sided *t* test; Fig 2.5G). Quantification shows no significant change in mEJC amplitudes (*p* = 0.796, Mann–Whitney; Fig 2.5H). Similarly, patient-derived $PTPN11^{N308D}$ mutants display increased mEJC frequency with no change in amplitude (Fig 2.5I). Quantification shows $PTPN11^{N308D}$ frequency (1.79 ± 0.13 Hz, *n* = 12) increased versus controls (1.09 ± 0.09 Hz, *n* = 13), which is a significant elevation (*p* = 0.001, Mann–Whitney; Fig 2.5J). There is no significant change in amplitudes (*p* = 0.168, Mann–Whitney; Fig 2.5K). These findings indicate that both LoF and GoF mutations alter neurotransmission by increasing presynaptic glutamate release rate. We confirmed results further by testing mEJCs in different RNAi conditions. We find mEJC frequencies increased with ubiquitous *csw* RNAi (Fig 2.6A and 2.6B) and neuron-targeted *csw* RNAi (Fig 2.6D and 2.6E), but no change with muscle-specific RNAi (Fig 2.6G and 2.6H Fig). None of these manipulations alter mEJC amplitude (Fig 2.6C, 2.6F and 2.6I). Taken together with targeted RNAi results, we conclude that a neuronal requirement regulates glutamate release from the presynaptic terminal. Quantal content determined by dividing EJC amplitude by mean mEJC amplitude shows elevated quantal content in the mutants (Fig 2.7A) as well as ubiquitous/neuronal *csw* RNAi (Fig 2.7B). Moreover, *PTPN11* LoF patient mutations driven neuronally phenocopy all GoF defects, including elevated neurotransmission (Fig 2.8A and 2.8B) and increased presynaptic fusion (Fig 2.8C and 2.8D), but no change in mEJC amplitude (Fig 2.8E), consistent with

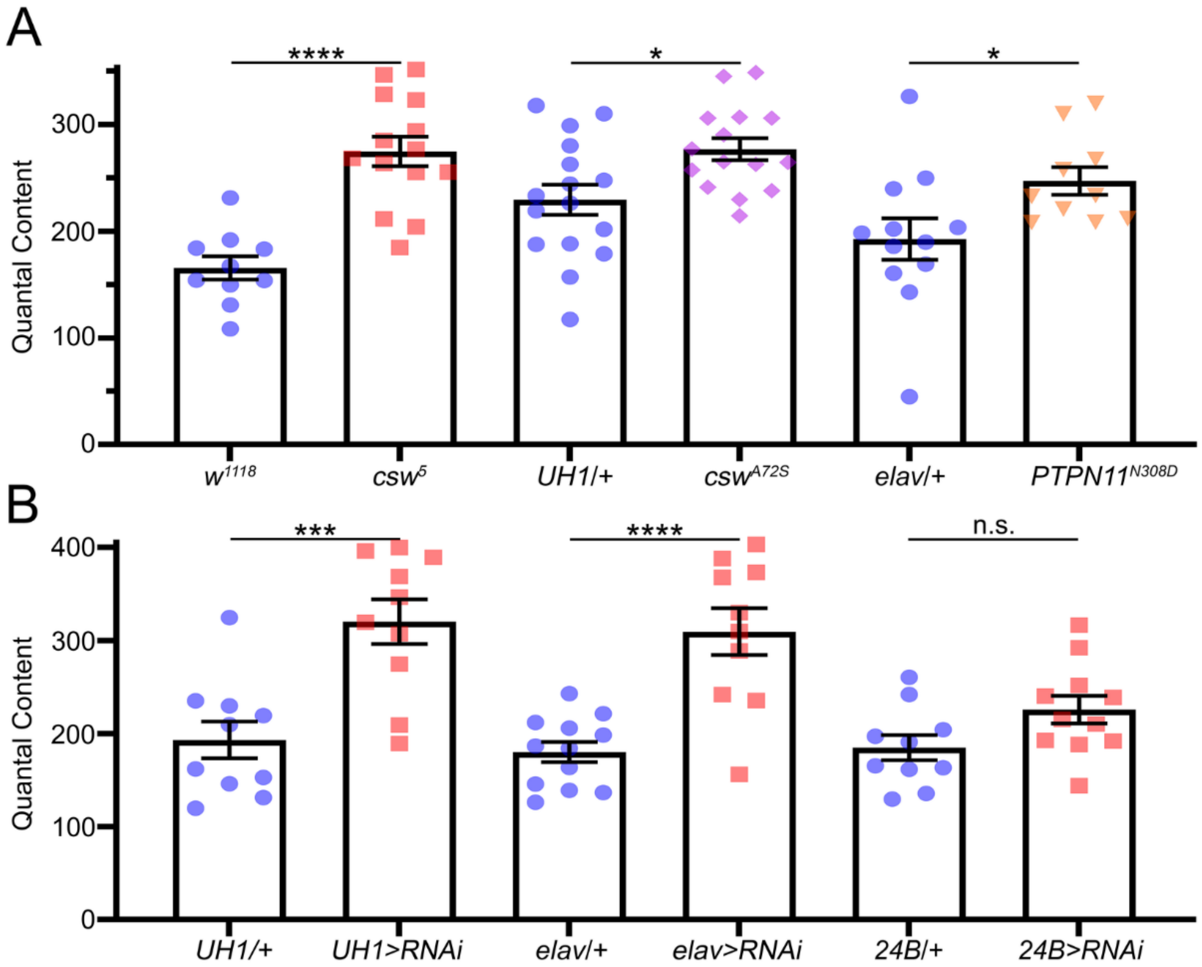

**Fig 2.7: All *csw/PTPN11* mutants exhibit increased synaptic quantal content release.**
The quantal content at each NMJ was calculated by dividing the evoked EJC traces by the mean mEJC amplitude. (A) Quantification of the quantal content of both the *csw/PTPN11* null and GoF mutants using two-sided *t* tests. (B) Quantification of the quantal content of *csw RNAi* ubiquitous (*UH1*), neuronal (*elav*), and muscle (*24B*) lines compared to their matched transgenic driver controls using two-sided *t* tests. Scatter plots show all the individual data points as well as mean ± SEM. *N* = number of NMJs. Significance: $p > 0.05$ (not significant, n.s.), $p < 0.05$ (*), $p > 0.001$ (***), and $p < 0.0001$ (****).

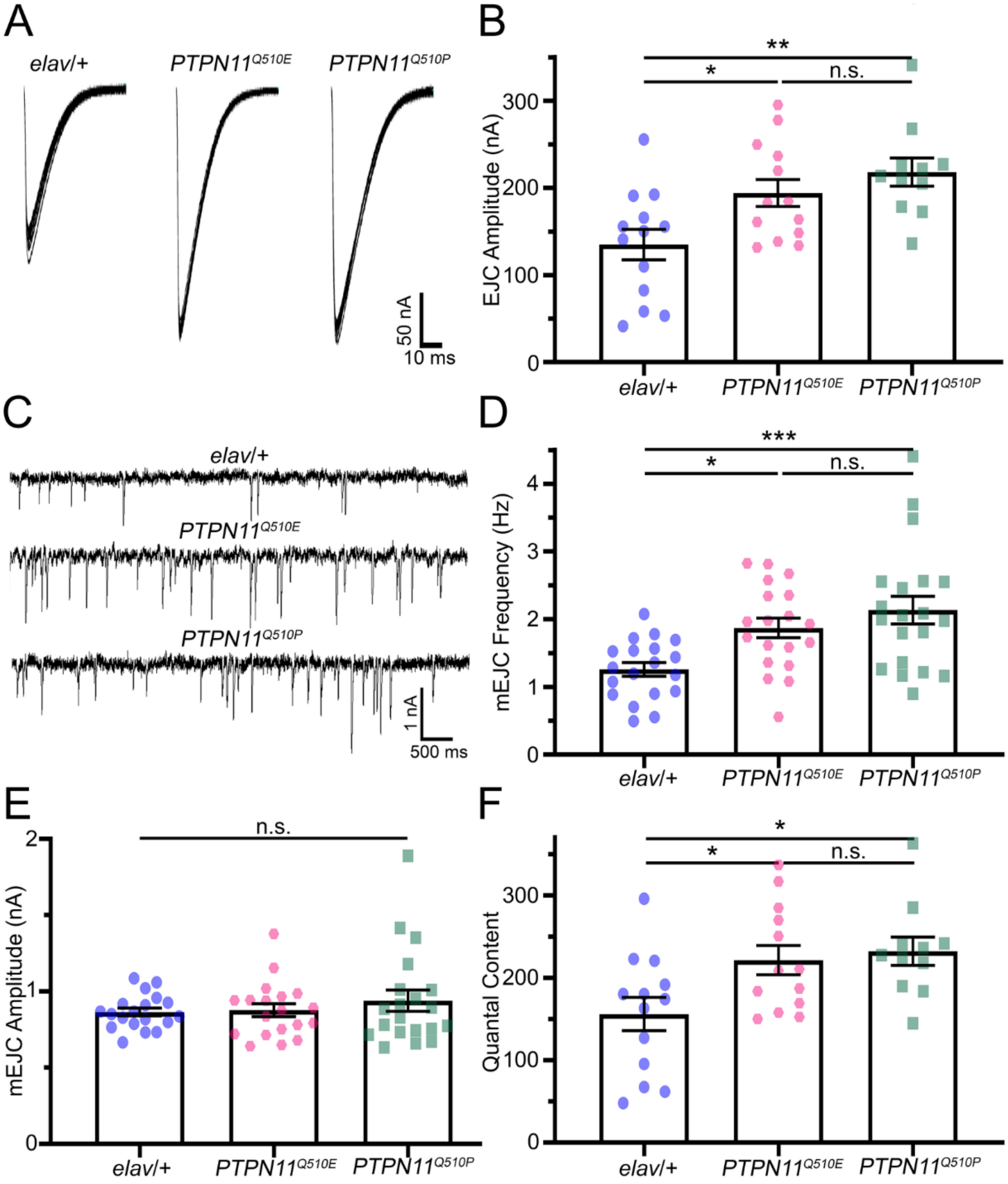

**Fig 2.8: Neuronal NSML model *PTPN11* mutants exhibit elevated presynaptic function.**
**(**A) Representative EJC traces for the transgenic driver control (*elav*-Gal4/*w*$^{1118}$), and *PTPN11* patient mutants *PTPN11*$^{Q510E}$ (*elav*-Gal4>*PTPN11*$^{Q510E}$) and *PTPN11*$^{Q510P}$ (*elav*-Gal4>*PTPN11*$^{Q510P}$) showing 10 superimposed evoked synaptic responses (1.0 mM Ca$^{2+}$). (B) Quantification of the mean EJC amplitudes in all 3 genotypes using one-way ANOVA and Tukey's multiple comparisons. (C) Representative mEJC traces (1.0 mM Ca$^{2+}$) in above driver control (top), *PTPN11*$^{Q510E}$ (middle), and *PTPN11*$^{Q510P}$ (bottom). (D) Quantification of the mEJC frequency using one-way ANOVA and Tukey's multiple comparisons. (E) Quantification of mEJC amplitude using a Kruskal–Wallis test. (F) Quantification of quantal content using one-way ANOVA and Tukey's multiple comparisons. Scatter plots show all the individual data points as well as mean ± SEM. *N* = number of NMJs. Significance: $p > 0.05$ (not significant, n.s.), $p < 0.05$ (*), $p < 0.001$ (**), and $p > 0.001$ (***).

the increase in quantal content (Fig 2.8F). This suggested that stimulation paradigms challenging neurotransmission maintenance should reveal changes in vesicle release dynamics in the absence of *csw/PTPN11* function.

### Corkscrew/PTPN11 regulates high frequency stimulation synaptic depression

To further investigate how *csw/PTPN11* affects presynaptic neurotransmission strength, we stimulated at a heightened frequency that has been shown to cause synaptic depression over a time course of several minutes.[23,135,136] Synaptic depression occurs when HFS causes synaptic vesicles to be released at a faster rate than they can be replenished in presynaptic boutons.[135,137] Based on published HFS protocols for the *Drosophila* NMJ,[23,135,138] we compared the genetic background control (*$w^{1118}$*), *csw* null LoF mutant (*$csw^{5}$*), and patient-derived *$PTPN11^{N308D}$* GoF mutant (*elav*-Gal4>*$PTPN11^{N308D}$*) with a HFS paradigm. To determine the baseline EJC amplitudes, we first stimulated for 1 minute under basal conditions (0.5 ms suprathreshold stimuli at 0.2 Hz in 1.0 mM external [$Ca^{2+}$]). We then stimulated at 100X greater frequency (20 Hz) for 5 minutes while continuously recording EJC responses. This sustained HFS train causes progressively decreased neurotransmission over time (depression). HFS transmission was quantified to analyze the synaptic vesicle readily releasable pool (RRP) and paired-pulse ratio (PPR) release probability. Representative HFS recordings and quantified results are shown in Figs 2.9 and 2.10.

During HFS, *$w^{1118}$* controls exhibit a steady decrease in EJC amplitudes throughout the train (Fig 2.9A, top). The *$PTPN11^{N308D}$* GoF mutants and *$csw^{5}$* LoF nulls show stronger maintained EJC amplitudes over time and prolonged resistance to depression (Figs 2.9A and 2.10A). RRP size was calculated by dividing the cumulative EJCs during the first 100 responses by mean mEJC amplitudes.[139] There is a sustained elevated response in both LoF and GoF mutants (Fig 2.9B). When compared with nonlinear regression and extra sum-of-squares, the stimulation train profiles are significantly greater for both LoF ($p < 0.0001$, $F_{(2,1296)} = 1064$) and GoF ($p < 0.0001$, $F_{(2,1996)} = 705.5$; Fig 2.9B) mutants, indicating increased resiliency to depression. The RRP size of *$csw^{5}$* nulls is significantly increased compared to *$w^{1118}$* background controls ($p = 0.001$, two-sided *t* test; Fig 2.9C, left). Similarly, *$PTPN11^{N308D}$* GoF mutants exhibit

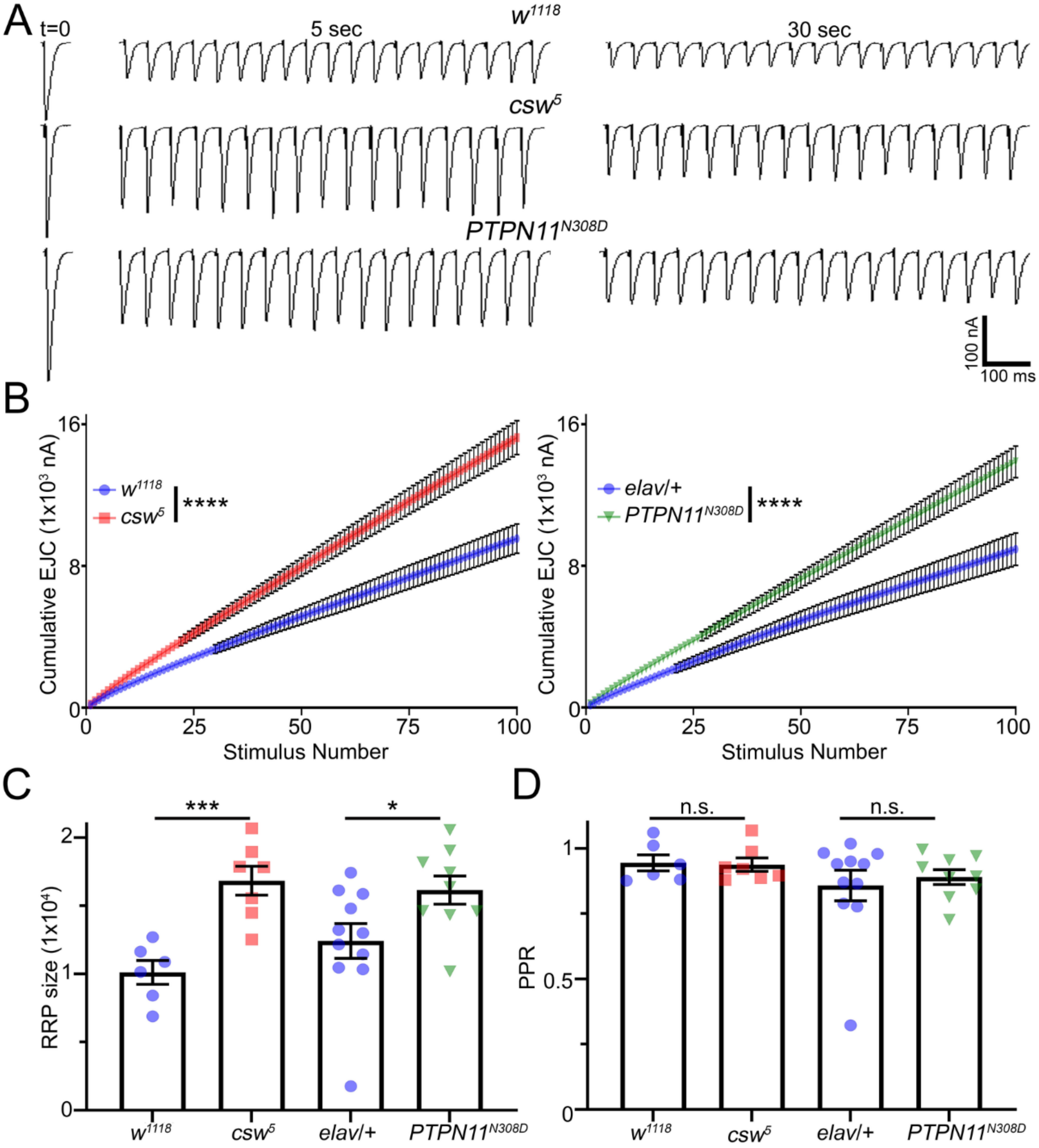

**Fig 2.9: HFS transmission depression ameliorated in *csw* nulls.**

Prolonged HFS drives progressive synaptic amplitude depression over several minutes of continuous recording at 20 Hz (1mM $Ca^{+2}$). (A) Representative nerve-stimulated EJC traces at the basal frequency (t = 0) and indicated time points during the HFS train for genetic background control (*w*$^{1118}$, top), *csw* null (*csw*$^{5}$, middle), and *PTPN11*$^{N308D}$ GoF mutant (*elav*-Gal4>*PTPN11*$^{N308D}$; bottom). (B) Quantification of cumulative EJC amplitudes over the first 100 stimulations via nonlinear regression exponential for each pair tested using extra sum-of-squares F tests. (C) Quantification of the RRP of *w*$^{1118}$ and *csw*$^{5}$ (two-sided *t* test) and *elav*-Gal4/*w*$^{1118}$ and *PTPN11*$^{N308D}$ (Mann–Whitney). (D) Quantification of the PPR of *w*$^{1118}$ and *csw*$^{5}$ (two-sided *t* test) and *elav*-Gal4/*w*$^{1118}$ and *PTPN11*$^{N308D}$ (Mann–Whitney). Scatter plots show all data points and mean ± SEM. *N* = number of NMJs. Significance: $p < 0.05$ (*), $p < 0.001$ (**), $p < 0.001$ (***), and $p < 0.0001$ (****).

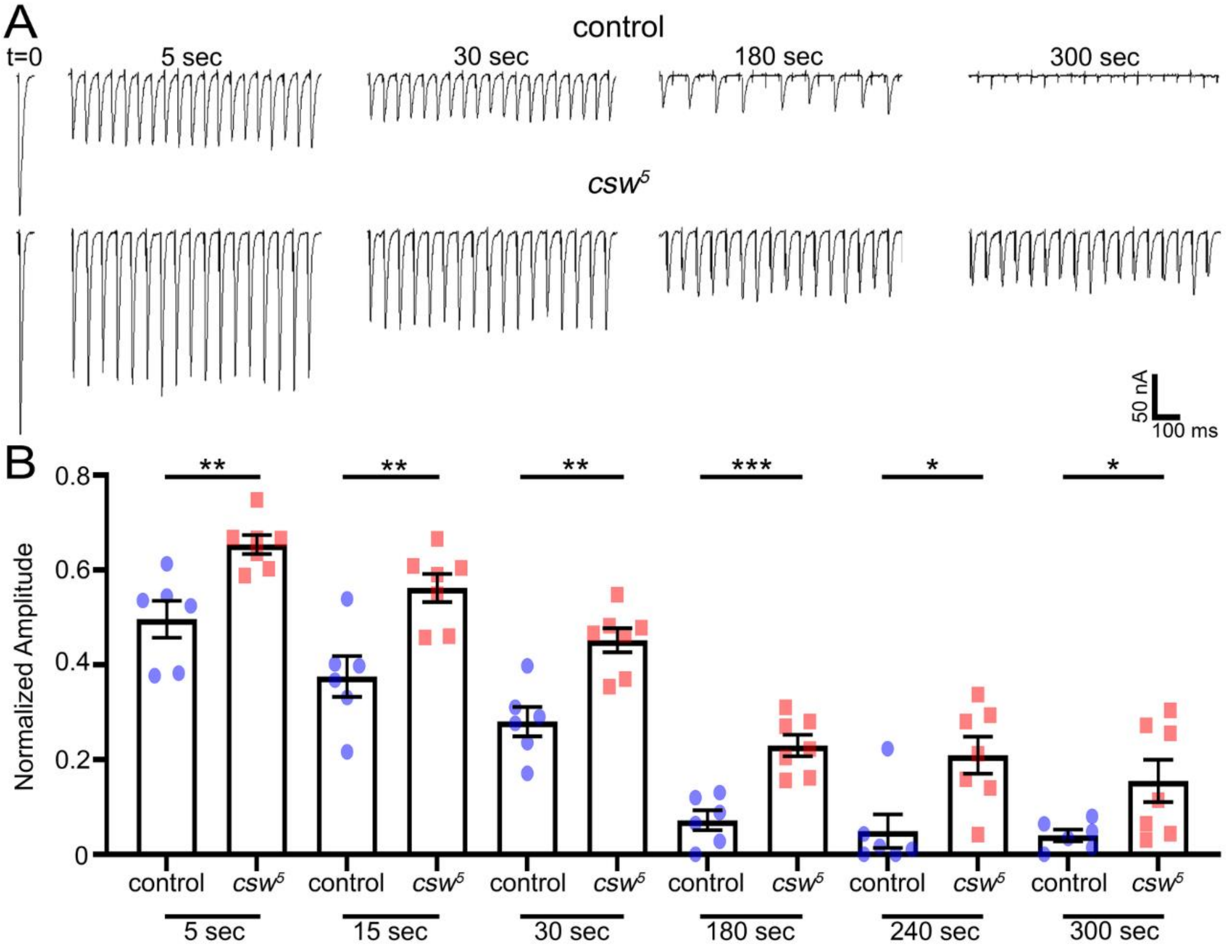

**Fig 2.10: HFS transmission depression ameliorated in *csw* nulls.**

Prolonged HFS at 20 Hz (1 mM Ca$^{+2}$) drives progressive synaptic amplitude depression over several minutes of continuous recording. (A) Representative evoked nerve-stimulated EJC traces at the basal frequency (t = 0) and indicated time points during the HFS train for the genetic background control ($w^{1118}$, top) and the *csw* null mutant ($csw^5$, bottom). (B) Quantification of normalized EJC amplitudes at the indicated time points during the HFS train using two-sided *t* tests. Scatter plots show all data points and mean ± SEM. *N* = number of NMJs. Significance: $p < 0.05$ (*), $p < 0.001$ (**), and $p < 0.001$ (***).

an increased RRP compared to transgenic *elav*/+ neuronal driver controls (*p* = 0.047, Mann–Whitney; Fig 2.9C, right). PPR analyzed for both mutants shows no in change in $csw^5$ nulls (*p* = 0.865, two-sided *t* test; Fig 2.9D, left) or $PTPN11^{N308D}$ GoF mutants (*p* = 0.941, Mann–Whitney; Fig 2.9D, right) compared to their respective controls. The depression resistance continues for 5 minutes of continuous stimulation (Fig 2.10B). Taken together, these results indicate mutants maintain transmission better with a HFS challenge. We therefore next turned to examining changes in activity-dependent synaptic function under both LoF and GoF mutant conditions.

### Corkscrew/PTPN11 enables short-term plasticity facilitation, augmentation and potentiation

Presynaptic activity drives numerous forms of short-term plasticity dependent on release mechanisms.[44,45] In high external [$Ca^{2+}$], strong stimulation results in neurotransmission depression as above, but with reduced external [$Ca^{2+}$], many forms of release strengthening are revealed, including short-term facilitation and maintained augmentation during stimulation trains, and PTP following the train.[43,47,49] Based on published *Drosophila* plasticity protocols,[41] we compared genetic background controls ($w^{1118}$ or *elav*-Gal4/$w^{1118}$), *csw* LoF nulls ($csw^5$), and *PTPN11* GoF animals (*elav*-Gal4>$PTPN11^{N308D}$) with the stimulation paradigm illustrated in Fig 2.11A. To determine baseline EJC amplitudes, we stimulated at the basal frequency (0.5 ms suprathreshold stimuli/0.2 Hz in 0.2 mM [$Ca^{2+}$]). We then applied a 10-Hz train for 1 minute, before returning to 0.2 Hz for PTP analyses (Fig 2.11A). In controls, this paradigm drives strong short-term facilitation during the initial stimuli of the train, followed by maintained transmission augmentation for the full duration of the train.[47] Following return to the basal stimulation frequency (0.2 Hz), heightened EJC amplitudes persist during the PTP period (Fig 2.11B; [47]). We normalized EJC amplitudes during and after the 10-Hz train to the initial mean EJC amplitude to show only transmission changes in response to stimulation. Quantified analyses on $w^{1118}$ control, $csw^5$ LoF, and $PTPN11^{N308D}$ GoF mutants were done for facilitation (<1 second), augmentation (>5 seconds), and PTP (following the HFS train). Representative short-term plasticity recordings and quantified results are shown in Fig 2.11.

Controls exhibit robust synaptic plasticity, including short-term facilitation (<1 second), maintained augmentation (>5 seconds), and persistent PTP (Fig 2.11C, top two blue lines). With HFS, $w^{1118}$ controls exhibit a >3-fold amplitude increase in <5 seconds, which strengthens to a 4-fold increase by 30 seconds. After the HFS train, control animals PTP at >2-fold basal transmission. In contrast, this short-term plasticity is strongly repressed in both the $csw^5$ LoF and $PTPN11^{N308D}$ GoF mutants (Fig 2.11C, bottom two red lines). When quantified via nonlinear regression and extra sum-of-squares, stimulation train profiles significantly differ for both LoF ($p < 0.0001$, $F_{(2,662)} = 38.95$) and GoF ($p < 0.0001$, $F_{(2,374)} = 25.85$; Fig 2.11C). During initial short-term facilitation (1 second), $w^{1118}$ controls show much stronger strengthening normalized to basal amplitude (2.15 ± 0.19, $n = 16$) compared to $csw^5$ LoF (1.52 ± 0.14, $n = 21$; $p = 0.005$, Mann–Whitney) and a trending decrease in $PTPN11^{N308D}$ GoF (1.44 ± 0.16, $n = 12$; $p = 0.229$, two-sided *t* test; Fig 2.11D). With maintained augmentation during the HFS train (30 seconds), $w^{1118}$ controls are highly elevated (4.27 ± 0.70, $n = 16$) compared to $csw^5$ LOF (2.67 ± 0.53, $n = 21$; $p = 0.009$, Mann–Whitney) and $PTPN11^{N308D}$ GOF (2.91 ± 0.53, $n = 12$; $p = 0.015$, Mann–Whitney; Fig 2.11E). At peak PTP after the HFS train, $w^{1118}$ controls exhibit a significant increase (3.02 ± 0.45, $n = 16$) compared to $csw^5$ LoF (1.63 ± 0.16, $n = 21$; $p = 0.003$, Mann–Whitney; Fig 2.11F). Likewise, the $PTPN11^{N308D}$ GoF (2.58 ± 0.33, $n = 11$) shows significantly decreased PTP compared to *elav*-Gal4/$w^{1118}$ controls (4.55 ± 0.5, $n = 9$; $p = 0.003$, two-sided *t* test; Fig 2.11F). These results show a role in presynaptic release dynamics, with altered responses to evoked stimulation. To understand the mechanism of these changes, we next turned to testing the role of MAPK/ERK signaling.

### Elevated corkscrew/PTPN11 synaptic transmission corrected with phospho-ERK inhibitors

NS and NSML phenotypes are hypothesized to converge due to both LoF/GoF disease states exhibiting constitutively elevated MAPK/ERK signaling.[94] Similarly, we hypothesize the mutant LoF/GoF neurotransmission elevation from heightened glutamate release also occurs downstream of elevated presynaptic MAPK/ERK signaling. To test this hypothesis, we used MAPK/ERK inhibitors (Trametinib and Vorinostat) to assay effects on glutamatergic synaptic function. Trametinib binds and inhibits MEK1/2,[140]

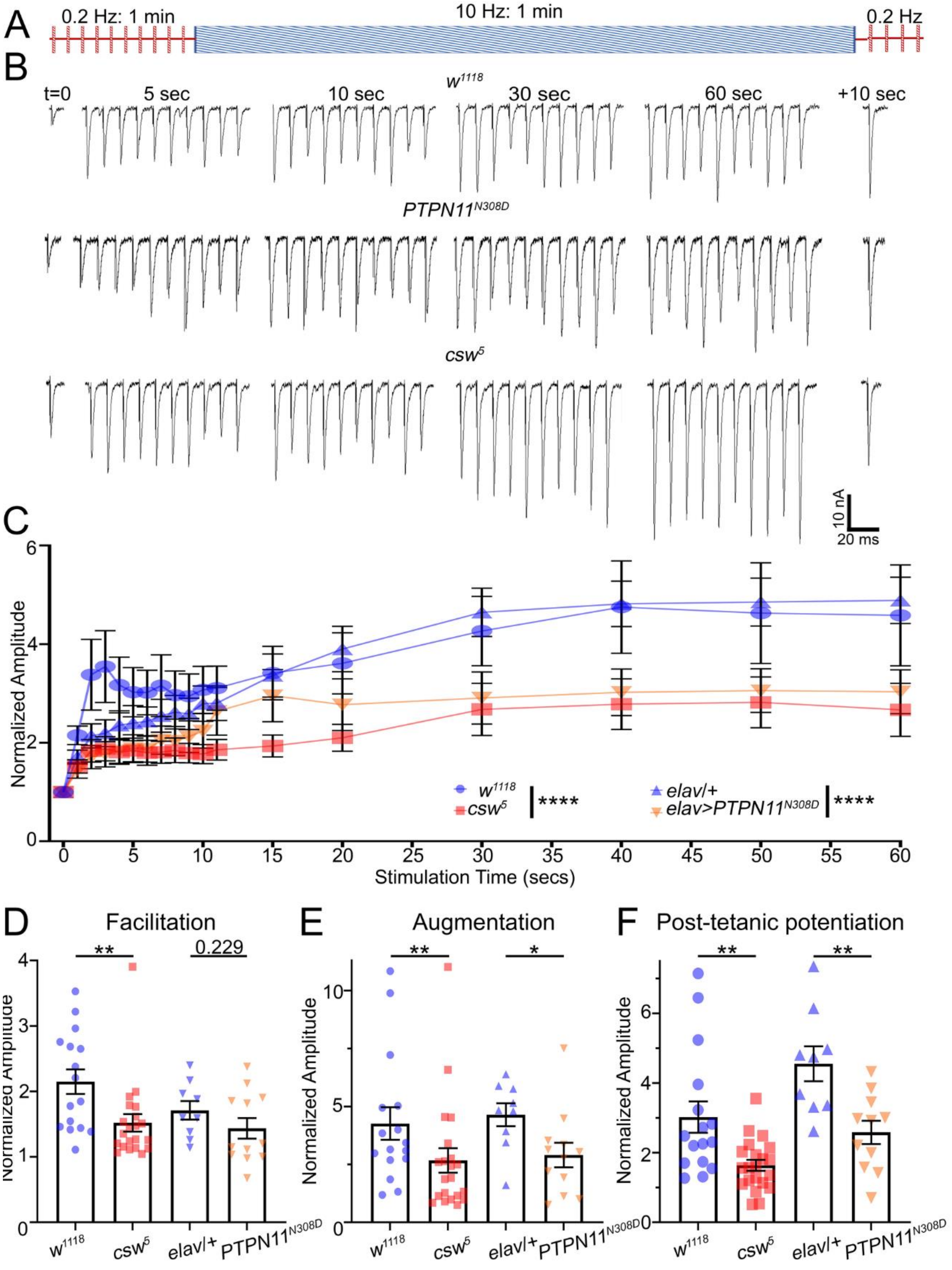

**Fig 2.11: Activity-dependent synaptic plasticity repressed in *csw*/*PTPN11* mutants.**
Synaptic plasticity during and following a short-term stimulation train to measure facilitation, augmentation, and PTP. (**A**) Stimulation paradigm: 1 minute at 0.2 Hz (0.2 mM Ca$^{2+}$), followed by 1 minute at 10 Hz, and then a return to 0.2 Hz. (**B**) Sample EJC traces at indicated time points during and following the 10 Hz train for control ($w^{1118}$, top), GoF $PTPN11^{N308D}$ (*elav*-Gal4>$PTPN11^{N308D}$; middle), and *csw* null ($csw^5$, bottom). (**C**) Quantification of EJC amplitude during the 10-Hz train normalized to basal EJC amplitude for each genotype. The nonlinear regression exponential for each pair tested using extra sum-of-squares F test. (**D-F**) Quantification of facilitation (1 second, **D**) and augmentation (30 seconds, **E**) during the 10-Hz train, and PTP (10 seconds following train, **F**) normalized to the basal EJC amplitude for each genotype using Mann–Whitney/two-sided *t* tests. Scatter plots show all data points and mean ± SEM. *N* = number of NMJs. Significance: $p < 0.05$ (*), $p < 0.001$ (**), and $p < 0.0001$ (****).

resulting in a direct inhibition of MAPK/ERK signaling.[91] Vorinostat acts as a HDAC inhibitor to also inhibit MAPK/ERK signaling.[91,141] Recent work using the *PTPN11* mutations from human patients has highlighted these two drugs as possible treatments for a variety of different NS/NSML mutations.[91] Both drugs are thus interesting not only for their ability to test elevated MAPK/ERK signaling upstream of neurotransmission, but also as possible future treatment avenues. We fed both drugs and then analyzed changes in EJC amplitudes using TEVC recording. For each drug, we compared the background control ($w^{1118}$) without drug treatments to controls with drug treatments (Trametinib and Vorinostat), as well as the *csw* null mutants ($csw^5$) without drug treatments to nulls with drug treatments (Trametinib and Vorinostat). Quantification of evoked EJC amplitudes in all 8 conditions tests whether each drug changes neurotransmission in control, as well as correction of the null $csw^5$ elevated neurotransmission (Fig 2.1A). We also analyzed mEJC recordings of the same genotypes to test for correction of $csw^5$ elevated mEJC frequency (Fig 2.5C and 2.5D). Representative EJC and mEJC traces and quantified results are shown in Fig 2.12.

Null $csw^5$ animals fed Trametinib have clearly decreased neurotransmission compared to untreated mutants, with EJC amplitudes comparable to control animals (Fig 2.12A). Quantification shows untreated controls (159.10 ± 7.35 nA, $n = 36$) and drugged controls (161.70 ± 12.01 nA, $n = 35$) are not significantly different ($p > 0.99$, Dunn's; Fig 2.12B). In contrast, $csw^5$ EJC amplitudes (226.20 ± 9.79 nA, $n = 30$) are significantly increased compared to controls with ($p < 0.0001$, Dunn's; Fig 2.12B) and without Trametinib ($p = 0.001$, Dunn's, Fig 2.12B). Critically, $csw^5$ nulls fed Trametinib (172.70 ± 11.37 nA, $n = 27$) are no longer significantly increased from controls with or without Trametinib ($p > 0.99$, Dunn's) but are significantly decreased compared to the untreated $csw^5$ nulls ($p = 0.003$, Dunn's; Fig 2.12B). Similar results occur with Trametinib treatment of $PTPN11^{N308D}$ GoF mutants (Fig 2.13A and 2.13B). Similarly, Vorinostat fed $csw^5$ nulls have EJC amplitudes restored to the control levels (Fig 2.12C). Quantification shows controls with (167.20 ± 7.01 nA, $n = 16$) and without (162.30 ± 9.46 nA, $n = 20$) Vorinostat are not significantly different ($p = 0.994$, Tukey's; Fig 2.12D). In contrast, $csw^5$ mutants (237.0 ± 14.72 nA, $n = 25$) are significantly increased versus controls with ($p = 0.001$, Tukey's) and without ($p = 0.0001$, Tukey's) Vorinostat (Fig 2.12D). Null $csw^5$ fed

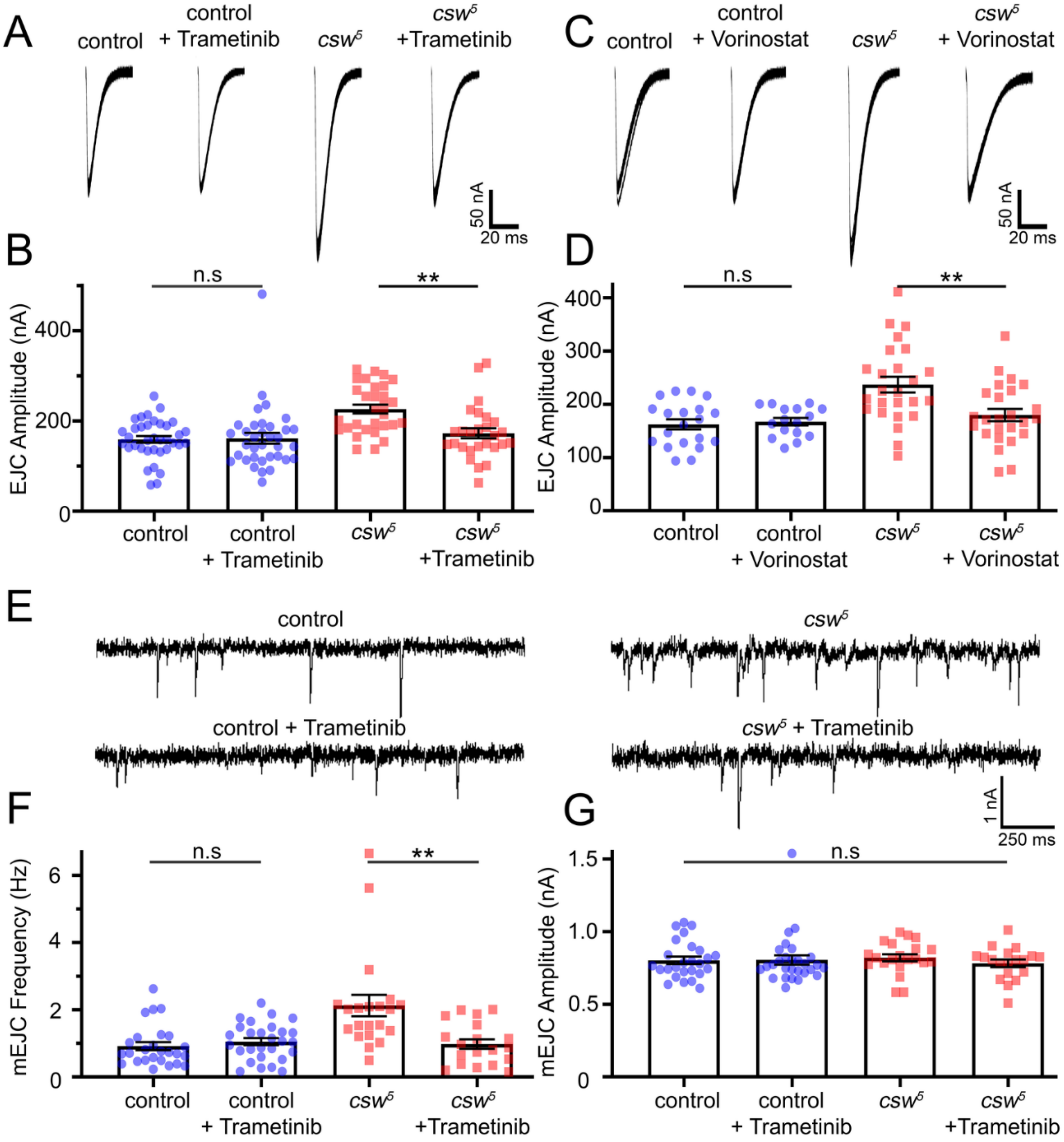

**Fig 2.12: Reducing pERK signaling restores synaptic function in *csw* nulls.**
TEVC recordings with and without two pERK inhibiting drugs (Trametinib and Vorinostat) comparing the genetic background control ($w^{1118}$) and *csw* null mutant ($csw^5$). (A) Representative EJC traces showing 10 superimposed responses (1.0 mM $Ca^{+2}$) comparing the control (left) and $csw^5$ null mutant (right), with and without Trametinib. (B) Quantification of mean EJC amplitudes for all 4 conditions using Kruskal–Wallis followed by Dunn's multiple comparisons. (C) Representative EJC traces comparing the control (left) and $csw^5$ null mutant (right), with and without Vorinostat. (D) Quantification of EJC amplitudes for all 4 conditions using one-way ANOVA followed by Tukey's multiple comparisons. (E) Representative mEJC traces (1.0 mM $Ca^{2+}$) in the $w^{1118}$ control (left) and $csw^5$ null mutant (right), with and without Trametinib. (F) Quantification of mEJC frequency in all 4 conditions using a Kruskal–Wallis followed by Dunn's multiple comparisons. (G) Quantification of mEJC amplitudes using a Kruskal–Wallis. Scatter plots show all the data points and the mean ± SEM. *N* = number of NMJs. Significance: $p > 0.05$ (not significant, n.s.) and $p < 0.001$ (**).

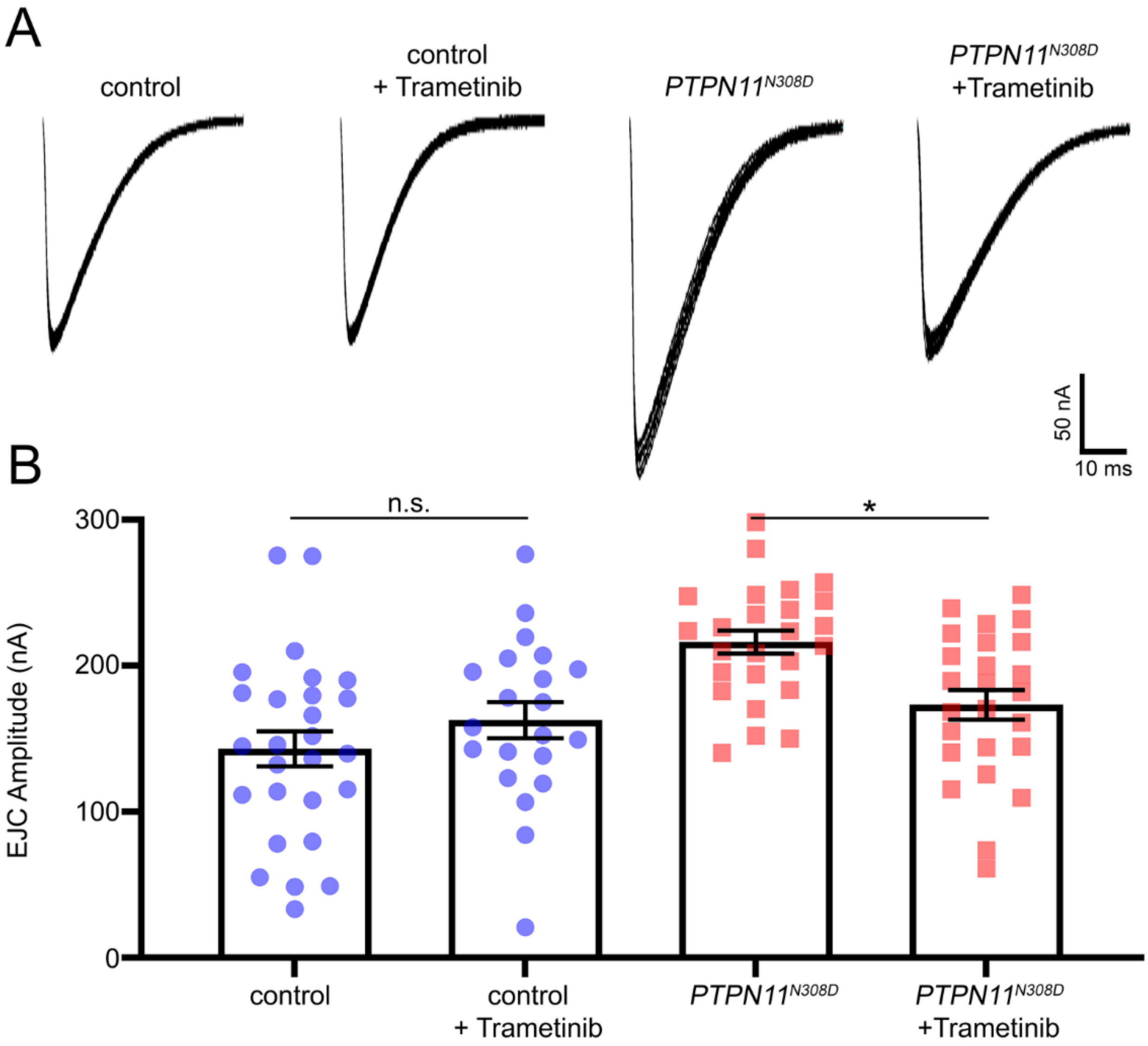

**Fig 2.13: Reducing ERK signaling restores NS model *PTPN11* synaptic function.**
TEVC recordings with and without the pERK inhibiting drug Trametinib comparing the driver control (*elav-Gal4/w$^{1118}$*) and NS GoF patient mutant (*elav-Gal4>PTPN11$^{N308D}$*). (A) Representative EJC traces showing 10 superimposed responses (1.0 mM Ca$^{+2}$) comparing the control (left) and *PTPN11$^{N308D}$* mutant (right), with and without Trametinib. (B) Quantification of mean EJC amplitudes for all 4 conditions using one-way ANOVA and Tukey's multiple comparisons. Scatter plots show all the data points and the mean ± SEM. *N* = number of NMJs. Significance: $p > 0.05$ (not significant, n.s.) and $p < 0.05$ (*).

Vorinostat (179.70 ± 11.55 nA, *n* = 25) are not significantly elevated compared to controls with (*p* = 0.897) and without (*p* = 0.727) Vorinostat but are significantly decreased compared to untreated *csw*$^5$ nulls (*p* = 0.003, Tukey's; Fig 2.12D). Trametinib decreases mEJC frequency in *csw*$^5$ nulls compared to untreated mutants, to levels matching controls (Fig 2.12E). Quantification shows untreated (0.92 ± 0.12 Hz *n* = 26) and drugged (1.05 ± 0.103 Hz, *n* = 28) controls are not significantly different (*p* > 0.99, Dunn's; Fig 2.12F). In contrast, c*sw*$^5$ mEJC frequency (2.13 ± 0.32 Hz, *n* = 21) is significantly increased compared to controls (no drug, *p* < 0.0001, Dunn's; Trametinib, *p* = 0.003, Dunn's; Fig 2.12F). Critically, c*sw*$^5$ nulls fed Trametinib (0.98 ± 0.14 Hz, *n* = 19) are no longer significantly increased from controls with or without the drug (*p* > 0.99, Dunn's) but are significantly decreased compared to untreated c*sw*$^5$ mutants (*p* = 0.001, Dunn's; Fig 2.12F). There are no changes in mEJC amplitude (*p* = 0.437, Kruskal–Wallis; Fig 2.12G). Thus, decreasing MAPK/ERK signaling restores presynaptic neurotransmission in *csw*$^5$ animals. We therefore next aimed to identify the upstream mechanism controlling this regulation.

### FMRP binds csw mRNA to suppress Csw protein expression upstream of MAPK/ERK signaling

The FMRP negative translational regulator is well known to inhibit MAPK/ERK signaling in the regulation of synaptic function.[76] Moreover, high-throughput RNA sequencing from isolated crosslinking immunoprecipitation shows FMRP binds *csw* homolog *PTPN11/SHP2* mRNA.[107] Therefore, we hypothesized FMRP binds *csw* mRNA to negatively regulate translation upstream of MAPK/ERK signaling. To test this hypothesis, we first performed RNA-immunoprecipitation (RIP) studies with tagged FMRP::YFP from larval lysates using magnetic GFP-trap beads.[142,143] We used Tubby::GFP lysates as the RIP negative control, with α-*tubulin* (FMRP does not bind) as the internal negative control, and *futsch/MAP1B* (known FMRP target) as the internal positive control [115]. Immunoprecipitated mRNAs were reverse transcribed and tested with specific primers on 2% agarose gels. We next used western blots from larval ventral nerve cord (VNC)/brain lysates to test neuronal Csw protein levels with a characterized anti-Csw antibody [82]. Antibody specificity was confirmed with the *csw*$^5$ null and protein levels compared between the genetic background control ($w^{1118}$) and FXS disease model (*dfmr1* null mutants). To compare neuronal Csw protein levels in these different genotypes, we normalized to glyceraldehyde 3-phosphate dehydrogenase (GAPDH), a housekeeping gene that we confirmed is not regulated by Csw. Normalized quantification was done to compare neuronal Csw protein levels in the $w^{1118}$ controls, $csw^{5}$ null mutants, and $dfmr1^{50M}$ null mutants. Representative RIP gels, western blots, and western blot quantified data are shown in Fig 2.14.

For the RIP analyses, *csw*, *futsch*, and α-*tubulin* mRNA bands are all present in both Tubby::GFP control and FMRP::YFP input lysates (Fig 2.14A). Immunoprecipitation pulls down *csw* mRNA from the FMRP::YFP third instar lysates, with no binding in the Tubby::GFP control (Fig 2.14A). Additionally, the positive control *futsch* mRNA is pulled down, but there is no detectable negative control α-*tubulin* mRNA. These results indicate FMRP binds *csw* mRNA, with the controls confirming binding interaction specificity. Based on this and above findings, we hypothesized FMRP partly inhibits NMJ synaptic transmission by suppressing Csw translation in neurons to decrease MAPK/ERK signaling. To test this hypothesis, western blot analyses were done to test Csw protein levels in larval brain/VNC lysates from controls ($w^{1118}$), $csw^{5}$, and $dfmr1^{50M}$ null mutants. At the predicted molecular weight (100 kDa), there is a clear Csw band present in controls (Fig 2.14B). This band is undetectable in $csw^{5}$ nulls, demonstrating specificity (Fig 2.14B). In the FXS disease model, there are clearly and consistently increased Csw protein levels in *dfmr1* null mutants (Fig 2.14B). Quantified comparisons normalized to GAPDH ($p < 0.0001$, ANOVA) show an increase in Csw levels in *dfmr1* nulls (1.55 ± 0.13) compared to controls (0.99 ± 0.029), which reveals a highly significant increase in the FXS disease model ($p = 0.0008$, Tukey's, Fig 2.14C). There is slight background in $csw^{5}$ (0.23 ± 0.06), which is very significantly decreased from controls ($p < 0.0001$, Tukey's) and *dfmr1* mutants ($p < 0.0001$, Tukey's; Fig 2.14C). Thus, *dfmr1* nulls have a strong increase in Csw levels in the larval neurons. Taken together, these findings show FMRP binds *csw* mRNA to negatively regulate Csw protein levels. We hypothesized this interaction negatively regulates presynaptic MAPK/ERK signaling.

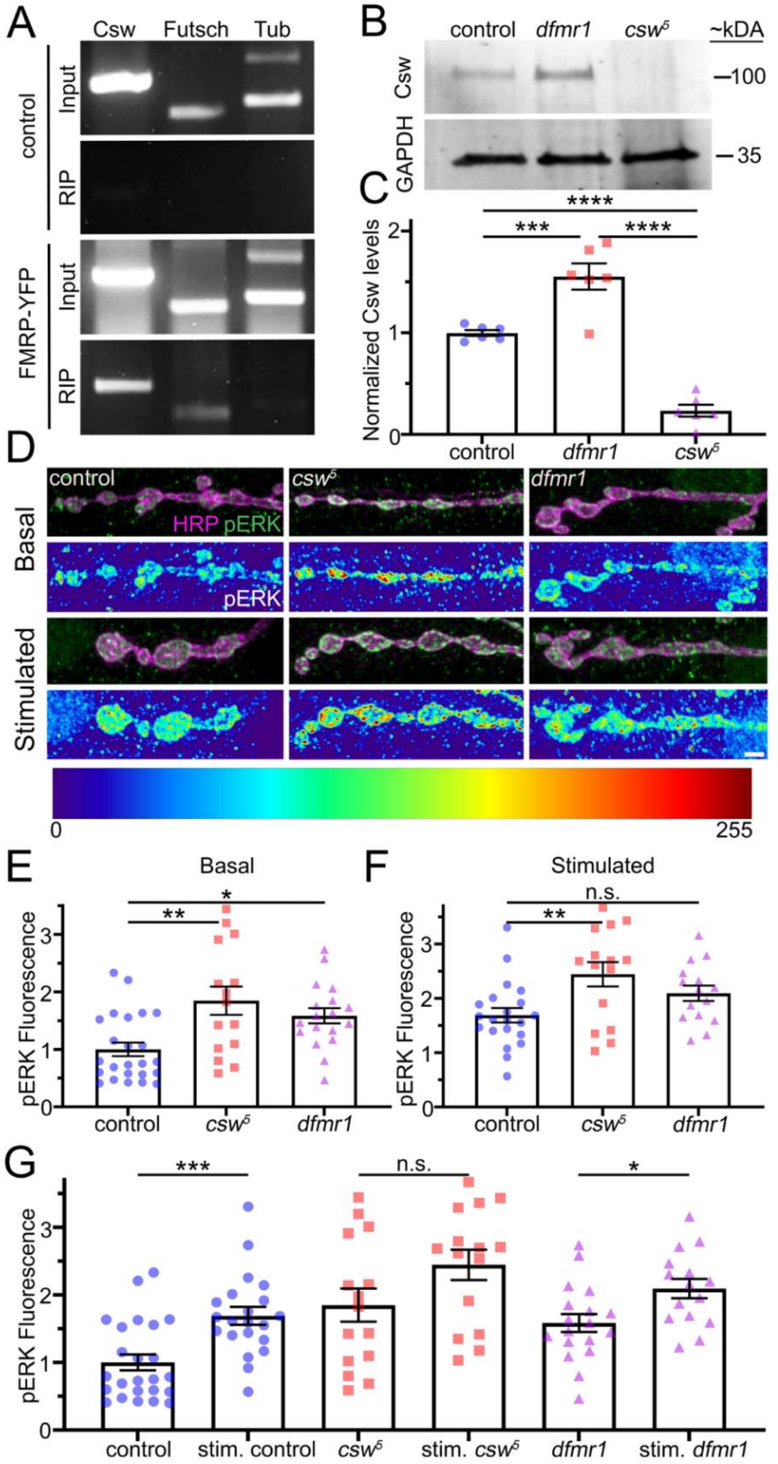

**Fig 2.14: FMRP binds *csw* mRNA to suppress neuronal Csw and presynaptic pERK levels.**
(A) RIP control (Tubby::GFP, top) and FMRP (FMRP::YFP, bottom), with *csw*, *futsch* (positive control), and α-*tubulin* (negative control) RNAs. (B) Western blot for Csw (100 kDa, top) and GAPDH control (35 kDA, bottom) $w^{1118}$ control, $dfmr1^{50M}$ null, and $csw^{5}$ null. (C) Quantification of Csw levels normalized to GAPDH using one-way ANOVA followed by Tukey's multiple comparisons. (D) Representative NMJ images of $w^{1118}$ control, $csw^{5}$ null, and $dfmr1^{50M}$ null colabeled for pERK (green) and presynaptic membrane marker anti-HRP (magenta). pERK fluorescence shown as a heat map. NMJs shown without stimulation (basal, top) and with 90 mM [K$^{+}$] HFS (high K$^{+}$, bottom). Scale bar: 2.5 µm. (E) Quantified normalized basal presynaptic anti-pERK fluorescence for all 3 genotypes using one-way ANOVA and Tukey's multiple comparisons. (F) Quantified normalized stimulated presynaptic anti-pERK fluorescence using one-way ANOVA and Tukey's multiple comparisons. (G) Quantification of normalized presynaptic pERK levels in all 3 genotypes under basal and stimulated conditions using two-sided *t* tests. Scatter plots show all data points and mean ± SEM. *N* = number of animals (C) or NMJS (E-G). Significance: $p > 0.05$ (not significant, n.s.), $p < 0.05$ (*), $p < 0.001$ (**), $p > 0.001$ (***), and $p < 0.0001$ (****).

### FMRP and Csw interact to inhibit presynaptic MAPK/ERK signaling and neurotransmission

We next set forth to test MAPK/ERK signaling within presynaptic boutons in order to begin investigating how FMRP and Csw interact to control presynaptic transmission. Elevated presynaptic pERK is well known to positively regulate neurotransmitter release function.[73] Based on this known role and our above studies, we hypothesized locally elevated pERK levels should occur in both *csw* and *dfmr1* null synaptic boutons. To test this hypothesis, we assayed NMJ terminals double-labeled with anti-pERK [144]and anti-horseradish peroxidase (HRP) to mark presynaptic bouton membranes. Using HRP to delineate presynaptic boutons, we measured pERK fluorescence intensity normalized to the genetic background control ($w^{1118}$). Presynaptic pERK signaling is activity-dependent. [145,146] To test this function, we compared presynaptic pERK levels in the basal resting condition to stimulation with acute (10 minute) high [$K^+$] depolarization (90 mM; [147,148]) in $w^{1118}$ control, $dfmr1^{50M}$ null mutant, and $csw^5$ null mutant. We hypothesized that FMRP and Csw interact to inhibit presynaptic pERK signaling-dependent transmission strength. To test this hypothesis, we assayed the double *trans*-heterozygous $csw^5$/+; $dfmr1^{50M}$ /+ mutant compared to both single heterozygous mutants alone.[40] We first used TEVC recordings to measure stimulation evoked EJC responses and spontaneous mEJC release events. We then used pERK/HRP double-labeled imaging to measure the presynaptic pERK fluorescence intensity levels. Representative raw data of recordings and images as well as quantified results are shown in Fig 2.14.

Activated pERK is weakly detectable at control synapses under basal resting conditions (Fig 2.14D, top). In $w^{1118}$ controls, pERK is localized at relatively higher levels in the presynaptic boutons, with lower levels of signaling in the adjacent muscle nuclei and very low sporadic levels throughout the muscle. Given the consistent presynaptic phenotypes above, we focused analyses on pERK signaling within presynaptic boutons. Compared to controls, both *csw* and *dfmr1* null mutants display consistently elevated pERK levels within the presynaptic boutons (Fig 2.14D, top), but with similar levels of pERK fluorescence in muscle compared to the controls. Similar results occur in *PTPN11* human patient mutants compared to driver controls (Fig 2.15A), with elevated pERK levels in all conditions (Fig 2.15B Fig). This increased presynaptic pERK signaling and lack of postsynaptic changes is consistent with presynaptic perturbations in

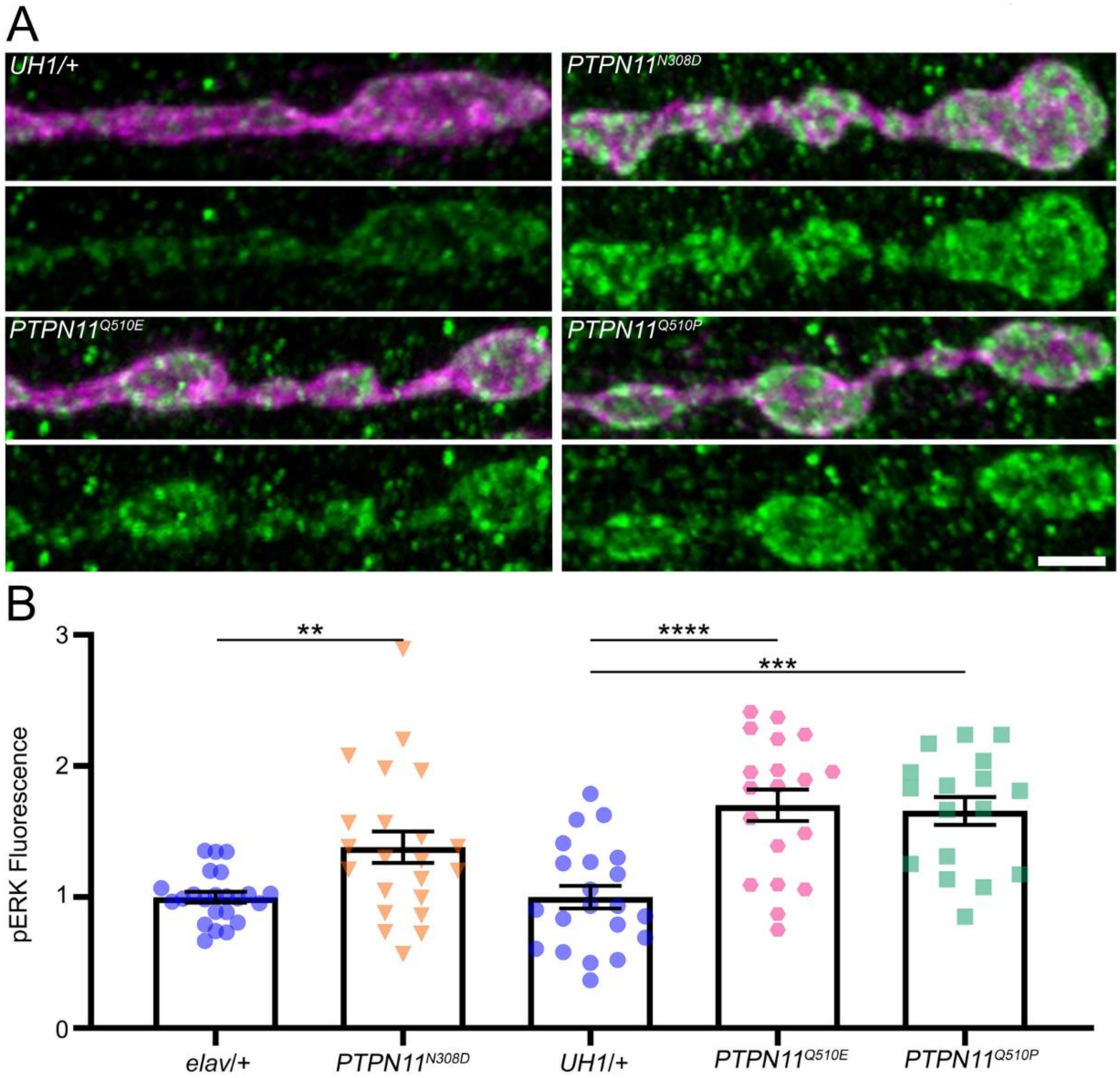

**Fig 2.15: *PTPN11* LoF and GoF mutants exhibit elevated presynaptic pERK levels.**
(A) Representative NMJ images of the driver control (*UH1*-Gal4/*w*$^{1118}$, top left), the GoF mutant (*elav>PTPN11*$^{N308D}$; top right), and two LoF mutants (*UH1*-Gal4>*PTPN11*$^{Q510E}$, bottom left, and *UH1-Gal4>PTPN11*$^{Q510P}$; bottom right) colabeled for presynaptic membrane marker anti-HRP (magenta) and pERK (green). Scale bar: 2.5 µm. (B) Quantified presynaptic anti-pERK fluorescence for all 5 genotypes using a two sided *t* test (*PTPN11*$^{N308D}$) and one-way ANOVA and Tukey's multiple comparisons (*PTPN11*$^{Q510E}$/ *PTPN11*$^{Q510P}$). Scatter plots show all data points and mean ± SEM. *N* = number of NMJs. Significance: $p < 0.001$ (**), $p > 0.001$ (***), and $p < 0.0001$ (****).

both *csw* and *dfmr1* null mutants. Quantification of the normalized pERK fluorescent intensity within the HRP-delineated presynaptic boutons shows very highly elevated levels in both the *csw* (1.85 ± 0.25, *n* = 15) and *dfmr1* (1.58 ± 0.13, *n* = 18) null mutants compared to controls (1.0 ± 0.12, *n* = 24), which is a significant increase (*p* = 0.001, one-way ANOVA; Fig 2.14E). When compared individually, there is no significant difference between *dfmr1* and *csw* mutants (*p* = 0.526, Tukey's), showing both *csw* (*p* = 0.001, Tukey's) and *dfmr1* (*p* = 0.024, Tukey's; Fig 2.14E) nulls increase pERK signaling to a similar degree compared to controls. This elevated presynaptic pERK in both disease models fits our hypothesis that elevated MAPK/ERK signaling causes the increased presynaptic transmission in both disease models. Given the above changes in activity-dependent presynaptic function in *csw* null mutants, we next wanted to test whether pERK levels are dynamic and change with a stimulation challenge, and whether activity-dependent impairments occur in the two disease models.

When NMJs are strongly stimulated by acute depolarization (90 mM [$K^+$] for 10 minutes), $w^{1118}$ controls exhibit sharply increased presynaptic pERK levels compared to the basal resting condition (Fig 2.14D, bottom). Both *dfmr1* and *csw* nulls show smaller pERK level increases upon stimulation. This elevation shows pERK levels can be further increased in null mutants, indicating that the mechanism behind the increase is not exhausted under basal conditions or is controlled by other mechanisms beyond activity. Quantification of presynaptic pERK fluorescent intensity levels normalized to rest (*p* = 0.007, one-way ANOVA) shows pERK elevation in controls (1.68 ± 0.12, *n* = 21), *csw* nulls (2.44 ± 0.22, *n* = 15), and *dfmr1* (2.09 ± 0.14, *n* = 15) nulls, with *csw* exhibiting a significant elevation compared to controls (*p* = 0.005, Tukey's; Fig 2.14F). When stimulated, pERK levels are similar in *csw* and *dfmr1* (*p* = 0.341, Tukey's); however, *dfmr1* nulls are no longer significantly increased compared to controls (*p* = 0.192, Tukey's; Fig 2.14F). To further assay activity-dependent changes, we directly compared the basal and stimulated pERK levels. Importantly, controls exhibit a significant activity-dependent presynaptic pERK increase when compared to rest (*p* = 0.0003, two-sided *t* test; Fig 2.14G). In contrast, *csw* nulls display only a trending elevation in stimulated pERK levels, without a significant increase from rest (*p* = 0.083, two-sided *t* test; Fig 2.14G). Likewise, *dfmr1* nulls display a reduced activity-dependent increase in stimulated presynaptic pERK levels compared to the basal condition, albeit still significant ($p = 0.014$, two-sided *t* test; Fig 2.14G). We conclude that the basal elevation in pERK levels in both disease models blunts further activation in response to stimulation. This activity-dependent defect correlates with the above impaired functional neurotransmission dynamics in response to stimulation. Based on the perturbed presynaptic pERK signaling in *csw* and *dfmr1* nulls, we hypothesized FMRP and Csw interact to inhibit synaptic MAPK/ERK signaling and transmission.

We therefore directly tested for this mechanism with *csw*/+; *dfmr1*/+ *trans*-heterozygotes. In TEVC recordings, these *trans*-heterozygotes show elevated neurotransmission compared to $w^{1118}$ controls and both of the single heterozygotes (Fig 2.16A). Quantification reveals that the *csw*/+; *dfmr1*/+ *trans*-heterozygotes have higher EJC amplitudes (237.80 ± 7.5810 nA, $n = 20$) compared to $w^{1118}$ controls (169.67 ± 8.1240 nA, $n = 32$), a significant increase ($p < 0.0001$, Dunnett's; Fig 2.16B). In contrast, both *csw*/+ (199.10 ± 10.92 nA, $n = 23$) and *dfmr1*/+ (194.0 ± 11.36 nA, $n = 18$) heterozygotes display similar EJC amplitudes comparable to the $w^{1118}$ control (Fig 2.16A), with no significant elevation ($p = 0.19/0.058$, Dunnett's; Fig 2.16B). In mEJC recordings, double *csw*/+; *dfmr1*/+ *trans*-heterozygotes display a clear increase in mEJC frequency compared to both $w^{1118}$ control and single heterozygotes (Fig 2.16C). Quantification shows *trans*-heterozygote mEJC frequency (2.60 ± 0.29 Hz, $n = 16$) elevated compared to $w^{1118}$ (1.34 ± 0.15 Hz, $n = 19$), a significant increase ($p = 0.0002$, Dunn's; Fig 2.16D). Both of the single heterozygotes, *csw*/+ (1.69 ± 0.19 Hz, $n = 16$) and *dfmr1*/+ (1.91 ± 0.26 Hz, $n = 15$), display a similar frequency comparable to $w^{1118}$ control (Fig 2.16C), with no significant change ($p = 0.428/0.151$, Dunn's; Fig 2.16D). There are no significant changes in the mEJC amplitudes ($p = 0.855$, Kruskal–Wallis; Fig 2.16E), confirming a presynaptic mechanism. Activated pERK labeling shows *csw*/+; *dfmr1*/+ *trans*-heterozygotes have elevated presynaptic signaling compared to $w^{1118}$ control and the single heterozygotes (Fig 2.16F). Quantification shows increased presynaptic pERK fluorescence intensity in the trans-heterozygote (1.64 ± 0.11, $n = 34$) normalized to control (1.0 ± 0.07, $n = 41$), a significant elevation ($p < 0.0001$, Dunn's; Fig 2.16G). Both of the single heterozygotes, *csw*/+ (1.02 ± 0.10, $n = 31$) and *dfmr1*/+ (1.23 ± 0.12, $n = 34$) have presynaptic pERK levels comparable to the control

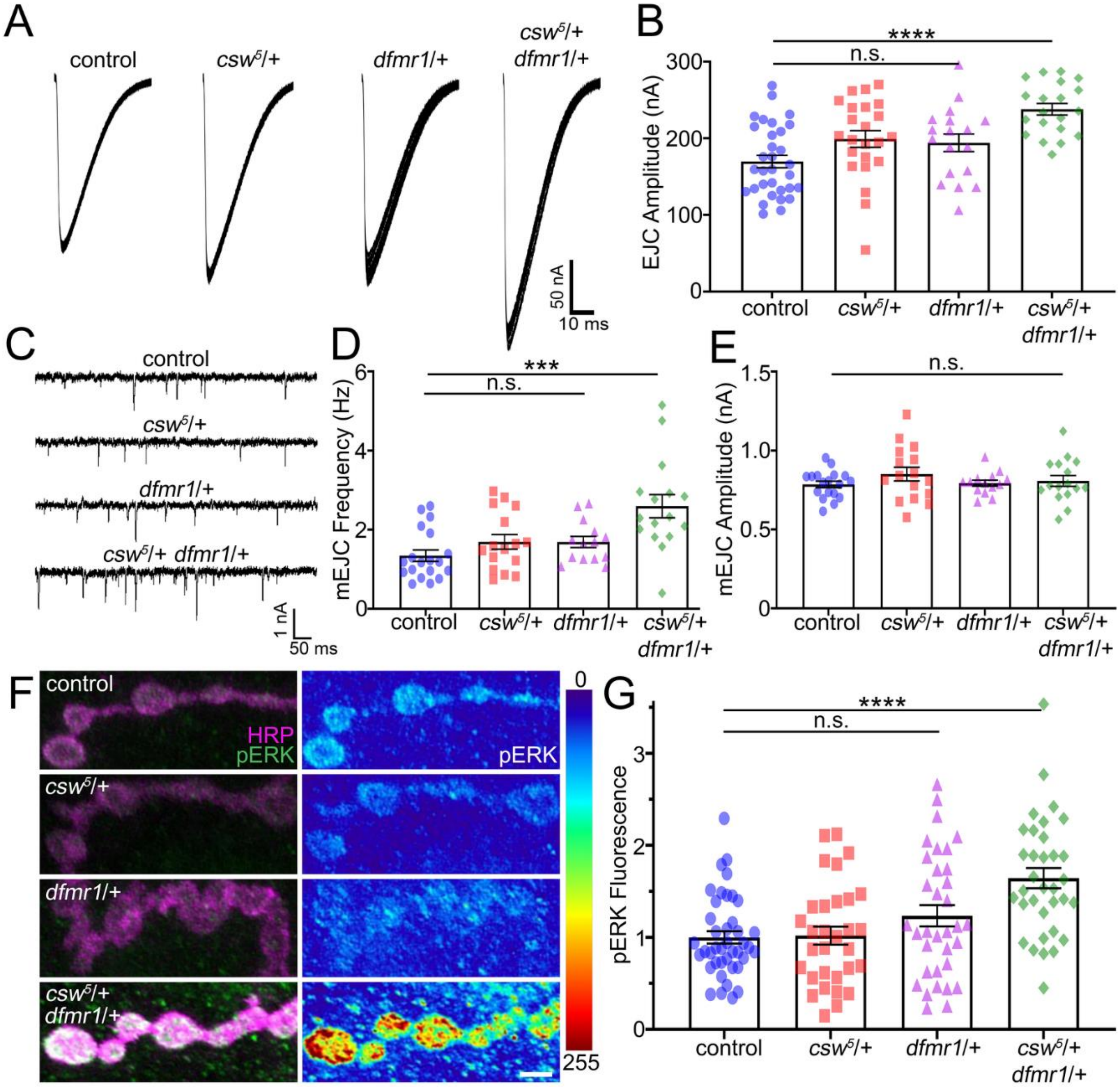

**Fig 2.16: *Trans*-heterozygous *csw*/+; *dfmr1*/+ recapitulate disease model phenotypes.**
(A) Representative evoked EJC traces showing 10 superimposed TEVC recordings in background control ($w^{1118}$), single heterozygotes ($csw^{5}$/+ and $dfmr1^{50M}$/+), and the *trans*-heterozygote ($csw^{5}$/+; $dfmr1^{50M}$/+). (B) Quantification of mean EJC amplitudes for all 4 genotypes using one-way ANOVA and Dunnett's multiple comparisons. (C) Representative mEJC traces from the same 4 genotypes. (D) Quantification of mEJC frequency for all 4 genotypes using Kruskal–Wallis and Dunn's multiple comparisons. (E) Quantification of mEJC amplitude for all 4 genotypes using Kruskal–Wallis. (F) Representative NMJ images from the same 4 genotypes colabeled for anti-pERK (green) and presynaptic membrane anti-HRP (magenta). pERK also shown as a heat map. Scale bar: 2.5 µm. (G) Quantification of normalized synaptic pERK fluorescence for all 4 genotypes using Kruskal–Wallis and Dunn's multiple comparison tests. Scatter plots show all data points and the mean ± SEM. *N* = number of NMJs. Significance: $p > 0.05$ (not significant, n.s.), $p < 0.001$ (**), $p > 0.001$ (***), and $p < 0.0001$ (****).

(Fig 2.16F), showing no significant change ($p$ > 0.999/0.312, Dunn's; Fig 2.16G). Taken together, these findings indicate FMRP and Csw interact to regulate presynaptic pERK signaling upstream of neurotransmitter release.

## Discussion

MAPK is well known to regulate activity-dependent signal transduction and synaptic plasticity within the nervous system.[53] Four MAPK families have been characterized, including extracellular signal-regulated kinase 1/2 (ERK1/2), ERK5, p38 MAPK, and the c-Jun N-terminal kinase (JNK; [70]). These families are activated similarly through an evolutionarily conserved cascade involving initial activation of GTPases (Ras/Rac) and a subsequent three-tiered protein kinase signaling system.[71] The best-characterized MAPK pathway, ERK1/2, has been extensively investigated within the nervous system, where ERK activation is very tightly regulated. Numerous neurological disease states display elevated ERK activity, including FXS, NS, and NSML, as well as neurodegenerative diseases such as Alzheimer's and Parkinson's disease.[72,76,94] Many studies have linked such elevated ERK signaling to cognitive deficits, particularly impairment of LTM consolidation. LTM requires spaced learning sessions during which ERK is activated and then decays in a temporal cycle. In *Drosophila* PTPN11/SHP2 homolog *csw* mutants, this ERK activation timing cycle is perturbed and LTM is disrupted.[52] Moreover, one of the targets of FMRP, a negative translational regulator, is *PTPN11/SHP2* mRNA,[107] suggesting a potential link between the FXS and NS/NSML disease states. Based on the common ERK signaling up-regulation in these disorders, we hypothesized FMRP regulates Csw translation to modulate synaptic ERK levels to control neurotransmission strength and functional plasticity.

This hypothesis provides the first proposed mechanistic connection between NS, NSML, and FXS disease conditions, through an ERK phosphorylation (pERK) signaling defect in presynaptic boutons. pERK is known to activate presynaptic function, with short-term roles in the control of neurotransmission strength and activity-dependent plasticity,[73,78] and longer-term nuclear translocation roles.[71] In the *Drosophila* NS/NSML disease models of *csw* LoF and GoF, we began with synaptic transmission assays at the

NMJ glutamatergic synapse.[46] We also tested human patient *PTPN11/SHP2* mutations to confirm functional requirements.[91] Our work reveals that all LoF/GoF mutations elevate neurotransmission strength, indicating that Csw/SHP2 is involved in inhibiting glutamatergic signaling. Consistently, previous *Drosophila* NS and NSML model studies also show that LoF and GoF mutations phenocopy one another, with a correlation to hyperactivated pERK signal transduction in both conditions.[82,94] Moreover, the *Drosophila* FXS disease model similarly increases NMJ glutamatergic synaptic transmission,[115] consistent with the FMRP mechanistic intersection. Localized pERK signaling occurs on both pre- and postsynaptic sides,[149,150] so we next used cell-targeted *csw* RNAi and measured spontaneous vesicle fusion events to separate these requirements. Our work reveals Csw/SHP2 has only a neuronal role in the regulation of presynaptic transmission. There is no detectable postsynaptic function. This new presynaptic Csw/SHP2 role is consistent with the abundant evidence for both MAPK/ERK and FMRP involvement in modulating glutamatergic release mechanisms.

Presynaptic vesicle fusion is a major determinant of neurotransmission strength, maintained functional resilience during strong demand, and activity-dependent plasticity.[42] HFS trains cause the transient activation of pERK signaling in presynaptic terminals,[145] correlating with increased vesicle fusion. To test if Csw/SHP2 similarly regulates glutamate release, we performed HFS synaptic depression assays to discover that all mutants have increased transmission resiliency under conditions of heightened demand,[135] with elevated glutamate release from presynaptic boutons. This role is consistent with activity-dependent presynaptic MAPK/ERK signaling driving greater presynaptic glutamate release by modulating the accessible number of synaptic vesicles available for fusion in the RRP.[127] Importantly, the mouse FXS disease model displays similar decreased short-term depression due to enhanced presynaptic glutamate release, also via up-regulation of the RRP without a change in PPR fusion.[118] The MAPK/ERK-dependent phosphorylation of presynaptic targets is likewise known to increase short-term plasticity, and blockade of this signaling process has been shown to strongly impair facilitation, maintained augmentation, and PTP.[145,151] Our results show that all three forms of synaptic plasticity are impaired in *csw* null and *PTPN11*$^{N308D}$ GoF animals, which both show decreased facilitation, augmentation, and PTP, consistent with other LoF/GoF phenocopy. We hypothesize that these plasticity defects correlate to the already increased basal transmission levels that cause a decrease in range for enhancement from presynaptic pERK activation, leading to a "ceiling effect" on presynaptic function. This predicts neurotransmission defects are linked to causal changes in presynaptic MAPK/ERK signaling.

Both NS and NSML disease states exhibit elevated MAPK/ERK signaling,[94] but there is heterogeneity in pERK activation levels and multiple pathways involved.[91] To confirm the neurotransmission increase is due to elevated MAPK/ERK signaling, we inhibited this pathway with both Trametinib and Vorinostat, two drugs well characterized to decrease pERK signaling.[141,152] With drug treatments, the elevated neurotransmission in *csw* and *PTPN11* mutants is restored to levels comparable to control animals, indicating that the elevated MAPK/ERK signaling is responsible for the heightened presynaptic function. This test does not rule out the possibility of other disrupted signaling pathways that may influence MAPK/ERK signaling, but does prove MAPK/ERK signaling is the cause of the elevated neurotransmission. The next task was to explore the new activity-dependent mechanism controlling this presynaptic Csw/SHP2 function. As previously discussed, NS, NSML, and FXS models/patients all display striking similarities in up-regulated MAPK/ERK signaling, synaptic phenotypes, and LTM impairments.[115,118,120] Moreover, RNA-binding FMRP is well characterized as an activity-dependent negative translational regulator of presynaptic mRNA targets.[153] Consistently, we find that *Drosophila* FMRP binds *csw* mRNA, as suggested in a mouse FMRP screen indicating *PTPN11/SHP2* binding.[107] Additionally, we find neuronal Csw protein levels are elevated in the FXS disease model (*dfmr1* null), consistent with the predicted FMRP translational repression.[106] Finally, we find that presynaptic pERK signaling is increased in both *dfmr1* and *csw* null mutants and that normal activity-dependent elevation in pERK signaling is impaired in both disease model conditions. The pERK enhancement levels are slightly different, but this to likely due to the relative effect of the two nulls on pERK signaling. The heightened basal presynaptic pERK signaling and repressed activity-dependent pERK signaling suggests that FMRP and Csw interact to modulate presynaptic glutamatergic neurotransmission.

One genetic test for pathway interaction employs nonallelic noncomplementation,[154] which demonstrates that the two gene products operate within a common mechanism, in this case, the up-regulation of MAPK signaling.[40] Both *dfmr1* and *csw* null mutants display elevated presynaptic neurotransmission with an increased probability of presynaptic glutamate release,[115] and *trans*-heterozygous *dfmr1*/+; *csw*/+ double mutants recapitulate both functional phenotypes. Importantly, both the *dfmr1* and $csw^5$ single heterozygous mutants do not display any phenotypes, despite the NSML autosomal dominant disease state. Similarly, Csw/PTPN11 overexpression does not cause any phenotypes, suggesting a change in the FXS background causes the elevated MAPK/ERK presynaptic signaling. These genetic tests indicate that FMRP and Csw/SHP2 act together to inhibit pERK signaling and presynaptic glutamate release. We propose the mechanism of mRNA-binding FMRP acting canonically as a negative translational regulator of Csw/SHP2 expression.[155] Both the *dfmr1* and *csw* null mutants display elevated MAPK/ERK signaling as indicated by pERK production,[70] and we demonstrate here pERK elevation in presynaptic boutons. Consistent with a common mechanism, *trans*-heterozygous *csw*/+; *dfmr1*/+ mutants recapitulate this heightened presynaptic pERK signaling. We propose the mechanism of FMRP working through Csw/SHP2 phosphatase enzymatic activity to inhibit presynaptic pERK production. Given that MAPK/ERK signaling is well established to modulate presynaptic glutamatergic release,[73] we suggest heightened presynaptic pERK signaling causes elevated glutamate release probability. We demonstrate this causal link with pharmacological treatments that block pERK production,[140] which act to restore normal glutamatergic synaptic signaling in the disease model animals.

In conclusion, we note that there are important differences between FXS and NS/NSML disease models. Previous FXS model work has shown increased NMJ architecture and mEJC amplitudes in *dfmr1* nulls,[115] which are absent in NS/NSML model *csw/PTPN11* mutants. FXS is a very complex disease state with many proteins misregulated,[115] and there was never an expectation that all FXS phenotypes would be recapitulated in *csw/PTPN11* mutants, especially for the unrelated postsynaptic changes. Nevertheless, the presynaptic parallels are striking. The mouse FXS model exhibits decreased short-term depression with no change in PPR, but an increase in RRP,[118] matching the *Drosophila* results shown here. Interestingly, these phenotypes match closer than mouse *H-ras*$^{G12V}$ mutants with increased pERK signaling, which exhibit enhanced short-term synaptic plasticity,[127] compared to the depressed plasticity shown here. Thus, although both basal transmission strength and functional plasticity properties are dependent on presynaptic MAPK/ERK signaling, there are likely other intersecting regulatory pathways. Moreover, FMRP and Csw/SHP2 could interact via multiple different mechanisms to regulate presynaptic MAPK/ERK signaling, and the elevated neurotransmission in the disease state models may not be completely dependent on presynaptic MAPK/ERK signaling. In the FXS model, Csw/SHP2 is both up-regulated and hyperactivated, and the mechanism of this activation is unknown. One possibility is decreased MAPK/ERK negative regulation, via other factors like Neurofibromin-1, which could further increase MAPK/ERK signaling.[156,157] Another possibility is that neuronal activity up-regulates and then activates Csw/SHP2 via two parallel mechanisms to increase MAPK/ERK signaling.[158,159] We have previously uncovered several other genetic mutants that likewise elevate neurotransmission and depress short-term plasticity,[40,160–162] which are also candidates for furthering our understanding in future studies. The possibility for a more extensive interactive molecular network is exciting, but it can currently only be concluded that FMRP and Csw/SHP2 both control MAPK/ERK signaling and modulate neurotransmission. This presynaptic mechanism connects the previously unlinked disorders of NS, NSML, and FXS, suggesting common therapeutic targets and new treatment avenues.

## Materials and Methods

### Drosophila Genetics

All the *Drosophila* stocks were reared on standard cornmeal/agar/molasses food at 25°C within 12-hour light/dark cycling incubators. All animals were reared to the wandering third instar stage for all experiments, with all genotypes and RNAi lines confirmed with a combination of transgenically marked balancer chromosomes, western blots, and sequencing. Due to the *corkscrew* gene being on the X chromosome, all experiments utilizing *csw*$^{5}$ mutants were conducted using males only, whereas all the *trans*-

heterozygous experiments were done using females only. All the other experiments were done on both of the sexes (males and females together). The two genetic background controls were $w^{1118}$ and the TRiP RNAi third chromosome background control.[133] The $dfmr1^{50M}$ null mutant,[115] $csw^{5}$ null mutant,[130] and the transgenic lines UAS-$csw^{WT}$ and UAS-*csw* RNAi[89,132] are all available from the *Drosophila* Bloomington Stock Center (BDSC; Indiana University, Bloomington, IN, USA). The UAS-$csw^{A72S}$ line[82] was obtained as a kind gift from Dr. Mario Rafael Pagani (Department of Physiology and Biophysics, School of Medicine, National Scientific and Technical Research Council, University of Buenos Aires, Buenos Aires, Argentina). All patient-derived UAS-*PTPN11* mutant lines[91] were obtained as a kind gift from Dr. Tirtha Das (Department of Cell, Developmental, and Regenerative Biology, Icahn School of Medicine at Mount Sinai, New York, NY, USA). Transgenic studies were performed with neural-specific *elav*-Gal4 [163], muscle-specific *24B*-Gal4,[164] and ubiquitous *daughterless UH1*-Gal4[21] driver lines, all obtained from BDSC. The genetic and transgenic lines used in this study are summarized below in Table 2.1:

| Line | Provider | Reference |
|---|---|---|
| $csw^{5}$ | BDSC 23874 | (Perrimon et al., 1985) |
| UAS-$csw^{WT}$ | BDSC 23878 | (Hamlet and Perkins, 2001) |
| UAS-$csw^{A72S}$ | Dr. Mario Rafael Pagani | (Oishi et al., 2006) |
| UAS-$PTPN11^{R498W}$ | Dr. Tirtha Das | (Das et al., 2021) |
| UAS-$PTPN11^{Y279C}$ | Dr. Tirtha Das | (Das et al., 2021) |
| UAS-$PTPN11^{Q510E}$ | Dr. Tirtha Das | (Das et al., 2021) |
| UAS-$PTPN11^{Q510P}$ | Dr. Tirtha Das | (Das et al., 2021) |
| UAS-*csw* RNAi | BDSC 33619 | (Ni et al., 2011) |
| TriP 3rd RNAi Ctl | BDSC 36303 | (Perkins et al., 2015) |
| $dfmr1^{50M}$ | BDSC 6930 | (Zhang et al., 2001) |
| *UAS-YFP-dfmr1* | Dr. Daniela Zarnescu | (Cziko et al., 2009) |

**Table 2.1**: *Drosophila* mutant and transgenic lines used in this study.

### Synaptic Electrophysiology

Wandering third instar dissections and TEVC recordings were done at 18°C in physiological saline (in mM): 128 NaCl, 2 KCl, 4 $MgCl_2$, 1.0 $CaCl_2$, 70 sucrose, and 5 HEPES (pH 7.2). Staged larvae were dissected longitudinally along the dorsal midline, the internal organs removed, and the body walls glued down (Vetbond, 3M). Peripheral motor nerves were cut at the base of the VNC. Dissected preparations were imaged with a Zeiss 40× water-immersion objective on a Zeiss Axioskop microscope. Muscle 6 in abdominal segments 3 to 4 was impaled with two intracellular electrodes (1 mm outer diameter borosilicate capillaries; World Precision Instruments, 1B100F-4) of approximately 15 MΩ resistance when filled with 3M KCl. The muscles were clamped at −60 mV using an Axoclamp-2B amplifier (Axon Instruments). For evoked EJC recordings, the motor nerve was stimulated with a fire-polished suction electrode using 0.5 ms suprathreshold voltage stimuli at 0.2 Hz from a Grass S88 stimulator. Nerve stimulation–evoked EJC recordings were filtered at 2 kHz. To quantify EJC amplitude, 10 consecutive traces were averaged, and the average peak value recorded. Spontaneous mEJC recordings were made in continuous 2-minute sessions and low-pass filtered at 200 Hz. Synaptic depression experiments were performed using the above EJC recording protocol for 1 minute to establish baseline, followed by a 20-Hz HFS train for 5 minutes at the same suprathreshold voltage. RRP size was estimated by dividing the cumulative EJC amplitudes during the first 100 responses to 20 Hz stimulation by the mean mEJC amplitudes. Due to these analyses being at 20 Hz, RRP size is likely underestimated. All synaptic plasticity experiments were performed in 0.2 mM $Ca^{2+}$ using 10 Hz stimulation trains for 1 minute, followed by 0.2 Hz recordings. All EJC responses within a 1-second bin were averaged, and the average value normalized to the basal EJC amplitude for each animal. Clampex 9.0 was used for all data acquisition, and Clampfit 10.6 was used for all data analyses (Axon Instruments).

### Drug treatments

Two drugs known to inhibit pERK production (Trametinib and Vorinostat) were used by feeding as published previously.[91,140,141] Both Trametinib (Cell Signaling, 62206S) and Vorinostat (Cell Signaling, 12520S) were dissolved in dimethylsulfoxide (DMSO; Fisher, 67-68-5) at 15 mM and 20 mM, respectively, to create stock solutions. Both drugs were then added to *Drosophila* food yeast paste and in the standard cornmeal/agar/molasses food in the final concentrations of 0.5 mM (Trametinib) and 1 mM (Vorinostat). *Drosophila* were induced to lay eggs on selection apple juice plates with drugged yeast paste food. Hatching first instars were selected and placed in standard vials containing Trametinib, Vorinostat, or control food with DMSO only. Larvae were reared in a 12-hour light/dark cycling incubators at 25°C and then collected as wandering third instars for TEVC studies.

**RNA immunoprecipitation**

Wandering third instars (20 larvae) of each genotype (UH1>FMRP-YFP or Tubulin-GFP) were homogenized in 200 µL of RNase-free lysis buffer (20 mM HEPES, 100 mM NaCl, 2.5 mM EDTA, 0.05% (v/v) Triton X-100, 5% (v/v) glycerol) with 1% *β*-mercaptoethanol 1× protease inhibitor cocktail (complete mini EDTA-free Tablets, Sigma, 11836170001) and 400U RNase inhibitor (Applied Biosystems, N8080119). The supernatant was collected and diluted to 300 µL to reduce nonspecific binding. Next, the samples were incubated with GFP-trap coupled magnetic agarose beads (Chromotek, GTMA20) for 3 hours at 4°C. The bound beads were washed with lysis buffer (3X, 10 minutes). The bound RNA was purified by incubating the bead-protein-RNA conjugates with a 500-µL TRIzol and chloroform mixture (Ambion, 15596026) for 10 minutes at RT, followed by centrifugation. To precipitate RNA, glycogen (1 µL) and 2-propenol (250 µL) were added to the isolated aqueous layer. Finally, the precipitated RNA was reverse transcribed into single-strand cDNA using the SuperScript VILO cDNA synthesis kit (Thermo Fisher, 11754050) and then subjected to primer-specific PCR, with 2% agarose gels used to analyze the PCR products. All primers used in this study are summarized above in Table 2.2.

| Primer | Sequence |
|---|---|
| *corkscrew* (forward) | CTACCGCAACATATTGCCATACGAC |
| *corkscrew* (reverse) | CTGCACGCACGTCTTGTTTT |
| *futsch* (forward) | TTCCTGGATATTGCAGGACGG |

| | |
|---|---|
| *futsch* (reverse) | CTCGGGCAATGTGTGCCATA |
| α-*tubulin* (forward) | ATTTACCCAGCACCACAAGTGT |
| α-*tubulin* (reverse) | GGCGATTGAGATTCATGTAGGTGG |

**Table 2.2:** Primers used for RNA immunoprecipitation. The length of PCR products is ~200 bp.

### Western Blots

Wandering third instar VNCs from 20 larvae were homogenized in 100 μL of lysis buffer (20 mM HEPES, 10 mM EDTA, 100 mM KCl, 0.1% (v/v) Triton X-100, 5% (v/v) glycerol) with a protease inhibitor cocktail (Roche, 04693132001) combined with a protease and phosphatase inhibitor cocktail (Abcam, ab201119). All samples were then sonicated and run in 4% to 15% Mini-PROTEAN TGX Stain-Free Precast Gels (BioRad, 4568083) alongside Precision Plus Protein all blue prestained protein standards (BioRad, 1610373). Next, total protein was transferred to PVDF membranes using a Trans-Blot Turbo system (BioRad). After transfer, the membrane was blocked by TBS intercept blocking buffer (LiCOR, 927–60000) for 1 hour at RT. The blocked membranes were incubated with primary antibodies overnight at 4°C. Antibodies used include rabbit anti-Csw (Lizabeth Perkins, F1088, 1:500) and goat anti-GAPDH (Abcam, ab157157, 1:2,000). The membrane was washed with Tris-buffer saline with 0.1% Tween-20 (TBST) and then incubated with secondary antibodies for 40 minutes at RT. Secondary antibodies used include Alexa Fluor 680 donkey anti-goat (Invitrogen, A21084, 1:10,000) and Alexa Fluor 800 goat anti-rabbit (Invitrogen, A32735, 1:10,000). After washing with TBST (3X, 10 minutes), the membranes were imaged using the Li-COR Odyssey CLx system.

### Immunocytochemistry imaging

Wandering third instars were dissected in physiological saline (see above) and fixed in 4% paraformaldehyde (EMS, 15714) diluted in PBS (Corning, 46–013-CM) for 10 minutes at RT. Preparations were then washed and permeabilized in PBS containing 0.2% Triton X-100 and 1% bovine serum albumin (BSA; 3X, 10 minutes), followed by blocking for 30 minutes at RT in the same solution. Preparations were incubated with primary antibodies overnight at 4°C. Primary antibodies used included rabbit anti-pERK1/ERK2 (Thr185, Tyr187) polyclonal antibody (Thermo Fisher, 44-680G, 1:100), goat Cy3-conjugated anti-

HRP (Jackson ImmunoResearch, 123–165–021, 1:200), and goat 488-conjugated anti-HRP (Jackson ImmunoResearch, 123–545–021, 1:200). Preparations were washed (3X, 10 minutes) and then incubated with secondary antibodies for 2 hours at RT. Secondary antibodies used included: donkey 488 anti-rabbit (Invitrogen, A21206) and donkey 555 anti-rabbit (Invitrogen, A31572). Preparations were washed (3X, 10 minutes) and then mounted in Fluoromount G (Electron Microscopy Sciences) onto 25 × 75 × 1 mm slides (Fisher Scientific, 12–544–2) with a 22 × 22–1 coverslip (Thermo Fisher Scientific, 12–542-B) sealed with clear nail polish (Sally Hansen). All NMJ imaging was performed using a Zeiss LSM 510 META laser-scanning confocal microscope, with images projected in Zen (Zeiss) and analyzed using ImageJ (NIH open source). All NMJ intensity measurements were made with HRP signal-delineated *z*-stack areas of maximum projection using ImageJ threshold and wand-tracing tools.

### Statistical analyses

All statistics were performed using GraphPad Prism software (v9.0). Data sets were subject to normality tests, with D'Agostino–Pearson tests utilized if $n > 10$ and Shapiro–Wilk tests if $n < 10$. With normal data, ROUT outlier tests with Q set to 1% were run, followed by either two-tailed Student *t* tests for two-way comparison with 95% confidence (2 data sets) or a one-way ANOVA followed by either a Tukey's multiple comparison test (3+ data sets, comparing all samples) or a Dunnett's multiple comparison test (3+ data sets, comparing to control). If data were not normal, Mann–Whitney tests (2 data sets) or Kruskal–Wallis followed by a Dunn's multiple comparisons tests (3+ data sets) were performed. In order to fully capture changes in the datasets for experiments containing time courses, nonlinear regressions were performed followed by F extra sum of squares tests to determine if the curves were significantly different. All figures show all individual data points as well as mean ± SEM, with significance displayed as $p \leq 0.05$ (*), $p \leq 0.01$ (**), $p \leq 0.001$ (***), $p \leq 0.0001$ (****), and $p > 0.05$ (not significant; n.s.).

# Chapter III

# PTPN11/Corkscrew activates local presynaptic MAPK signaling to regulate Synapsin, synaptic vesicle pools, and neurotransmission strength, with a dual requirement in neurons and glia

Shannon N. Leahy[1], Dominic J. Vita[1] and Kendal Broadie[1-4*]

Department of Biological Sciences[1], Department of Cell and Developmental Biology[2], Department of Pharmacology[3], and Vanderbilt Brain Institute[4], Vanderbilt University and Medical Center, Nashville, TN 37235 USA

This paper is published under the same title in the Journal of Neuroscience, 2024

**Competing Interests:** The authors declare no competing financial interests.

**Funding:** This work was supported by National Institutes of Mental Health Grant MH084989 to K.B. The funders had no role in study design, data collection and analysis, decision to publish, or preparation of the manuscript.

**Author Contributions:** Shannon N. Leahy, Designed research, performed research, analyzed data, wrote first draft of the paper, wrote the paper Dominic J. Vita, Performed research, analyzed data and Kendal Broadie edited the paper

Published by: Society for Neuroscience
Received: June 4, 2023
Accepted: March 5, 2024
Published: March 12, 2024

## Abstract

Cytoplasmic protein tyrosine phosphatase (PTP) non-receptor type 11 (PTPN11) and *Drosophila* homolog Corkscrew (Csw) regulate the mitogen-activated protein kinase (MAPK) pathway via a conserved autoinhibitory mechanism. Disease causing loss-of-function (LoF) and gain-of-function (GoF) mutations both disrupt this autoinhibition to potentiate MAPK signaling. At the *Drosophila* neuromuscular junction (NMJ) glutamatergic synapse, LoF/GoF mutations elevate transmission strength and reduce activity-dependent synaptic depression. In both sexes of LoF/GoF mutations, the synaptic vesicles (SV) colocalized Synapsin phosphoprotein tether is highly elevated at rest, but quickly reduced with stimulation, suggesting a larger SV reserve pool with greatly heightened activity-dependent recruitment. Transmission electron microscopy of mutants reveals an elevated number of SVs clustered at the presynaptic active zones, suggesting that the increased vesicle availability is causative for the elevated neurotransmission. Direct neuron-targeted extracellular signal-regulated kinase (ERK) GoF phenocopies both increased local presynaptic MAPK/ERK signaling and synaptic transmission strength in mutants, confirming the presynaptic regulatory mechanism. Synapsin loss blocks this elevation in both presynaptic PTPN11 and ERK mutants. However, *csw* null mutants cannot be rescued by wildtype Csw in neurons: neurotransmission is only rescued by expressing Csw in both neurons and glia simultaneously. Nevertheless, targeted LoF/GoF mutations in either neurons or glia alone recapitulates the elevated neurotransmission. Thus, PTPN11/Csw mutations in either cell type is sufficient to upregulate presynaptic function, but a dual requirement in neurons and glia is necessary for neurotransmission. Taken together, we conclude PTPN11/Csw acts in both neurons and glia, with LoF and GoF similarly upregulating MAPK/ERK signaling to enhance presynaptic Synapsin-mediated SV trafficking.

## Significance statement

Noonan syndrome (NS) is, by far, the most common RASopathy; a group of clinically-classified genetic syndromes caused by MAPK pathway alterations: it affects 1 in every 1000-2000 people. Patients present with cognitive deficits caused by *PTPN11* mutations; with gain-of-function the most common basis for NS, and loss-of-function resulting in NS with multiple lentigines (NSML). We find NS/NSML patient-derived LoF/GoF *PTPN11* mutations, as well as *Drosophila* homolog *corkscrew* LoF/GoF mutations, all increase presynaptic MAPK signaling, Synapsin turnover, and synaptic vesicle availability at presynaptic release sites. Surprisingly, we find *PTPN11/corkscrew* to be required in both glia and neurons to control neurotransmission strength. These findings suggest disease interventions manipulating presynaptic vesicle trafficking mechanisms, as well as therapeutic strategies targeting both glia and neurons.

## Introduction

Noonan syndrome (NS) and NS with multiple lentigines (NSML) are autosomal dominant disorders caused by mutations in *protein tyrosine phosphatase non-receptor type 11* (*PTPN11*) in ~50% of NS and >95% of NSML patients.[81,97] The NS/NSML disease states share most symptoms, including cognitive impairments in 30-50% of patients.[3,4] Surprisingly, NS is caused by gain-of-function (GoF) and NSML by loss-of-function (LoF) mutations in *PTPN11,* encoding the Src homology-2 (SH2)-domain containing PTP-2 (SHP2) cytoplasmic phosphatase that positively modulates MAPK/ERK signaling.[74] SHP2 function is regulated by autoinhibition, with phosphatase and N-SH2 domains interacting during inactivation, and an open conformation adopted only with signaling activation.[84] Both GoF/LoF disease mutations favor the SHP2 open conformation with an exposed catalytic domain, leading to elevated MAPK/ERK signaling.[88] In the mouse NS disease model, long-term potentiation (LTP) and memory deficits are rescued by MAPK/ERK inhibition.[90] In *Drosophila* NS and NSML disease models, MAPK/ERK-dependent long-term memory (LTM) is likewise disrupted.[52,91] Although these previous investigations clearly indicate MAPK/ERK-dependent deficits in the nervous system, the underlying neuronal mechanism that causes these impairments has yet to be fully determined.

At the *Drosophila* neuromuscular junction (NMJ) glutamatergic synapse, we previously tested *PTPN11* homolog *corkscrew (csw)* LoF/GoF mutations as well as human patient-derived *PTPN11* LoF/GoF transgenes targeted to neurons for synaptic phenotypes.[165] All of these mutations increase presynaptic MAPK/ERK signaling and elevate neurotransmission, with defects corrected by MAPK/ERK inhibitors. Electrophysiological recordings suggest synaptic vesicle (SV) release is heightened to increase signaling strength in basal resting conditions, with compensatory reductions during activity-dependent synaptic depression and short-term plasticity.[165] Vesicles can be functionally classified into the readily releasable pool (RRP), rapid recycling pool, and reserve pool.[54] The RRP available for immediate release represents vesicles physically docked at the presynaptic active zone (AZ) and primed for exocytosis.[25] The RRP is replenished from the vesicle recycling pool, with greater replacement during conditions of elevated demand.[166] The reserve pool is recruited by high usage levels; for example, during high frequency stimulation (HFS). The Synapsin phosphoprotein tethers vesicles well away from the membrane, with phosphorylation causing SV disassociation and SV recruitment to AZ fusion sites.[67] Loss of this Synapsin regulation results in an inability to sustain proper release dynamics.[60] Given Synapsin is a MAPK target,[167] we hypothesized a causal mechanism in our NS/NSML disease models.

To test this hypothesis, this study employs confocal imaging of SV-associated Synapsin, electron microscopy synaptic ultrastructure analyses, and two-electrode voltage-clamp (TEVC) electrophysiology recordings of *PTPN11/csw* mutants. We first test SV-associated Synapsin in both basal and stimulated conditions. In *PTPN11/csw* LoF and GoF mutants, we find elevated Synapsin colocalized with SVs under basal conditions, and a dramatic loss of SV-associated Synapsin with acute stimulation. These findings suggest strongly altered Synapsin-dependent SV trafficking in the NS/NSML disease models. We next use transmission electron microscopy to visualize synaptic ultrastructure. In mutants, we find an increase in SVs clustered at presynaptic active zones. These findings suggest increased vesicle availability underlies the elevated mutant neurotransmission strength. We next test a neuron-targeted ERK$^{GoF}$ line to assay the presynaptic MAPK/ERK mechanism. We find higher MAPK signaling drives increased presynaptic function, and Synapsin loss blocks elevated neurotransmission with presynaptic NS/NSML mutations and ERK$^{GoF}$. To rescue these phenotypes, we reintroduced neuron-targeted wildtype *csw* into *csw* null mutants. Surprisingly, we find absolutely no improvement. Only rescue in both neurons and glia restores neurotransmission, indicating an unexpected dual requirement in both cell types. However, we find that glial-targeted *PTPN11/csw* LoF and GoF alone elevate neurotransmission, showing that disrupted glial function is sufficient to increase synaptic strength.

## Materials and Methods

### Drosophila genetics

All *Drosophila* stocks were reared on standard cornmeal/agar/molasses food at 25°C in 12-hour light/dark cycling incubators. All animals were reared to the wandering third instar stage, with all genotypes confirmed with a combination of sequencing, Western blots, and transgenically marked balancer chromosomes. Due to the *corkscrew* gene being on the X chromosome, all experiments utilizing $csw^5$ mutants were conducted on males only. All other experiments were done on both sexes (males and females together). The two genetic background controls were 1) $w^{1118}$ for all of mutants back-crossed in the $w^{1118}$ background, and 2) the Transgenic RNAi Project (TRiP) RNAi 3rd chromosome background control for the TRiP RNAi lines.[133] The $csw^5$ null,[130] $syn^{97}$,[65,168] $ERK^1$ hypomorph,[169] wildtype transgenic UAS-$csw^{WT}$ line,[170] gain-of-function UAS-$ERK^{SEM}$ line,[171] and UAS-*csw* RNAi lines[133] were all obtained courtesy of the *Drosophila* Bloomington Stock Center (BDSC; Indiana University, Bloomington, IN, USA). All of the NS/NSML patient-derived UAS-*PTPN11* mutant lines[91] were a kind gift from Dr. Tirtha Das (Department of Cell, Developmental, and Regenerative Biology, Icahn School of Medicine at Mount Sinai, New York, NY, USA.). Transgenic driver studies were performed with the pan-neuronal *elav*-Gal4,[172] glutamatergic neuron-specific *vglut*-Gal4,[173] and glial-specific *repo*-Gal4,[172] which were all obtained from the BDSC. Recombinant lines were confirmed via PCR, chromosome markers, and cell markers (e.g. membrane mCD8::GFP).

### Immunocytochemistry imaging

Wandering third instars were dissected in physiological saline (in mM): 128 NaCl, 2 KCl, 4 $MgCl_2$, 0.2 $CaCl_2$, 70 sucrose, and 5 HEPES (pH 7.2). Preparations were fixed in 4% paraformaldehyde (EMS, 15714) diluted in phosphate-buffered saline (PBS; Corning, 46–013-CM) for 10 mins at room temperature (RT). Preparations were then washed and permeabilized in PBS containing 0.2% Triton X-100 and 1% Bovine Serum Albumin (BSA; 3X, 10 mins), followed by blocking for 30 mins at RT in the same solution. Preparations were incubated with primary antibodies overnight at 4°C. Primary antibodies used included: rabbit anti-phospho-ERK1/ERK2 (Thr185, Tyr187) polyclonal antibody (ThermoFisher, 44-680G, 1:100), rabbit anti-vesicular glutamate transporter (vglut, 1:1000,[174] mouse anti-Synapsin (Developmental Studies Hybridoma Bank (DSHB), 3C11, 1:100), goat Cy3-conjugated anti-horseradish peroxidase (HRP; Jackson ImmunoResearch, 123–165-021, 1:200), and goat 647-conjugated anti-HRP (Jackson

ImmunoResearch, 123-605-021, 1:200). Following primary incubations, preparations were again washed (3X, 10 mins), and then incubated with secondary antibodies for 2 hrs at RT. Secondary antibodies used included: donkey 488 anti-rabbit (Invitrogen, A21206, 1:250) and donkey 555 anti-mouse (Invitrogen, A31570, 1:250). Preparations were again washed (3X, 10 mins), and then mounted in Fluoromount G (Electron Microscopy Sciences) on 25 × 75 × 1 mm slides (Fisher Scientific, 12–544-2) with 22 × 22 mm coverslips (Thermo Fisher Scientific, 12–542-B), sealed with clear nail polish (Sally Hansen). All NMJ imaging was performed using a Zeiss LSM 510 META laser-scanning confocal microscope, with images projected in Zen (Zeiss) and analyzed using ImageJ (NIH open source). All imaging was done with identical settings, kept consistent between all genotypes and stimulation conditions. Fluorescence intensity was calculated from maximum projection of the full HRP signal-delineated *z*-stack with using ImageJ threshold and wand-tracing tools. Thresholds were set consistently to avoid image saturation and maximize the fluorescence signal range (0-255). To compare across different trials, NMJ intensity values were normalized to the mean intensity value of basal controls for each trial (absolute units).

### Colocalization assays

Synaptic vesicle (SV) colocalization was done with vesicular glutamate transporter (vglut) and Synapsin antibody co-labeling at the wandering third instar NMJ (as above). Image settings were identical in all conditions. Glutamatergic SVs were marked with anti-vglut labeling,[175] which has been used previously in anti-Synapsin colocalization analysis.[176] With Image J, a NMJ synaptic bouton region of interest (ROI) was determined by selection with anti-horseradish peroxidase (HRP) presynaptic membrane labeling.[177] Before analyzing, acquisition images were split by channel and fluorescent background from outside the NMJ region was subtracted to ensure no false overlap. Using the HRP channel, the synaptic bouton ROI was the converted to a mask, and colocalization analyses of anti-vglut and anti-Synapsin within this defined mask ROI were then performed using the Coloc2 plugin, with the Pearson correlation coefficient (PCC) quantified.[176]

## Electron microscopy

Wandering third instars were dissected in physiological saline (as above) and fixed overnight at 4°C in 2.5% glutaraldehyde (EMS, 16020) in 0.1M sodium cacodylate (SC) buffer (EMS, 11650), followed by a secondary fixation in 1% osmium tetroxide (EMS, 19172) in SC buffer for 1 hr at room temperature (RT). Preparations were washed in 0.1 M SC buffer (3X, 10 mins) and then $ddH_2O$ (3X, 15 mins). Labeling was done *en bloc* using 2% uranyl acetate (EMS, 22400) for 2 hrs in the dark, and then preparations were rinsed in $ddH_2O$ (3X, 15 mins). Preparations were next dehydrated through an ethanol series (30, 50, 70, 90, 95, 100, 100%), followed by propylene oxide (EMS, 20401) infiltration and then resin embedding (Embed-812; EMS, 14121). Body wall muscles 6/7 from abdominal segments 3/4 were dissected free, and then embedded into a semihardened resin block. The muscles from 10 animals were put into each block. Blocks were polymerized at 60°C for 48 hrs. Blocks were thick sectioned for ~150 µm (to NMJ depth) using a DiATOME diamond knife on a Leica Ultracut UCT ultramicrotome. Thin sections were then cut at 65 nm and collected on uncoated 200 mesh copper grids (EMS, T200H-Cu). Five sections were collected per grid, with two consecutive grids collected at a time. Blocks were then thick sectioned an additional 10 µm before collecting on grids again to prevent reimaging the same bouton. Only muscle 6 type 1b boutons surrounded by subsynaptic reticulum (SSR) containing a presynaptic active zone t-bar were analyzed to quantify bouton area, synaptic vesicle (SV) number and distribution in ImageJ. All imaging was done with a Philips/FEI T-12 TEM operating at 100 kV, with images collected using a 4 megapixel AMT CCD camera.

## Synaptic electrophysiology

All NMJ two-electrode voltage-clamp (TEVC) recordings were done as previously reported.[165] Briefly; wandering third instar dissections were done at 18°C in physiological saline (as above). Animals were dissected longitudinally along the dorsal midline, and all internal organs and ventral nerve cord (VNC) removed. The peripheral motor nerves were cut at the base of the VNC, and the body walls glued down (Vetbond, 3M). Dissected preparations were imaged with a Zeiss 40× water-immersion objective on a Zeiss Axioskop microscope. Muscle 6 in abdominal segments 3/4 was impaled with two intracellular electrodes (1 mm outer diameter borosilicate capillaries; World Precision

Instruments, 1B100F-4) of ∼15 MΩ resistance (3M KCl). The muscle was clamped at −60 mV with an Axoclamp-2B amplifier (Axon Instruments), and the motor nerve was stimulated with a fire-polished glass suction electrode using 0.5 ms suprathreshold voltage stimuli at 0.2 Hz (Grass S88 stimulator). Nerve stimulation-evoked evoked excitatory junction current (EJC) recordings were filtered at 2 kHz. To quantify EJC amplitudes, 10 consecutive traces were averaged, and the average peak value recorded. Spontaneous miniature EJC (mEJC) recordings were made in continuous 2-minute sessions and low-pass filtered at 200 Hz. The quantal content for each evoked recording was calculated by dividing the EJC amplitude by the mean mEJC amplitude. Clampex 9.0 was used for all data acquisition, and Clampfit 10.6 was used for all data analyses (Axon Instruments).

### Western blots

Wandering third instar neuromusculature from 10 dissected larvae were homogenized in 100 µL lysis buffer (20 mM HEPES, 10 mM EDTA, 100 mM KCl, 0.1% (v/v) Triton X-100, 5% (v/v) glycerol) with protease inhibitor (Roche, 04693132001) combined with protease and phosphatase inhibitor cocktail (Abcam, ab201119). Samples were sonicated and run on 4-15% Mini-PROTEAN TGX Stain-Free Precast Gels (BioRad, 4568083) alongside Precision Plus Protein all blue prestained protein standards (BioRad, 1610373). The total protein was transferred to PVDF membranes using a Trans-Blot Turbo system (BioRad), and the membrane was blocked by TBS intercept blocking buffer (LiCOR, 927–60000) for 1 hr at RT. Blocked membranes were incubated with primary antibodies for 1.5 hrs at RT. Antibodies used included: rabbit anti-phospho-ERK1/ERK2 (Thr185, Tyr187) polyclonal antibody (ThermoFisher, 44-680G, 1:1,000) and goat anti-GAPDH (Abcam, ab157157, 1:2,000). The membrane was washed with Tris-buffer saline with 0.1% Tween-20 (TBST), and then incubated with secondary antibodies for 40 minutes at RT. Secondary antibodies used included; Alexa Fluor 680 donkey anti-goat (Invitrogen, A21084, 1:10,000) and Alexa Fluor 800 goat anti-rabbit (Invitrogen, A32735, 1:10,000). Membranes were washed in Tris-buffered saline with 0.1% Tween (TBST, 3X, 10 mins), and then imaged using the Li-COR Odyssey CLx system.

### Statistical analyses

All statistics were performed using GraphPad Prism software (version 9.5). Data sets were subject to normality tests, with D'Agostino-Pearson tests utilized (n>10) or Shapiro-Wilk tests (n<10). With normal data either 1) two-tailed student's *t*-tests for two-way comparison with 95% confidence (2 data sets) or 2) one-way ANOVA followed by a Tukey's multiple comparison test (3+ data sets, comparing all samples). If data were not normal, Mann-Whitney tests (2 data sets) or Kruskal–Wallis followed by a Dunn's multiple comparisons tests (3+ data sets) were performed. Data sets with multiple sources of variation were analyzed with a two-way ANOVA, followed by a Tukey's multiple comparison test. Figures show all individual data points as well as the mean±SEM, with significance displayed in figures as p≤0.05 (*), p≤0.01 (**), p≤0.001 (***), p≤0.0001 (****), and p>0.05 (not significant; n.s.). Exact p values for all comparisons are provided in the text.

## Results

### Corkscrew regulates presynaptic Synapsin levels and activity-dependent dynamic maintenance

At the *Drosophila* glutamatergic neuromuscular junction (NMJ), *corkscrew* null mutants (*csw*$^{5}$) have elevated neurotransmission under basal resting conditions and decreased synaptic depression with heightened stimulation.[165] We hypothesize these MAPK/ERK-dependent alterations arise from changes in synaptic vesicle (SV) availability in these different synapse activity states. Synapsin is an SV-associated phosphoprotein that regulates availability in an activity-dependent mechanism.[68,75,178] Reserve pool SVs are tethered in the bouton interior by Synapsin and released upon phosphorylation during strong stimulation.[61,62,68] In this traffic mechanism, MAPK/ERK acts to phosphorylate Synapsin, leading to vesicle disassociation and mobilization for exocytosis.[62,67] We therefore hypothesize that the Csw phosphatase modulates MAPK/ERK signaling to regulate this Synapsin function in presynaptic boutons. To test this hypothesis, we triple-labeled NMJ boutons with the presynaptic membrane marker anti-horseradish peroxidase (HRP), the SV marker anti-vesicle glutamate transporter (vglut), and anti-Synapsin (syn;[174,179]). Synapsin fluorescent intensity and SV colocalization were measured under resting conditions (basal) and following 10-minute depolarization stimulation with 90mM [$K^+$] (stimulated;[21,165]). We compared the matched genetic background control (*$w^{1118}$*) to the *$csw^5$* null mutant. Representative images and quantifications are shown in Figure 3.1.

In *$w^{1118}$* controls at rest, Synapsin is highly enriched in synaptic boutons and strongly associates with SV markers (Fig. 3.1A, top left). When controls are acutely stimulated (10 minutes), Synapsin is maintained at nearly indistinguishable levels (Fig. 3.1A, top right). In contrast, *csw* nulls (*$csw^5$*) exhibit sharply increased Synapsin levels under basal conditions (Fig. 3.1A, bottom left). When stimulated, *csw* mutants show a striking decrease in Synapsin levels (Fig. 3.1A, bottom right). In high magnification images of single boutons, Synapsin colocalization with SVs is decreased with stimulation in *csw* nulls (Fig. 3.1A, bottom). Quantification of Synapsin fluorescence intensity shows a highly significant interaction between genotype and stimulation with a two-way ANOVA ($F_{(1,66)}$=15.5, p=0.0002; Fig. 3.1B). Under resting (basal) conditions, Synapsin in *$csw^5$* null mutants (1.67±0.18, n=19) is highly elevated normalized to controls (1.0±0.08, n=19), a significant upregulation based on Tukey's multiple comparisons (p=0.002; Fig. 3.1B). In controls, normalized Synapsin levels after stimulation do not change significantly (0.83±0.14, n=16, p=0.7989; Fig. 3.1B). However, in *$csw^5$* nulls, Synapsin after stimulation is very significantly decreased (0.47±0.08, n=16, $p=8.07 \times 10^{-8}$; Fig. 3.1B). Imaging limitations prevent identification of where Synapsin goes in the stimulated null condition, but it is presumed dispersed in the cytosol.[68]

To further assay Synapsin dynamics, we quantified Synapsin-SV colocalization using a Pearson correlation coefficient (PCC;[180]). Quantification shows higher colocalization in *$csw^5$* null mutants (0.80±0.01, n=19) compared to controls (0.74±0.02, n=19), a significant change based on an unpaired t-test ($t_{(36)}$=2.277, p=0.029; Fig. 1C, left). With stimulation Synapsin-SV colocalization in controls (0.71±0.05, n=16) and mutants (0.65±0.05 n=16) are no longer significantly different based on an unpaired t-test ($t_{(30)}$=0.7635, p=0.4511; Fig. 3.1C, right). Quantification of vglut fluorescence intensity shows a significant interaction between genotype and stimulation in a two-way ANOVA ($F_{(1,65)}$=19.8, $p=3.37\times10^{-5}$; Fig. 3.1B). Under resting (basal) conditions, vglut fluorescence intensity in *$csw^5$* null mutants (1.33±0.01, n=19) is highly elevated relative to control (0.78±0.07, n=18), with significant upregulation in Tukey's multiple comparisons ($p=4.45\times10^{-5}$). In controls, normalized vglut fluorescence intensity level after stimulation does not change significantly (0.78±0.08, n=16, p>0.999). In contrast, *csw*$^{5}$ null vglut fluorescence intensity after stimulation is significantly decreased (0.59±0.07, n=16, $p=1.2\times10^{-7}$). Taken together, these results indicate that Csw regulates Synapsin and Synapsin-SV colocalization. We therefore next investigated impacts on presynaptic vesicle pools.

### Corkscrew regulates the distribution of synaptic vesicles around presynaptic active zones

The above results suggest altered synaptic vesicle pools in *csw*$^{5}$ null mutants. Previous electrophysiological recordings indicate *csw* mutants have elevated neurotransmission strength from heightened vesicle fusion probability, suggesting a larger population of available vesicles.[165] We hypothesize *csw* mutants would have an increased SV number in close proximity to presynaptic active zone fusion sites.[25,50] To test this hypothesis, we examined synaptic ultrastructure using transmission electron microscopy.[21,23,162] As previous electrophysiology recordings were done on ventral longitudinal muscle 6 in abdominal segments 3/4, we restricted our ultrastructural examination to the same NMJ terminals. Muscles were isolated from dissected wandering third instars, embedded in resin, and sectioned in 65 nm increments.[21,162] NMJ type 1b boutons were classified based on the surrounding muscle folded subsynaptic reticulum (SSR), and bouton sections containing a single electron-dense t-bar active zone (AZ) were selected for all analyses.[25,26,181] This identification method is well-established, as SSR around type 1b boutons clearly differentiate them from the smaller type Is boutons.[134] Comparing genetic background controls (*w*$^{1118}$) and *csw* null mutants (*csw*$^{5}$), we quantified bouton area and synaptic vesicle size, number, and distribution. To measure vesicle docking, we counted all vesicles in direct proximity (<20 nm; ½ SV diameter) to the presynaptic density containing an AZ t-bar.[28–31] To measure internal SV distribution, we counted all vesicles in 0-200 nm and 200-400 nm domains from the AZ t-bar.[25] Representative images and accompanying quantifications are shown in Figure 3.2.

The synaptic ultrastructure in controls and *csw*$^{5}$ null mutants is largely indistinguishable. The genetic background controls (*w*$^{1118}$) and *csw*$^{5}$ nulls have a similar bouton appearance, with the characteristic AZ t-bar and surrounding vesicles (Fig. 3.2A).

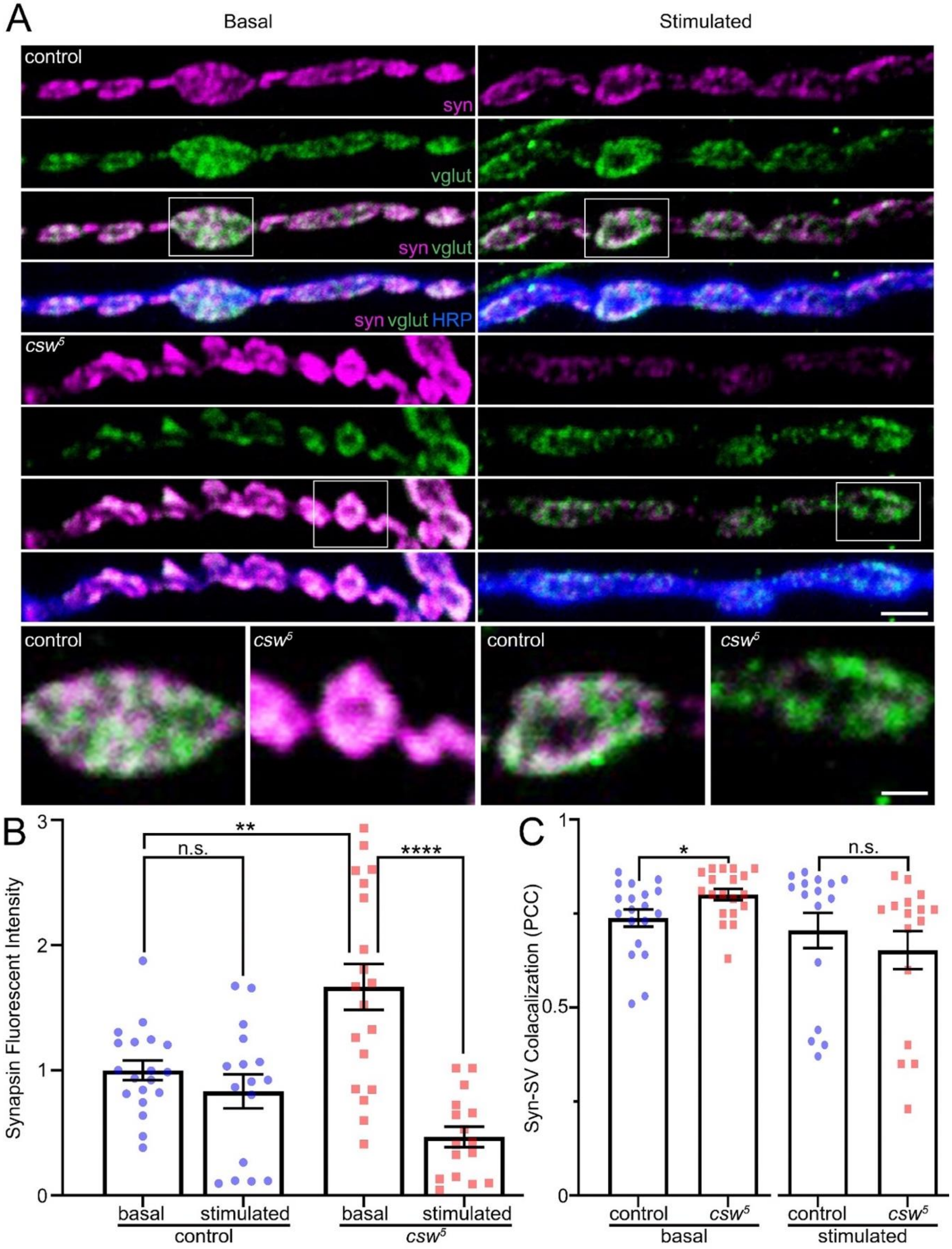

**Figure 3.1: Csw loss elevates Synapsin and causes stimulation-dependent Synapsin loss**
**A)** Representative wandering third instar neuromuscular junction (NMJ) synaptic boutons labeled for Synapsin (syn, magenta), the vesicular glutamate transporter (vglut, green), and horseradish peroxidase (HRP, blue) in $w^{1118}$ genetic background control and $csw^5$ null mutant. NMJs without stimulation (basal, left) and after acute, 10-minute 90 mM $[K^+]$ depolarizing stimulation (stimulated, right). Scale bar: 2.5 µm. Higher magnification bouton images are shown below. Scale bar: 1 µm. **B)** Quantification of Synapsin fluorescence intensity in all four conditions (basal and stimulated). Statistical comparisons done using two-way ANOVA, followed by Tukey's multiple comparisons test. **C)** Quantification of Synapsin and vglut colocalization in basal (left) and stimulated (right) conditions using Pearson's correlation coefficient analyses. Statistical comparisons done using two-sided t-tests. Scatter plots show all the data points with mean±SEM. Data points: NMJ number. Significance: $p<0.05$ (*), $p<0.01$ (**), $p<0.0001$ (****), and $p>0.05$ not significant (n.s.).

Compared to controls, mutants have no significant change in synaptic bouton area or perimeter, vesicle density or size (Table 3.1).

| **Analysis Parameter** | **Mean** | **SEM** | **n** | **test** | **Statistics** |
|---|---|---|---|---|---|
| Bouton Area (μm$^2$) | | | | | |
| $w^{1118}$ | 2.714 | 0.792 | 7 | Mann-Whitney | p=0.681 |
| $csw^5$ | 2.001 | 0.645 | 9 | | U=27 |
| Bouton perimeter (μm) | | | | | |
| $w^{1118}$ | 6.633 | 1.311 | 7 | t-test | p=0.729 |
| $csw^5$ | 6.025 | 1.126 | 9 | | $t_{(14)}$=0.353 |
| SV Density (SV/μm$^2$) | | | | | |
| $w^{1118}$ | 91.48 | 11.690 | 7 | t-test | p=0.085 |
| $csw^5$ | 57.95 | 13.030 | 9 | | $t_{(14)}$=1.857 |
| SV Diameter (nm) | | | | | |
| $w^{1118}$ | 39.74 | 2.555 | 7 | t-test | p=0.644 |
| $csw^5$ | 41.27 | 2.059 | 9 | | $t_{(14)}$=0.472 |

**Table 3.1: Synaptic bouton ultrastructure parameters**

However, there is an increase in the SV number clustered around the AZ in the mutants (Fig. 3.2A), with a greater number of docked SVs (arrows; Fig. 3.2B). To quantify these parameters, we first measured the bouton area occupied by SVs. Compared to the control coverage (68.67±6.89%, n=7), vesicles in the *csw*$^5$ null mutants occupy less area (41.46±9.07%, n=9), which is significant based on an unpaired t-test ($t_{(14)}$=2.272, p=0.0394, Fig. 3.2C). Thus, vesicles are more spatially cohesive in the mutant boutons. We next measured SV density in concentric rings around the AZ. In the 0-200 nm region, the control (16.01±1.754 SV/μm$^2$, n=11) and *csw*$^5$ null (15.27±1.3 SV/μm$^2$, n=12) densities are not significantly with an unpaired t-test ($t_{(21)}$=0.3427, p=0.7353, Fig. 3.2D left). In sharp contrast, the 200-400 nm region shows a strikingly higher SV density in the controls (13.96±1.47 SV/μm$^2$, n=11) compared to *csw*$^5$ nulls (8.75±1.62 SV/μm$^2$, n=12), with a significant elevation based on an unpaired t-test ($t_{(21)}$=2.375, p=0.0271, Fig. 3.2D right). This indicates that the reserve pool is specifically disrupted in *csw*$^5$ null mutants.[25] In addition, AZ docking measured as SVs with ½ a vesicle diameter from the presynaptic density (<20 nm, arrowheads) is lower in controls (2.083±0.288 SVs, n=12) compared to *csw*$^5$ nulls (3.33±0.373 SVs, n=9), which have a significantly more docked SVs based on an unpaired t-test ($t_{(19)}$=2.702, p=0.0141, Fig. 3.2E). Taken together, these results reveal

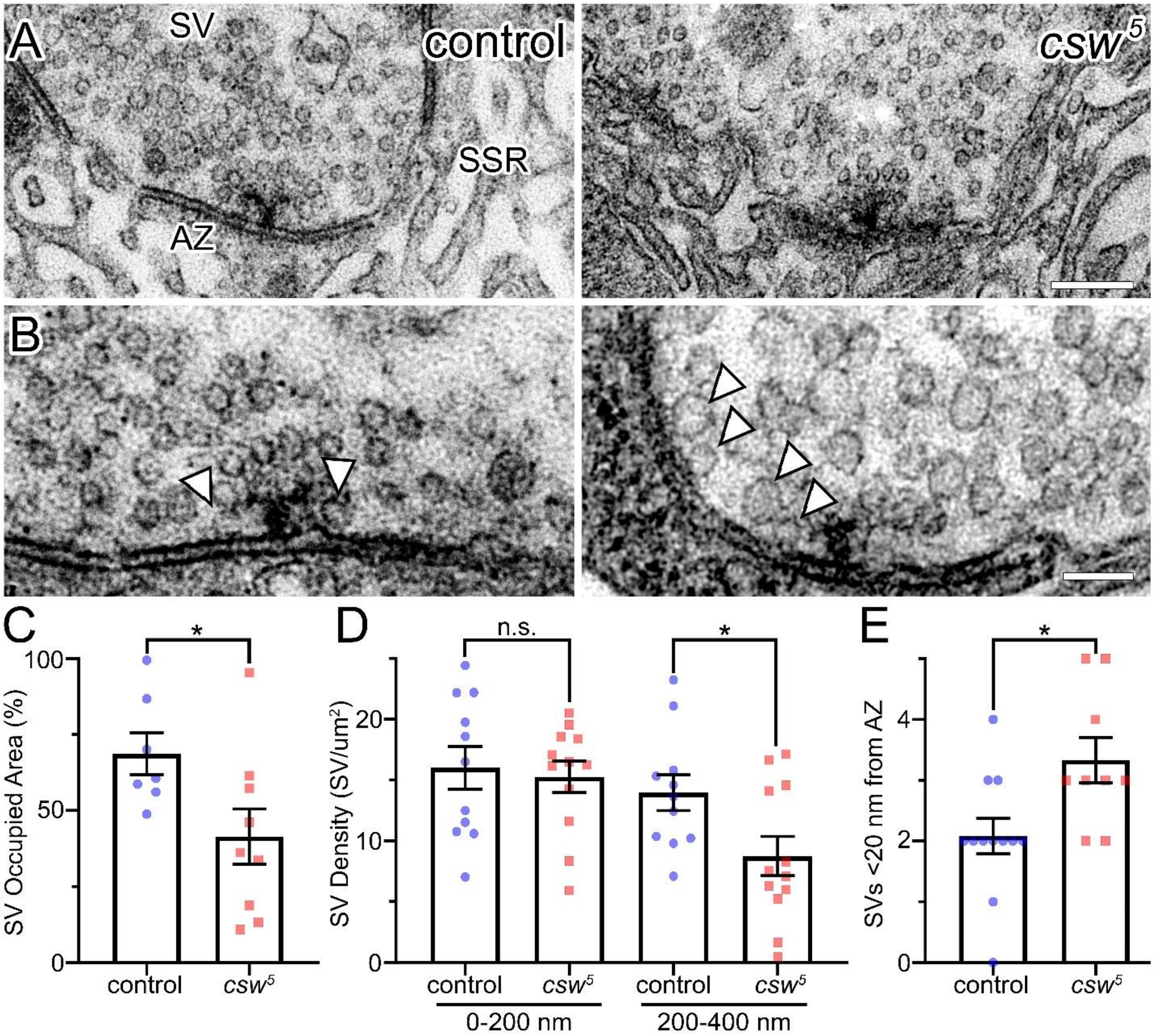

**Figure 3.2: Csw loss increases presynaptic active zone clustered and docked vesicle pools**
**A)** Representative transmission electron microscope (TEM) images of wandering third instar NMJ presynaptic active zones from *w*$^{1118}$ genetic background control (left) and *csw*$^5$ null mutant (right). Abbreviations: synaptic vesicle (SV), active zone (AZ), subsynaptic reticulum (SSR). Scale bar: 200 nm. **B**) Higher magnification AZ images showing SVs near the electron-dense t-bar. Arrows indicate the vesicles <20 nm from the AZ membrane. Scale bar: 100 nm. **C)** Quantification of percentage of the bouton area occupied by SVs with a two-sided t-test. **D**) Quantification of SV density (number of SVs/μm$^2$) within 0-200 nm and 200-400 nm from t-bar with two-sided t-tests. **E)** Quantification of docked SVs (number <20 nm to the presynaptic membrane density containing an AZ t-bar) with two-sided t-test. Scatter plots show all data points with mean±SEM. Data points: bouton number (C,D), AZ number (E). Significance: p<0.05 (*), p>0.05 not significant (n.s.).

a disrupted reserve pool and more docked SVs at AZ release sites in *csw* null mutants. We next turned to investigating this presynaptic mechanism in NS/NSML patient-derived point mutations.

### PTPN11 regulates Synapsin synaptic vesicle association under basal and stimulated conditions

*Drosophila csw*$^{5}$ null mutants have defects in presynaptic Synapsin dynamics and vesicle pool regulation. To further test a presynaptic regulatory mechanism in the NS/NSML disease states, we next analyzed neuron-targeted, patient-derived point mutations. These mutations include gain-of-function (GoF) *PTPN11*$^{N308D}$ and loss-of-function (LoF) *PTPN11*$^{Q510P}$ associated with NS and NSML, respectively.[91] We have previously discovered that both of these GoF/LoF mutations targeted to neurons elevate neurotransmission strength based on electrophysiology recordings.[165] Moreover, like *csw*$^{5}$ nulls, we have found that these patient-derived point mutations increase presynaptic MAPK/ERK signaling and decrease synaptic depression during heightened activity.[165] We therefore hypothesized that neuronal *PTPN11* mutations with increased neurotransmission would phenocopy the *csw*$^{5}$ null increased basal Synapsin levels and activity-dependent Synapsin loss. We once again utilized triple-labeled antibody imaging at the NMJ to investigate Synapsin levels at rest (basal) and in the 10-minute high [K+] depolarizing stimulation condition (stimulated). The presynaptic bouton membrane was again marked with anti-HRP, and the total SV population was again marked with anti-vglut. Anti-Synapsin fluorescence intensity and SV colocalization measurements were done in single synaptic boutons. Tests were done with the neuronal driver alone control (*elav*-Gal4/*w*$^{1118}$) compared to neuron-targeted *PTPN11* GoF (*elav*-Gal4>*PTPN11*$^{N308D}$) and LoF (*elav*-Gal4>*PTPN11*$^{Q510P}$) mutations. Representative basal/stimulated images and quantifications for all three genotypes are shown in Figure 3.3.

Like the *w*$^{1118}$ genetic background, neuronal driver controls (*elav*-Gal4/*w*$^{1118}$) maintain the SV-associated Synapsin at the same levels in basal and stimulated conditions (Fig. 3.3A, left). In contrast, GoF (*PTPN11*$^{N308D}$) and LoF (*PTPN11*$^{Q510P}$) both increase SV-associated Synapsin at rest and exhibit a sharp decrease in Synapsin with stimulation (Fig. 3.3A, middle and right). In high magnification single boutons, Synapsin colocalization with SVs is decreased with stimulation in both mutants (Fig. 3.3A, bottom).

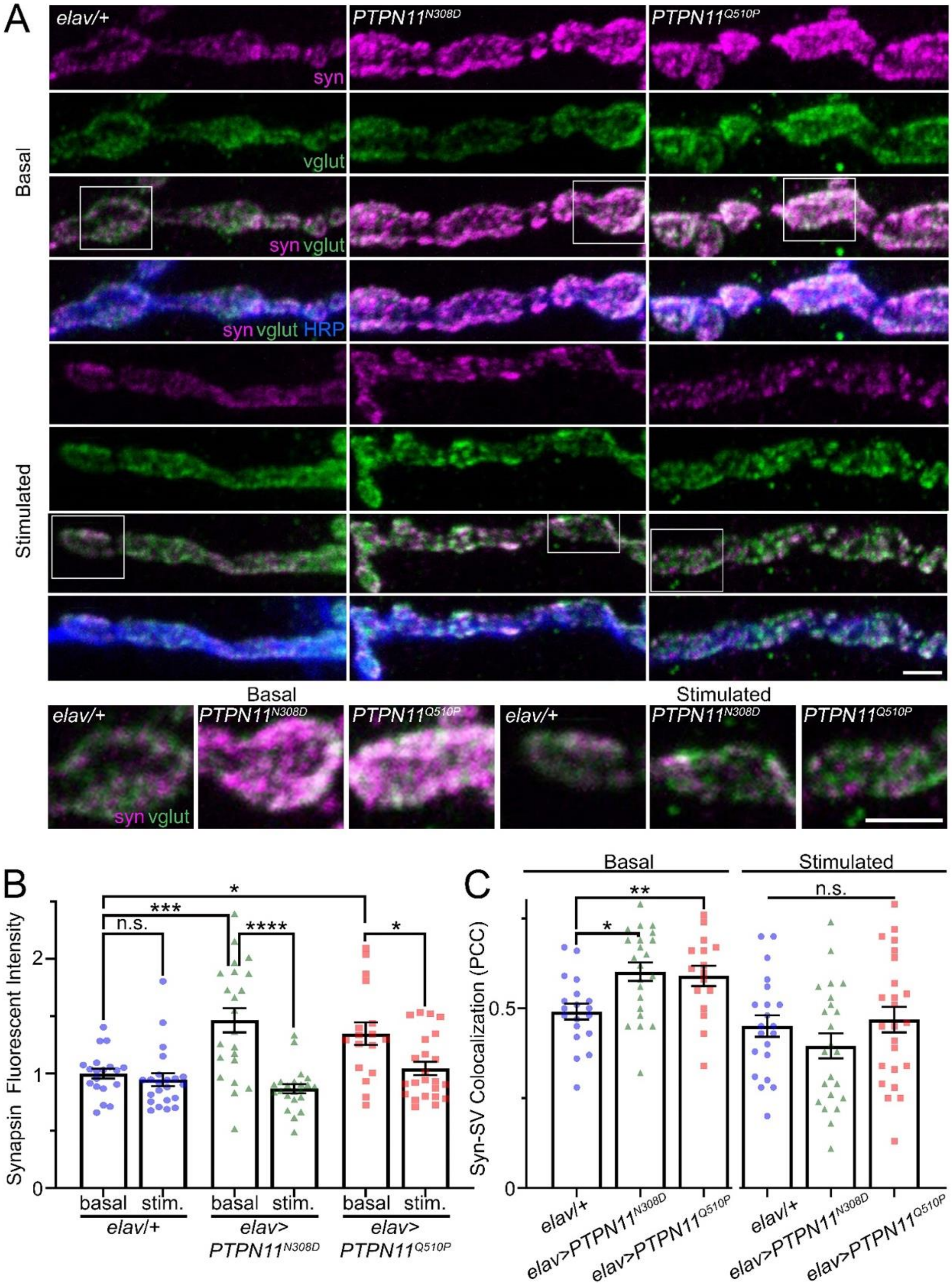

**Figure 3.3: NS/NSML transgenes increase Synapsin levels with stimulation-dependent loss**
Representative NMJ synaptic boutons labeled for Synapsin (syn, magenta), vesicular glutamate transporter (vglut, green) and horseradish peroxidase (HRP, blue) in neuronal transgenic driver control (*elav*-Gal4/$w^{1118}$, left), and driving $PTPN11^{N308D}$ (*elav*-Gal4>$PTPN11^{N308D}$, middle) and $PTPN11^{Q510P}$ (*elav*-Gal4>$PTPN11^{Q510P}$, right). NMJs without stimulation (basal, top) and 10 min 90 mM [$K^+$] (stimulated, bottom). Scale bar: 2.5 μm. Higher magnification bouton images are shown below. Scale bar: 2.5 μm. **B)** Quantification of Synapsin fluorescence intensity in all six conditions (basal and stimulated). Statistical comparison done using a two-way ANOVA, followed by Tukey's multiple comparisons test. **C)** Quantification of Synapsin and vglut colocalization in basal (left) and stimulated (right) conditions using Pearson's correlation coefficient analyses. Statistical comparisons done using one-way ANOVAs followed by Tukey's multiple comparisons tests. Scatter plots show all data points with mean±SEM. Data points: NMJ number. Significance: $p<0.05$ (*), $p<0.01$ (**), $p<0.001$ (***), $p<0.0001$ (****), and not significant (n.s.).

Quantification shows a significant interaction between genotype and stimulation in a two-way ANOVA ($F_{(2,119)}$=7.538, p=0.0008; Fig. 3.3B). At rest (basal), neuronal *PTPN11*$^{N308D}$ (1.47±0.11, n=22, p=0.0002) and *PTPN11*$^{Q510P}$ (1.35±0.10, n=17, p=0.0193) have significantly elevated Synapsin normalized to driver controls (1.0±0.04, n=19; Fig. 3.3B). With stimulation, Synapsin levels in controls do not change significantly (0.95±0.06, n=22, p=0.9954; Fig. 3.3B). However, *PTPN11*$^{N308D}$ (0.87±0.04, n=22, p=$1.796\times10^{-7}$) and *PTPN11*$^{Q510P}$ (1.04±0.06, n=23, p=0.0438) are significantly decreased from basal levels (Fig. 3.3B). This effect is confirmed with Pearson correlation coefficient Synapsin-SV colocalization analyzed by one-way ANOVA ($F_{(2,54)}$=5.779, p=0.0053; Fig. 3.3C, left). Quantification shows significantly increased colocalization in *PTPN11*$^{N308D}$ (0.60±0.03, n=22, p=0.0068) and *PTPN11*$^{Q510P}$ (0.59±0.03, n=16, p=0.0301) vs. driver control (0.49±0.02, n=19; Fig. 3.3C). Compared to Synapsin-SV colocalization following stimulation (0.45±0.03 n=21), neither *PTPN11*$^{N308D}$ (0.4±0.03, n=23) nor *PTPN11*$^{Q510P}$ (0.47±0.04, n=24) are significantly different based on a one-way ANOVA ($F_{(2,65)}$=1.296, p=0.2805; Fig. 3.3C right). Taken together, these results indicate neuronal GoF/LoF *PTPN11* mutations increase Synapsin, with aberrant activity-dependent Synapsin loss. To test MAPK-signaling dependence, we next analyzed a neuronal extracellular signal-regulated kinase (ERK) GoF condition.

### Neuronal ERK gain-of-function phenocopies PTPN11/csw mutant synapse regulation

In our previous studies, we showed *PTPN11/csw* mutants elevate both local presynaptic MAPK/ERK signaling and presynaptic neurotransmission, with the defects prevented by feeding pharmaceutical MAPK/ERK inhibitors.[165] These drug analyses demonstrate a requirement for MAPK/ERK signaling in both GoF and LoF mutants, but do not rule out other pathway contributions. To start testing the specificity of the MAPK/ERK-dependent presynaptic mechanism, we first assay whether neuron-targeted *ERK*$^{GoF}$ (*elav*-Gal4>*ERK*$^{SEM}$;[182])recapitulates the *PTPN11/csw* mutant synaptic phenotypes. To confirm elevated activation we test the MAPK signaling endpoint of phospho-ERK (pERK;[183]) with Western blots and look for specific local pERK activation with NMJ double-label imaging with anti-pERK (green) and anti-HRP (magenta). Using HRP to delineate presynaptic membranes, we measure pERK fluorescence intensity

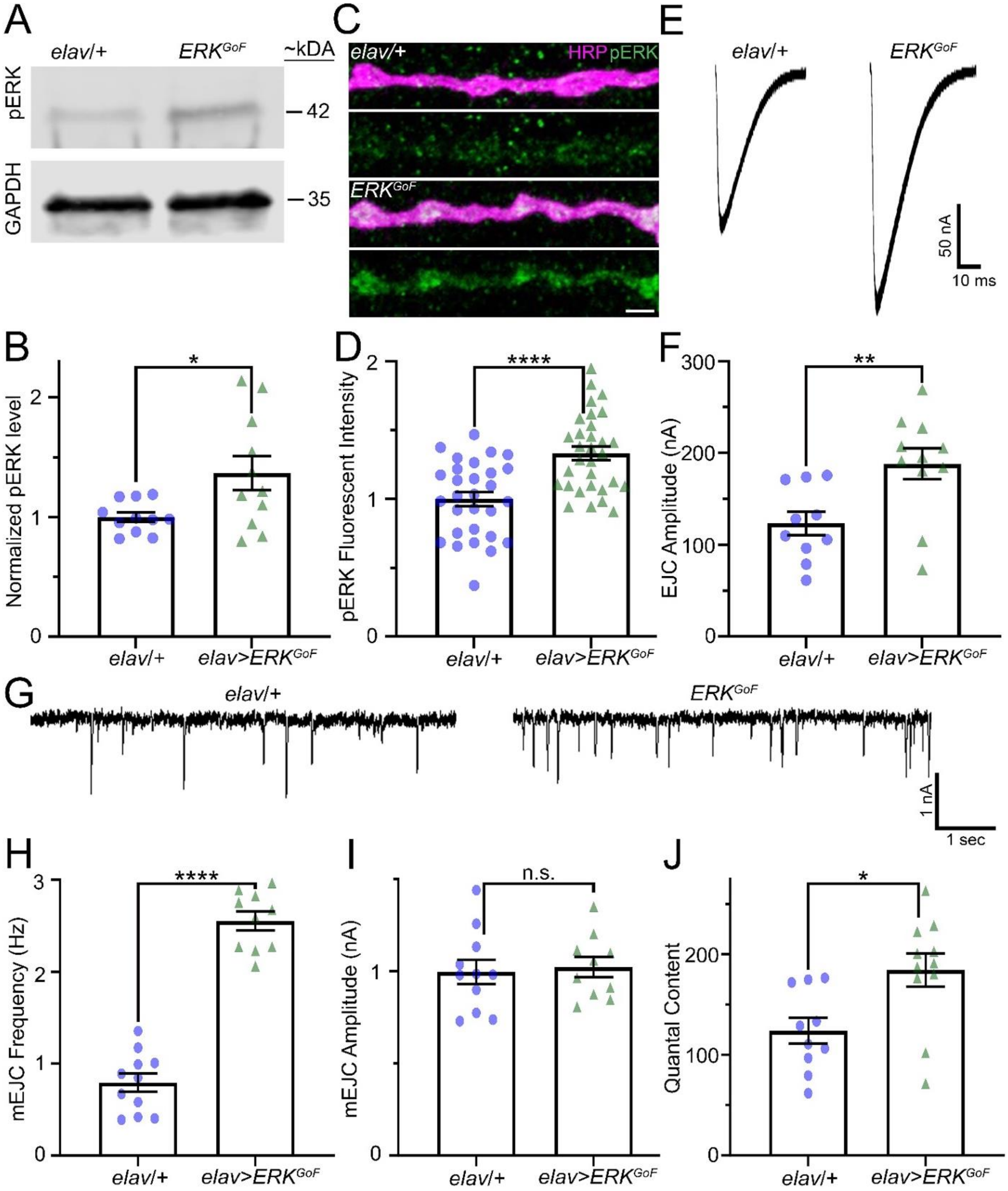

**Figure 3.4: Neuronal ERK$^{GoF}$ recapitulates PTPN11 pERK and neurotransmission defects**
**A)** Representative Western blot for pERK (42 kDA, top) and GAPDH loading control (35 kDA, bottom) in driver control (*elav*-Gal4/*w*$^{1118}$) and ERK$^{GoF}$ (*elav*-Gal4>*ERK*$^{SEM}$). **B)** Quantification of pERK levels normalized to GAPDH with a two-sided *t* test. **C)** Representative NMJ images co-labeled for anti-phospho-ERK (pERK, green) and presynaptic membrane marker anti-horseradish peroxidase (HRP, magenta) in driver control and ERK$^{GoF}$. Scale bar: 2.5 µm. **D)** Quantified pERK presynaptic fluorescence levels normalized to control with a two-sided *t* test. **E)** Representative two-electrode voltage-clamp (TEVC) recordings showing excitatory junction current (EJC) traces with 10 superimposed evoked responses (1.0 mM Ca$^{2+}$) from neuronal driver control (left) and ERK$^{GoF}$ (right). **F)** Quantification of EJC amplitudes with a two-sided *t* test. **G)** Representative miniature EJC (mEJC) traces (1.0 mM Ca$^{+2}$) from neuronal driver control (left) and ERK$^{GoF}$ (right). **H)** Quantification of the mEJC frequency using a two-sided *t* test. **I)** Quantification of mEJC amplitude using a two-sided *t* test. **J)** Quantification of quantal content using a two-sided *t* test. Scatter plots show all data points with mean±SEM. Data points: animal number (B) and NMJ number (D-J). Significance: $p<0.05$ (*), $p<0.01$ (**), $p<0.0001$ (****), and not significant (n.s.).

normalized to the transgenic driver control (*elav*-Gal4/$w^{1118}$). We next use two-electrode voltage-clamp (TEVC) electrophysiological recording to test *elav*-Gal4 neuron-targeted $ERK^{GoF}$ compared to the transgenic control by assaying excitatory junction current (EJC) responses driven by motor nerve stimulation. We also test spontaneous release with miniature EJC (mEJC) recordings, assessing both event frequency and amplitude. Representative images, recordings, and quantified results are shown in Figures 3.4.

We first confirmed increased signaling activation in Western blots measuring pERK levels with neuronally-targeted *elav*-Gal4>UAS-$ERK^{SEM}$ (shown as $ERK^{GoF}$) compared to driver controls (*elav*-Gal4/$w^{1118}$). At the predicted pERK molecular weight (42 kDa), there is a clearly increased band with $ERK^{GoF}$ (Fig. 3.4A). Normalized to a GAPDH loading control, the $ERK^{GoF}$ band (1.37±0.14, n=11) is increased over control (1.0±0.04, n=11), a significant elevation based on an unpaired t-test ($t_{(20)}$=2.478, p=0.0222, Fig. 3.4B). We next confirmed pERK is locally increased in NMJ boutons similar to NS/NSML mutants. In *elav*-Gal4 controls, pERK is only weakly detectable in boutons (Fig. 3.4C, top). In contrast, pERK levels are elevated with neuronal $ERK^{GoF}$ (Fig. 3.4C, bottom). Quantification of pERK with neuronal $ERK^{GoF}$ (1.33±0.05, n=31) normalized to control (1.0±0.05, n=29), shows a significant elevation in an unpaired t-test ($t_{(58)}$=4.626, p= $2.1375 \times 10^{-5}$; Fig. 3.4D). We next tested effects on neurotransmission. Compared to the driver controls, neuron-targeted $ERK^{GoF}$ causes elevated neurotransmission (Fig. 3.4E). EJC amplitudes in controls (123.40±12.79 nA, n=10) are increased with neural $ERK^{GOF}$ (188.25±16.86 nA, n=11), a significant strengthening with a two-sided t-test ($t_{(19)}$=3.019, p=0.0071; Fig. 3.4F). In spontaneous mEJC recordings, SV fusion events are greatly elevated by neuronal $ERK^{GOF}$ (Fig. 3.4G). Compared to the control frequency (0.79±0.1 Hz, n=11), there are many more events with $ERK^{GoF}$ (2.55±0.1 Hz, n=10), a significant increase based on a two-sided t-test ($t_{(19)}$=12.45, p=$1.39 \times 10^{-10}$; Fig. 3.4H). The mEJC amplitude is not altered ($t_{(19)}$=0.3096, p=0.7602, Fig. 4I). Compared to the control quantal content (124.01±12.86, n=10), quanta are increased by neuronal $ERK^{GOF}$ (184.25±16.5, n=11), a significant elevation with a two-sided t-test ($t_{(19)}$=2.838, p=0.0105, Fig. 3.4J). Taken with above results, we conclude heightened presynaptic pERK signaling elevates vesicle fusion probability, phenocopying *PTPN11/csw* mutants in a Synapsin-dependent mechanism.

### Removal of Synapsin blocks the elevated neurotransmission in PTPN11/csw and ERK mutants

To further test a mechanistic connection between PTPN11, ERK, and Synapsin elevating neurotransmission, we next expressed neuronally-driven *PTPN11*$^{Q150P}$ or *ERK*$^{GoF}$ transgenes in a *synapsin* null mutant. Our goal was to investigate the effects of preventing aberrantly elevated Synapsin on neurotransmission strength in these two mutant conditions. In our previous studies, we found that neuronally-targeted *PTPN11* mutations strongly elevate basal neurotransmission, which can be rescued by introducing pharmaceutical MAPK/ERK inhibitors.[165] These previous findings, alongside the highly increased Synapsin levels in *csw/PTPN11* mutants (Figs. 3.1,3.3) and elevated presynaptic ERK activity and strengthened neurotransmission in *ERK*$^{GoF}$ (Fig. 3.4), led us to hypothesize that PTPN11, ERK, and Synapsin act together to regulate basal neurotransmission amplitudes. Notably, however, Synapsin has been previously reported to have no effect on basal NMJ function,[66] generating an apparent quandary. To test this question, we again use TEVC electrophysiology to assay the neuronal *PTPN11* point mutant (*elav-Gal4>PTPN11*$^{Q510P}$), a *synapsin* null mutant (*syn*$^{97}$) and, in this null mutant background, neuronal *PTPN11*$^{Q510P}$ (*syn*$^{97}$*; elav-Gal4>PTPN11*$^{Q510P}$) and *ERK*$^{GoF}$ (*syn*$^{97}$*; elav>ERK*$^{SEM}$) compared to the driver control (*elav*-Gal4/*w*$^{1118}$). To further test these genetic interactions, we also assay the *csw*$^{5}$ null mutant, *ERK*$^{1}$ hypomorph (*ERK*$^{1}$/+), and the double mutant (*csw*$^{5}$*; ERK*$^{1}$/+) compared to the genetic background control (*w*$^{1118}$). We measure spontaneous mEJC events and evoked EJC responses from motor nerve stimulation.[40,165] Representative traces and quantifications are shown in Figure 3.5 and 3.6.

Driver control (*elav*-Gal4/+) and *synapsin* nulls (*syn*$^{97}$) show similar neurotransmission, and neuronally-driven *PTPN11*$^{Q510P}$ and *ERK*$^{GoF}$ no longer elevate neurotransmission amplitudes in the *synapsin* null background compared to the neuron-targeted *PTPN11* mutant (Fig. 3.5A). Quantification reveals controls (164.8±14.81 nA, n=13) are not significantly different from *syn*$^{97}$ nulls (141.1±15.41 nA n=10; p=0.7542), nor in this background, neuronal *PTPN11*$^{Q510P}$ (148.1±13.94 nA n=10; p=0.9167) or neuronal *ERK*$^{GoF}$ (142.7±11.67 nA n=10; p=0.7997) when compared via a one-way ANOVA and Tukey's multiple comparisons test ($F_{(4,47)}$=5.878, p=0.0006; Fig. 3.5B). In

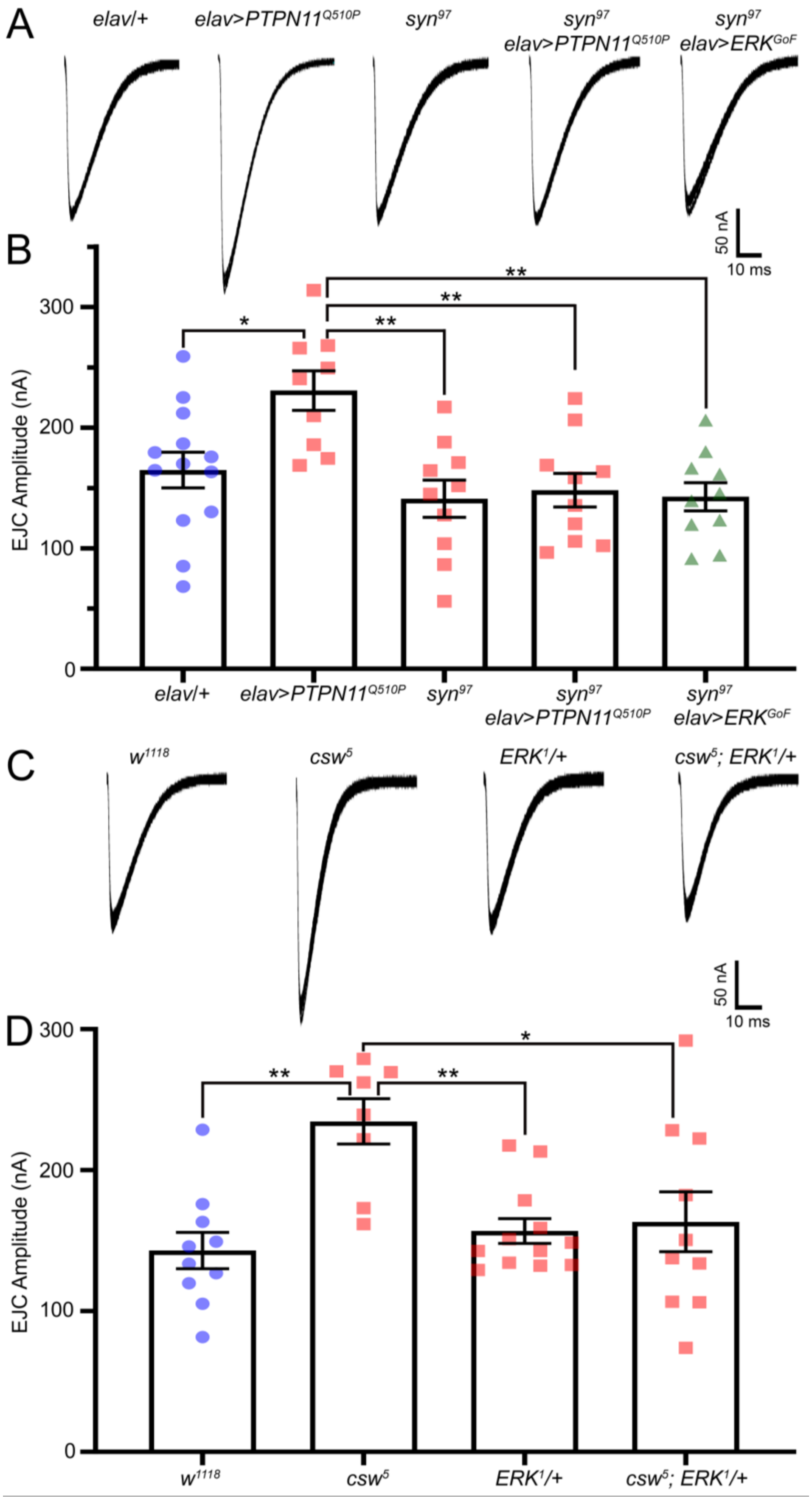

**Figure 3.5: *synapsin* null blocks elevated neurotransmission in *PTPN11* and *ERK* mutants**

**A)** Representative two-electrode voltage-clamp (TEVC) recordings of excitatory junction current (EJC) traces showing 10 superimposed evoked synaptic responses (1.0 mM $Ca^{2+}$). From left to right: neuronal driver control (*elav*-Gal4/*w*$^{1118}$), neuronal *PTPN11* (*elav*-Gal4>*PTPN11*$^{Q510P}$), synapsin null (*syn*$^{97}$), neuronal *PTPN11*$^{Q510P}$ with *synapsin* null (*syn*$^{97}$; *elav*-Gal4>*PTPN11*$^{Q510P}$), and neuronal *ERK*$^{GoF}$ with *synapsin* null (*syn*$^{97}$; *elav*-Gal4> *ERK*$^{SEM}$). **B)** EJC amplitude quantification using one-way ANOVA followed by Tukey's multiple comparisons test. **C)** Representative two-electrode voltage-clamp (TEVC) recordings of excitatory junction current (EJC) traces showing 10 superimposed evoked synaptic responses (1.0 mM $Ca^{2+}$). From left to right: control (*w*$^{1118}$), *csw*$^{5}$ null (*csw*$^{5}$), *ERK* heterozygote (*ERK*$^{1}$/*w*$^{1118}$) and *csw*$^{5}$ with ERK heterozygote (*csw*$^{5}$; *ERK*$^{1}$/*w*$^{1118}$). **D)** Quantification of EJC amplitudes using one-way ANOVA followed by Tukey's multiple comparisons test. Scatter plots show all the data points with mean±SEM. Data points: NMJ number. Significance: $p<0.05$ (*), $p<0.01$ (**), and $p>0.05$ not significant (n.s.).

contrast, neuronal *PTPN11*$^{Q510P}$ (230.7±16.43 nA n=9) is highly elevated compared to driver control (p=0.0188), *syn*$^{97}$ nulls (p=0.0013), and neuronal *PTPN11*$^{Q510P}$ (p=0.0035) and neuronal *ERK*$^{GoF}$ (p=0.0017) in this background. This genetic suppression suggests heightened MAPK/ERK signaling to elevate Synapsin function increases neurotransmission strength. To further test this idea, we next assayed whether reduced ERK could prevent the *csw*$^{5}$ null elevated neurotransmission.[165] As reported, *csw*$^{5}$ nulls have elevated neurotransmission compared to background controls (*w*$^{1118}$; Fig. 3.5C, left). *ERK*$^{1}$ heterozygotes (*ERK*$^{1}$/+) appear similar to controls, but *csw*$^{5}$ with heterozygous *ERK*$^{1}$ no longer have elevated neurotransmission (Fig. 3.5C, right). Quantification indicates significant differences between genotypes based on a one-way ANOVA ($F_{(3,36)}$=6.435, p=0.0013; Fig. 3.5D). Compared to the control EJC amplitude (142.9±12.9, n=10), *csw*$^{5}$ nulls (234.6±16.1, n=8) have significantly elevated EJC amplitudes (p=0.0013; Fig. 3.5D). In sharp contrast, there is no significant elevation based on a Tukey's multiple comparisons test in either *ERK*$^{1}$/+ (156.8±8.84, n=12; p=0.9029) or *csw*$^{5}$; *ERK*$^{1}$/+ (163.3±21.3, n=10; p=0.7705; Fig. 3.5D). There is also no significant difference in neurotransmission between *ERK*$^{1}$ and *csw*$^{5}$; *ERK*$^{1}$/+ (p=0.9881), but *csw*$^{5}$ nulls are significantly elevated compared to *csw*$^{5}$; *ERK*$^{1}$/+ (p=0.0155) and *ERK*$^{1}$/+ heterozygotes (p=0.005; Fig. 3.5D). Thus, reducing ERK genetically in *csw* nulls effectively restores neurotransmission strength back to normal levels.

We next used mEJC recordings to test spontaneous neurotransmission events (Fig. 3.6A). Quantification reveals the driver control mEJC frequency (0.76±0.07 Hz, n=12) is not significantly different from *syn*$^{97}$ null mutants (1.12±0.11 Hz, n=14, p=0.1076) or in this background, neuronal *PTPN11*$^{Q510P}$ (1.11±0.09 Hz, n=14, p=0.1273) and *ERK*$^{GoF}$ (0.98±0.13 Hz, n=10, p=0.6468) when compared with one-way ANOVA and Tukey's multiple comparisons ($F_{(4,63)}$=8.384, p=1.733×$10^{-5}$; Fig. 3.6B top). In contrast, neuronal *PTPN11*$^{Q510P}$ (1.51±0.09 Hz n=18) is elevated compared to the driver control (p=7.19×$10^{-6}$), *syn*$^{97}$ null mutant (p=0.0297), and in this background, neuronal *PTPN11*$^{Q510P}$ (p=0.0236) and neuronal *ERK*$^{GoF}$ (p=0.0039; Fig. 3.6B top). Similarly, when analyzed via a one-way ANOVA and Tukey's multiple comparisons ($F_{(3,38)}$=11.371, p=1.83×$10^{-5}$) *csw*$^{5}$ nulls (1.83±0.17 Hz, n=9) have a significantly elevated mEJC frequency compared to the background control (0.81±0.1 Hz, n=13; p=1.29×$10^{-5}$), *ERK*$^{1}$/+

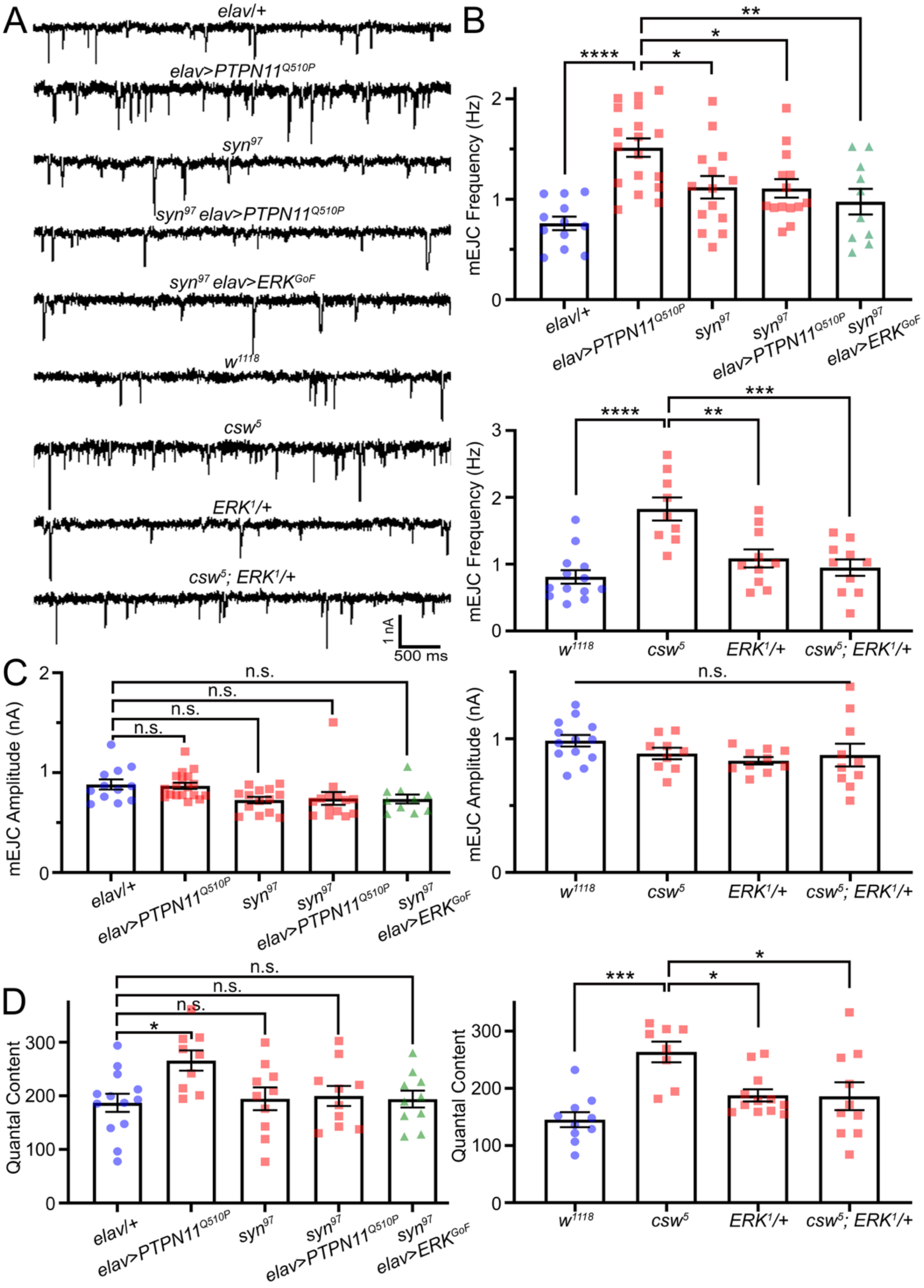

**Figure 3.6: *synapsin* null blocks elevated vesicle fusion in *PTPN11* and *ERK* mutants**
**A)** Representative mEJC traces (1.0 mM $Ca^{+2}$) from top to bottom: the neuronal driver control (*elav*-Gal4/$w^{1118}$), neuronal *PTPN11* point mutant (*elav*-Gal4>$PTPN11^{Q510P}$), *synapsin* null ($syn^{97}$), neuronal $PTPN11^{Q510P}$ in the *synapsin* null ($syn^{97}$; *elav*-Gal4>$PTPN11^{Q510P}$), neuronal $ERK^{GoF}$ in the *synapsin* null ($syn^{97}$; *elav*-Gal4> $ERK^{SEM}$), genetic background control ($w^{1118}$), $csw^{5}$ null ($csw^{5}$), *ERK* heterozygous mutant ($ERK^{1}/w^{1118}$) and ERK heterozygote in the $csw^{5}$ null ($csw^{5}$; $ERK^{1}/w^{1118}$). **B)** Quantification of mEJC frequencies in all 9 genotypes using one-way ANOVAs followed by Tukey's multiple comparisons. **C)** Quantification of mEJC amplitudes in all 9 genotypes using Kruskal-Wallis followed by Dunn's multiple comparisons test (left) or a one-way ANOVA (right). **D)** Quantification of the evoked neurotransmission quantal content in all 9 genotypes using one-way ANOVAs followed by Tukey's multiple comparisons tests. Scatter plots show all the data points with mean±SEM. Data points: NMJ number. Significance: $p<0.05$ (*), $p<0.01$ (**), $p<0.001$ (***), $p<0.0001$ (****), and not significant (n.s.).

heterozygote (1.09±0.14 Hz, n=10; p=0.0025), and *csw*$^5$; *ERK*$^1$/+ double mutant (0.95±0.12 Hz, n=10; p=0.0003; Fig. 3.6B bottom) In contrast, there is no significant elevation compared to the control frequency of either *ERK*$^1$/+ (p=0.4139) or *csw*$^5$; *ERK*$^1$/+ (p=0.8628; Fig. 3.6B bottom). In all 9 conditions, there is no change in mean mEJC amplitudes compared to their controls (Fig. 3.6C). Thus, specific changes in spontaneous release frequencies are consistent with the evoked neurotransmission strengths.

When analyzing the stimulation-evoked quantal content, quantification reveals that the *elav*/+ driver control (187±16.8, n=13) is not significantly different from the *syn*$^{97}$ null mutant (194.6±21.24, n=10, p=0.9981; Fig. 3.6D, left). In this *syn*$^{97}$ background, there is also no significant difference in quantal content with neuron-targeted *PTPN11*$^{Q510P}$ (199.8±18.79, n=10, p=0.9859) or *ERK*$^{GoF}$ (194±15.86 n=10, p=0.9986; Fig. 3.6D, left). In contrast, neuronal *PTPN11*$^{Q510P}$ alone does elevate quantal content (265.9±18.93 n=9, p=0.0279) compared using a one-way ANOVA followed by Tukey's multiple comparisons ($F_{(4,47)}$=2.858, p=0.0336; Fig. 3.6D, left). Similarly, the *csw*$^5$ null mutant quantal content (263.6±18.09, n=8) is significantly elevated when analyzed via a one-way ANOVA and Tukey's multiple comparisons test ($F_{(3,36)}$=7.526, p=0.0005) compared to *w*$^{1118}$ background controls (145.1±13.09, n=10; p=0.0002), *ERK*$^1$/+ heterozygotes (187.5±10.57, n=12; p=0.017, and *csw*$^5$; *ERK*$^1$/+ double mutants (186.1±24.26, n=10; p=0.0198; Fig. 3.6D, right). In sharp contrast, there is no significant change in quantal content in either *ERK*$^1$/+ heterozygotes (p=0.2593) or *csw*$^5$; *ERK*$^1$/+ double mutants (p=0.325). Thus, genetically reducing ERK levels in the *csw* null mutant effectively restores presynaptic release function back towards normal levels. To confirm this neuronal presynaptic mechanism, we next aimed to rescue *csw* null elevated neurotransmission by re-introducing wildtype *csw* into motor neurons.

### Corkscrew is necessary in both neurons and glia to rescue csw null neurotransmission elevation

To simply confirm the *PTPN11/csw* role is neuronal as expected, we next tested genetic rescue of the *csw* null elevated neurotransmission by expressing wildtype *csw* (*csw*$^{WT}$) only in the motor neurons.[170] We previously showed that ubiquitous *csw*$^{WT}$ expression fully rescues the *csw*$^5$ null neurotransmission.[165] To drive neuronal *csw*$^{WT}$, we utilized *vglut*-Gal4, a glutamatergic neuronal driver with strong expression in the motor neurons.[173] To test this genetic rescue condition, we again employed TEVC electrophysiology recordings to measure stimulation evoked EJC amplitude. In the neuronal driver control (*vglut*-Gal4/$w^{1118}$), motor nerve stimulation drives normal, consistent neurotransmission amplitudes (Fig, 3.7A, left). To our enormous surprise, $csw^5$ null mutants with neuronally-targeted $csw^{WT}$ ($csw^5$; *vglut*-Gal4>$csw^{WT}$) still display strongly elevated mutant neurotransmission with the same clear increase in EJC amplitudes (Fig. 3.7A, left). Quantified $csw^5$ null with neuronal $csw^{WT}$ neurotransmission amplitudes (206.80±17.61 nA, n=10) remain obviously elevated compared to neuronal driver controls (149.0±7.79 nA, n=15), a very significant increase based on a two-sided t-test ($t_{(23)}$=3.369, p=0.0027, Fig. 3.7B, left). This elevated neurotransmission is comparable with the *csw* null phenotype, indicating that neuronal expression of $csw^{WT}$ has no effect in rescuing the neurotransmission strength phenotype.

The NMJ is a tripartite synapse consisting of the presynaptic neuron, postsynaptic muscle, and perisynaptic glia.[32,35] In our previous work, we found the postsynaptic muscle is unaffected in *csw* mutants.[165] Additionally, glial mutations are known to lead to behavioral defects in *Drosophila.*[184] Therefore, we tried to re-introduce $csw^{WT}$ in glia to rescue neurotransmission. For this test, we utilized the glial driver *repo*-Gal4, which expresses in all glial cells.[172,185] As above for motor neurons, $csw^5$ null mutants with glial-targeted $csw^{WT}$ ($csw^5$; *repo*-Gal4>$csw^{WT}$) still displays highly elevated neurotransmission with a clear increase in EJC amplitude compared to the driver control (Fig. 3.7A, middle). The EJC amplitudes of $csw^5$ null with glial $csw^{WT}$ (207.70±8.47 nA, n=11) remain elevated compared to glial driver control (175.20±7.48 nA, n=14), a significant elevation based on an unpaired t-test ($t_{(23)}$=2.879, p=0.0085; Fig. 3.7B, middle). As a consequence of these unexpected results, we next tried re-introducing $csw^{WT}$ in both motor neurons and glia in the *csw* null mutant. Finally, $csw^5$ nulls with neuronal and glial $csw^{WT}$ together ($csw^5$; *vglut*-Gal4; *repo*-Gal4>$csw^{WT}$) show fully rescued transmission compared to the dual driver control (*vglut*-Gal4; *repo*-Gal4/$w^{1118}$; Fig. 7A, right). When quantified, $csw^5$ nulls with neuronal and glial $csw^{WT}$ (148.50±11.52 nA, n=10) are indistinguishable from the dual driver transgenic control (145.30±11.04 nA, n=10), with no significant difference based on a two-sided t-test ($t_{(18)}$=0.2039, p=0.8407; Fig 3.7B, right). Taken together, these

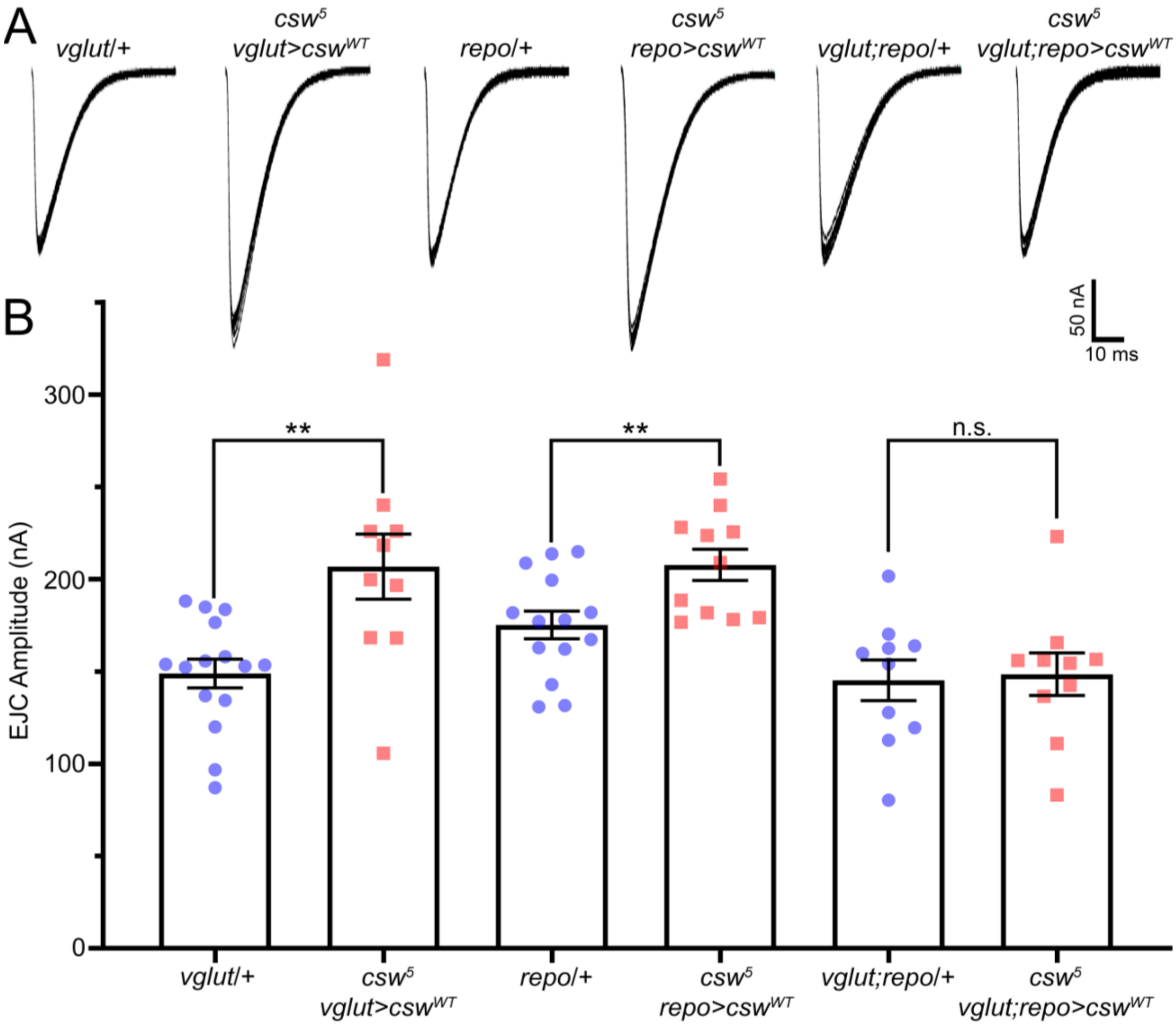

**Figure 3.7: Both neuronal and glial Csw is required to rescue *csw* null neurotransmission**
Null *csw*$^{5}$ elevated neurotransmission is rescued only with wildtype Csw in both the motor neurons and glia, indicating a requirement in both cell types. **A)** Representative EJC recordings showing 10 superimposed traces in *csw*$^{5}$ null and driver controls, and with motor neuron, glial, or combined driven wildtype Csw (*csw*$^{WT}$) to test neurotransmission rescue. From left to right: motor neuron transgenic driver control (*vglut*-Gal4/*w*$^{1118}$) and neuronal rescue (*csw*$^{5}$; *vglut*-Gal4>*csw*$^{WT}$), glial transgenic driver control (*repo*-Gal4/*w*$^{1118}$) and glial rescue (*csw*$^{5}$; *repo*-Gal4>*csw*$^{WT}$), and the dual neuron + glial driver control (*vglut*-Gal4*;* *repo*-Gal4/*w*$^{1118}$) and the dual combined cell type rescue (*csw*$^{5}$; *vglut*-Gal4*;repo*-Gal4>*csw*$^{WT}$). **B)** Quantification of the mean EJC amplitudes in all six conditions with two-sided *t* tests. Scatter plots show all the data points with mean±SEM. Data points: NMJ number. Significance: $p<0.01$ (**) and $p>0.05$ not significant (n.s.).

results indicate a requirement for Csw in both neurons and glia to control neurotransmission strength.

We next used mEJC recordings to test spontaneous neurotransmission events (Fig. 3.8A). In *csw*$^5$ null mutants, neither neuronal nor glial wildtype *csw* expression (*csw*$^{WT}$) can rescue the elevated mEJC frequency (Fig. 3.8A, top). Compared to control frequency (1.02±0.14 Hz, n=11), mEJCs remain elevated with neuronal *csw*$^{WT}$ (1.97±0.16 Hz, n=11), a significant two-sided t-test increase ($t_{(20)}$=4.612, p=0.0002; Fig. 3.8B, left). Likewise, relative to the glial driver control (0.74±0.1 Hz, n=11), frequency is still heightened with glial *csw*$^{WT}$ (1.47±0.43 Hz, n=8), a significant increase based on a two-sided t-test ($t_{(17)}$=4.194, p=0.0006; Fig. 3.8B, middle). However, neuronal and glial *csw*$^{WT}$ together show fully rescue the *csw*$^5$ null elevated mEJC frequency (Fig. 3.8A, bottom). When quantified, *csw*$^5$ nulls with neuronal and glial *csw*$^{WT}$ (0.61±0.09 Hz, n=11) were indistinguishable from dual driver controls (0.77±0.12 Hz, n=10), with no significant difference based on a two-sided t-test ($t_{(19)}$=1.105, p=0.2829, Fig. 3.8B, right). In all 6 conditions, there is no change in mean mEJC amplitudes (Fig. 3.8C). When analyzing quantal content with two-sided t-tests *csw*$^5$ null mutants with neuronal *csw*$^{WT}$ (199.28±16.97, n=10) and glial *csw*$^{WT}$ (239.46±9.76, n=11) are significantly elevated from their respective neuronal (144.48±7.56, n=15; $t_{(23)}$=3.306, p=0.0031; Fig. 3.8D, left) and glial driver controls (177.06±7.56, n=14; $t_{(23)}$=5.141, p=3.29 x $10^{-5}$; Fig. 3.8D, middle). This shows that neither neuronal nor glial *csw* expression alone can rescue the neurotransmission defect. In sharp contrast, the quantal content of *csw*$^5$ null mutants with dual neuronal and glial *csw*$^{WT}$ (172.03±13.34, n=10) is rescued compared to the dual driver controls (158.03±12.01, n=10), with no significant change remaining based on a two-sided t-test ($t_{(18)}$=0.7798, p=0.4456, Fig. 3.8D, right). The results indicate both neuronal and glial function is needed. We next tested whether glial-targeted *PTPN11/csw* mutations alone cause neurotransmission defects.

### Glial-targeted PTPN11/csw LoF and GoF independently increases neurotransmission strength

To test the unexpected glial function for *PTPN11/csw*, we first drove *csw* RNAi in glia to assay synaptic transmission strength.[133] To further test the *PTPN11* glial role, we also targeted the GoF (*PTPN11*$^{N308D}$) NS mutation and LoF (*PTPN11*$^{Q510P}$) NSML

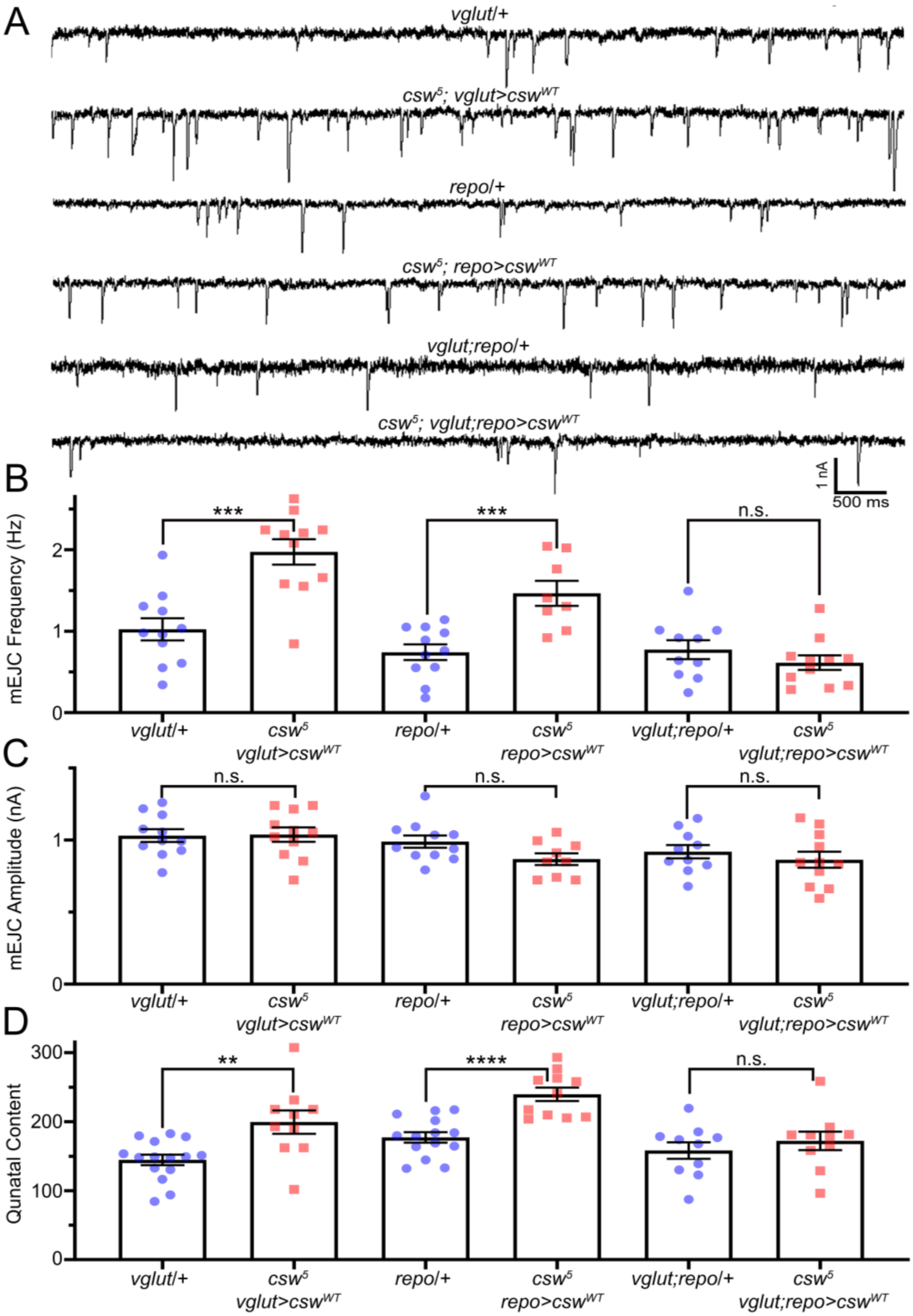

**Figure 3.8: Both neuronal and glial Csw is required to rescue spontaneous transmission**
Null *csw*$^5$ elevated spontaneous neurotransmission frequency is only rescued with wildtype Csw in both motor neurons and glia, indicating a dual requirement. **A)** Representative mEJC traces (1.0 mM Ca$^{+2}$) in *csw*$^5$ null and driver controls, and with motor neuron, glial, or combined wildtype Csw (*csw*$^{WT}$). From top to bottom: motor neuron driver control (*vglut*-Gal4/*w*$^{1118}$), neuronal rescue (*csw*$^5$; *vglut*-Gal4>*csw*$^{WT}$), glial driver control (*repo*-Gal4/*w*$^{1118}$), glial rescue (*csw*$^5$; *repo*-Gal4> *csw*$^{WT}$), neuron + glial driver control (*vglut*-Gal4*;* *repo*-Gal4/*w*$^{1118}$), and combined cell type rescue (*csw*$^5$; *vglut*-Gal4*;* *repo*-Gal4>*csw*$^{WT}$). **B)** Quantification of the mEJC frequency in all 6 conditions using two-sided *t* tests. **C)** Quantification of mEJC amplitude in all 6 conditions using two-sided *t* tests. **D)** Quantification of the quantal content in all 6 conditions using two-sided *t* tests. Scatter plots show all the data points with mean±SEM. Data points: NMJ number. Significance: p<0.01 (**), p<0.001 (***), p<0.0001 (****), and not significant (n.s.).

mutation exclusively to glia.[91] We had previously established each of these three conditions cause elevated neurotransmission strength when targeted exclusively to presynaptic neurons.[165] Compared to glial driver controls (*repo*-Gal4/$w^{1118}$), both glial-targeted *PTPN11* GoF (*repo*-Gal4>$PTPN11^{N308D}$) and *PTPN11* LoF (*repo*-Gal4>$PTPN11^{Q510P}$) conditions strongly elevate neurotransmission strength (Fig. 3.9A, left). Quantification indicates significant differences between genotypes based on a one-way ANOVA ($F_{(2,34)}$=7.502, p=0.002; Fig. 3.9B, left). Compared to the glial driver control EJC amplitude (170.20±9.39 nA, n=15), both $PTPN11^{N308D}$ (221.0±10.32 nA, n=11, p=0.006) and $PTPN11^{Q510P}$ (219.20±13.51 nA, n=11, p=0.008) show a very significant elevation based on a Tukey's multiple comparisons test (Fig. 3.9B, left). There is no significant difference in EJC amplitudes between GoF and LoF conditions (p=0.994, Fig. 3.9B). Similarly, glial-targeted *csw* knockdown (*repo*-Gal4>*csw* RNAi*)* causes clearly elevated evoked neurotransmission compared to the glial driver control (*repo*-Gal4/TRiP BDSC 36303 control; Fig. 3.9A, right). Quantification shows the glial-targeted *csw* RNAi amplitude (226.9±11.3 nA, n=11) is elevated compared to the glial driver control (177.60±9.59 nA, n=12), with a significant increase based on a two-sided t-test ($t_{(21)}$=3.343, p=0.0031; Fig. 3.9B, right). These results show glia-targeted *PTPN11/csw* LoF and GoF mutations drive elevated evoked neurotransmission strength, as we previously established also occurs with neuronal manipulations.[165]

We finally wanted to test whether the glial-mediated increase in neurotransmission is due to higher presynaptic vesicle release probability. Spontaneous mEJC recordings reveal clearly elevated event frequencies in all of the above glial-targeted *PTPN11/csw* mutations (Fig. 3.9C). Compared to glial *repo*-Gal4/+ driver control frequency (1.13±0.16 Hz, n=17), there is an increase with glial $PTPN11^{N308D}$ (2.14±0.34 Hz, n=15, p=0.0104) and glial $PTPN11^{Q510P}$ (2.02±0.19 Hz, n=17, p=0.0207), significant elevations based on a one-way ANOVA followed by Tukey's multiple comparisons ($F_{(2,46)}$=5.771, p=0.0058; Fig. 3.9D, left). This increase in mEJC frequency also occurs with glial *csw* RNAi (1.57±0.29 Hz, n=10) compared to glial driver controls (0.92±0.14 Hz, n=12), significantly elevated with a two-sided t-test ($t_{(20)}$=2.117, p=0.047; Fig. 3.9D, right). In contrast, there is no significant change in mEJC amplitudes compared to controls (0.86±0.06 nA, n=17) in glial $PTPN11^{N308D}$ (0.82±0.04 nA, n=15) or $PTPN11^{Q510P}$ (0.88±0.03 nA, n=17) analyzed via a

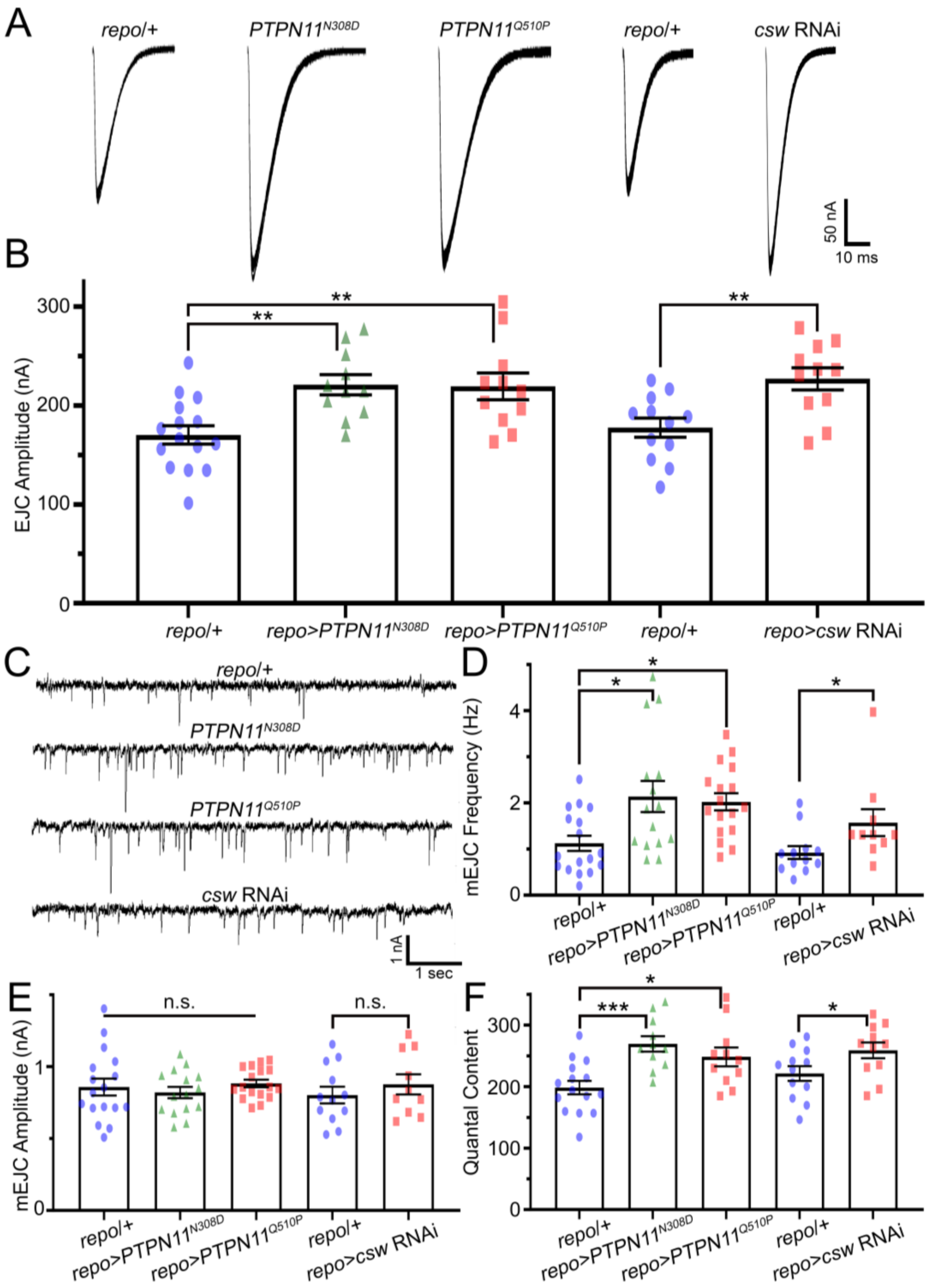

**Figure 3.9: Glial-targeted *PTPN11/csw* loss- and gain-of-function elevate neurotransmission**
Glial human *PTPN11* mutations from NS/NSML disease states, and *csw* knockdown, all increase synaptic function, indicating that glia-specific changes are sufficient to elevate neurotransmission. **A)** Representative EJC recordings showing 10 superimposed traces for each of the conditions. From left to right: the glial transgenic driver control (*repo*-Gal4/*w*$^{1118}$), the glial-driven *PTPN11* patient-derived point mutations *PTPN11*$^{N308D}$ (*repo*-Gal4>*PTPN11*$^{N308D}$) and *PTPN11*$^{Q510P}$ (*repo*-Gal4>*PTPN11*$^{Q510P}$), glial driver RNAi background control (*repo*-Gal4/TRiP Ctl), and glial-driven *csw* RNAi (*repo*-Gal4>*csw* RNAi). **B)** Quantification of the EJC amplitudes in all five conditions, using one-way ANOVA followed by Tukey's multiple comparisons test (*PTPN11*) and two-sided *t* tests (RNAi). **C)** Representative mEJC traces (1.0 mM Ca$^{+2}$) from top to bottom: glial driver control (*repo*-Gal4/*w*$^{1118}$), and glial-driven *PTPN11*$^{N308D}$, *PTPN11*$^{Q510P}$ and *csw* RNAi **D)** Quantification of mEJC frequency in all 5 conditions; one-way ANOVA followed by Tukey's multiple comparisons test (*PTPN11*) and two-sided *t* tests (RNAi). **E)** Quantification of mEJC amplitudes, using one-way ANOVA (*PTPN11*) and two-sided *t* tests (RNAi). **F)** Quantification of the quantal content in all 5 conditions, using one-way ANOVA followed by Tukey's multiple comparisons test (*PTPN11*) and two-sided *t* tests (RNAi). Scatter plots show all data points with mean±SEM. Data points: NMJ number. Significance: $p<0.05$ (*), $p<0.01$ (**), $p<0.001$ (***), and not significant (n.s.).

one-way ANOVA ($F_{(2,46)}$=0.4970, p=0.6116; Fig. 3.9E, left), or the glial driver control (0.80±0.06 nA, n=12) versus *csw* RNAi (0.88±0.07 nA, n=10) compared with a two-sided t-test ($t_{(20)}$=0.8183, p=0.4228; Fig. 3.9E, right). Moreover, compared to the quantal content in the glial driver control (198.3±10.94, n=15), the number of stimulus-evoked quanta is elevated with both glial-targeted *PTPN11*$^{N308D}$ (269.4±12.58, n=11, p=0.0009) and *PTPN11*$^{Q510P}$ (248.3±15.3, n=11, p=0.0217) analyzed with a one-way ANOVA ($F_{(2,34)}$=8.746, p=0.0009; Fig. 3.9F, left). This increase in quantal content also occurs with *csw* RNAi (258.91±12.9, n=11) compared to control (221.35±11.95, n=12) based on a two-sided t-test ($t_{(21)}$=2.139, p=0.0443; Fig. 3.9F, right). Taken together, we conclude that *PTPN11/csw* regulates presynaptic neurotransmission via dual roles in both neurons and glia, with targeted LoF/GoF mutations in either cell type sufficient to cause strongly elevated neurotransmission, but a necessary requirement for function in both neurons and glia.

## Discussion

Corkscrew (Csw) regulates MAPK/ERK signaling in critical neuronal functions, such as the proactive interference modulation of learning and memory.[186] Mutation of the human homolog *PTPN11* causes Noonan syndrome (NS) through gain-of-function (GoF) and NS with Multiple Lentigines (NSML) through loss-of-function (LoF), with striking cognitive impairments.[81] Both directions elevate MAPK/ERK signaling to cause similar disease symptoms.[3,91] Similarly, we discovered *Drosophila* NS/NSML models both elevate presynaptic MAPK/ERK signaling to heighten neurotransmission and reduce synaptic depression.[165] These results suggested a presynaptic mechanism of vesicle recruitment. To test this hypothesis, we began by analyzing Synapsin in the strongest neurotransmission condition; *csw* nulls (Figure 3.1). Synapsin phosphoprotein tethers regulate neurotransmission strength by restraining vesicles in the reserve pool,[61,67] which replenishes the readily releasable pool (RRP) upon sustained exocytosis.[62] In mammals, Synapsin is encoded by 3 genes, whereas *Drosophila* has one single homolog.[75] In mouse glutamatergic neurons, *synapsin* triple knockout increases synaptic depression rate,[64] and uniquely Synapsin IIA rescues this phenotype.[63] Likewise, Synapsin IA/B overexpression increases the short-term depression rate, indicating that Synapsin dysregulation in either direction can increase depression.[24] In *Drosophila csw* null mutants, Synapsin levels and SV colocalization are elevated at rest and strongly depleted with acute stimulation (Figure 3.1). This is presumed to represent cytosolic dispersion, although we cannot verify this hypothesis with immunocytochemical imaging.

With stimulation, Synapsin is phosphorylated by several kinases, including MAPK/ERK, to cause SV disassociation and enable RRP recruitment.[54,67] With stimulation, *csw* nulls display dramatic loss of anti-Synapsin signal and colocalization with SV markers, whereas matched genetic controls do not change (Figure 3.1). This suggests that absence of Csw causes aberrant Synapsin disassociation from SVs. The increased activity-dependent recruitment of Synapsin-bound vesicles in *csw* nulls (Figure 3.1) accounts for sustained resistance to synaptic depression.[165] Consistent with *csw* results, *Drosophila synapsin* nulls have reduced facilitation.[187] A transgenic mouse model with increased ERK-dependent Synapsin I phosphorylation displays an increased frequency of synaptic vesicle fusion events, but also increased paired-pulse facilitation.[127] However, mouse *synapsin* triple knockouts also shows reduced short-term synaptic plasticity.[151] Thus, there is good overlap between *Drosophila* and mouse results regarding the ERK-dependent regulation of Synapsin controlling presynaptic vesicle fusion probability, but a difference in the consequences affecting synaptic plasticity, which is likely due to the multiple Synapsin isoform interactions in mammals.[127,151,165] The very striking changes in Synapsin dynamics in *csw* null mutants (Figure 3.1) suggest altered presynaptic vesicle pools.

We tested synaptic vesicle pools in *csw* null mutants by imaging synaptic ultrastructure with transmission electron microscopy.[21,23] The *csw* nulls display normal synapse architecture, including presynaptic bouton and postsynaptic subsynaptic reticulum (Figure 3.2, Table 3.1). Overall, synaptic bouton and vesicle morphology are all unchanged, with SV distribution specifically disrupted. SVs cluster closer together, possibly accounting for the elevation in the SV marker vglut under the same conditions (Figure 3.1). This is agreement with the constitutively active ERK *H-ras*$^{G12V}$ mouse model, that also displays no defects in gross synaptic ultrastructure.[127] Likewise, Synapsin overexpression does not alter gross SV number or density, but does change the SV distribution.[24] In analyzing SV distribution relative to presynaptic active zones, we discovered a decrease at 200-400 nm removed from the t-bar (Figure 3.2). This alteration in vesicle density associated with the reserve pool is consistent with direct Synapsin involvement. In *Drosophila synapsin* nulls, SVs are spread toward the bouton interior, with reduced vesicle density in the center of the bouton.[67] Docked vesicles within ½ of a vesicle diameter (<20 nm) of the active zone membrane are elevated in *csw* null mutants (Figure 3.2). This is consistent with an increase in the RRP[25] and we measured increases in the functional RRP previously via electrophysiology in *csw* nulls.[165] Likewise, the constitutively active ERK $H\text{-}ras^{G12V}$ mouse model displays an increase in docked synaptic vesicles.[127] These results reveal altered MAPK/ERK-dependent presynaptic vesicle pool distributions that provide an explanation for the *csw* null mutants neurotransmission strength elevation.

To confirm this presynaptic mechanism in NS and NSML disease models, we next tested Synapsin in NS ($PTPN11^{N308D}$, GoF) and NSML ($PTPN11^{Q510P}$, LoF) conditions. [3,91] $PTPN11^{N308D}$ occurs in ~25% of NS patients[4], and $PTPN11^{Q510P}$ confers NSML symptoms.[91] Like *csw* nulls, both patient-derived mutations increase Synapsin and SV association (Figure 3.3). With stimulation, Synapsin-bound vesicles are aberrantly recruited, providing the basis for sustained synaptic depression resistance.[165] Inhibition of MAPK/ERK signaling alleviates both NS and NSML disease model phenotypes.[90,91,165] However, this pathway is highly regulated, and intersecting pathways can affect function.[183] Therefore, to confirm the specificity for neurotransmission, we tested targeted ERK gain-of-function ($ERK^{GoF}$). This constitutively-active ERK mutant at the endpoint of the MAPK pathway allows for the most specific analysis of MAPK signaling on neurotransmission.[171] Constitutively active ERK recapitulates the elevated presynaptic pERK levels and strengthened neurotransmission in the *PTPN11/csw* mutants (Figure 3.4), to place activated ERK on site for presynaptic regulation of vesicle dynamics.[73,165] To further confirm this mechanism, we targeted neuronal PTPN11 and $ERK^{GoF}$ mutations in a *synapsin* null background to find a block of the elevated neurotransmission (Figure 3.5,3.6). This is internally consistent, but unexpected due to Synapsin loss not affecting basal neurotransmission strength.[66] However, unlike *synapsin* knockout, NS/NSML mutations likely affect a wide range of differential pathways throughout development, so other mechanisms may also be going awry. To finally confirm this presynaptic mechanism, we turned to genetic rescue by expressing wildtype Corkscrew within glutamatergic neurons in an otherwise global *csw* null mutant.

Cell-targeted genetic rescue is the gold-standard for demonstrating cellular requirements.[188] Based on our previous work and above results, we were confident that driving wildtype Csw in motor neurons (*csw*$^{WT}$) would demonstrate a neuron-specific requirement. To our astonishment, neuron expression fails to provide any rescue whatsoever of the *csw* null elevated neurotransmission strength (Figures 3.7,3.8). Our previous work showed no postsynaptic muscle role for Csw,[165] so we next examined the third cell type at the tripartite NMJ synapse; glia.[32] However, glial *csw*$^{WT}$ expression also fails to provide any rescue of the *csw* null elevated neurotransmission strength (Figures 3.7,3.8). We therefore next turned to driving *csw*$^{WT}$ in motor neurons and glia simultaneously, to find this fully rescues the *csw* null elevated neurotransmission strength (Figures 3.7,3.8). Thus, Csw is needed in both neurons and glia together to regulate neurotransmission amplitude. However, we previously found that neuron-targeted *PTPN11/csw* LoF and GoF transgenes are both sufficient to replicate *csw* null mutant elevated neurotransmission.[165] Likewise, we find glial-targeted transgenes also sufficient to elevate synaptic strength (Figure 3.9). These results show that *PTPN11/csw* mutations in either glia or neurons alone cause the defect, but that *PTPN11/csw* function in both cell types is necessary to properly regulate neurotransmission. *PTPN11/csw* has known glial roles for the regulation of neurogenesis and gliogenesis,[189,190] and in response to injury,[37,191,192] but this is the first work to reveal a glial role for *PTPN11/csw* in neurotransmission.

Glial roles in regulating neurotransmission have been previously discovered, such as the Repo transcription factor regulation of glutamate neurotransmitter cycling [193]. However, based on both spontaneous and quantal content analyses, glial PTPN11/Csw acts in the regulation of glutamatergic signaling via a common pathway with the neuronal presynaptic MAPK/ERK-dependent regulation of Synapsin. There are three characterized glial subclasses at the NMJ; perineurial (PG), subperineurial (SPG), and wrapping glia (WG;[32]). Each glial subclass has functions at the NMJ that could contribute to elevation of neurotransmission strength. Based on accumulating current evidence, it is likely that

*PTPN11/csw* functions within the glial subclasses with the most active roles in modulating neurotransmission (SPG or WG), and future experiments will focus on elucidating the exact glial subclass(es) involved. In this study, we establish that *PTPN11/csw* acts both within motor neurons and glia, with LoF/GoF similarly upregulating MAPK/ERK signaling to control Synapsin-mediated synaptic vesicle trafficking in an activity-dependent mechanism. Future interventions to improve cognitive outcomes in NS and NSML patients can utilize these findings by targeting co-joined glial and neuronal mechanisms regulating presynaptic vesicle trafficking mechanisms.

# Chapter IV

## Conclusions and Future Directions

Noonan Syndrome (NS) and Noonan Syndrome with multiple lentigines (NSML) are characterized by related cognitive and behavioral symptoms, however, the driving underlying synaptic mechanism was previously unexplored. NS and NSML are known to be primarily caused by gain-of-function (GoF) and loss-of-function (LoF) respectively of protein tyrosine phosphatase non-receptor type 11 (PTPN11).[81] Fragile X syndrome (FXS) is characterized by increased synaptic neurotransmission and neural circuit hyper-connectivity driven by the loss of the mRNA-binding translational repressor Fragile X Mental Retardation Protein (FMRP).[115] FMRP was first proposed to bind *PTPN11* mRNA via an unbiased, cross-linking interaction screen.[107] Based on this finding, we hypothesized that NS/NSML disease states involve PTPN11-dependent synaptic dysfunction. The goal of my dissertation work was to determine if PTPN11 has a synaptic role and, if so, to define the mechanism of action downstream of FMRP regulation. Using a *Drosophila* FXS disease model, I found the *Drosophila PTPN11* homolog (*corkscrew*; *csw*) mRNA is bound by FMRP, with protein levels elevated in the absence of FMRP. Using *Drosophila* NS/NSML disease models, I established neurotransmission increased, as in the FXS model, with a similar elevation in trans-heterozygous mutant combinations. I found that FMRP regulates PTPN11 to modulate local mitogen-activated protein kinase (MAPK)/extracellular signal-regulated kinase (ERK) signaling in presynaptic terminals. I discovered that PTPN11/Csw acts via MAPK/ERK signaling to regulate synaptic vesicle (SV) availability for neurotransmission. I found disease mutation defects can be corrected by genetically or pharmaceutically reducing ERK function. I determined that the Synapsin (Syn) phospho-tether regulating SV availability acts downstream of PTPN11/Csw and ERK, with Syn loss blocking the elevated neurotransmission of PTPN11 and ERK mutants. Finally, I discovered PTPN11 is required in both neurons and glia for regulating synaptic function. Below, I expand on my published findings and offer directions for future investigations.

## PTPN11/Csw regulates basal glutamatergic neurotransmission

My thesis work shows PTPN11/Csw is a negative regulator of neurotransmission in the *Drosophila* neuromuscular junction (NMJ) model glutamatergic synapse system, suggesting a similar PTPN11 function in mammalian brain glutamatergic synapses. To confirm the conservation of mechanisms uncovered in this thesis, this work could be repeated in NS and NSML mammalian models such as the mouse model hippocampal neurons[64,90] or glutamatergic human induced pluripotent stem cell (hiPSC).[194,195] In this section of the discussion, I focus on synthesizing previous results (Chapter II and III) directly demonstrating neurotransmission changes are PTPN11/Csw-dependent and highlighting future directions to strengthen current conclusions.

In this thesis I found that either removing Csw ($csw^5$ null mutant) or overexpressing a NS model GoF mutation ($csw^{A72S}$) elevates neurotransmission. In contrast, overexpressing wildtype csw ($csw^{WT}$) does not affect neurotransmission. This elevated neurotransmission held true when expressing other NS mutations, ($PTPN11^{N308D}$) as well as NSML mutations ($PTPN11^{Q510E\ or\ Q510P}$; Fig. 2.1). Again, overexpressing wildtype *PTPN11* does not affect neurotransmission (Fig. 2.4). To further test specificity, I also expressed $csw^{WT}$ in the *csw* null background and found this rescues the Csw-dependent neurotransmission changes (Fig. 2.4). Based on this work, it appears that PTPN11 phosphatase GoF and LoF both elevate neurotransmission and proper phosphatase activity is necessary for proper neurotransmission responses. To further confirm the phosphatase dependence of these phenotypes, future work could be done with $csw^{R465M}$, a phosphatase-dead mutation.[52] Previous studies with this mutant have shown that long-term memory paradigms are phosphatase-dependent.[52] When expressed alongside a LoF (NSML) mutation, $csw^{R465M}$ eliminated phosphatase activity and blocked associated phenotypes.[94] When $csw^{R465M}$ is expressed alone, aberrant ERK activation and associated phenotypes have not been reported, with the mutant line indistinguishable from controls.[94] Based on these findings, I hypothesize that $csw^{R465M}$ when expressed alongside any of the GoF or LoF mutations within this thesis would block the aberrant increase in synaptic transmission at the NMJ, indicating disease neurotransmission changes seen are specifically phosphatase-dependent.

Upon establishing that PTPN11/Csw elevated neurotransmission, the next step in starting to determine a mechanism was to establish where in the synapse PTPN11/Csw is required. To do this, in this thesis, I exploited the UAS/Gal4 binary transgenic system to knockdown expression either presynaptically (motor neuron) or postsynaptically (muscle)[7]. Muscle knockdown did not cause any changes, but neuronal knockdown elevated neurotransmission, just like ubiquitous knockdown (Fig. 2.5). To further test whether PTPN11 acts solely through a neuronal pathway, I additionally expressed NSML mutations exclusively in neurons to elevate neurotransmission (Fig. 2.8). With these findings, I then analyzed spontaneous SV fusion events in all the above conditions to find that all with elevated neurotransmission show an increase in spontaneous fusion frequency with no change in response amplitude (Fig. 2.5; 2.6). This indicates that there is a change exclusively on the presynaptic side, elevating the probability of SV fusion. Quantal content analyses of the above conditions likewise indicate more vesicles released (Fig. 2.7). In agreement, docked SVs visualized with transmission electron microscopy are increased (Fig. 3.2). All the above results indicate PTPN11/Csw neuronal specificity in elevating neurotransmission. This was expected, as *PTPN11*$^{N308D}$ targeted to motor neurons is sufficient to elevate neurotransmission (Fig. 2.1). Expressed ubiquitously, *PTPN11*$^{N308D}$ causes embryonic lethality. Null *csw* mutants and ubiquitously expressed *csw* RNAi likewise causes lethality, but not neuronal or muscle knockdown.

In mammalian systems, total loss of *PTPN11* similarly causes embryonic lethality.[196] The *Drosophila csw* null survives only due to maternally-deposited mRNA allowing animals to pass embryonic development. Without this, the embryo dies and looks like a corkscrew, giving the gene gets its name.[83,89] Given this situation, we can study the complete *Drosophila* knockout with relative ease in comparison to other model organisms, making it a great model for understanding the role of Csw at the synapse. One future direction that would greatly benefit from exploiting the late *Drosophila* lethality involves further investigating a unique liquid-liquid phase separation (LLPS) mechanism newly uncovered.[74] A recent study demonstrated a LLPS dependent mechanism with *PTPN11* disease mutations, with mutant protein recruiting and activating wildtype protein to drive

MAPK activation.[74] My work with the complete *Drosophila csw* null mutant precludes this from being the only way Csw acts to regulate MAPK signaling, raising the question of whether this is the same mechanism. Due to NS and NSML being autosomal dominant, all my work was done expressing these mutations in a wildtype background that had wildtype csw already present. There is the possibility that these mutant forms of PTPN11/Csw need the wildtype protein present to elevate neurotransmission. This seems unlikely, due to the *csw* null phenocopying all mutant neurotransmission phenotypes but is worth investigating to help further understand what exactly is occurring. This can be tested by driving these same mutations in a *csw* null mutant background. These future experiments will determine if wildtype Csw protein is necessary for disease phenotypes in the *Drosophila* model. If not, then the mechanism is either not shared between species, or more likely, the mechanism of PTPN11 action is not yet fully appreciated.

### MAPK/ERK signaling drives basal glutamatergic neurotransmission

Based on previous work showing NS and NSML consistently act via MAPK/ERK signaling hyper-activation, we hypothesized that all of our mutants also acted through this signaling mechanism.[52,74,82] The MAPK/ERK signaling pathway is highly conserved, and has many known roles, however a neuron-specific role is regulating SV pools[145]. The MAPK/ERK pathway is one of the signaling pathways known to have its endpoint phosphorylating Synapsin leading to SV tether disassociation and SV recruitment for exocytosis.[62,73,145] In this section of the discussion, I focus on synthesizing previous results (Chapter II and III) directly demonstrating basal neurotransmission changes are MAPK/ERK dependent and highlighting future directions to strengthen current conclusions.

The specific MAPK/ERK signaling role in PTPN11 driven neurotransmission is supported by an elevation in local pERK levels within the presynaptic boutons for all NS and NSML *PTPN11* point mutations with elevated neurotransmission (Fig. 2.13). To test this directly, *csw* null and NS model animals ($PTPN11^{N308D}$) were treated with Trametinib, a drug that inhibits the MAPK/ERK signaling pathway via inhibition of mitogen-activated protein kinase kinase (MEK), responsible for phosphorylating ERK at the endpoint of the pathway.[197,91] Likewise, Vorinostat inhibits kinase phosphorylation to disrupt MAPK signaling,[91,141,198] with positive outcomes for treating behavior and memory in the FXS mouse model.[121] Consistently, *Drosophila* NMJ neurotransmission defects are reversed when treated with either drug, indicating disease MAPK/ERK signaling dependence (Fig 2.12; 2.15). These drugs are already FDA approved and used to treat different diseases with elevated MAPK signaling[121,197,198] making them especially appealing as drugs to help alleviate cognitive symptoms seen in patients. Future work should be done in testing if these drugs are capable of alleviating behavioral and learning phenotypes in NS and NSML models. Previously, NS *Drosophila* disease models have had learning and memory mechanisms tested via repeated training sessions spaced over time.[52] It was determined that GoF *csw* mutations aberrantly prolong the resting interval by altering the MAPK signaling timing, leading to improper learning and memory function.[52] An ideal way to determine if Trametinib and Vorinostat can alleviate cognitive symptoms seen in *Drosophila* would be by utilizing this previously established experimental methodology. In addition, in the mammalian mouse system this same learning and memory pathway can be tested with and without drug treatments via the Morris water maze test.[90] If these drugs consistently alleviate disease model cognitive dysfunction, then patients may positively benefit from treatment with one or both of these drugs.

To further test MAPK/ERK mechanism specificity, I genetically manipulated ERK by using the UAS/Gal4 system to express activated ERK ($ERK^{SEM}$) exclusively in neurons. $ERK^{SEM}$ still needs to be phosphorylated by the MAPK pathway, but resists inactivation once turned on,[199] making it ideal to investigate what activated ERK alone will do at the NMJ. Neuronal $ERK^{SEM}$ recapitulates the elevated local pERK levels, neurotransmission, mEJC frequency, and quantal content seen in *PTPN11* mutants, further indicating that PTPN11 acts via pERK (Fig. 3.4). $ERK^{SEM}$ has been shown to lead to changes at the *Drosophila* NMJ, but no previous work directly measures its effects on synaptic function.[169] Moreover, genetically decreasing ERK by 50% using a heterozygote null mutant ($ERK^{1}$/+) in the *csw* null background blocks the elevated mEJC frequency, quantal content, and neurotransmission strength of the mutant (Fig. 3.5; 3.6). These results alongside above pharmacological rescue strongly indicate that PTPN11 dependent neurotransmission is dependent on MAPK/ERK activation. Since the MAPK pathway endpoint, pERK, is known to phosphorylate Synapsin[73,145] and we observe increased docked SVs in our *csw* null mutants (Fig. 3.2), we also tested whether a *synapsin* null mutant (*syn*$^{97}$)[200,201] could block elevated neurotransmission of a NSML patient-derived *PTPN11* mutant or *ERK*$^{SEM}$. The null *syn*$^{97}$ mutant blocks elevated neurotransmission in both conditions (Fig. 3.5; 3.6). This is surprising due to *synapsin* nulls not being previously reported to affect basal neurotransmission strength.[64] Based on these results, I currently hypothesize that PTPN11 driven MAPK/ERK signaling leads to elevated basal pERK levels causing Syn to disassociate from SVs, allowing for more vesicular recruitment to presynaptic active zones. To test this hypothesis, synaptic transmission electron microscopy in *PTPN11/csw* mutants should be used in both in the *syn* null and syn wildtype background to investigate the number of docked SVs. Additionally, Syn labeled with immunogold TEM at rest and during stimulation in both mutant conditions would allow for better visualization of Syn-SV association.[68]

To test whether basal functional changes are caused exclusively by changes in Syn-dependent SV dynamics and not NMJ connectivity changes, we analyzed NMJ structure. In the *csw* null (csw$^{5}$) and GoF (*csw*$^{A72S}$) there are no changes in NMJ area, branching, or type 1b synaptic bouton number (Fig. 2.2). This was a bit unexpected, as the FXS *Drosophila* model, which display similar elevated neurotransmission defects, has clear structural overelaboration at the NMJ.[115] Although not shown, there is also no change in the smaller synaptic bouton classes. This confirms that elevated function is not due to synaptic overelaboration. Another possibility is an increase in active zone (AZ) synapse number as assayed by anti-Bruchpilot (BRP) labeling.[21,23] In these same mutants, there is no change in the BRP synapse marker nor in transmission electron microscopy counts of electron-dense AZs (Fig. 2.3; 3.2). This agrees with ultrastructural results in an elevated MAPK/ERK mouse model[127]. Under most conditions, the AZ is apposed with postsynaptic glutamate receptors, making a functional synaptic unit. On the postsynaptic side, glutamate receptor density can be assayed with anti-GluRIIC labeling.[21,23] In null and GoF mutants, no changes are found in glutamate receptor density

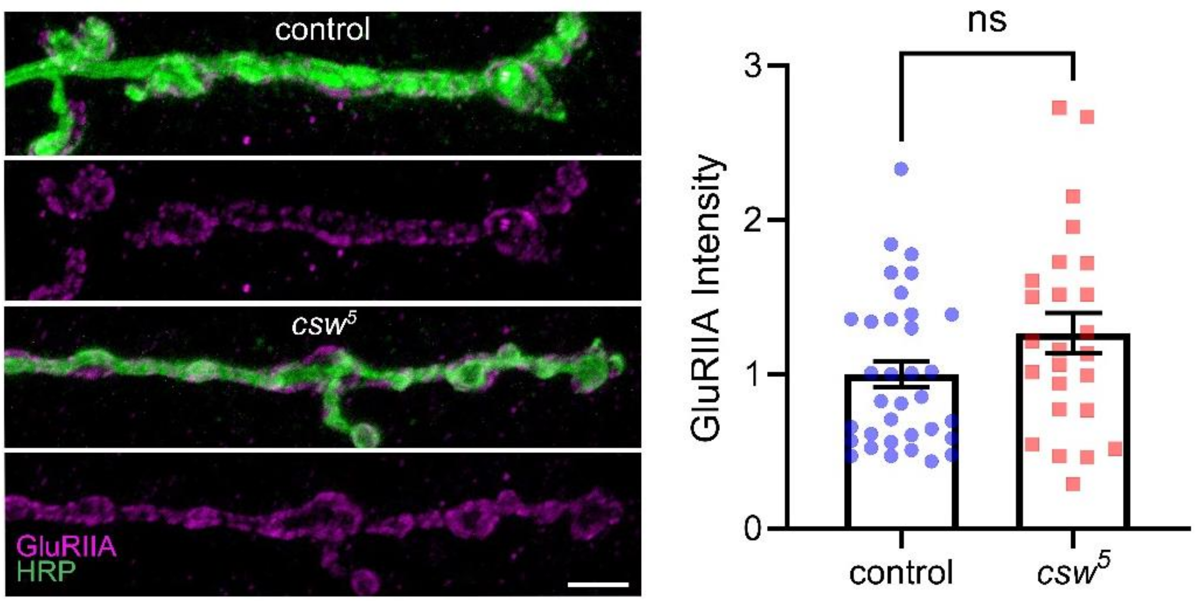

**Figure 4.1: Csw loss does not affect GluRIIA levels at the *Drosophila* NMJ**
Representative wandering third instar NMJ synaptic boutons labeled with anti-glutamate receptor subunit IIA (GluRIIA, magenta) and anti-horseradish peroxidase (HRP, green) in $w^{1118}$ genetic background control and $csw^5$ null mutant. Quantification of mean GluRIIA fluorescent intensity using a two-sided *t* test. Scatter plots show all the data points with mean±SEM. Data points: NMJ number. Significance: $p>0.05$ not significant (n.s.). Scale bar: 5 um.

nor BRP/GluRIIC ratio, indicating there is no change in overall synapse number (Fig. 2.3). One remaining structural change yet unexplored is the possibility that the GluRIIA/GluRIIB ratio has shifted, which can greatly alter neurotransmission strength.[202,203] Although none of this thesis work supports a change on the postsynaptic side, there is some literature evidence supporting this. A study of transfected cultured hippocampal neurons with $PTPN11^{\mathrm{D61G}}$ reported an increase in surface-labeled GluA1 AMPA receptors with no change in overall receptor number.[90] So, it is possible that part of the *PTPN11* increased neurotransmission is due to a disruption in the glutamate subtype ratio favoring GluRIIA. A preliminary experiment testing anti-GluRIIA fluorescent intensity in *csw* nulls does not show an over change in GluRIIA-containing receptors (Fig 4.1). A caveat to this experiment is that it is measuring fluorescent intensity, not density as previously analyzed. Moreover, the data do appear to be trending towards an increase, so future work should continue to test the range of *PTPN11/csw* mutants. For now these results indicate that there are no gross structural changes driving functional changes, indicating that MAPK/ERK dependent SV dynamics are exclusively driving neurotransmission defects in NS and NSML mutants.

### Heterogeneity of NS/NSML diseases reflected by variable MAPK/ERK activation

NS and NSML conditions show strong heterogeneous manifestation of symptoms[80,81,93,96] that I hypothesize is due mainly to the variable elevation of the MAPK/ERK signaling pathway. There has been work on genotype-phenotype correlations explaining this disease variability, although this focuses on the different genes that can lead to each disease. For cognitive deficits, 30-50% of patients have reported symptoms, and recent work highlights *PTPN11* mutations as being highly represented in this population of patients.[3,4] However, despite this, many patients with *PTPN11* mutations do not exhibit any notable cognitive deficits,[3] indicating that variability is not driven exclusively by the different gene mutations. In contrast, mouse and *Drosophila* NS disease models exhibit high penetrance learning and memory deficits.[52,90] This may be due to differences in mutation strength or genetic backgrounds. A major future direction of this work could be exploring the heterogeneity of disease states, connecting the behavioral and synaptic levels. Numerous patient-derived *PTPN11* mutations have been used throughout this dissertation research, but a larger scope is available.[91] In the future, these other *PTPN11* mutations can be analyzed for synaptic function and local NMJ pERK levels as has been done in this thesis. Then all *PTPN11* mutant larvae can have their learning and memory tested via the established three-cycle, two-odor reciprocal aversive odor–high-salt learning assay[204] and analyzed against each other to test for patterns. One of the more notable point mutant lines not yet analyzed is $PTPN11^{D61G}$, which leads to learning and memory deficits and enhanced excitatory neurotransmission in a heterozygous mouse model.[90] However, a possible quandary with this data is that, NS patients and the mouse models with this mutation develop juvenile myelomonocytic leukemia (JMML), a cancer with features characteristic of both myelodysplastic and myeloproliferative disorders.[205,206] A unique use of this patient derived mutation would be to study JMML in the *Drosophila* with all the advantages of the model available. Additional

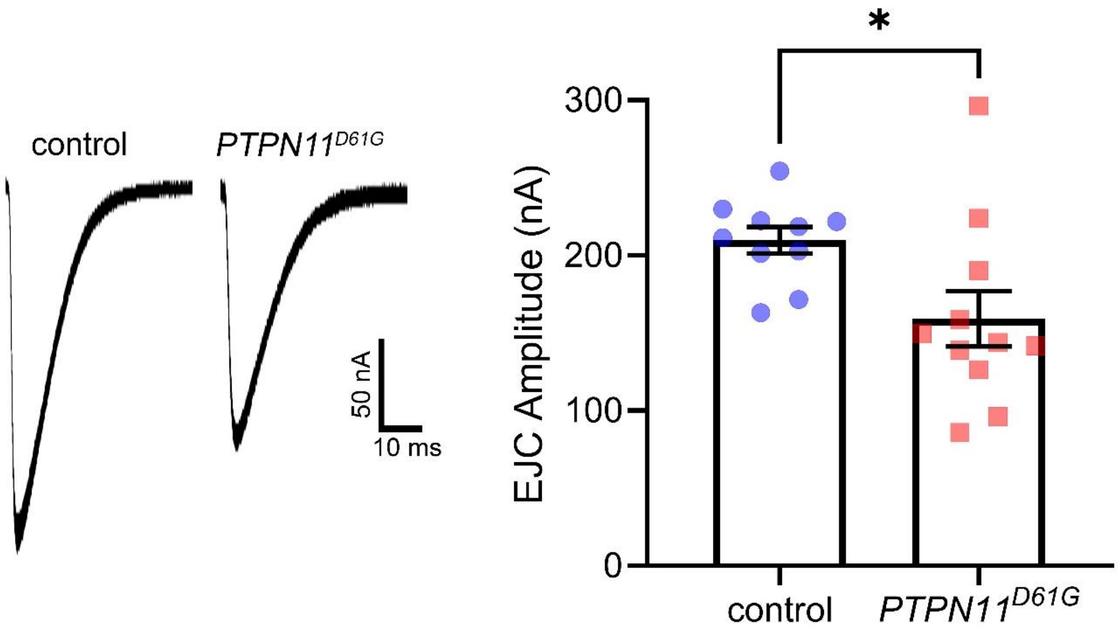

**Figure 4.2: Ubiquitous NS/JMML *PTPN11*$^{D61G}$ mutation decreases neurotransmission** Representative two-electrode voltage-clamp (TEVC) recordings of excitatory junction current (EJC) traces showing 10 superimposed evoked synaptic responses (1.0 mM $Ca^{2+}$) of ubiquitous driver control (*UH1*-Gal4/*w*$^{1118}$) and NS/JMML *PTPN11*$^{D61G}$ (*UH1*-Gal4>*PTPN11*$^{D61G}$). Quantification of the mean EJC amplitudes using two-sided *t* tests. Scatter plots show all data points with mean±SEM. Data points: NMJ number. Significance: $p<0.05$ (*).

*PTPN11* mutations of interest include NSML *PTPN11*$^{R498W}$ and *PTPN11*$^{Y279C}$ which analysis of together with *PTPN11*$^{D61G}$ at the synaptic and behavioral levels would strengthen studies of heterogeneity of disease outcomes.

In interest of studying this disease heterogeneity, I started preliminary work into the synaptic underpinnings of these various *PTPN11* mutations not yet reflected in this thesis. Current genotypes seen in Chapters II and III are all largely indistinguishable, making them unideal for studying disease heterogeneity alone. My preliminary examination of *PTPN11*$^{D61G}$ showed decreased neurotransmission strength, in disagreement with the mouse model[90] (Fig. 4.2). This may be due to the mouse model being a heterozygote, versus *PTPN11*$^{D61G}$ overexpression in our *Drosophila* model. Gene dosage–dependent effects have been reported.[207] Future work should characterize this point mutant for other synaptic and myeloproliferative phenotypes. It is possible that targeted neuronal expression would resemble other *PTPN11* mutations, and what is being observed is general malaise due to JMML complications. Another important case is the *PTPN11*$^{R498W}$ point mutant, a LoF NSML disease mutation.[91] Ubiquitous expression of *PTPN11*$^{R498W}$ does not elevate local pERK levels or neurotransmission strength (Fig. 4.3). Although pERK levels are trending towards elevation, it is not statistically significant like other *PTPN11* mutations with elevated neurotransmission (Fig. 4.3). Based on this correlation, it appears that this point mutant does not elevate pERK levels high enough to influence basal neurotransmission. These differences in pERK levels and synaptic expression, if correlated with variable outcome in learning in memory tests, would support the model that what matters most for cognitive disease heterogeneity within the same mutated gene is the strength of MAPK/ERK pathway activation. Additionally, these future assays could also be done with other NS and NSML causing genes beyond PTPN11 to further analyze how much these various genes converge mechanistically at the synaptic level.

### PTPN11/Csw regulates functional short-term plasticity at glutamatergic synapses

In response to experience, neural circuit function can be modified via a process known as synaptic plasticity.[49,208] In this mechanism, pre-existing synapses can be modified in neurotransmission strength for various durations, varying from sub-second to seemingly permanently.[208] It is established that ERK signaling plays a role in the regulation of activity-dependent synaptic functional changes,[69,78,151] and has a role in various behaviors dependent on this process, including learning and memory.[24,66,78] My thesis work establishes a role for PTPN11/Csw in various forms of short-term plasticity at the *Drosophila* NMJ, closely but not perfectly, mirroring what is seen in a mouse model with elevated ERK signaling.[127] There are two general opposing forms of short-term plasticity; facilitation and depression. Synapses tend to exhibit one or the other depending on the recent history of activation, as well as the probability of neurotransmitter release. Synapses with a higher likelihood of neurotransmitter release tend to exhibit depression, while those with lower probabilities exhibit facilitation.[42,47,137,208] The *Drosophila* NMJ tends to exhibit depression under physiological conditions,[41,209] but can be manipulated

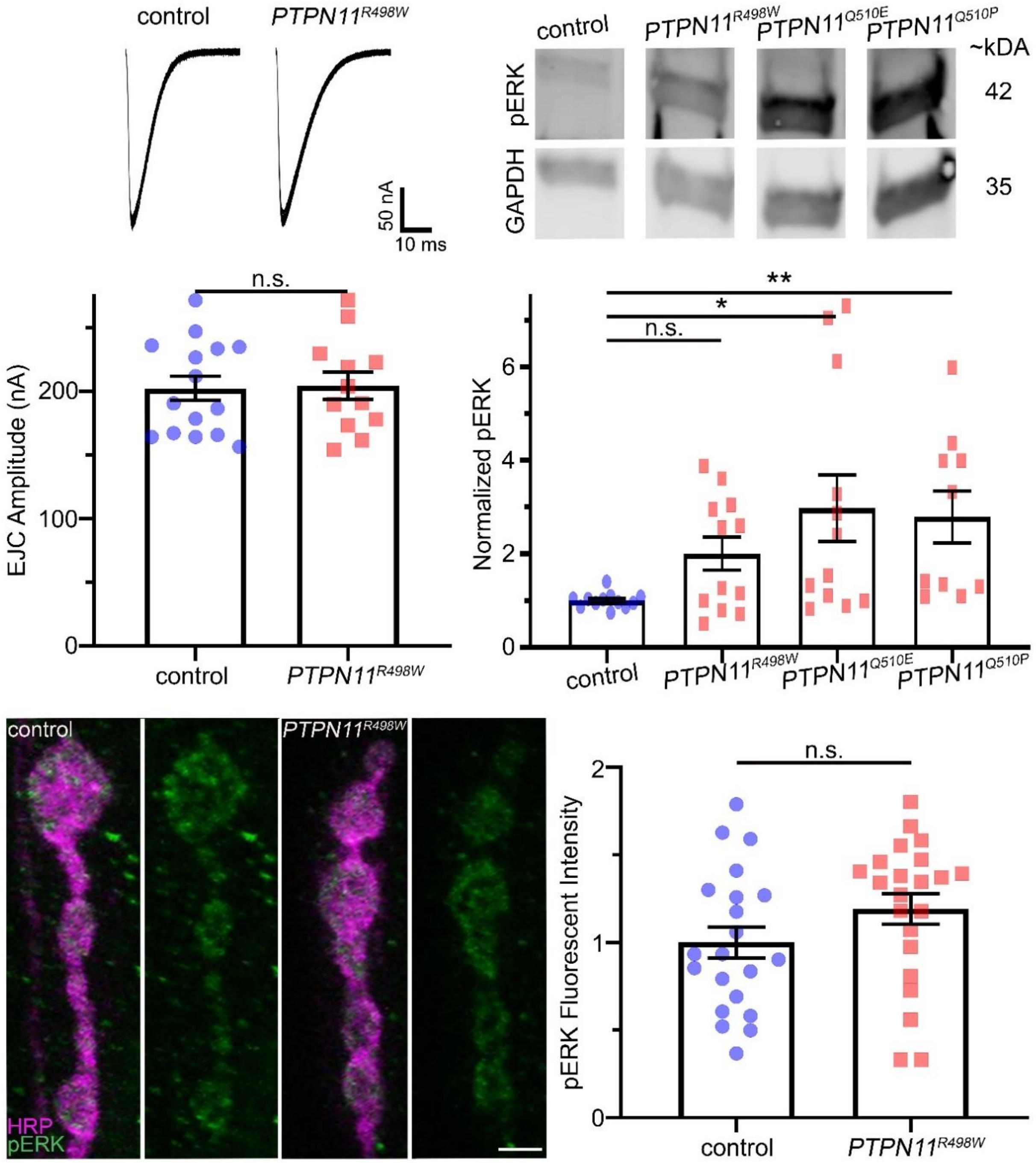

**Figure 4.3: NSML *PTPN11*$^{R498W}$ mutant does not exhibit any neuronal phenotypes**
Analysis of ubiquitous driver control (*UH1*-Gal4/*w*$^{1118}$) and NSML *PTPN11*$^{R498W}$ (*UH1*-Gal4>*PTPN11*$^{R498W}$). Top Left: Representative TEVC recordings of EJC traces (1.0 mM $Ca^{2+}$). Quantification of the mean EJC amplitudes using a two-sided *t* test. Top Right: Representative Western blot for pERK (42 kDA, top) and GAPDH loading control (35 kDA, bottom). Quantification of pERK levels normalized to GAPDH with a one-way ANOVA followed by Tukey's multiple comparisons. Bottom: Representative NMJ images co-labeled for anti-pERK (green) and presynaptic membrane marker anti-HRP (magenta). Scale bar: 2.5 µm. Scatter plots show all the data points with mean±SEM. Data points: NMJ (EJC, ICC) or animal (WB) Significance: $p<0.05$ (*), $p<0.01$ (**), and not significant (n.s.).

to exhibit facilitation,[41,209] allowing for the genetic modeling of both forms to explore mechanisms.

Under conditions of depression at the NMJ, *csw* nulls and NS *PTPN11* mutants display sustained elevated neurotransmission compared to controls (Fig. 2.9). From the initial stimulations the readily releasable pool (RRP) can be estimated, which is elevated compared to controls in both, without a change in paired pulse ratio (Fig. 2.9). This finding indicates more SVs available for fusion, but that the probability of release is unchanged in these mutants. This functional test aligns with transmission electron microscopy showing an elevation in docked SVs in these mutants (Fig 3.2). With sustained high frequency stimulation (HFS), *csw* null mutants continue to respond when controls have exhausted all available SVs (Fig. 2.10). I hypothesized these changes were driven by enhanced ERK signaling, similar to basal neurotransmission changes. ERK is phosphorylated during HFS, and ERK then phosphorylates Synapsin, enhancing neurotransmitter release during sustained stimulation.[68,145] In *csw* nulls, local NMJ pERK levels are already elevated at the basal state, and depolarizing stimulation elevates pERK further (Fig. 2.14). In *PTPN11/csw* mutants, Synapsin is aberrantly decreased and dissociates from SVs with stimulation (Fig. 3.1; 3.3). This work together supports the previously proposed model of ERK-dependent Syn phosphorylation enhancing neurotransmitter release when the RRP is significantly depleted by high usage.[62,65,68] In our mutants this process is dependent on PTPN11. However, this conclusion should be further tested by repeating genetic and pharmaceutical experiments during basal neurotransmission. If the current model is correct, inhibiting the MAPK/ERK pathway would block the resistance to synaptic depression, and changes in Syn with stimulation. Additionally, the ERK GoF mutant that recapitulates basal synaptic neurotransmission should also display sustained resistance to synaptic depression, and Syn changes with stimulation. A pilot experiment with this mutation indeed shows that ERK GoF alone can increase basal Syn levels that decrease with HFS stimulation, similar to *PTPN11/csw* mutants (Fig 4.4). More work investigating Syn dynamics would increase our understanding of this mechanism overall. This can be done with genetic *syn* manipulations, as well as more imaging focused on studying Syn turnover.[61,65,67,201] Transmission electron microscopy with immunogold labeling of Syn with and without

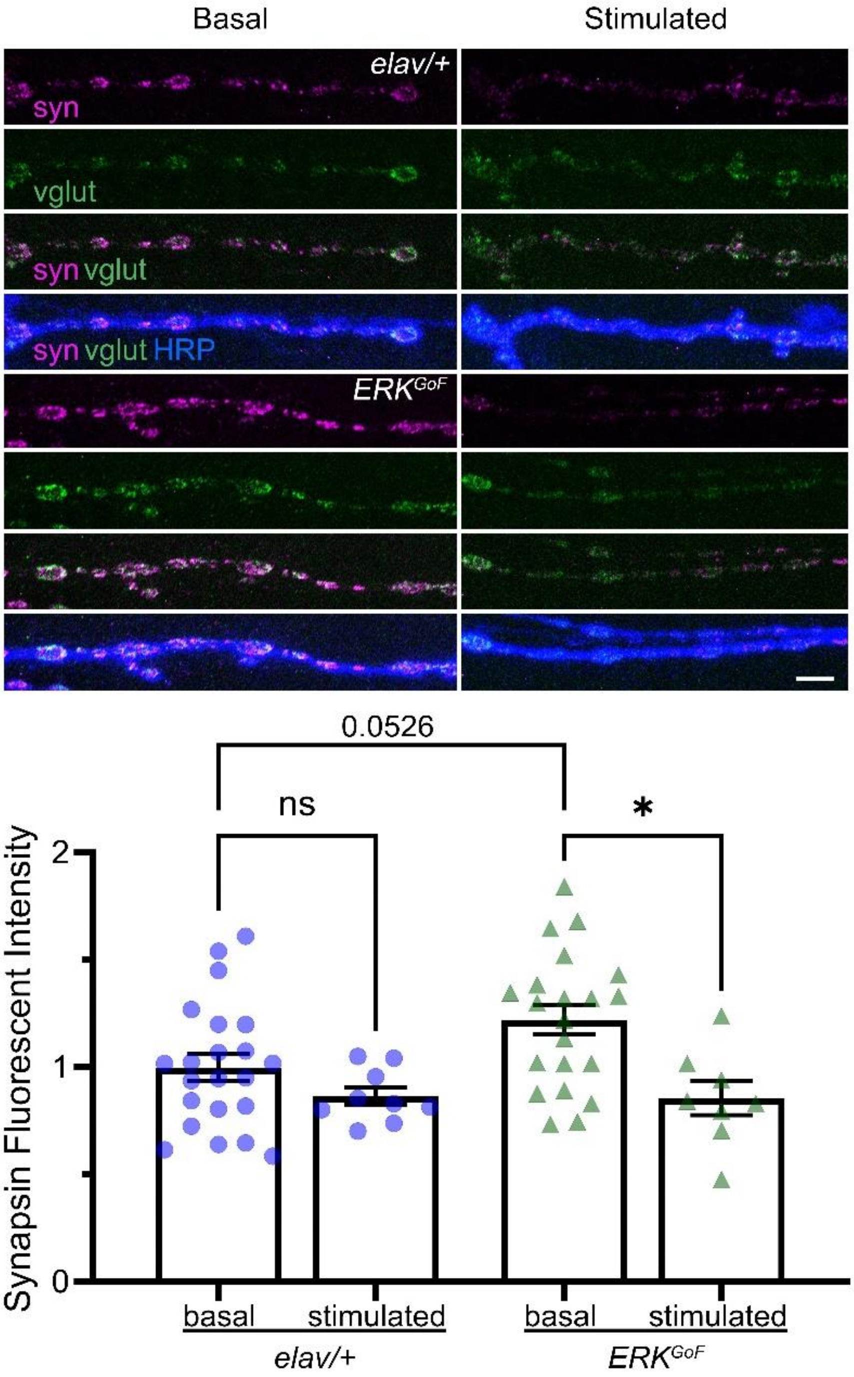

**Figure 4.4: Neuronal ERK$^{GoF}$ recapitulates PTPN11 basal and stimulation syn defects** Representative NMJ synaptic boutons labeled for Synapsin (syn, magenta), vesicular glutamate transporter (vglut, green) and horseradish peroxidase (HRP, blue) in neuronal transgenic driver control (*elav*-Gal4/*w$^{1118}$*) and driving *ERK$^{GoF}$* (*elav*-Gal4>*ERK$^{GoF}$*) NMJs without stimulation (basal, left) and 10 min 90 mM [K$^+$] (stimulated, right). Scale bar: 5 µm. Quantification of Synapsin fluorescence intensity in all four conditions (basal and stimulated). Statistical comparison done using a two-way ANOVA, followed by Tukey's multiple comparisons test. Scatter plots show all data points with mean±SEM. Data points: NMJ number. Significance: $p<0.05$ (*), and not significant (n.s.).

stimulation would allow for better analysis of SV association.[68] This would allow, in turn, a better understanding of SV dispersion dependent on Syn turnover. Furthermore, imaging with a phospho-Syn specific antibody[210] would allow for better analysis of activity-dependent phosphorylation/dephosphorylation.

While studying SV dynamics in *PTPN1/csw* mutants in HFS conditions of synaptic depression, I focused on RRP and reserve pools, both of which were implicated by the literature of being involved via aberrant MAPK/ERK signaling.[62,63,151] However, the RRP is replenished from the SV recycling pool which can maintain release with moderate stimulation,[54] and changes in recycling could easily be contributing to our sustained synaptic function defects. Previous studies have shown depolarizing stimulation and 10 Hz HFS both lead exclusively to recycling pool recruitment, while >30 Hz stimulation additionally recruits the reserve pool.[54,61] Interestingly, in our stimulation conditions the reserve pool should not be recruited, yet based on Syn data it is being aberrantly recruited.[60,166] To focus more directly on the recycling pool, future experiments should utilize FM1-43 dye imaging. FM dyes insert into the plasma membrane with a >40-fold increase in fluorescence.[148] With stimulation, this dye is internalized during SV endocytosis, then trafficked to different SV pools. Upon washing off excess non-specific plasma membrane dye, one can analyze endocytosis and SV pool size. A second round of stimulation allows for visualization of exocytosis efficiency.[148] A preliminary experiment shows no detectable change in SV endocytosis or exocytosis in *csw* nulls or GoF mutants (Fig 4.5). This finding suggests recycling dynamics are unaffected in NS/NSML states, and that changes in synaptic function are based exclusively on changes in the RRP and reserve pool. However, further work with *PTPN11* mutants should test this conclusion, including varying the stimulation strength (5, 10, 20, 30 Hz) and timing of FM-dye loading (30 sec, 1 min, 5 min) and unloading (10 sec, 30 sec, 2 min) of *csw* null, and NS/NSML PTPN11 mutants to get a holistic view of recycling in disease mutations.

The other forms of short-term plasticity all involve strengthening future neurotransmission responses over different time scales, including short-term facilitation (<1 second), and maintained augmentation (>5 seconds) during stimulation trains, and post-tetanic potentiation following the train.[43,47,49] *PTPN11/csw* mutants display

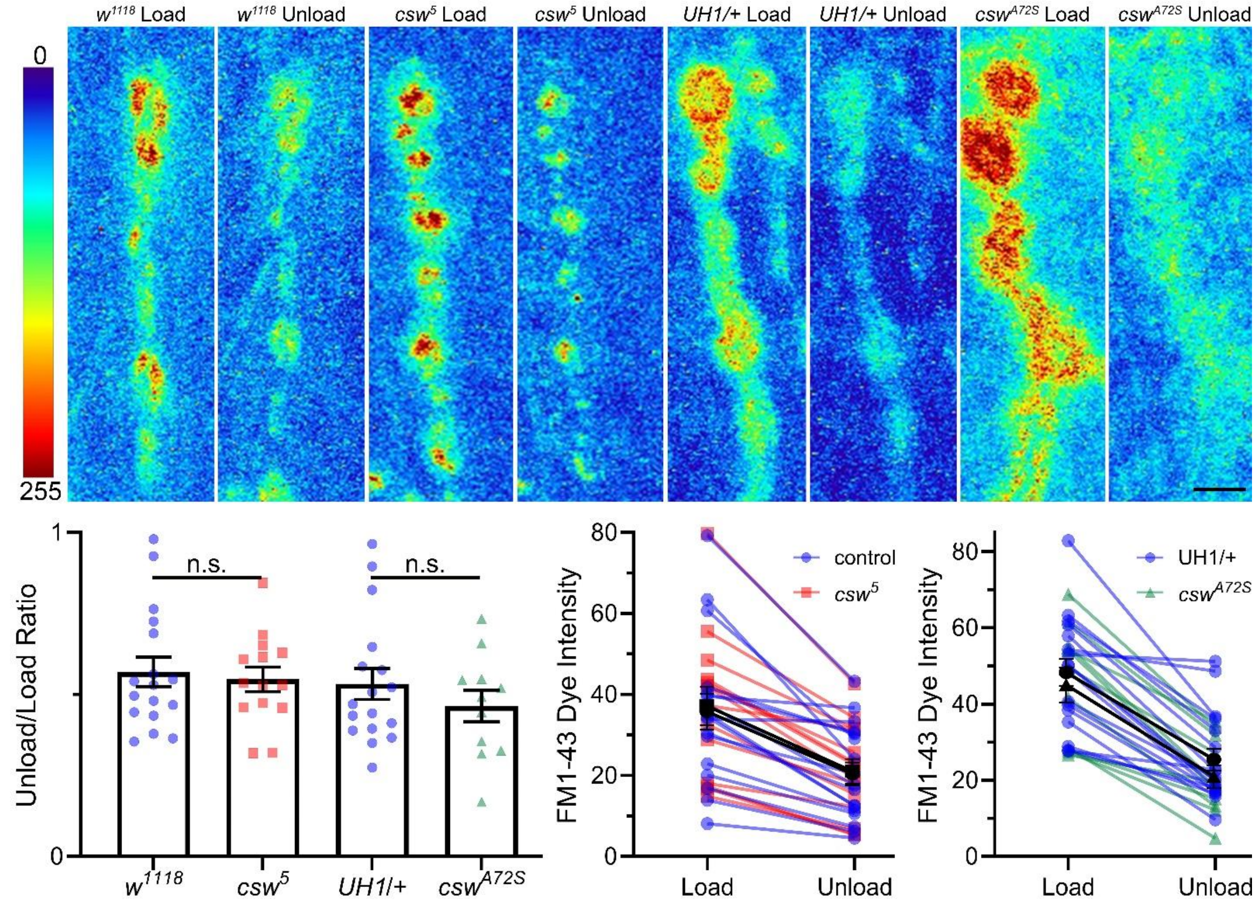

**Figure 4.5 Csw loss- and gain-of-function do not alter synaptic vesicle trafficking**
Top: Representative synaptic bouton images of FM 1-43 dye imaging with depolarization induced loading (left for each genotype) and unloading (right for each genotype). Genotypes from left to right: *w*$^{1118}$, *csw*$^{5}$, *UH1*/+ (*UH1*-Gal4/*w*$^{1118}$) and *csw*$^{A72S}$ (*UH1*-Gal4>*csw*$^{A72S}$). Fluorescent intensity is represented as a heat map. Scale bar: 5 um. Bottom Left: Quantification of unload/load ratio using two-sided *t* tests. Bottom Right: Each NMJ with connected load and unload FM 1-43 dye intensities. Overall mean values are shown in black with corresponding genotype shape. Scatter plots show all the data points with mean±SEM. Data points: NMJ Significance: not significant (n.s.).

decreased facilitation, augmentation, and post-tetanic potentiation compared to controls under conditions that allow for facilitation (Fig. 2.11). There has been no previous work to implicate Csw or PTPN11 having a role in this form of short-term plasticity. This result is somewhat surprising, as presynaptic plasticity is enhanced in a mouse model with elevated ERK signaling.[127] I hypothesize these plasticity effects may be due to the already elevated basal pERK decreasing the range for ERK-dependent enhancement, leading to a ceiling effect. Genetic and pharmaceutical experiments blocking ERK activation should test this hypothesis. Additionally, the ERK GoF mutant that recapitulates basal synaptic neurotransmission should also display decreased facilitation, augmentation, and post-tetanic potentiation if PTPN11/csw driven elevated ERK signaling is solely responsible. Notably, however, a mouse model with enhanced ERK signaling does not exhibit any changes in basal neurotransmission,[127] indicating that there may be some part of this mechanism that is not being explained by PTPN11/Csw regulation of the ERK pathway. One possibility is FMRP involvement, as the FXS mouse model is similarly resistant to short-term depression due to an elevated RRP without a change in fusion probability, although it does display enhanced augmentation.[118] Analysis of these various forms of short-term plasticity in a NS/NSML background with overexpression or knockdown of FMRP would elucidate if FMRP drives this process.

## PTPN11/Csw and FMRP interact to regulate neurotransmission strength

Previously, a large-scale screen identified *PTPN11* mRNA binding with FMRP.[107] Given the canonical function of FMRP as a translational repressor,[104,106,112] the interaction suggests PTPN11 protein expression is downregulated by FMRP. To test this interaction in the *Drosophila* model, we performed an RNA-immunoprecipitation assay to find that anti-FMRP pulls down *csw* mRNA (Fig. 2.14). Additionally, Western blot analysis revealed that Csw protein expression is upregulated in the FXS disease model (*dfmr1* null mutants; Fig. 2.14). This indicates that under normal conditions, FMRP works to downregulate Csw expression, and that this expression becomes unregulated in the FXS condition. Unfortunately, due to current tool limitations, immunohistochemistry work testing Csw synaptic localization in controls and *dfmr1* nulls has not been possible. In future experiments, a better Csw antibody or a GFP-tagged Csw construct should be made to test Csw localization and changes in the FXS disease model. I next turned to analyzing MAPK/ERK activation, as it has been clearly established that PTPN11/Csw regulates this pathway.[82,90,96] Likewise, FXS patients and disease models show elevated MAPK/ERK signaling,[76,121] suggesting that PTPN11/Csw may play a role in this mechanism. In both *dfmr1* and *csw* null mutants, I found pERK levels elevated at the NMJ in basal conditions and further elevated with acute stimulation (Fig 2.14). Recognizably *dfmr1* cannot be acting on *csw* in the null condition, as there is no mRNA or protein to regulate. This work simply highlights that both genes are involved in regulating local ERK signaling. Notably, this elevation of pERK at the NMJ in *dfmr1* mutants was an intermediate between controls and *csw* nulls, suggesting that there may still be some available ERK that is not being aberrantly activated in the FXS state. The difference in pERK activation may account for why the FXS mouse model still exhibits augmentation,[118] while Drosophila *PTPN11/csw* mutants do not. Future studies investigating the ratio of ERK to pERK available in these disease conditions using both immunohistochemistry and western blot analysis would prove or disprove this hypothesis. Upon establishing that *dfmr1* and *csw* nulls both exhibit elevated pERK levels in presynaptic boutons, we next wanted to firmly establish their interaction in neurotransmission.

To test an interaction, we expressed *csw* and *dfmr1* nulls as trans-heterozygotes.[154] This means the animals have 50% of each protein, which is enough for normal functions unless the two proteins interact in a shared mechanism.[154] The single heterozygotes show no phenotypes, but in the double heterozygotes show an elevation in local presynaptic pERK levels, spontaneous SV fusion frequency, and neurotransmission amplitude (Fig. 2.16). These findings indicate that FMRP and Csw interact to regulate pERK-dependent presynaptic neurotransmission. However, it does not establish any specifics to this interaction. To clarify this interaction, future work should genetically manipulate FMRP levels and test Csw translation in basal and activity modulated conditions. This can be done by utilizing the same basal and short-term synaptic plasticity assays seen in this thesis but with manipulated FMRP levels in the *csw* null and NS/NSML disease models. This manipulation can be done by utilizing the UAS/Gal4 system and would determine if FMRP is regulating Csw phosphatase function in presynaptic boutons. I hypothesize that FMRP is playing an activity-dependent role in activating PTPN11/Csw phosphatase activity and that this regulation is going awry in FXS models to elevate MAPK/ERK signaling. This could be tested by blocking Csw phosphatase activity in a *dfmr1* background and testing the effects on pERK levels and neurotransmission. Although FMRP appears to regulate PTPN11/Csw in NS/NSML disease models, I suspect the native autoinhibition mechanism is the main driver synaptic phenotypes. This could be tested by manipulating FMRP levels in an NS/NSML background and the effects on pERK levels and neurotransmission.

In this dissertation work, I establish the FMRP and Csw interaction at excitatory glutamatergic synapses, linking FXS to NS/NSML disease states for the first time. However, these diseases are all quite complex in their symptoms. To further investigate what is occurring in these diseases, future work into understanding what is occurring at central synapses, inhibitory synapses, and the interplay between different synapses at the circuit level (excitation/inhibition balance) is necessary. One good circuit for study is the adult *Drosophila* brain mushroom body, the learning and memory center[211]. FMRP roles in this circuit are already well established,[212,213] allowing for ease in comparing changes shared or specific to NS/NSML disease states. Additionally, changes in this circuit can be tested via learning and memory paradigms utilizing olfactory T-maze conditional training.[52,120] Both FXS and NS *Drosophila* models have reported disrupted learning and memory abilities using this behavioral testing,[52,120] so I would hypothesize interaction between these proteins to lead to changes at the circuit level prompting these behavioral changes. These interactions could be easily analyzed by testing *csw* and *dfmr1* null trans-heterozygotes mushroom body circuitry function via a combination of electrophysiology and ERK SPARK imaging[211] and learning and memory performances with the T-maze to see if it is impaired. Understanding these connections is paramount to determining future treatment options.

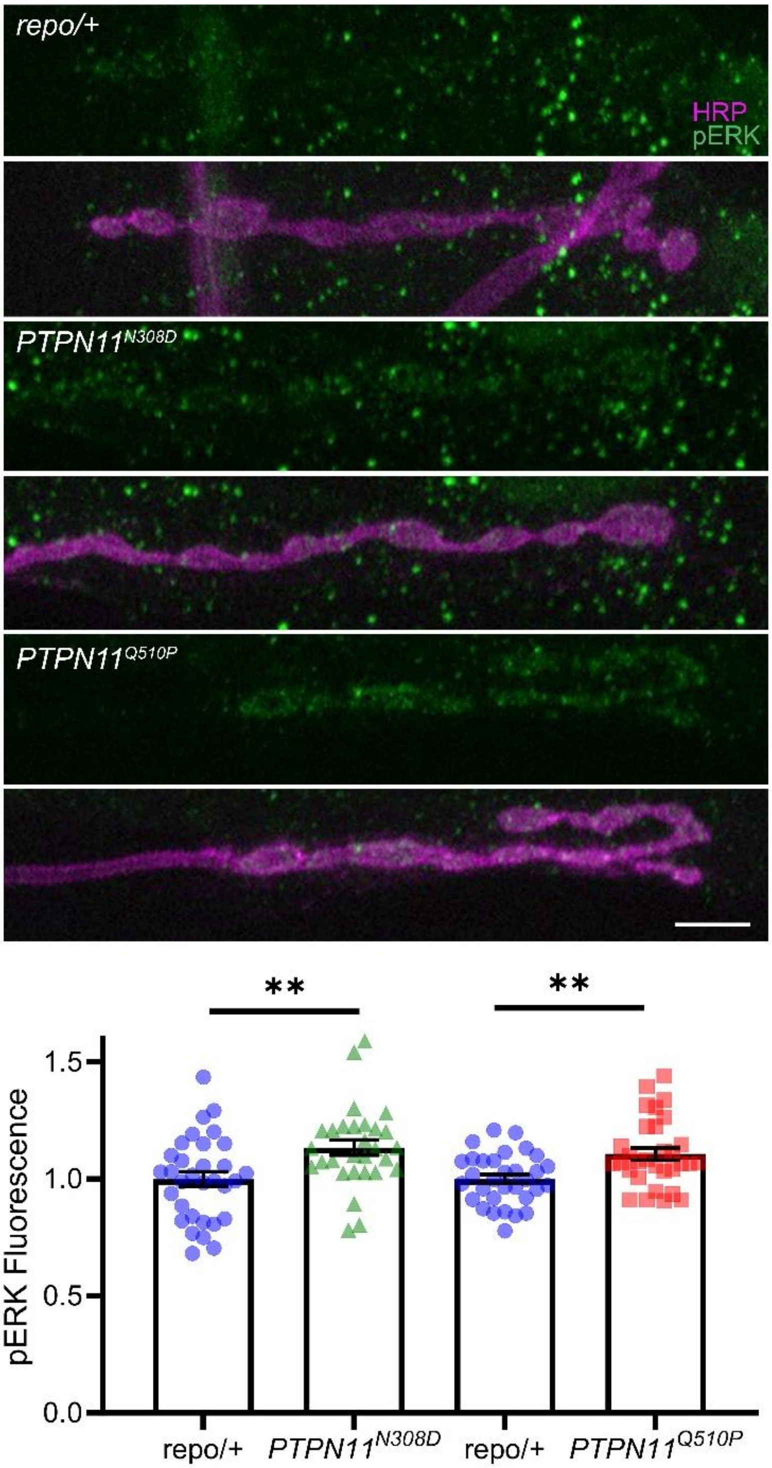

**Figure 4.6: Glial NS/NSML mutants increase local NMJ pERK levels**
Top: Representative NMJ images co-labeled for anti-pERK (green) and presynaptic membrane marker anti-HRP (magenta) of glial transgenic driver control (*repo*-Gal4/*w*$^{1118}$), and driving *PTPN11*$^{N308D}$ (*repo*-Gal4>*PTPN11*$^{N308D}$) and *PTPN11*$^{Q510P}$ (*repo*-Gal4>*PTPN11*$^{Q510P}$) in glia. Scale bar: 5 µm. Bottom: Quantification of pERK fluorescence intensity in all three conditions. Statistical comparisons done using two-sided *t* tests. Scatter plots show all the data points with mean±SEM. Data points: NMJ Significance: p<0.01 (**).

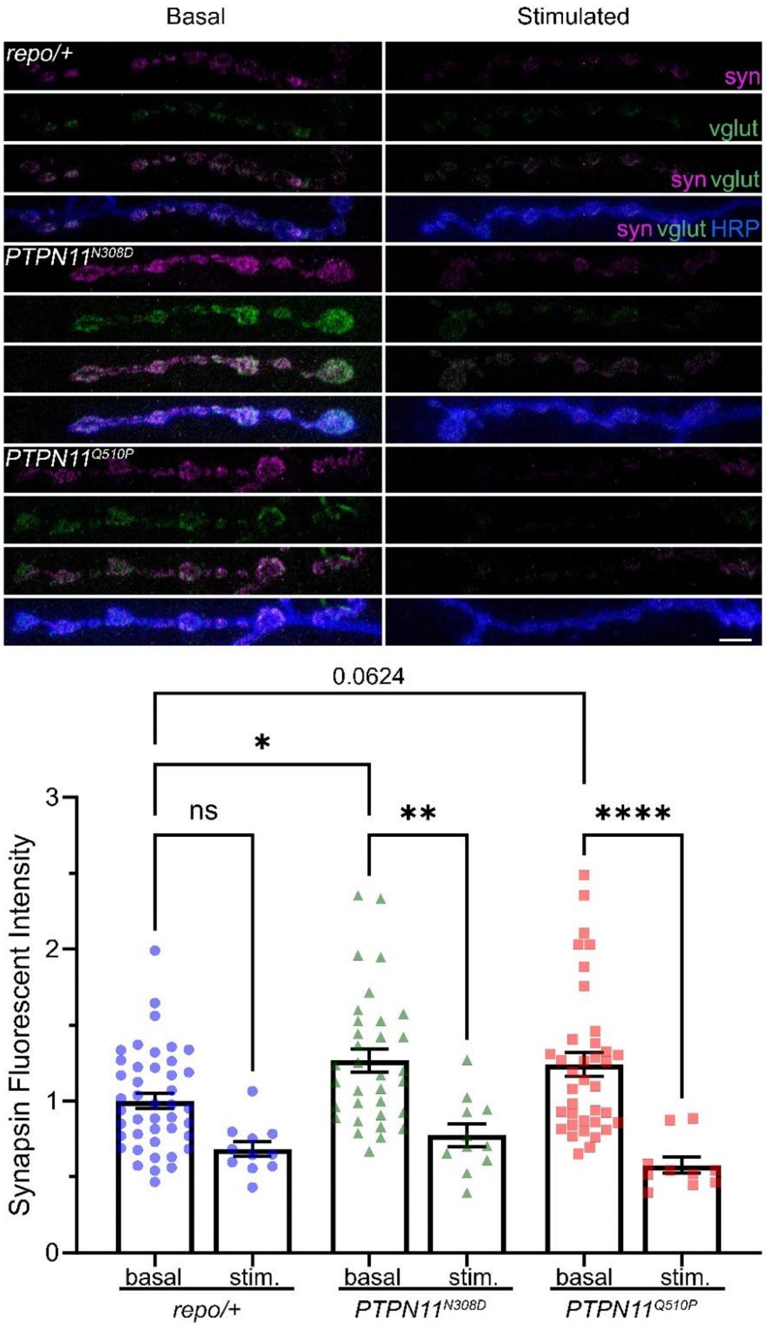

**Figure 4.7: Glial NS/NSML mutants increase Syn levels with stimulation-dependent loss**
Representative NMJ synaptic boutons labeled for Synapsin (syn, magenta), vesicular glutamate transporter (vglut, green) and horseradish peroxidase (HRP, blue) in glial transgenic driver control (*repo*-Gal4/$w^{1118}$, top) and driving *PTPN11*$^{N308D}$ (*repo* Gal4>*PTPN11*$^{N308D}$, middle) and *PTPN11*$^{Q510P}$ (*repo*-Gal4>*PTPN11*$^{Q510P}$, bottom) in glia. NMJs without stimulation (basal, left) and 10 min 90 mM [K$^+$] (stimulated, right). Scale bar: 5 µm. Quantification of Synapsin fluorescence intensity in all six conditions (basal and stimulated). Statistical comparison done using a two-way ANOVA, followed by Tukey's multiple comparisons test. Scatter plots show all data points with mean±SEM. Data points: NMJ number. Significance: $p<0.05$ (*), $p<0.01$ (**),$p<0.0001$ (****), and not significant (n.s.).

## PTPN11/Csw has glial roles in regulating glutamatergic neurotransmission

In my dissertation work, I discovered a glial role for *PTPN11/Csw* in regulating neurotransmission. Previously, I found ubiquitous expression of wildtype *csw* in the *csw* null background rescues neurotransmission defects. Based on all previous work in establishing the neuronal mechanism, I expected that re-expression of wildtype *csw* exclusively in neurons would rescue neurotransmission. Contrary to this expectation, I found *csw* is required in both neurons and glia to rescue neurotransmission, indicating a dual requirement in both cell types (Fig. 3.7; 3.8). This is especially intriguing, as the only known glial roles previously reported for *PTPN11/csw* are the regulation of neurogenesis and gliogenesis in early development,[189,190] and in response to injury in adults.[37,191,192] Glia involvement in regulating neurotransmission is well established,[33,35,193] and the NMJ is a tripartite synapse consisting of presynaptic neuron, postsynaptic muscle, and perisynaptic glia. At the *Drosophila* NMJ, glia are known to have roles regulating glutamatergic transmission, such as clearing released glutamate via excitatory amino acid transporters (EAATs).[214] This is important since impaired glutamate uptake can elevate neurotransmission and cause excitotoxicity. However, glial *PTPN11*/*csw* loss increases neurotransmission via an elevated frequency of SV fusion and increased quantal content, indicating a presynaptic change (Fig. 3.9). To confirm this presynaptic mechanism, I did a preliminary experiment with glial-targeted NS and NSML *PTPN11* point mutations and found that local NMJ pERK levels are elevated, albeit weakly (Fig 4.6). Likewise, Syn levels are elevated under basal conditions, and drastically decreased with stimulation (Fig 4.7). Together, these changes phenocopy neuron-targeted NS and NSML *PTPN11* point mutations, suggesting that glial *PTPN1/csw* is acting in the same presynaptic mechanism. This rules out perisynaptic processes (such as EAATs) being the primary cause of elevated neurotransmission with glial-targeted manipulations. Instead, the most likely cause is a change in glia-to-neuron crosstalk.

Since glial *PTPN11* is able to drive changes in neurotransmission, an opportunity arises to target glia in NS and NSML patient treatment options alongside neurons.

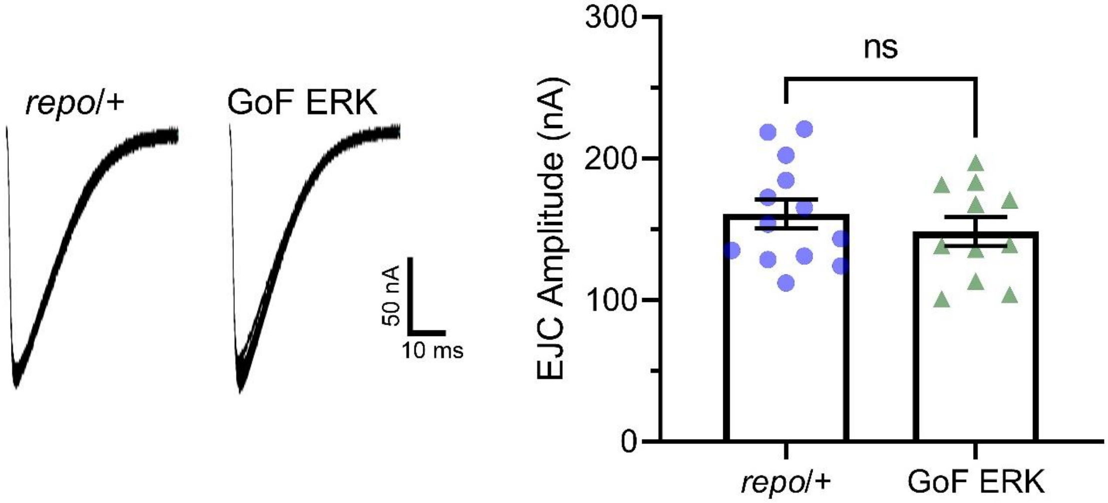

**Figure 4.8: Glial PTPN11 is not acting by upregulating glial MAPK/ERK signaling** Representative two-electrode voltage-clamp (TEVC) recordings of excitatory junction current (EJC) traces showing 10 superimposed evoked synaptic responses (1.0 mM $Ca^{2+}$) in glial driver control (*repo*-Gal4/$w^{1118}$) and glial $ERK^{GoF}$ (*repo*-Gal4>$ERK^{SEM}$). Quantification of the mean EJC amplitudes using a two-sided *t* test. Scatter plots show all the data points with mean±SEM. Data points: NMJ number. Significance: p>0.05 not significant (n.s).

Therefore, understanding the mechanism of glial action is paramount in designing these treatments. Future work into this glial role should expand on the mechanism already established, hopefully elucidating targets for possible pharmaceutical interventions. Clear points of interest include 1) the phosphatase role PTPN11 is normally performing in glia, 2) the trigger(s) of PTPN11 activation, 3) the glia-to-neuron signal initiating the neuronal pathway, 4) the glial receptor and downstream signaling cascade, and 5) the specific glial subtypes involved. As PTPN11/Csw is well established to work via MAPK/ERK signaling, it is easy to hypothesize that glial function normally regulates this pathway in glia to lead to changes in presynaptic neurotransmission. However, preliminary results show that the ERK GoF mutant that recapitulates all neuronal phenotypes when expressed in neurons, does not elevate neurotransmission when expressed in glia (Fig 4.8). This finding suggests that glial PTPN11/Csw is acting independent of the MAPK/ERK signaling pathway, which is unexpected based on all previous work. Other signaling pathways are known to be affected in NS and NSML patient-derived point mutants, such as EGFR, Notch, and JAK/STAT pathways[82,91] and one of these may be the driving force behind the glial signaling mechanism. Future analysis of these pathways utilizing targeted genetics to specifically perturb glial signaling pathways, as well as immunochemistry analysis of the endpoint markers of these pathways should be done to define the glial-specific PTPN11/Csw mechanism.

One way to further focus on the glial mechanism is to determine the glial subtypes involved. At the *Drosophila* NMJ, there are three known glial subtypes; perineurial glia (PG), subperineurial glia (SPG), and wrapping glia (WG).[32] Each class has roles at the NMJ that could contribute to elevation of neurotransmission strength. The PG and SPG classes together form the blood-brain barrier that maintains ionic homeostasis.[33] SPG are known to secrete the Wnt ligand Wingless (Wg; Wnt-1) to modulate neurotransmission efficacy.[36] Knockdown of glial specific Wg elevates spontaneous event frequency but decreases action potential dependent synaptic functional responses[36]. A preliminary screen using the UAS/Gal4 binary transgenic system to drive *csw* RNAi in these various subtypes indicates that Csw has a role in regulating neurotransmission in PG and SPG classes, but not in wrapping glia (Fig 4.9). As these two classes are known to work together to from the blood-brain barrier it is possibly being disrupted in NS and NSML leading to changes in neurotransmission. However, I hypothesize that the SPG Wnt-1/Wg signal is what triggers the neuronal PTPN11/Csw driven pathway, as glial-derive Wg has already been shown to regulate presynaptic neurotransmission.[36] In this proposed mechanism, PG do not have a direct role, but are instead necessary to enable proper SPG signaling. This proposed mechanism can be explored in the future by exploiting *wingless* tagged with GFP, allowing for the visualization of glial specific signaling. Additionally, knocking down *wingless* signaling in these specific glial subtypes and analyzing synaptic function responses would allow for us to directly link the glial signal to neuronal function.

Finally, a clear candidate for regulating the PTPN11/Csw glial mechanism is FMRP. The work done in this dissertation to show the FMRP interaction was done exclusively with null mutant animals, so cell type specificity was not tested (Fig. 2.16). However, the Broadie Lab has clearly established that FMRP is involved in neuron-to-glia signaling, and that glial roles are disrupted in FXS.[185,215] Additionally, both FMRP and Csw have been established to interact with the Draper receptor,[37,185] albeit in the different contexts of development and injury models, respectively.[37,185,215] Thus, it is reasonable to

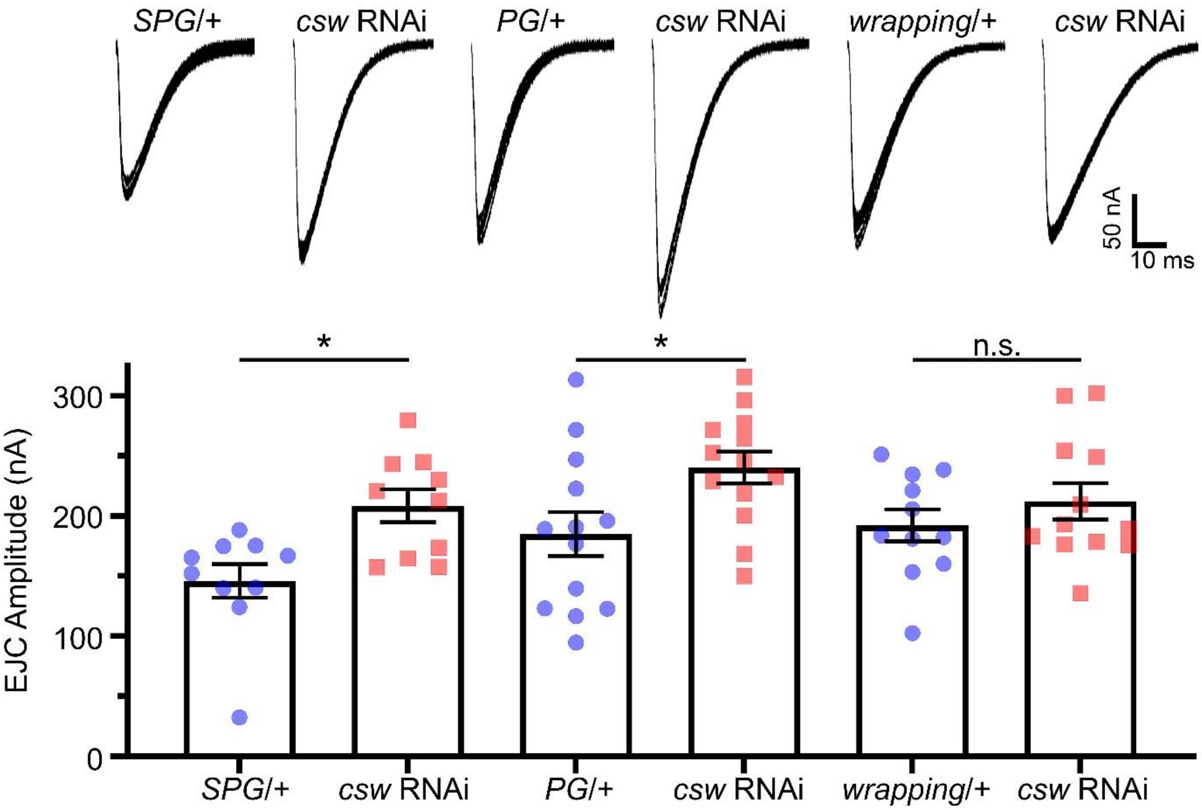

**Figure 4.9: SPG and PG glia are involved in elevating basal neurotransmission** Representative two-electrode voltage-clamp (TEVC) recordings of excitatory junction current (EJC) traces showing 10 superimposed evoked synaptic responses (1.0 mM $Ca^{2+}$). Top Left: SPG driver control (*SPG*-Gal4/TRiP Ctl) and SPG glial *csw* RNAi (*SPG*-Gal4>*csw* RNAi). Top Middle: PG driver control (*PG*-Gal4/TRiP Ctl) and PG glial *csw* RNAi (*PG*-Gal4>*csw* RNAi). Top Right: wrapping glial driver control (*wrapping*-Gal4/TRiP Ctl) and wrapping glial *csw* RNAi (*wrapping*-Gal4>*csw* RNAi). Bottom: Quantification of the mean EJC amplitudes using a two-sided *t* tests. Scatter plots show all the data points with mean±SEM. Data points: NMJ number. Significance: $p<0.05$ (*), $p>0.05$ not significant (n.s).

hypothesize that FMRP regulation of PTPN11/Csw within glia is going awry in NS and NSML, as well as FXS. This is a really exciting avenue to expand on, due to the possibility of broadening our overall understanding of three diseases by exploring this glial-specific mechanism, and possibly uncovering common therapeutic targets and new treatment avenues. To start exploring these interactions, I would genetically knockdown and overexpress FMRP specifically in glia in the *csw* null mutant, as well as the NS/NSML patient-derived *PTPN11* point mutant backgrounds, to examine effects on presynaptic neurotransmission. Additionally, I would genetically knockdown and overexpress *csw* specifically in glia in the *dfmr1* null background (FXS model) and examine presynaptic neurotransmission. These experiments should establish if these proteins are interacting within glia to shape presynaptic neurotransmission, before moving on to test more specific glial subtype functions and mechanistic interactions.

## Final Conclusions

My dissertation research has established that PTPN11/Csw regulates both basal glutamatergic neurotransmission strength and short-term plasticity through presynaptic MAPK/ERK signaling that in turn phosphorylates Synapsin to control SV fusion availability. When PTPN11/Csw phosphatase activity is perturbed by complete loss or point mutations, causing disruption of its autoinhibition mechanism, PTPN11/Csw aberrantly upregulates presynaptic MAPK/ERK signaling to cause Synapsin-dependent increases in glutamate release probability. Thus, more SVs are available in an enlarged readily-releasable pool, sustaining neurotransmission under conditions of greater demand. My thesis work clearly indicates that PTPN11/Csw has a presynaptic role in glutamatergic neurons, which is likely linked to NS/NSML perturbed learning and memory abilities, as well as the other behavioral impairments. I have also discovered an exciting novel PTPN11/Csw role within glia for the control of presynaptic neurotransmission. Future work into clarifying the glial mechanism of action may lead to new therapeutic strategies. Finally, I have established that FMRP regulates Csw to control presynaptic neurotransmission, connecting the FXS, NS, and NSML disease states for the first time. This interconnection expands our overall understanding of each of these cognitive impairment neurological conditions, and this link will hopefully lead to breakthroughs in future treatments via this shared mechanism.

## References

1. Xiong, H., Tang, F., Guo, Y., Xu, R. & Lei, P. Neural circuit changes in neurological disorders: Evidence from in vivo two-photon imaging. *Ageing Res Rev* **87**, 101933 (2023).
2. Lepeta, K. *et al.* Synaptopathies: synaptic dysfunction in neurological disorders – A review from students to students. *J Neurochem* **138**, 785 (2016).
3. Wingbermühle, E. *et al.* Cognitive Phenotype and Psychopathology in Noonan Syndrome Spectrum Disorders through Various Ras/MAPK Pathway Associated Gene Variants. *J Clin Med* **11**, (2022).
4. Pierpont, E. I. *et al.* Genotype differences in cognitive functioning in Noonan syndrome. *Genes Brain Behav* **8**, 275–282 (2009).
5. Ugur, B., Chen, K. & Bellen, H. J. Drosophila tools and assays for the study of human diseases. *Dis Model Mech* **9**, 235 (2016).
6. Ogienko, A. A. *et al.* Drosophila as a Model Organism to Study Basic Mechanisms of Longevity. *Int J Mol Sci* **23**, (2022).
7. Duffy, J. B. GAL4 system in Drosophila: a fly geneticist's Swiss army knife. *Genesis* **34**, 1–15 (2002).
8. Berger, C., Renner, S., Lüer, K. & Technau, G. M. The commonly used marker ELAV is transiently expressed in neuroblasts and glial cells in the Drosophila embryonic CNS. *Dev Dyn* **236**, 3562–3568 (2007).
9. Heigwer, F., Port, F. & Boutros, M. RNA Interference (RNAi) Screening in Drosophila. *Genetics* **208**, 853 (2018).
10. Mirzoyan, Z. *et al.* Drosophila melanogaster: A Model Organism to Study Cancer. *Front Genet* **10**, (2019).
11. Menon, K. P., Carrillo, R. A. & Zinn, K. Development and plasticity of the Drosophila larval neuromuscular junction. *Wiley Interdiscip Rev Dev Biol* **2**, 647–670 (2013).
12. Chen, I. & Lui, F. Neuroanatomy, Neuron Action Potential. *StatPearls* (2023).
13. Van Vactor, D. & Sigrist, S. J. Presynaptic Morphogenesis, Active Zone Organization and Structural Plasticity in Drosophila. *Curr Opin Neurobiol* **43**, 119 (2017).
14. Nose, A. Generation of neuromuscular specificity in Drosophila: novel mechanisms revealed by new technologies. *Front Mol Neurosci* **5**, (2012).
15. Hoang, B. & Chiba, A. Single-cell analysis of Drosophila larval neuromuscular synapses. *Dev Biol* **229**, 55–70 (2001).
16. Stocker, B. *et al.* Structural and Molecular Properties of Insect Type II Motor Axon Terminals. *Front Syst Neurosci* **12**, (2018).
17. Fouquet, W. *et al.* Maturation of active zone assembly by Drosophila Bruchpilot. *J Cell Biol* **186**, 129–145 (2009).
18. Chen, K. & Featherston, D. E. Discs-large (DLG) is clustered by presynaptic innervation and regulates postsynaptic glutamate receptor subunit composition in Drosophila. *BMC Biol* **3**, (2005).
19. Qin, G. *et al.* Four different subunits are essential for expressing the synaptic glutamate receptor at neuromuscular junctions of Drosophila. *J Neurosci* **25**, 3209–3218 (2005).
20. Han, Y. *et al.* Excess glutamate release triggers subunit-specific homeostatic receptor scaling. *Cell Rep* **42**, (2023).
21. Kopke, D. L., Lima, S. C., Alexandre, C. & Broadie, K. Notum coordinates synapse development via extracellular regulation of Wingless trans-synaptic signaling. *Development* **144**, 3499–3510 (2017).

22. Guangming, G., Junhua, G., Chenchen, Z., Yang, M. & Wei, X. Neurexin and Neuroligins Maintain the Balance of Ghost and Satellite Boutons at the Drosophila Neuromuscular Junction. *Front Neuroanat* **14**, (2020).
23. Bhimreddy, M., Rushton, E., Kopke, D. L. & Broadie, K. Secreted C-type lectin regulation of neuromuscular junction synaptic vesicle dynamics modulates coordinated movement. *J Cell Sci* **134**, (2021).
24. Vasileva, M., Renden, R., Horstmann, H., Gitler, D. & Kuner, T. Overexpression of synapsin Ia in the rat calyx of Held accelerates short-term plasticity and decreases synaptic vesicle volume and active zone area. *Front Cell Neurosci* **7**, (2013).
25. Hur, J. H., Lee, S. H., Kim, A. Y. & Koh, Y. H. Regulation of synaptic architecture and synaptic vesicle pools by Nervous wreck at Drosophila Type 1b glutamatergic synapses. *Experimental & Molecular Medicine 2018 50:3* **50**, e462–e462 (2018).
26. Hong, H. *et al.* Structural Remodeling of Active Zones Is Associated with Synaptic Homeostasis. *The Journal of Neuroscience* **40**, 2817 (2020).
27. Wichmann, C. & Sigrist, S. J. The active zone T-bar--a plasticity module? *J Neurogenet* **24**, 133–145 (2010).
28. Bao, H. *et al.* AP180 maintains the distribution of synaptic and vesicle proteins in the nerve terminal and indirectly regulates the efficacy of Ca2+- triggered exocytosis. *J Neurophysiol* **94**, 1888–1903 (2005).
29. Long, A. A. *et al.* Presynaptic Calcium Channel Localization and Calcium-Dependent Synaptic Vesicle Exocytosis Regulated by the Fuseless Protein. *The Journal of Neuroscience* **28**, 3668 (2008).
30. Mohrmann, R., Matthies, H. J., Woodruff, E. & Broadie, K. Stoned B Mediates Sorting of Integral Synaptic Vesicle Proteins. *Neuroscience* **153**, 1048 (2008).
31. Jetti, S. K. *et al.* Molecular logic of synaptic diversity between Drosophila tonic and phasic motoneurons. *Neuron* **111**, 3554-3569.e7 (2023).
32. Brink, D. L., Gilbert, M., Xie, X., Petley-Ragan, L. & Auld, V. J. Glial Processes at the Drosophila Larval Neuromuscular Junction Match Synaptic Growth. *PLoS One* **7**, 37876 (2012).
33. Yildirim, K., Petri, J., Kottmeier, R. & Klämbt, C. Drosophila glia: Few cell types and many conserved functions. *Glia* **67**, 5–26 (2019).
34. Stork, T. *et al.* Organization and Function of the Blood–Brain Barrier in Drosophila. *Journal of Neuroscience* **28**, 587–597 (2008).
35. Calderon, M. R. *et al.* Delta/Notch signaling in glia maintains motor nerve barrier function and synaptic transmission by controlling matrix metalloproteinase expression. *Proc Natl Acad Sci U S A* **119**, e2110097119 (2022).
36. Kerr, K. S. *et al.* Glial wingless/Wnt regulates glutamate receptor clustering and synaptic physiology at the Drosophila neuromuscular junction. *J Neurosci* **34**, 2910–2920 (2014).
37. Logan, M. A. *et al.* Negative regulation of glial engulfment activity by Draper terminates glial responses to axon injury. *Nat Neurosci* **15**, 722 (2012).
38. Zhang, B. & Stewart, B. Voltage-clamp analysis of synaptic transmission at the Drosophila larval neuromuscular junction. *Cold Spring Harb Protoc* **2010**, (2010).
39. Bykhovskaia, M. & Vasin, A. Electrophysiological analysis of synaptic transmission in Drosophila. *Wiley Interdiscip Rev Dev Biol* **6**, (2017).
40. Kopke, D. L. *et al.* Carrier of Wingless (Cow) Regulation of Drosophila Neuromuscular Junction Development. *eNeuro* **7**, (2020).
41. Repicky, S. & Broadie, K. Metabotropic Glutamate Receptor–Mediated Use–Dependent Down-Regulation of Synaptic Excitability Involves the Fragile X Mental Retardation Protein. *J Neurophysiol* **101**, 672–687 (2009).
42. Jackman, S. L. & Regehr, W. G. The Mechanisms and Functions of Synaptic Facilitation. *Neuron* **94**, 447–464 (2017).

43. Kalkstein, J. M. & Magleby, K. L. Augmentation Increases Vesicular Release Probability in the Presence of Masking Depression at the Frog Neuromuscular Junction. *The Journal of Neuroscience* **24**, 11391 (2004).
44. Vandael, D., Borges-Merjane, C., Zhang, X. & Correspondence, P. J. Short-Term Plasticity at Hippocampal Mossy Fiber Synapses Is Induced by Natural Activity Patterns and Associated with Vesicle Pool Engram Formation. *Neuron* **107**, 509-521.e7 (2020).
45. Xue, R. *et al.* Doc2-mediated superpriming supports synaptic augmentation. *Proceedings of the National Academy of Sciences* **115**, E5605–E5613 (2018).
46. Harris, K. P. & Littleton, J. T. Transmission, Development, and Plasticity of Synapses. *Genetics* **201**, 345–375 (2015).
47. Regehr, W. G. Short-Term Presynaptic Plasticity. *Cold Spring Harb Perspect Biol* **4**, a005702 (2012).
48. Chung, S., Li, X. & Nelson, S. B. Short-term depression at thalamocortical synapses contributes to rapid adaptation of cortical sensory responses in vivo. *Neuron* **34**, 437–446 (2002).
49. Zucker, R. S. & Regehr, W. G. Short-term synaptic plasticity. *Annu Rev Physiol* **64**, 355–405 (2002).
50. Kaeser, P. S. & Regehr, W. G. The readily releasable pool of synaptic vesicles Definitions and measurements of RRP. *Curr Opin Neurobiol* **43**, 63–70 (2017).
51. Bliss, T. V. P. & Cooke, S. F. Long-term potentiation and long-term depression: a clinical perspective. *Clinics* **66**, 3 (2011).
52. Pagani, M. R., Oishi, K., Gelb, B. D. & Zhong, Y. The phosphatase SHP2 regulates the spacing effect for long-term memory induction. *Cell* **139**, 186–198 (2009).
53. Medina, J. H. & Viola, H. ERK1/2: A Key Cellular Component for the Formation, Retrieval, Reconsolidation and Persistence of Memory. *Front Mol Neurosci* **0**, 361 (2018).
54. Rizzoli, S. O. & Betz, W. J. Synaptic vesicle pools. *Nature Reviews Neuroscience 2005 6:1* **6**, 57–69 (2005).
55. Denker, A. & Rizzoli, S. O. Synaptic vesicle pools: an update. *Front Synaptic Neurosci* **2**, (2010).
56. Kaeser, P. S. & Regehr, W. G. The readily releasable pool of synaptic vesicles. *Curr Opin Neurobiol* **43**, 63 (2017).
57. Goel, P. *et al.* Homeostatic scaling of active zone scaffolds maintains global synaptic strength. *J Cell Biol* **218**, 1706 (2019).
58. Delgado, R., Maureira, C., Oliva, C., Kidokoro, Y. & Labarca, P. Size of vesicle pools, rates of mobilization, and recycling at neuromuscular synapses of a Drosophila mutant, shibire. *Neuron* **28**, 941–953 (2000).
59. Gan, Q. & Watanabe, S. Synaptic Vesicle Endocytosis in Different Model Systems. *Front Cell Neurosci* **12**, (2018).
60. Pieribone, V. A. *et al.* Distinct pools of synaptic vesicles in neurotransmitter release. *Nature 1995 375:6531* **375**, 493–497 (1995).
61. Akbergenova, Y. & Bykhovskaia, M. Synapsin maintains the reserve vesicle pool and spatial segregation of the recycling pool in Drosophila presynaptic boutons. *Brain Res* **1178**, 52–64 (2007).
62. Zhang, M. & Augustine, G. J. Synapsins and the Synaptic Vesicle Reserve Pool: Floats or Anchors? *Cells 2021, Vol. 10, Page 658* **10**, 658 (2021).
63. Gitler, D., Cheng, Q., Greengard, P. & Augustine, G. J. Synapsin IIa controls the reserve pool of glutamatergic synaptic vesicles. *J Neurosci* **28**, 10835–10843 (2008).
64. Gitler, D. *et al.* Molecular determinants of synapsin targeting to presynaptic terminals. *J Neurosci* **24**, 3711–3720 (2004).
65. Godenschwege, T. A. *et al.* Flies lacking all synapsins are unexpectedly healthy but are impaired in complex behaviour. *European Journal of Neuroscience* **20**, 611–622 (2004).

66. Sun, J., Bronk, P., Liu, X., Han, W. & Südhof, T. C. Synapsins regulate use-dependent synaptic plasticity in the calyx of Held by a Ca2+/calmodulin-dependent pathway. *Proc Natl Acad Sci U S A* **103**, 2880 (2006).
67. Akbergenova, Y. & Bykhovskaia, M. Synapsin regulates vesicle organization and activity-dependent recycling at Drosophila motor boutons. *Neuroscience* **170**, 441–52 (2010).
68. Winther, Å. M. E. *et al.* An Endocytic Scaffolding Protein together with Synapsin Regulates Synaptic Vesicle Clustering in the Drosophila Neuromuscular Junction. *The Journal of Neuroscience* **35**, 14756 (2015).
69. Mayford, M. Protein kinase signaling in synaptic plasticity and memory. *Curr Opin Neurobiol* **17**, 313–317 (2007).
70. Cargnello, M. & Roux, P. P. Activation and Function of the MAPKs and Their Substrates, the MAPK-Activated Protein Kinases. *Microbiology and Molecular Biology Reviews* **76**, 496–496 (2012).
71. Plotnikov, A., Zehorai, E., Procaccia, S. & Seger, R. The MAPK cascades: Signaling components, nuclear roles and mechanisms of nuclear translocation. *Biochimica et Biophysica Acta (BBA) - Molecular Cell Research* **1813**, 1619–1633 (2011).
72. Kim, E. K. & Choi, E. J. Pathological roles of MAPK signaling pathways in human diseases. *Biochimica et Biophysica Acta (BBA) - Molecular Basis of Disease* **1802**, 396–405 (2010).
73. Giachello, C. N. G. *et al.* MAPK/Erk-dependent phosphorylation of synapsin mediates formation of functional synapses and short-term homosynaptic plasticity. *J Cell Sci* **123**, 881–893 (2010).
74. Zhu, G. *et al.* Phase Separation of Disease-Associated SHP2 Mutants Underlies MAPK Hyperactivation. *Cell* **183**, 490-502.e18 (2020).
75. Mirza, F. J. & Zahid, S. The Role of Synapsins in Neurological Disorders. *Neurosci Bull* **34**, 349 (2018).
76. Wang, X. *et al.* Activation of the extracellular signal-regulated kinase pathway contributes to the behavioral deficit of fragile x-syndrome. *J Neurochem* **121**, 672–679 (2012).
77. Johnson, E. M. *et al.* PTPN11 Gain-of-Function Mutations Affect the Developing Human Brain, Memory, and Attention. *Cerebral Cortex (New York, NY)* **29**, 2915 (2019).
78. Sweatt, J. D. Mitogen-activated protein kinases in synaptic plasticity and memory. *Curr Opin Neurobiol* **14**, 311–317 (2004).
79. Noonan, J. A. Hypertelorism with Turner phenotype. A new syndrome with associated congenital heart disease. *Am J Dis Child* **116**, 373–380 (1968).
80. Tartaglia, M., Gelb, B. D. & Zenker, M. Noonan syndrome and clinically related disorders. *Best Pract Res Clin Endocrinol Metab* **25**, 161 (2011).
81. Bouchikhi, I. El *et al.* Noonan syndrome-causing genes: Molecular update and an assessment of the mutation rate. *Int J Pediatr Adolesc Med* **3**, 133 (2016).
82. Oishi, K. *et al.* Transgenic Drosophila models of Noonan syndrome causing PTPN11 gain-of-function mutations. *Hum Mol Genet* **15**, 543–553 (2006).
83. Perkins, L. A., Larsen, I. & Perrimon, N. corkscrew encodes a putative protein tyrosine phosphatase that functions to transduce the terminal signal from the receptor tyrosine kinase torso. *Cell* **70**, 225–236 (1992).
84. Hof, P., Pluskey, S., Dhe-Paganon, S., Eck, M. J. & Shoelson, S. E. Crystal structure of the tyrosine phosphatase SHP-2. *Cell* **92**, 441–450 (1998).
85. Köhn, M. Turn and Face the Strange: A New View on Phosphatases. *ACS Cent Sci* **6**, 467 (2020).
86. Virshup, D. M. & Shenolikar, S. From Promiscuity to Precision: Protein Phosphatases Get a Makeover. *Mol Cell* **33**, 537–545 (2009).
87. Chen, Y. N. P. *et al.* Allosteric inhibition of SHP2 phosphatase inhibits cancers driven by receptor tyrosine kinases. *Nature* **535**, 148–152 (2016).

88. Yu, Z. H. *et al.* Structural and Mechanistic Insights into LEOPARD Syndrome-Associated SHP2 Mutations. *J Biol Chem* **288**, 10472 (2013).
89. Johnson Hamlet, M. R. & Perkins, L. A. Analysis of corkscrew signaling in the Drosophila epidermal growth factor receptor pathway during myogenesis. *Genetics* **159**, 1073 (2001).
90. Lee, Y. S. *et al.* Mechanism and treatment for the learning and memory deficits associated with mouse models of Noonan syndrome. *Nat Neurosci* **17**, 1736 (2014).
91. Das, T. K. *et al.* Drosophila RASopathy models identify disease subtype differences and biomarkers of drug efficacy. *iScience* **24**, (2021).
92. Nakagama, Y. *et al.* Noonan syndrome-associated biallelic LZTR1 mutations cause cardiac hypertrophy and vascular malformations in zebrafish. *Mol Genet Genomic Med* **8**, (2020).
93. Pierpont, E. I. Neuropsychological Functioning in Individuals with Noonan Syndrome: a Systematic Literature Review with Educational and Treatment Recommendations. *Journal of Pediatric Neuropsychology 2015 2:1* **2**, 14–33 (2015).
94. Oishi, K. *et al.* Phosphatase-defective LEOPARD syndrome mutations in PTPN11 gene have gain-of-function effects during Drosophila development. *Hum Mol Genet* **18**, 193 (2009).
95. Martinez-Molina, M., Fabregat-Pratdepadua, M. & Bielsa Marsol, I. Noonan Syndrome with Multiple Lentigines. *Actas Dermosifiliogr* (2022) doi:10.1016/j.ad.2022.05.028.
96. Gelb, B. D. & Tartaglia, M. Noonan syndrome and related disorders: dysregulated RAS-mitogen activated protein kinase signal transduction. *Hum Mol Genet* **15 Spec No 2**, (2006).
97. Tartaglia, M., Aoki, Y. & Gelb, B. D. The molecular genetics of RASopathies: An update on novel disease genes and new disorders. *Am J Med Genet C Semin Med Genet* **190**, 425 (2022).
98. Martin, J. P. & Bell, J. A PEDIGREE OF MENTAL DEFECT SHOWING SEX-LINKAGE. *J Neurol Psychiatry* **6**, 154–157 (1943).
99. Protic, D. D. *et al.* Fragile X Syndrome: From Molecular Aspect to Clinical Treatment. *Int J Mol Sci* **23**, (2022).
100. Bailey, D. B., Raspa, M., Olmsted, M. & Holiday, D. B. Co-occurring conditions associated with FMR1 gene variations: findings from a national parent survey. *Am J Med Genet A* **146A**, 2060–2069 (2008).
101. Bailey, D. B., Raspa, M., Bishop, E. & Holiday, D. No change in the age of diagnosis for fragile x syndrome: findings from a national parent survey. *Pediatrics* **124**, 527–533 (2009).
102. Ciaccio, C. *et al.* Fragile X syndrome: a review of clinical and molecular diagnoses. *Ital J Pediatr* **43**, (2017).
103. Kidd, S. A. *et al.* Fragile X syndrome: a review of associated medical problems. *Pediatrics* **134**, 995–1005 (2014).
104. Richter, J. D. & Zhao, X. The molecular biology of FMRP: new insights into fragile X syndrome. *Nature Reviews Neuroscience 2021 22:4* **22**, 209–222 (2021).
105. Leehey, M. A. Fragile X-associated Tremor/Ataxia Syndrome (FXTAS): Clinical Phenotype, Diagnosis and Treatment. *J Investig Med* **57**, 830 (2009).
106. Darnell, J. C. & Klann, E. The Translation of Translational Control by FMRP: Therapeutic Targets for Fragile X Syndrome. *Nat Neurosci* **16**, 1530 (2013).
107. Darnell, J. C. *et al. FMRP Stalls Ribosomal Translocation on MRNAs Linked to Synaptic Function and Autism*. (2011).
108. Razak, K. A., Dominick, K. C. & Erickson, C. A. Developmental studies in fragile X syndrome. *Journal of Neurodevelopmental Disorders 2020 12:1* **12**, 1–15 (2020).

109. Lozano, R., Azarang, A., Wilaisakditipakorn, T. & Hagerman, R. J. Fragile X syndrome: A review of clinical management. *Intractable Rare Dis Res* **5**, 145–157 (2016).
110. Myrick, L. K. *et al.* Independent role for presynaptic FMRP revealed by an FMR1 missense mutation associated with intellectual disability and seizures. *Proc Natl Acad Sci U S A* **112**, 949–956 (2015).
111. Starke, E. L., Zius, K. & Barbee, S. A. FXS causing missense mutations disrupt FMRP granule formation, dynamics, and function. *PLoS Genet* **18**, e1010084 (2022).
112. Ascano, M. *et al.* FMRP targets distinct mRNA sequence elements to regulate protein expression. *Nature 2012 492:7429* **492**, 382–386 (2012).
113. Drozd, M., Bardoni, B. & Capovilla, M. Modeling Fragile X Syndrome in Drosophila. *Front Mol Neurosci* **11**, 124 (2018).
114. Dahlhaus, R. Of men and mice: modeling the fragile X syndrome. *Front Mol Neurosci* **11**, 333192 (2018).
115. Zhang, Y. Q. *et al.* Drosophila fragile X-related gene regulates the MAP1B homolog Futsch to control synaptic structure and function. *Cell* **107**, 591–603 (2001).
116. Willemsen, R. & Kooy, R. F. Mouse models of fragile X-related disorders. *Dis Model Mech* **16**, (2023).
117. D'Hooge, R. *et al.* Mildly impaired water maze performance in maleFmr1 knockout mice. *Neuroscience* **76**, 367–376 (1997).
118. Deng, P.-Y., Sojka, D. & Klyachko, V. A. Abnormal Presynaptic Short-Term Plasticity and Information Processing in a Mouse Model of Fragile X Syndrome. *The Journal of Neuroscience* **31**, 10971 (2011).
119. Coffee, R. L., Tessier, C. R., Woodruff, E. A. & Broadie, K. Fragile X mental retardation protein has a unique, evolutionarily conserved neuronal function not shared with FXR1P or FXR2P. *Dis Model Mech* **3**, 471–485 (2010).
120. Bolduc, F. V., Bell, K., Cox, H., Broadie, K. S. & Tully, T. Excess protein synthesis in Drosophila Fragile X mutants impairs long-term memory. *Nat Neurosci* **11**, 1143–1145 (2008).
121. Ding, Q., Wu, X., Li, X. & Wang, H. Vorinostat Corrects Cognitive and Non-Cognitive Symptoms in a Mouse Model of Fragile X Syndrome. *Int J Neuropsychopharmacol* **25**, 147–159 (2022).
122. Jacquemont, S. *et al.* The challenges of clinical trials in fragile X syndrome. *Psychopharmacology (Berl)* **231**, 1237 (2014).
123. Grabb, M. C. & Potter, W. Z. CNS Trial Failures: Using the Fragile X Syndrome-mGluR5 drug target to highlight the complexities of translating preclinical discoveries into human trials. *J Clin Psychopharmacol* **42**, 234 (2022).
124. Barford, D. & Neel, B. G. Revealing mechanisms for SH2 domain mediated regulation of the protein tyrosine phosphatase SHP-2. *Structure* **6**, 249–254 (1998).
125. Rauen, K. A. The RASopathies. *Annu Rev Genomics Hum Genet* **14**, 355–369 (2013).
126. Hale, C. R. *et al.* FMRP regulates mRNAs encoding distinct functions in the cell body and dendrites of CA1 pyramidal neurons. *Elife* **10**, (2021).
127. Kushner, S. A. *et al.* Modulation of presynaptic plasticity and learning by the H-ras/extracellular signal-regulated kinase/synapsin I signaling pathway. *J Neurosci* **25**, 9721–9734 (2005).
128. Çaku, A., Pellerin, D., Bouvier, P., Riou, E. & Corbin, F. Effect of lovastatin on behavior in children and adults with fragile X syndrome: an open-label study. *Am J Med Genet A* **164A**, 2834–2842 (2014).
129. Muscas, M., Louros, S. R. & Osterweil, E. K. Lovastatin, not Simvastatin, Corrects Core Phenotypes in the Fragile X Mouse Model. *eNeuro* **6**, (2019).

130. Perrimon, N., Engstrom, L. & Mahowald, A. P. A pupal lethal mutation with a paternally influenced maternal effect on embryonic development in Drosophila melanogaster. *Dev Biol* **110**, 480–491 (1985).
131. Chou, V. T., Johnson, S., Long, J., Vounatsos, M. & Van Vactor, D. dTACC restricts bouton addition and regulates microtubule organization at the Drosophila neuromuscular junction. *Cytoskeleton (Hoboken)* **77**, 4 (2020).
132. Ni, J.-Q. *et al.* A genome-scale shRNA resource for transgenic RNAi in Drosophila. *Nature Methods 2011 8:5* **8**, 405–407 (2011).
133. Perkins, L. A. *et al.* The transgenic RNAi project at Harvard medical school: Resources and validation. *Genetics* **201**, 843–852 (2015).
134. Karunanithi, S., Marin, L., Wong, K. & Atwood, H. L. Quantal Size and Variation Determined by Vesicle Size in Normal and Mutant Drosophila Glutamatergic Synapses. *The Journal of Neuroscience* **22**, 10267 (2002).
135. Kauwe, G. & Isacoff, E. Y. Rapid feedback regulation of synaptic efficacy during high-frequency activity at the Drosophila larval neuromuscular junction. *Proc Natl Acad Sci U S A* **110**, 9142 (2013).
136. Louis Newman, Z. *et al.* Input-specific plasticity and homeostasis at the Drosophila larval neuromuscular junction HHS Public Access eTOC Blurb. *Neuron* **93**, 1388–1404 (2017).
137. Dobrunz, L. E. & Stevens, C. F. Heterogeneity of Release Probability, Facilitation, and Depletion at Central Synapses. *Neuron* **18**, 995–1008 (1997).
138. Stevens, R. J., Akbergenova, Y., Jorquera, R. A. & Littleton, J. T. Abnormal Synaptic Vesicle Biogenesis in Drosophila Synaptogyrin Mutants. *Journal of Neuroscience* **32**, 18054–18067 (2012).
139. Baccino-Calace, M., Schmidt, K. & Müller, M. The E3 ligase Thin controls homeostatic plasticity through neurotransmitter release repression. *Elife* **11**, (2022).
140. Smith, J. A., Mayeux, P. R. & Schnellmann, R. G. Delayed MEK/ERK Inhibition by Trametinib Attenuates Systemic Inflammatory Responses and Multi-Organ Injury in Murine Sepsis. *Crit Care Med* **44**, e711 (2016).
141. Zhong, H. M., Ding, Q. H., Chen, W. P. & Luo, R. Bin. Vorinostat, a HDAC inhibitor, showed anti-osteoarthritic activities through inhibition of iNOS and MMP expression, p38 and ERK phosphorylation and blocking NF-κB nuclear translocation. *Int Immunopharmacol* **17**, 329–335 (2013).
142. Cziko, A.-M. J. *et al.* Genetic Modifiers of dFMR1 Encode RNA Granule Components in Drosophila. *Genetics* **182**, 1051–1060 (2009).
143. Levi, O. & Arava, Y. mRNA association by aminoacyl tRNA synthetase occurs at a putative anticodon mimic and autoregulates translation in response to tRNA levels. *PLoS Biol* **17**, e3000274 (2019).
144. Linke, R. *et al.* The MEK1/2-ERK1/2 pathway is activated in chronic rhinosinusitis with nasal polyps. *Arch Immunol Ther Exp (Warsz)* **62**, 217–229 (2014).
145. Vara, H., Onofri, F., Benfenati, F., Sassoè-Pognetto, M. & Giustetto, M. ERK activation in axonal varicosities modulates presynaptic plasticity in the CA3 region of the hippocampus through synapsin I. *Proc Natl Acad Sci U S A* **106**, 9872 (2009).
146. Engholm-Keller, K. I. *et al.* The temporal profile of activity-dependent presynaptic phospho-signalling reveals long-lasting patterns of poststimulus regulation. (2019) doi:10.1371/journal.pbio.3000170.
147. Ramaswami, M., Krishnan, K. S. & Kelly, R. B. Intermediates in synaptic vesicle recycling revealed by optical imaging of Drosophila neuromuscular junctions. *Neuron* **13**, 363–375 (1994).
148. Kopke, D. L. & Broadie, K. FM Dye Cycling at the Synapse: Comparing High Potassium Depolarization, Electrical and Channelrhodopsin Stimulation. *J Vis Exp* **2018**, 57765 (2018).

149. Corvol, J.-C. *et al.* Depolarization Activates ERK and Proline-rich Tyrosine Kinase 2 (PYK2) Independently in Different Cellular Compartments in Hippocampal Slices *. *Journal of Biological Chemistry* **280**, 660–668 (2005).
150. Boggio, E. M., Putignano, E., Sassoè-Pognetto, M., Pizzorusso, T. & Giustetto, M. Visual Stimulation Activates ERK in Synaptic and Somatic Compartments of Rat Cortical Neurons with Parallel Kinetics. *PLoS One* **2**, e604 (2007).
151. Cheng, Q., Song, S. H. & Augustine, G. J. Molecular Mechanisms of Short-Term Plasticity: Role of Synapsin Phosphorylation in Augmentation and Potentiation of Spontaneous Glutamate Release. *Front Synaptic Neurosci* **10**, (2018).
152. Liu, L. *et al.* The BRAF and MEK Inhibitors Dabrafenib and Trametinib: Effects on Immune Function and in Combination with Immunomodulatory Antibodies Targeting PD-1, PD-L1, and CTLA-4. *Clinical Cancer Research* **21**, 1639–1651 (2015).
153. Richter, J. D. & Zhao, X. The molecular biology of FMRP: new insights into fragile X syndrome. *Nature Reviews Neuroscience 2021 22:4* **22**, 209–222 (2021).
154. Kidd, T., Bland, K. S. & Goodman, C. S. Slit is the midline repellent for the robo receptor in Drosophila. *Cell* **96**, 785–794 (1999).
155. Bagni, C. & Zukin, R. S. A Synaptic Perspective of Fragile X Syndrome and Autism Spectrum Disorders. *Neuron* vol. 101 1070–1088 Preprint at https://doi.org/10.1016/j.neuron.2019.02.041 (2019).
156. Casingal, C. R., Kikkawa, T., Inada, H., Sasaki, Y. & Osumi, N. Identification of FMRP target mRNAs in the developmental brain: FMRP might coordinate Ras/MAPK, Wnt/β-catenin, and mTOR signaling during corticogenesis. *Mol Brain* **13**, 1–13 (2020).
157. Greenblatt, E. J. & Spradling, A. C. Fragile X mental retardation 1 gene enhances the translation of large autism-related proteins. *Science* **361**, 709–712 (2018).
158. Tsang, B. *et al.* Phosphoregulated FMRP phase separation models activity-dependent translation through bidirectional control of mRNA granule formation. *Proc Natl Acad Sci U S A* **116**, 4218–4227 (2019).
159. Napoli, I. *et al.* The Fragile X Syndrome Protein Represses Activity-Dependent Translation through CYFIP1, a New 4E-BP. *Cell* **134**, 1042–1054 (2008).
160. Parkinson, W. M. *et al.* Synaptic roles for phosphomannomutase type 2 in a new Drosophila congenital disorder of glycosylation disease model. *Dis Model Mech* **9**, 513–527 (2016).
161. Dani, N., Zhu, H. & Broadie, K. Two Protein N-Acetylgalactosaminyl Transferases Regulate Synaptic Plasticity by Activity-Dependent Regulation of Integrin Signaling. *Journal of Neuroscience* **34**, 13047–13065 (2014).
162. Dear, M. L., Dani, N., Parkinson, W., Zhou, S. & Broadie, K. Two classes of matrix metalloproteinases reciprocally regulate synaptogenesis. *Development (Cambridge)* **143**, 75–87 (2016).
163. Osterwalder, T., Yoon, K. S., White, B. H. & Keshishian, H. A conditional tissue-specific transgene expression system using inducible GAL4. *Proceedings of the National Academy of Sciences* **98**, 12596–12601 (2001).
164. Barwell, T. *et al.* Regulating the UAS/GAL4 system in adult Drosophila with Tet-off GAL80 transgenes. *PeerJ* **5**, (2017).
165. Leahy, S. N., Song, C., Vita, D. J. & Broadie, K. FMRP activity and control of Csw/SHP2 translation regulate MAPK-dependent synaptic transmission. *PLoS Biol* **21**, (2023).
166. Kuromi, H. & Kidokoro, Y. Two distinct pools of synaptic vesicles in single presynaptic boutons in a temperature-sensitive Drosophila mutant, shibire. *Neuron* **20**, 917–925 (1998).
167. Cheng, Q., Song, S. H. & Augustine, G. J. Calcium-Dependent and Synapsin-Dependent Pathways for the Presynaptic Actions of BDNF. *Front Cell Neurosci* **11**, (2017).

168. Ojelade, S. A. *et al.* cindr, the Drosophila Homolog of the CD2AP Alzheimer's Disease Risk Gene, Is Required for Synaptic Transmission and Proteostasis. *Cell Rep* **28**, 1799 (2019).
169. Beck, K. *et al.* Loss of the Coffin-Lowry syndrome-associated gene RSK2 alters ERK activity, synaptic function and axonal transport in Drosophila motoneurons. *DMM Disease Models and Mechanisms* **8**, 1389–1400 (2015).
170. Johnson Hamlet, M. R. & Perkins, L. A. Analysis of Corkscrew Signaling in the Drosophila Epidermal Growth Factor Receptor Pathway During Myogenesis. *Genetics* **159**, 1073–1087 (2001).
171. Ariss, M. M., Terry, A. R., Islam, A. B. M. M. K., Hay, N. & Frolov, M. V. Amalgam regulates the receptor tyrosine kinase pathway through Sprouty in glial cell development in the Drosophila larval brain. *J Cell Sci* **133**, (2020).
172. Ogienko, A. A., Andreyeva, E. N., Omelina, E. S., Oshchepkova, A. L. & Pindyurin, A. V. Molecular and cytological analysis of widely-used Gal4 driver lines for Drosophila neurobiology. *BMC Genet* **21**, 1–11 (2020).
173. Mahr, A. & Aberle, H. The expression pattern of the Drosophila vesicular glutamate transporter: a marker protein for motoneurons and glutamatergic centers in the brain. *Gene Expr Patterns* **6**, 299–309 (2006).
174. Daniels, R. W. *et al.* Increased Expression of the Drosophila Vesicular Glutamate Transporter Leads to Excess Glutamate Release and a Compensatory Decrease in Quantal Content. *Journal of Neuroscience* **24**, 10466–10474 (2004).
175. Daniels, R. W. *et al.* A single vesicular glutamate transporter is sufficient to fill a synaptic vesicle. *Neuron* **49**, 11–16 (2006).
176. Vanlandingham, P. A. *et al.* AP180 couples protein retrieval to clathrin-mediated endocytosis of synaptic vesicles. *Traffic* **15**, 433–450 (2014).
177. Jan, L. Y. & Jan, Y. N. Antibodies to horseradish peroxidase as specific neuronal markers in Drosophila and in grasshopper embryos. *Proc Natl Acad Sci U S A* **79**, 2700 (1982).
178. Vasin, A. *et al.* Two Pathways for the Activity-Dependent Growth and Differentiation of Synaptic Boutons in Drosophila. *eNeuro* **6**, 60–79 (2019).
179. James, T. D., Zwiefelhofer, D. J. & Frank, C. A. Maintenance of homeostatic plasticity at the drosophila neuromuscular synapse requires continuous IP3-directed signaling. *Elife* **8**, (2019).
180. Adler, J. & Parmryd, I. Quantifying colocalization by correlation: The Pearson correlation coefficient is superior to the Mander's overlap coefficient. *Cytometry Part A* **77A**, 733–742 (2010).
181. Justs, K. A. *et al.* Presynaptic Mitochondrial Volume and Packing Density Scale with Presynaptic Power Demand. *The Journal of Neuroscience* **42**, 954 (2022).
182. Kim, M. *et al.* Inhibition of ERK-MAP kinase signaling by RSK during Drosophila development. *EMBO J* **25**, 3056–3067 (2006).
183. Guo, Y.-J. *et al.* ERK/MAPK signalling pathway and tumorigenesis. *Exp Ther Med* **19**, 1997 (2020).
184. Petley-Ragan, L. M., Ardiel, E. L., Rankin, C. H. & Auld, V. J. Accumulation of Laminin Monomers in Drosophila Glia Leads to Glial Endoplasmic Reticulum Stress and Disrupted Larval Locomotion. *J Neurosci* **36**, 1151–1164 (2016).
185. Vita, D. J., Meier, C. J. & Broadie, K. Neuronal fragile X mental retardation protein activates glial insulin receptor mediated PDF-Tri neuron developmental clearance. *Nature Communications 2021 12:1* **12**, 1–16 (2021).
186. Zhao, J. *et al.* Genetic dissection of mutual interference between two consecutive learning tasks in Drosophila. *Elife* **12**, (2023).

187. Blanco-Redondo, B. *et al.* Implications of the Sap47 null mutation for synapsin phosphorylation, longevity, climbing proficiency and behavioural plasticity in adult Drosophila. *J Exp Biol* **222**, (2019).
188. Lutz, B., Lu, H. C., Eichele, G., Miller, D. & Kaufman, T. C. Rescue of Drosophila labial null mutant by the chicken ortholog Hoxb-1 demonstrates that the function of Hox genes is phylogenetically conserved. *Genes Dev* **10**, 176–184 (1996).
189. Gauthier, A. S. *et al.* Control of CNS cell-fate decisions by SHP-2 and its dysregulation in Noonan syndrome. *Neuron* **54**, 245–262 (2007).
190. Zhu, Y. *et al.* Loss of Shp2 within radial glia is associated with cerebral cortical dysplasia, glial defects of cerebellum and impaired sensory-motor development in newborn mice. *Mol Med Rep* **17**, 3170–3177 (2018).
191. Servidei, T. *et al.* The protein tyrosine phosphatase SHP-2 is expressed in glial and neuronal progenitor cells, postmitotic neurons and reactive astrocytes. *Neuroscience* **82**, 529–543 (1997).
192. Kim, H. Y., Park, E. J., Joe, E. & Jou, I. Curcumin suppresses Janus kinase-STAT inflammatory signaling through activation of Src homology 2 domain-containing tyrosine phosphatase 2 in brain microglia. *J Immunol* **171**, 6072–6079 (2003).
193. Mazaud, D. *et al.* Transcriptional Regulation of the Glutamate/GABA/Glutamine Cycle in Adult Glia Controls Motor Activity and Seizures in Drosophila. *J Neurosci* **39**, 5269–5283 (2019).
194. Hamada, A. *et al.* Induction of Noonan syndrome-specific human-induced pluripotent stem cells under serum-, feeder-, and integration-free conditions. *In Vitro Cell Dev Biol Anim* **56**, 888–895 (2020).
195. Baldassari, S. *et al.* Vesicular Glutamate Release from Feeder-FreehiPSC-Derived Neurons. *Int J Mol Sci* **23**, 10545 (2022).
196. Saxton, T. M. *et al.* Abnormal mesoderm patterning in mouse embryos mutant for the SH2 tyrosine phosphatase Shp-2. *EMBO J* **16**, 2352 (1997).
197. Hoffner, MSN, ANP-BC, AOCNP, B. & Benchich, MSN, NP-C, AOCNP, K. Trametinib: A Targeted Therapy in Metastatic Melanoma. *J Adv Pract Oncol* **9**, 741 (2018).
198. Wozniak, M. B. *et al.* Vorinostat interferes with the signaling transduction pathway of T-cell receptor and synergizes with phosphoinositide-3 kinase inhibitors in cutaneous T-cell lymphoma. *Haematologica* **95**, 613 (2010).
199. Oellers, N. & Hafen, E. Biochemical Characterization of RolledSem, an Activated Form of Drosophila Mitogen-activated Protein Kinase. *Journal of Biological Chemistry* **271**, 24939–24944 (1996).
200. Kleber, J. *et al.* Synapsin is required to “boost” memory strength for highly salient events. *Learning & Memory* **23**, 9 (2016).
201. Vasin, A. *et al.* Synapsin Regulates Activity-Dependent Outgrowth of Synaptic Boutons at the Drosophila Neuromuscular Junction. *The Journal of Neuroscience* **34**, 10554 (2014).
202. Diantonio, A., Petersen, S. A., Heckmann, M. & Goodman, C. S. Glutamate Receptor Expression Regulates Quantal Size and Quantal Content at the Drosophila Neuromuscular Junction. *Journal of Neuroscience* **19**, 3023–3032 (1999).
203. DiAntonio, A. Glutamate Receptors At The Drosophila Neuromuscular Junction. *Int Rev Neurobiol* **75**, 165–179 (2006).
204. Weber, D., Richter, V., Rohwedder, A., Großjohann, A. & Thum, A. S. Learning and Memory in Drosophila Larvae. *Cold Spring Harb Protoc* **2023**, 150–156 (2023).
205. Strullu, M. *et al.* Juvenile myelomonocytic leukaemia and Noonan syndrome. *J Med Genet* **51**, 689–697 (2014).
206. Tartaglia, M. *et al.* Somatic mutations in PTPN11 in juvenile myelomonocytic leukemia, myelodysplastic syndromes and acute myeloid leukemia. *Nat Genet* **34**, 148–150 (2003).

207. Araki, T. *et al.* Mouse model of Noonan syndrome reveals cell type- and gene dosage-dependent effects of Ptpn11 mutation. *Nat Med* **10**, 849–857 (2004).
208. Citri, A. & Malenka, R. C. Synaptic plasticity: multiple forms, functions, and mechanisms. *Neuropsychopharmacology* **33**, 18–41 (2008).
209. Hallermann, S., Heckmann, M. & Kittel, R. J. Mechanisms of short-term plasticity at neuromuscular active zones of Drosophila. *HFSP J* **4**, 72 (2010).
210. Svenningsson, P. *et al.* Alterations in 5-HT1B receptor function by p11 in depression-like states. *Science* **311**, 77–80 (2006).
211. Sears, J. C. & Broadie, K. Use-Dependent, Untapped Dual Kinase Signaling Localized in Brain Learning Circuitry. *J Neurosci* **44**, e1126232024 (2024).
212. Pan, L., Zhang, Y. Q., Woodruff, E. & Broadie, K. The Drosophila Fragile X Gene Negatively Regulates Neuronal Elaboration and Synaptic Differentiation. *Current Biology* **14**, 1863–1870 (2004).
213. Michel, C. I., Kraft, R. & Restifo, L. L. Defective Neuronal Development in the Mushroom Bodies of Drosophila Fragile X Mental Retardation 1 Mutants. *The Journal of Neuroscience* **24**, 5798 (2004).
214. Stacey, S. M. *et al.* Drosophila Glial Glutamate Transporter Eaat1 Is Regulated by Fringe-Mediated Notch Signaling and Is Essential for Larval Locomotion. *The Journal of Neuroscience* **30**, 14446 (2010).
215. Song, C. & Broadie, K. Fragile X mental retardation protein coordinates neuron-to-glia communication for clearance of developmentally transient brain neurons. *Proc Natl Acad Sci U S A* **120**, (2023).